

Dissertation

Submitted to the
Combined Faculty of Natural Sciences and Mathematics
Heidelberg University, Germany
for the degree of
Doctor of Natural Sciences (Dr. rer. nat.)

Presented by
M.Sc. Swaantje Brzelinski
Born in Neunkirchen

Oral examination: 31.07.2020

Dynamics of the Late Oligocene Antarctic Ice Sheet

Referees: Prof. Dr. Oliver Friedrich

PD Dr. André Bornemann

ABSTRACT

Superimposed on a global long-term cooling trend from the warm conditions of the Paleogene into the colder Neogene [e.g., Zachos et al. (2001a)], the Oligocene epoch [33.9–23.03 Ma, Vandenberghe et al. (2012)] represents a transitional phase of Cenozoic climate evolution. It marks the onset of the Cenozoic “icehouse” that is thought to have commenced with the initiation of large ice sheets on Antarctica [e.g., Lear et al. (2000); DeConto et al. (2008)]. While the long-term evolution of the Oligocene Antarctic Ice Sheet (AIS) has been well established over the last two decades (Lear et al., 2000; Cramer et al., 2009), its short-term dynamics are not well understood. Furthermore, available proxy records of the Late Oligocene show opposing signals regarding the pacing and magnitude of Antarctic ice-volume variability, which hampers a full and mechanistic understanding of Late Oligocene ice-volume and climate dynamics. This thesis aims to address this paradox and contribute to a more sophisticated understanding of the Late Oligocene climate and cryosphere dynamics. Therefore, high-resolution benthic and planktic foraminiferal proxy records are generated based on deep-sea sediments drilled within the framework of the Integrated Ocean Drilling Program (IODP) Expedition 342 at Site U1406 (northwestern Atlantic). These records provide adequate fidelity to study the fundamental processes and mechanisms underlying ice-sheet waning and waxing on orbital timescales during the Late Oligocene. In the first part of this thesis, novel and unprecedented insights into short-term processes and mechanisms of AIS fluctuations are presented. Investigations of this thesis evidence that the Late Oligocene AIS was highly dynamic on orbital timescales. The AIS generally shifted between two states of glaciation, i.e., volumes of half the modern to slightly bigger than modern global ice-volumes, and smaller than to half the modern global ice volume. Insolation forcing is identified as a key player in modulating changes in the extent and dynamics of the AIS: The influence of eccentricity periodicities is higher when AIS volumes are smaller, whereas bigger ice-volume react more sensitively to changes in obliquity. Very large angles of the Earth’s spin axis are shown to cause severe deglaciation pulses. Potential consequences of those AIS dynamics are explored in the second part of this thesis. The first high-resolution planktic foraminiferal proxy record from the high Northern Atlantic (Site U1406) is presented. Potential changes in surface ocean characteristics in response to glacial dynamics of the Southern Hemisphere during the Late Oligocene are explored. It is shown that the meridional position and strength of the North Atlantic Current (NAC) during the Late Oligocene has varied as a function of glacial dynamics of the Southern Hemisphere. There are indications that the NAC variability caused changes in nutrient concentrations and alterations in the amount of northward heat transport, which has broader implications for the climate in the circum-North Atlantic region.

KURZFASSUNG

Das globale Klima der letzten ~50 Ma ist durch einen langfristigen Abkühlungstrend geprägt [e.g., Zachos et al. (2001a)]. Im Verlauf vom warmen Paläogen hin zum kühleren Neogen markiert das Oligozän [33.9–23.03 Ma, Vandenberghe et al. (2012)] eine klimatische Übergangsphase – gekennzeichnet durch die Initialisierung des antarktischen Eisschildes [e.g., Lear et al. (2000); DeConto et al. (2008)]. Längerfristige Dynamiken des antarktischen Eisschildes während des Oligozäns wurden in den letzten zwei Dekaden weitreichend erforscht und etabliert (Lear et al., 2000; Cramer et al., 2009). Kurzfristige Schwankungen hingegen sind weniger gut verstanden. Zudem zeigen Klimaarchive des späten Oligozäns gegensätzliche Signale in Bezug auf die Dynamik und das Volumen des antarktischen Eisschildes. Diese Umstände erschweren es, dass ein umfassenderes und mechanistischeres Verständnis zu Eisvolumina und Klimadynamiken des späten Oligozäns gewonnen werden kann. Das Ziel dieser Arbeit ist es, dieses Paradox zu beleuchten und fundiertere Einblicke in spät-oligozäne Eis- und Klimadynamiken zu gewinnen. Dafür wurden Tiefseesedimente herangezogen, die im Zuge der IODP Expedition 342 im Nordatlantik (Site U1406) erbohrt wurden. Es wurden zeitlich hoch aufgelöste Datensätze basierend auf Sauerstoff- und Kohlenstoff-Isotopen, sowie Mg/Ca Verhältnissen benthischer und planktischer Foraminiferen für das Intervall 25.95 bis 24.53 Ma generiert. Diese erlauben es, Rückschlüsse auf grundlegende Prozesse und Mechanismen zu ziehen, die der Dynamik des antarktischen Eisschildes während des späten Oligozäns auf orbitalen Zeitskalen zugrunde liegen. Im ersten Teil dieser Doktorarbeit werden neue und bisher nicht bekannte Einblicke zu kurzfristigen Prozessen und Mechanismen antarktischer Eisschwankungen dargelegt: Ergebnisse zeigen, dass das antarktische Eisschild eine hohe Dynamik auf orbitalen Zeitskalen hatte und sich zwischen zwei Vereisungsstadien bewegte. Ein Vereisungszustand beschreibt Eisvolumina, die halb so groß bis größer als das modernem globale Eisvolumen sind. Im zweiten Vereisungszustand hingegen sind Eisvolumina kleiner gleich 50 % des heutigen globalen Eisvolumens. Weiterführend wird gezeigt, dass die Insolation ein intrinsischer Faktor für das Ausmaß von Eisdynamiken und -volumen der Antarktis ist. Der Einfluss von Exzentrizität ist höher, wenn antarktisches Eisvolumen kleiner ist. Größere Eisvolumina reagieren hingegen sensitiver auf Obliquität. Phasen von extremer Erdneigung verursachen drastische Abschmelzereignisse. Eventuelle Auswirkungen dieser Eisschwankungen auf die generelle ozeanische Zirkulation und das globale Klima werden durch die Analyse von hoch-aufgelösten Klimadaten planktischer Foraminiferen ermittelt. Im ersten Klimaarchiv dieser Art für den Zeitabschnitt 25.95 bis 24.53 Ma kann gezeigt werden, dass die Stärke und meridionale Position des Nordatlantikstroms (NAC) in Abhängigkeit von Eisdynamiken der Südhemisphäre variiert hat. Damit einhergehend waren Veränderungen der Nährstoffverteilung in Oberflächenwasser des Nordatlantiks, sowie des nordwärtsgerichteten Wärmetransports zu beobachten mit vermeintlichen Auswirkungen auf das generelle Klima der Nordatlantikregion.

ACKNOWLEDGEMENTS

I would like to say a big thank you to the following people, who have contributed to the success of this thesis:

To my supervisor, Oliver Friedrich, for offering me the possibility of this PhD project, for his constant support, patience, advice, invaluable assistance and for the numerous opportunities I have had during my PhD, especially my participation in IODP Expedition 378. Thank you! To André Bornemann, for offering me the possibility of this PhD project, for reading my abstracts and many manuscript versions, your support during the last three and a half years and for being a referee to this thesis. To Paul Wilson for the collaboration in line with this PhD project, for his valuable input and fruitful discussions during your stay in Heidelberg, and for reading my manuscripts. To Bridget Wade for her help with planktic foraminiferal taxonomy and offering me to participate in the NERC Advanced Training Short Course on planktic foraminifera. To Jörg Pross for his fruitful discussions and advice on different aspects of this PhD project, for his support in writing abstracts, proposals, and my application for IODP Expedition 378, and for including me in the Meteor Cruise M144. Thank you also for being a member of my examination panel. To Diederik Liebrand and Tim van Peer for their endless support in providing U1406 age models and depth scales, their fruitful discussions and advice on orbital parameters, and their general enthusiasm for the (Late) Oligocene. To André Bahr for discussions and advice on orbital parameters and Mg/Ca sample processing. To Jörg Lippold for being a member of my examination panel, for support and contribution to the DFG proposal to further explore Late Oligocene glacial dynamics. To Richard Norris for his advice and discussions that contributed to the success of this PhD project, and support for my IODP Expedition 378 application. To Gerhard Schmiedl, through whom I discovered the fascinating world of foraminifera, and who introduced me to Oliver Friedrich.

To all members of the “Sedimentology and marine paleoenvironmental dynamics” and “Palynology and paleoenvironmental dynamics” working groups at Heidelberg University. For all the fun coffee breaks, summer barbecues and working group seminars.

To all Hiwi's that have contributed to the outcome of this thesis, including Barbara, Philipp, Verena, Franz, Lisa, Stephen, Emily, Selina and Hernan.

To Silvia, Christian, and Stefan for invaluable support during Mg/Ca measurements and general laboratory assistance at Heidelberg University. To Bernd for his endless efforts in keeping the Kiel Devise running so smoothly.

To all members of the Meteor cruise M144 that have made that experience ever more enjoyable.

To Ulla Röhl and Debbie Thomas, and all members of IODP Expedition 378. Sailing on this expedition was a fantastic opportunity and a memorable adventure.

To my dearest Blumis. You have welcomed me in Heidelberg with more love than I could have ever hoped for. Your constant support is a precious gift. Also, I would like to thank my friends for their support and many good memories of the past years. Special thanks go to my family for always being there for me and supporting me through ups and downs. I could not have written this thesis without you!

I thank my grandma Ami, who was my greatest supporter and shared my passion for the natural wonders of the earth.

Funding for this research was provided by the German Research Foundation (grants FR2544/12-1 and FR2544/12-2). Samples for the purpose of this research are provided by IODP. The European Consortium for Ocean Research Drilling (ECORD) is gratefully thanked for selecting me for an ECORD Scholarship and the participation in IODP Expedition 378.

CONTENTS

1	Objectives and outline.....	1
1.1	Thesis objectives.....	1
1.2	Thesis Outline.....	2
2	Introduction	3
2.1	Overview of Oligocene climate	3
2.1.1	<i>Oligocene glaciation history: From (multi)-million-year scale to orbital scale ice-sheet dynamics</i>	4
2.1.2	<i>Dynamics of the Oligocene AIS</i>	6
2.2	Foraminifera as proxies for paleoclimate and paleoceanography	8
2.3	Benthic and planktic foraminifera in the modern ocean	9
2.3.1	<i>Benthic foraminifera</i>	9
2.3.2	<i>Planktic foraminifera</i>	10
2.4	The use of stable isotopes of foraminifera	11
2.4.1	<i>Stable oxygen isotopes ($\delta^{18}O$)</i>	11
2.4.2	<i>Stable carbon isotopes ($\delta^{13}C$)</i>	16
2.4.2.1	<i>External factors</i>	16
2.4.2.2	<i>Internal factors</i>	17
2.5	The use of foraminiferal Mg/Ca ratios as a paleothermometer	19
2.5.1	<i>Benthic foraminiferal Mg/Ca</i>	21
2.5.2	<i>Planktic foraminiferal Mg/Ca</i>	21
2.6	The influence of diagenesis on foraminifera-based geochemical proxies	23
2.7	Investigated Foraminiferal Species	23
2.7.1	<i>Cibicidoides mundulus</i>	23
2.7.2	<i>Oridorsalis umbonatus</i>	24
2.7.3	<i>Catapsydrax dissimilis</i>	24
3	Study Area	27
3.1	The Northwestern Atlantic.....	27
3.1.1	<i>Geography.....</i>	27
3.1.2	<i>Modern oceanography of the North Atlantic</i>	28
3.1.3	<i>Oligocene oceanography of the North Atlantic</i>	29
3.2	IODP Site U1406	30
4	Methods	32
4.1	Sample material and sediment processing.....	32

4.2	Stable isotope measurements	33
4.3	Mg/Ca measurements	33
4.4	Paleotemperature reconstruction and Mg/Ca_{sw} corrections.....	34
4.5	$\delta^{18}\text{O}_{\text{sw}}$ calculations.....	35
4.5.1	<i>$\delta^{18}\text{O}_{\text{ivf-sw}}$ reconstructions for Site U1406</i>	36
4.5.2	<i>Uncertainties associated with seawater $\delta^{18}\text{O}_{\text{sw}}$ reconstruction</i>	36
4.5.3	<i>Spectral analyses.....</i>	37
4.6	Age model	37
5	Obliquity-paced Antarctic ice-volume fluctuations during the Late Oligocene.....	39
5.1	Results and discussion	40
5.1.1	<i>Stable oxygen isotope record.....</i>	40
5.1.2	<i>Assessment of contamination and diagenetic effects on the Mg/Ca ratios.....</i>	40
5.1.3	<i>BWT variability.....</i>	41
5.1.4	<i>Trends of Site U1406 $\delta^{18}\text{O}_{\text{sw}}$.....</i>	41
5.1.5	<i>Glacial-interglacial $\delta^{18}\text{O}_{\text{sw}}$ variability across study interval (25.95–25.78 Ma)</i>	42
5.1.6	<i>Possibility of a precursory bipolar glaciation.....</i>	46
5.1.7	<i>Influence of orbital pacing on the Late Oligocene AIS.....</i>	47
5.1.8	<i>$p\text{CO}_2$ forcing</i>	48
6	Antarctic ice-sheet response to combined eccentricity and obliquity forcing of the Late Oligocene	51
6.1	Introduction.....	51
6.2	Results and discussion	52
6.2.1	<i>Stable oxygen isotope record.....</i>	52
6.2.2	<i>Assessment of contamination and diagenetic effects on the Mg/Ca ratios.....</i>	53
6.2.3	<i>Late Oligocene BWT variability</i>	54
6.2.4	<i>Trends of Site U1406 $\delta^{18}\text{O}_{\text{sw}}$.....</i>	54
6.2.5	<i>Spectral and time series analysis.....</i>	56
6.2.6	<i>Re-evaluation of previously defined Oligocene glacial events.....</i>	56
6.2.7	<i>AIS variability across the study interval inferred from the Site U1406 $\delta^{18}\text{O}_{\text{sw}}$ record.....</i>	59
6.2.8	<i>Possibility of a precursory bipolar glaciation.....</i>	60
6.2.9	<i>Orbital Forcing of the Late Oligocene AIS.....</i>	60
6.2.10	<i>Amplitude response of Site U1406 $\delta^{18}\text{O}_{\text{sw}}$ to eccentricity and obliquity forcing</i>	62

6.2.11	<i>pCO₂ forcing</i>	65
7	Response of the high North Atlantic Ocean to AIS dynamics during the Late Oligocene	67
7.1	Introduction	67
7.2	Results and discussion	68
7.2.1	<i>Assessment of contamination and diagenetic effects on the Mg/Ca ratios</i>	68
7.2.2	<i>Sub-thermocline temperatures</i>	68
7.2.3	<i>Stable Site UI406 $\delta^{18}\text{O}$ and $\delta^{13}\text{C}$ records</i>	70
7.2.3.1	<i>Stable oxygen isotopes</i>	70
7.2.3.2	<i>Stable carbon isotopes</i>	71
7.2.4	<i>Site UI406 $\delta^{18}\text{O}_{\text{ivf-sw}}$</i>	71
7.2.5	<i>Variations in Site UI406 coarse fraction as a tracer for paleoproductivity</i>	71
7.2.6	<i>Changing influences of water masses in the North Atlantic as a driver of productivity changes at Site UI406</i>	73
7.2.7	<i>The response of the high North Atlantic to AIS dynamics during the Late Oligocene</i>	75
8	Conclusions and Outlook	80
8.1	Conclusions	80
8.1.1	<i>Late Oligocene AIS dynamics</i>	80
8.1.2	<i>The response of the North Atlantic to AIS dynamics during the Late Oligocene</i>	81
8.2	Societal significance of Late Oligocene AIS dynamics	82
8.3	Future perspectives	83
9	References	85
	Appendix	103

LIST OF FIGURES

Figure 2.1-1: Climatic evolution of the last 50 Myr.....	4
Figure 2.1-2: Modern global map displaying all core localities mentioned in the text.....	6
Figure 2.1-3: High-resolution $\delta^{18}\text{O}_{\text{BF}}$ records spanning the Oligocene including the EOT and the Oligocene-Miocene transition.	7
Figure 2.3-1: Conceptual TROX-Model.	10
Figure 2.4-1: Meridional net transport of water vapor.	13
Figure 2.4-2: Dominant influences on the oxygen isotope composition of foraminifera (see text for references).....	14
Figure 2.4-3: Influences of oceanic $\delta^{13}\text{C}_{\text{DIC}}$ on the carbon isotope composition of foraminifera) (see text for references).	18
Figure 2.7-1: Scanning electron microscope (SEM) and reflected light microscope micrographs of <i>O. umbonatus</i> , <i>C. mundulus</i> and <i>C. dissimilis</i> from IODP Site U1406.....	26
Figure 3.1-1: Modern north-south salinity profile of the deep western Atlantic (40°S to 60°N) after World Ocean Atlas (Boyer et al., 2013).	28
Figure 3.1-2: Modern sea-surface temperature distribution and surface circulation of the North Atlantic after World Ocean Atlas (Boyer et al., 2013).	29
Figure 3.2-1: Location IODP Site U1406.....	31
Figure 5.2-1: Paired isotope analyses of <i>C. mundulus</i> and <i>O. umbonatus</i>	41
Figure 5.2-2: Evaluation of <i>Oridorsalis umbonatus</i> test contamination.....	42
Figure 5.2-3: Geochemical proxy data from IODP Site U1406.....	43
Figure 5.2-4: Spectral Analysis of $\delta^{18}\text{O}_{\text{BF}}$, Mg/Ca and $\delta^{18}\text{O}_{\text{sw}}$ time series.	44
Figure 5.2-5: Sensitivity tests for Site U1406 $\delta^{18}\text{O}_{\text{sw}}$ -based ice-volume estimates.....	47
Figure 5.2-6: Comparison of ice-sheet dynamics across the study interval during the Late Oligocene.	49
Figure 6.3-1: Paired isotope analyses of <i>C. mundulus</i> and <i>O. umbonatus</i>	53
Figure 6.3-2: Evaluation of <i>O. umbonatus</i> test contamination.....	54
Figure 6.3-3: Geochemical proxy data from IODP Site U1406 for the interval 25.95 to 24.53 Ma.....	55
Figure 6.3-4: Time series analysis of $\delta^{18}\text{O}_{\text{BF}}$, Mg/Ca and $\delta^{18}\text{O}_{\text{sw}}$	58
Figure 6.3-5: Ice-volume estimates of ODP Site 690 and 1264 in comparison to Site U1406.....	61
Figure 6.3-6: Orbital forcing of Site U1406 $\delta^{18}\text{O}_{\text{sw}}$	63
Figure 6.3-7: Amplitude response of Site U1406 $\delta^{18}\text{O}_{\text{sw}}$ to eccentricity and obliquity forcing.	66
Figure 7.3-1: Evaluation of <i>C. dissimilis</i> test contamination.	69

Figure 7.3-2: Benthic and planktic proxy records of Site U1406..... 72

Figure 7.3-3: Evaluation of surface-water productivity at Site U1406. 76

Figure 7.3-4: Modern subsurface (600 m water depth) salinity (A) and temperature distribution (B) of the North Atlantic after World Ocean Atlas (Boyer et al., 2013). 77

Figure 7.4-1: Response of Northern Hemisphere subTs and $\delta^{18}\text{O}_{\text{ivf-sw}}$ to Southern Hemisphere glaciation dynamics. 79

LIST OF TABLES

Table 2.7-1: Deviations from oxygen and carbon isotopic equilibrium between foraminiferal tests and ambient seawater for selected species.	25
Table 5.2-1: Comparison of ice-volume estimates resulting from Site U1406 $\delta^{18}\text{O}_{\text{sw}}$ -based sensitivity tests.	45

LIST OF ABBREVIATIONS AND ACRONYMS

AABW	Antarctic Bottom Water
AAIW	Antarctic Intermediate Water
AIS	Antarctic Ice Sheet
AMOC	Atlantic Meridional Overturning Circulation
APC	Advanced piston corer
BWT	Bottom-water temperature
CaCO ₃	Calcium carbonate
CCSF	Core-composite depth below seafloor
CCV	Calcium carbonate veins
CF	Coarse fraction
DSDP	Deep Sea Drilling Project
DWBC	Deep Western Boundary Current
EAIS	East Antarctic Ice Sheet
EOT	Eocene-Oligocene transition
IODP	International Ocean Drilling Program
IRD	Ice-rafted debris
JAR	J-Anomaly Ridge
kyr	Thousand years
INADW	Lower component NADW
LSW	Labrador Sea Water
Ma	Mega annum (proverbially) = million years ago
MAR	Mid-Atlantic Ridge
Mg/Ca _{sw}	Mg/Ca ratio of seawater
MOGI	Mid-Oligocene Glacial Interval
Myr	Million years
NAC	North Atlantic Current
NADW	North Atlantic Deep Water
NCW	Northern Component Water
ODP	Ocean Drilling Project
<i>p</i> CO ₂	Partial pressure of atmospheric carbon dioxide
psu	Practical salinity unit
δ ¹³ C _{DIC}	Dissolved inorganic carbon of the ocean water
SEM	Scanning Electron Microscopy
SMOW	Standard Mean Ocean Water
SPG	Subpolar gyre

SSS	Sea-surface salinity
SST	Sea-surface temperature
STG	Subtropical gyre
subS	Sub-thermocline salinity
subT	Sub-thermocline temperature
TROX	Trophic conditions and OXYgen concentrations
uNADW	Upper component NADW
VPDB	Vienna Pee Dee Belemnite
XCB	Extended core barrel techniques
XRF	X-Ray Fluorescence
$\delta^{13}\text{C}$	Stable carbon isotopic composition
$\delta^{18}\text{O}$	Stable oxygen isotopic composition
$\delta^{18}\text{O}_{\text{ivf-sw}}$	Ice-volume free planktic foraminiferal $\delta^{18}\text{O}_{\text{sw}}$ signal
$\delta^{18}\text{O}_{\text{sw}}$	Oxygen isotopic composition of seawater
$[\text{CO}_3^{2-}]$	Carbonate ion concentration
(HCO_3^-)	Bicarbonate
$\Delta\delta^{13}\text{C}_{\text{PF-BF}}$	Planktic to benthic $\delta^{13}\text{C}$ gradient

1 OBJECTIVES AND OUTLINE

1.1 Thesis objectives

The transition from a world lacking large-scale continental ice shields to one dominated by such (Zachos et al., 2001a) makes the Oligocene epoch [33.9–23.03 Ma, Vandenberghe et al. (2012)] (Figure 2.1-1) one of the most interesting periods of the Cenozoic paleoclimate evolution. Long-term dynamics of the Oligocene AIS have been well constrained (Lear et al., 2000; Cramer et al., 2009), however state of the art short-term AIS variability is not well understood (Pekar et al., 2006; Hauptvogel et al., 2017; Liebrand et al., 2017). It is however crucial to assess short-term climate variability at submillennial [<1000 years (kyr)] timescales in order to meet the pacing of ongoing anthropogenic climate change, and (ii) at orbital timescales (10^5 – 10^4 kyr) to get a mechanistic understanding of the underlying short-term dynamics.

The selected target interval for this thesis is the Late Oligocene. The objectives of this thesis are twofold:

- 1) To investigate the dynamics of the AIS during the Late Oligocene. Specifically,
 - a. to identify dominant astronomical pacemakers and to test those for existing pacing theories;
 - b. to approximate the magnitude of ice-volume change and to draw a comparison to previous ice-volume estimates for the Late Oligocene;
 - c. to explore forcing mechanisms behind observed glaciation dynamics and whether those are comparable to the Pleistocene.
- 2) To assess the response of the North Atlantic in response to the glacial dynamics of the AIS during the Late Oligocene that is yet unknown.

To achieve the aims presented above, high-resolution benthic and planktic proxy records were generated on deep-sea sediment cores that were drilled within the framework of IODP Expedition 342 in the northwestern Atlantic (Site U1406) (Figure 2.1-2).

1.2 Thesis Outline

Chapter 2 gives a general introduction to the Oligocene's climate history with brief introductions to oceanographic, geographic, and cryospheric boundary conditions. A particular focus is drawn to the evolution of the Oligocene glaciation history that is expounded in more detail. Glaciation dynamics, together with underlying processes, are introduced. The remainder of this introduction presents background information on benthic and planktic foraminifera as paleoclimatologic and paleoceanographic proxies, specifically those used in this thesis. Additionally, the specific benthic and planktic foraminiferal species used in this thesis are presented.

Chapter 3 presents the study area of the northwestern Atlantic, including specifics about the geographical setting and its tectonic evolution. In addition, modern and Oligocene surface- and deep-water circulations systems are presented. A detailed description of IODP Site U1406 is also provided.

Chapter 4 summarizes the methods employed within the framework of this thesis. Information on the sample material, sample processing, and detailed procedures of geochemical analyses and applied calibrations are presented.

In **Chapter 5**, high-resolution benthic foraminiferal stable isotope ($\delta^{18}\text{O}_{\text{BF}}$) and Mg/Ca records from IODP Site U1406 over a short interval, spanning 25.95 to 25.78 Ma, are presented. The combined signal of the two proxy records is used to elucidate the temperature and ice-volume component of $\delta^{18}\text{O}_{\text{BF}}$. Ice-volume estimates are calculated and compared to previous studies. Along with complementary spectral analyses, this combined approach will give unprecedented insights into the Antarctic cryosphere's sensitivity to orbital pacing across the study interval.

As an extension to the investigations of **Chapter 5**, the high-resolution $\delta^{18}\text{O}_{\text{BF}}$ and Mg/Ca records from IODP Site U1406 are expanded over the interval 25.95 to 24.53 Ma and presented in **Chapter 6**. The following targets are addressed: Firstly, the concept of Oligocene glaciations will be re-assessed. Secondly, ice volumes will be estimated and set into comparison to previously inferred ice-volumes across the study interval. Thirdly, the orbital pacing of the AIS dynamics will be analyzed based on spectral and wavelet analyses. These results will be discussed in light of the Late Oligocene AIS's sensitivity to changing orbital forcing.

Chapter 7 aims to examine the response of the high Northern Atlantic to the dynamics of the Late Oligocene AIS presented in **Chapters 5** and **6**. Changes in subsurface-water characteristics are investigated for variabilities in the strength and position of the North Atlantic Current (NAC) that has a profound influence on the Late Oligocene's climatological and oceanographical configuration of the North Atlantic. Therefore, a multiproxy geochemical data set is generated on sample material from IODP Site U1406, including the gradient of planktic to benthic foraminiferal carbon isotopes ($\delta^{13}\text{C}$), coarse fraction data, sub-surface temperatures and subsurface salinity data.

Chapter 8 summarizes scientific outcomes, presents conclusions and wider implications resulting from the research results presented in this thesis. Furthermore, **Chapter 8** contains a section that explores future avenues for research that would complement the herein presented major findings.

2 INTRODUCTION

2.1 Overview of Oligocene climate

The Oligocene epoch [33.9–23.03 Ma, Vandenberghe et al. (2012)] (Figure 2.1-1) is situated in between the early Paleogene greenhouse climate and the Neogene icehouse climate and constitutes the earliest phase of the Earth's Cenozoic glaciation history with the initiation of permanent ice-sheets on Antarctica broadly contemporaneous with the Eocene-Oligocene boundary (EOT) (Zachos et al., 1996). At its younger end, the Oligocene is bracketed by ice-sheet expansion across the Oligocene-Miocene boundary (Miller et al., 1991b; Zachos et al., 2001a).

Superimposed on a long-term cooling trend, indicated by decreasing atmospheric $p\text{CO}_2$ concentrations of ~650 ppmv prior to 27 Ma to ~400 ppmv post 24 Ma (Henderiks and Pagani, 2008; Beerling and Royer, 2011; Zhang et al., 2013), the early Oligocene forms an interval of relative climate stability followed by climatic features such as an extended period of transient glaciation across the “middle” Oligocene, the late Oligocene warming and other high-frequency climate variability [e.g., Pälike et al. (2006); Liebrand et al. (2016, 2017)].

The exact size and locations of the ice sheets on Antarctica following their initiation across the EOT is a matter of ongoing debate. Additionally, the presence or absence of land ice on West Antarctica [e.g., Wilson and Luyendyk (2009)] and in the Northern Hemisphere [e.g., Moran et al. (2006)] are still poorly understood. The occurrence of ice-rafted debris (IRD) and dropstones in the North Atlantic (Moran et al., 2006; Eldrett et al., 2007; Tripathi et al., 2008) as well as the formation of Northern Hemisphere winter sea ice, indicated by diatom assemblages (Stickley et al., 2009, 2012), reflect at least the existence of short-lived, small glaciations in southern Greenland. However, based on modelling studies, the Oligocene is assumed to have resided in a unipolar glaciation state with no significant ice in the Northern Hemisphere (DeConto and Pollard, 2003; DeConto et al., 2008).

The initiation of the AIS across the EOT caused a strengthening of the Atlantic Meridional Overturning Circulation (AMOC) (Goldner et al., 2014) with active deep-water formation in the high northern latitudes of the Atlantic Ocean [e.g., Coxall et al. (2018)] and southern latitudes [e.g., Scher et al. (2006)]

filling the Atlantic Ocean with northern-sourced North Atlantic Deep Water (NADW) southern-sourced Antarctic Bottom Water (AABW), respectively. Oligocene bottom-water temperatures in the Atlantic Ocean were, on average, $\sim 5^\circ\text{C}$ (Lear et al., 2000). Constraints on the surface-water temperature are very sparse but indicate slightly warmer than modern sea-surface temperatures of $24\text{--}26^\circ\text{C}$ in the North Atlantic (Liu et al., 2018).

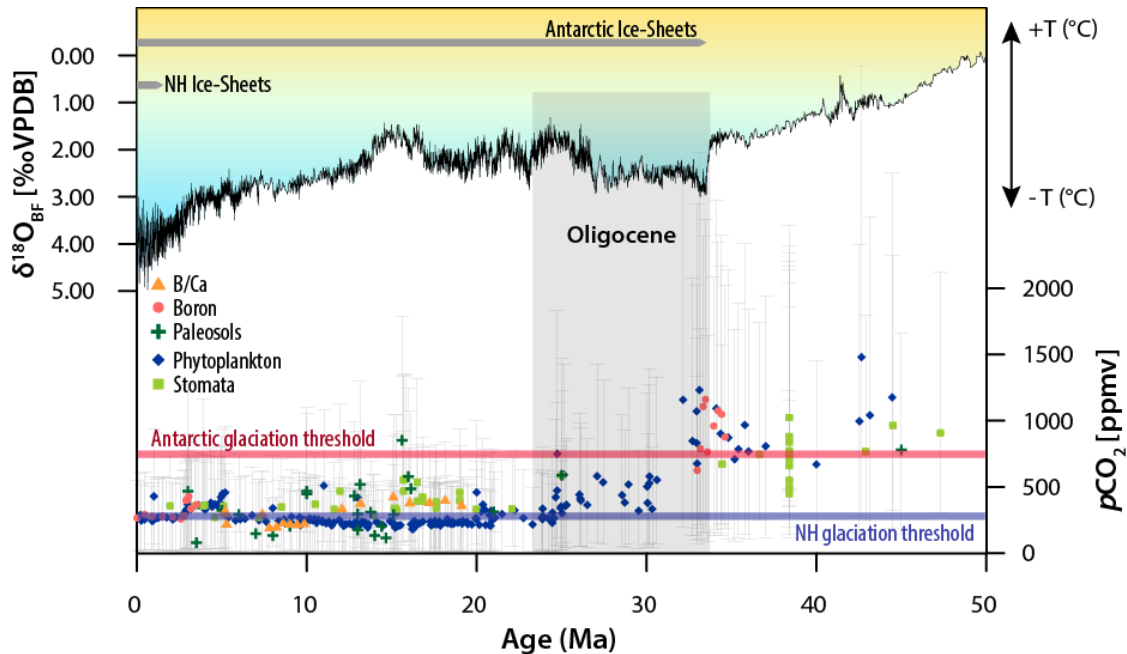


Figure 2.1-1: Climatic evolution of the last 50 Myr. Global compilation of $\delta^{18}\text{O}_{\text{BF}}$ data (Zachos et al., 2001a) together with a global compilation of atmospheric $p\text{CO}_2$ proxy records (Beerling and Royer, 2011; Zhang et al., 2013). Grey horizontal lines represent onset of Antarctic and Northern Hemisphere (=NH) glaciation (Zachos et al., 2001a). Red and blue horizontal lines represent $p\text{CO}_2$ thresholds for major Antarctic and NH glaciation resulting from a coupled climate-ice-sheet model (DeConto and Pollard, 2003; DeConto et al., 2008). Vertical black arrow in parallel with orange to blue shading indicate global temperature based on (Zachos et al., 2001a, 2008). Oligocene epoch [33.9–23.03 Ma, Vandenberghe et al. (2012)] is highlighted with a grey box.

2.1.1 Oligocene glaciation history: From (multi)-million-year scale to orbital scale ice-sheet dynamics

Based on early, low-resolution $\delta^{18}\text{O}_{\text{BF}}$ records, Miller and Fairbanks (1985) identified three noticeable cold events on multi-million-year (Myr) timescales during the Oligocene: Across the EOT, during the ‘middle’ Oligocene, and across the Oligocene-Miocene boundary. Miller et al. (1987) characterized these intervals based on covarying high $\delta^{18}\text{O}_{\text{BF}}$ ($>1.8\text{‰}$), and low-latitude planktic foraminiferal $\delta^{18}\text{O}$ ($\delta^{18}\text{O}_{\text{PF}}$) values, which they interpreted to represent significant ice sheet growth. Further support for glaciation was given by coeval occurrences of Antarctic glaciomarine sediments from the Ross Sea [Cape Roberts Project: MSST-1, CIROS-1; Barrett, (1986)], Prydz Bay [ODP Site 739, 742; Barron and Larsen, (1989)] and the Kerguelen Plateau [Site 748; Zachos et al. (1992)] (Figure 2.1-2).

The identification of Oligocene glaciations based on stable oxygen isotope records led to definitions of so-called isotope zones (Miller et al., 1991b, 1991a). The base of each Oi-zone was defined on the

maximum $\delta^{18}\text{O}_{\text{BF}}$ value and an alphanumeric name given to the zone (numbering from the base of the Oligocene onwards) (Miller et al., 1991). These isotope zones have been correlated to biozones and magnetostratigraphy, as well as to sequence boundaries identified by Haq et al. (1987), reflecting glacioeustatic lowerings, which lend support to glaciation during Oi-zones (Miller et al., 1991b). Initially, only two Oligocene oxygen isotope zones (Oi-1, Oi-2) were described (Miller et al., 1991b) due to relatively low-resolution $\delta^{18}\text{O}_{\text{BF}}$ records and often discontinuous, single hole drilling. The greater availability of sediment cores recovered by the Deep Sea Drilling Project (DSDP), the Ocean Drilling Project (ODP) and IODP have increased the number of high-resolution isotope records of Oligocene age over the last decades.

Based on higher-resolved $\delta^{18}\text{O}_{\text{BF}}$ records, the Oi-zonation scheme was updated by referring to prominent, recurring $\delta^{18}\text{O}_{\text{BF}}$ excursions as Oi-events. Additional global $\delta^{18}\text{O}_{\text{BF}}$ enrichments were identified, referred to as Oi-1a (32.8 Ma), Oi-1b (31.7 Ma), Oi-2a (28.3 Ma), Oi-2b (27.1 Ma) and Oi-2c (25.1 Ma) events (Pekar and Miller, 1996; Miller et al., 1998) (Figure 2.1-3). These were defined based on large $\delta^{18}\text{O}_{\text{BF}}$ increases ($>0.5\text{‰}$) with high maximum $\delta^{18}\text{O}_{\text{BF}}$ ($>2.0\text{‰}$) attained based on comparison of multiple ODP $\delta^{18}\text{O}_{\text{BF}}$ records (Pekar and Miller, 1996; Miller et al., 1998) (Figure 2.1-3). The global utility was established by correlation of Oi-events among the different $\delta^{18}\text{O}_{\text{BF}}$ records with biostratigraphy, Sr isotopic stratigraphy, and calibrated to magnetostratigraphy. Support for glaciation during Oi-events Oi-1a, Oi-1b, Oi-2a, and Oi-2b was given by coeval eustatic lowerings expressed as unconformities on passive margins on the New Jersey coastal plain (Pekar and Miller, 1996; Miller et al., 1998).

High-resolution studies of the Oligocene climate initiated with sediment records recovered during ODP Leg 154 [Site 926; equatorial Atlantic; Zachos et al. (1997); Pälike et al. (2006a)] (Figure 2.1-3). In contrast to the above-mentioned individual Oi-events on multi-Myr spacing, high-resolution stable isotope stratigraphy established an orbital influence on recurring $\delta^{18}\text{O}_{\text{BF}}$ maxima on astronomical timescales throughout the Oligocene (Zachos et al., 1997; Pälike et al., 2006a), which was supported by the generation of similar records at ODP Site 1090 [subantarctic Atlantic Ocean; Billups et al. (2004)], and ODP Site 1218 [equatorial Pacific Ocean; Wade and Pälike (2004); Lear et al. (2004)] (Figure 2.1-3). These high-resolution (≤ 10 kyr) $\delta^{18}\text{O}_{\text{BF}}$ records revealed a larger number of heavy $\delta^{18}\text{O}_{\text{BF}}$ time intervals that were renamed based on the ~ 400 kyr cycle of Earth's eccentricity (Wade and Pälike, 2004). The ODP Site 1218 benthic foraminiferal stable carbon isotope ($\delta^{13}\text{C}_{\text{BF}}$) and $\delta^{18}\text{O}_{\text{BF}}$ records show a strong response to astronomical forcing: (i) $\delta^{18}\text{O}_{\text{BF}}$ maxima occur during nodes (i.e., minima) of the ~ 1.2 -Myr-amplitude modulation of obliquity, (ii) high-amplitude variability of $\delta^{18}\text{O}_{\text{BF}}$ during eccentricity maxima, and (iii) continuous pacing of $\delta^{13}\text{C}_{\text{BF}}$ by the long-term periodicities of eccentricity (~ 400 kyr) (Wade and Pälike, 2004). Pälike et al. (2006b) illustrated the link between Oligocene $\delta^{13}\text{C}_{\text{BF}}$, $\delta^{18}\text{O}_{\text{BF}}$, and astronomical forcing has through box modelling experiments: Solar forcing drives changes in productivity and carbon burial on eccentricity timescales due to the long residence time of carbon in the ocean. Periods of increased carbon burial will cause atmospheric $p\text{CO}_2$ levels to decrease, which in turn causes global cooling and preconditions ice-sheet expansion. To that effect, Zachos et al. (1997)

suggested that enhanced carbon burial is likely an effect of enhanced upwelling intensities triggered by strengthened meridional temperature gradients during glacial, i.e., cold episodes. It was therefore concluded that the dynamics of the carbon cycle in response to changes in solar insolation might modulate global climate change on eccentricity timescales during the Oligocene (Pälike et al., 2006b). A strong imprint of eccentricity in Oligocene climate dynamics was confirmed by a more recent study (Liebrand et al., 2016) presenting a high-resolution (~ 3 kyr) $\delta^{13}\text{C}_{\text{BF}}$ and $\delta^{18}\text{O}_{\text{BF}}$ record covering an Oligocene interval from as early as 30.1 Ma from ODP Site 1264 (South Atlantic) (Figure 2.1-3). Liebrand et al. (2017) established that ~ 2.4 -Myr eccentricity cycles pace recurring episodes of high-amplitude ~ 110 kyr variability in $\delta^{18}\text{O}_{\text{BF}}$.

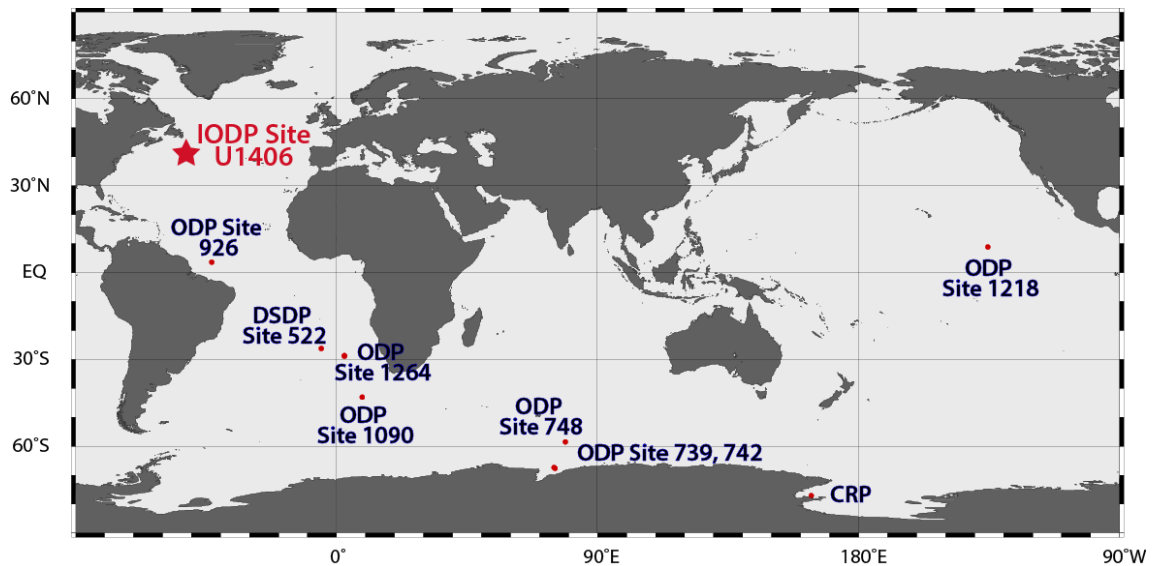


Figure 2.1-2: Modern global map displaying all core localities mentioned in the text. Integrated Ocean Drilling Program (IODP) Site U1406 highlighted with a red star (Norris et al., 2014a). Other discussed localities (red circles, blue font) are the Cape Roberts Project [CRP; Barrett (1989)], Ocean Drilling Project Site 739, 742 [Prydz Bay, Barron and Larsen (1989)], and ODP Site 748 [Kerguelen Plateau, Zachos et al. (1992)], ODP Site 1090 [subantarctic Atlantic Ocean, Billups et al. (2004)].

2.1.2 Dynamics of the Oligocene AIS

Whereas model output data predict a very stable AIS once formed (DeConto and Pollard, 2003; Pollard and DeConto, 2005), ice-proximal (Barrett, 1986; Naish et al., 2001; Hambrey et al., 2002; Galeotti et al., 2016; Fielding, 2018) and ice-distal proxy records (Wade and Pälike, 2004; Lear et al., 2004; Pälike et al., 2006a, 2006b; Liebrand et al., 2016, 2017) indicate variability of the AIS across the Oligocene. Not only is there a major discrepancy between studies that infer a stable versus a dynamic AIS during the Oligocene, but there is also controversy in regards to the degree of AIS dynamics inferred from ice-proximal and ice-distal proxy records, which is especially pronounced across the Late Oligocene.

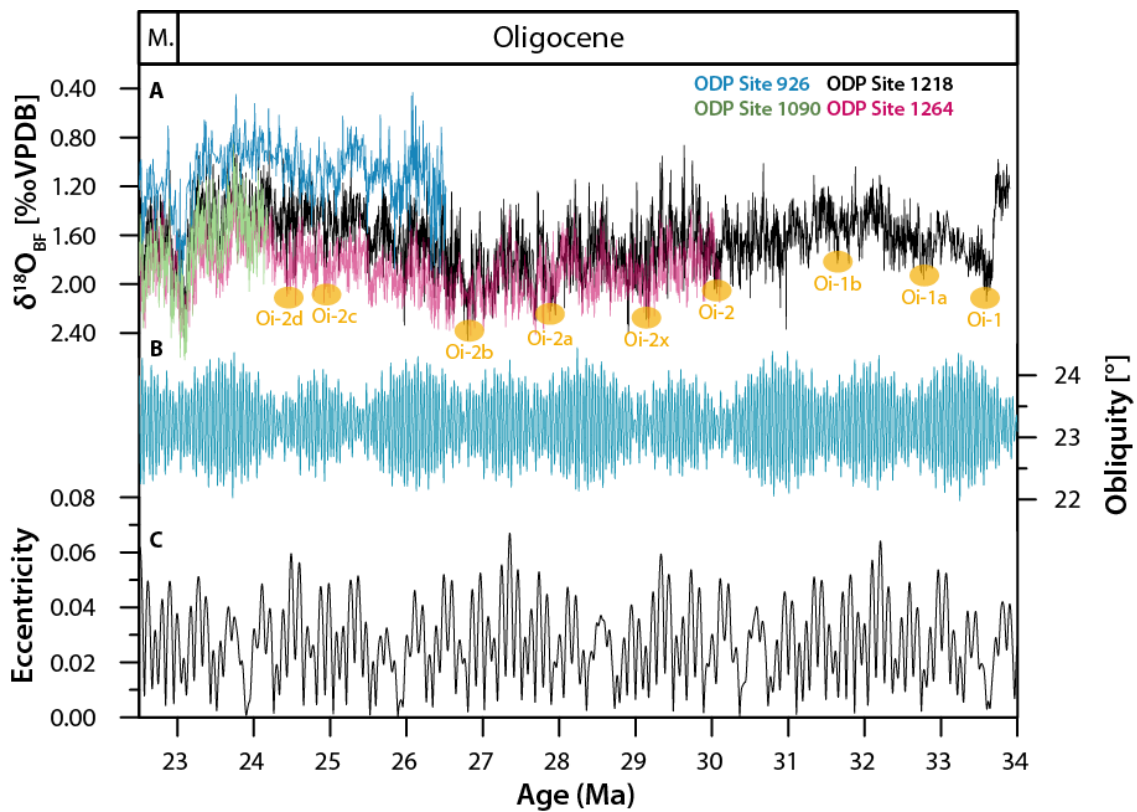


Figure 2.1-3: High-resolution $\delta^{18}\text{O}_{\text{BF}}$ records spanning the Oligocene including the EOT and the Oligocene-Miocene transition. (A) $\delta^{18}\text{O}_{\text{BF}}$ records from ODP Site 926 [equatorial Atlantic; Pälike et al. (2006a)], ODP Site 1090 [subantarctic Atlantic Ocean; Billups et al. (2004)], ODP Site 1218 [equatorial Pacific Ocean; Pälike et al., (2006b)], and ODP Site 1264 [South Atlantic; Liebrand et al., (2016)]. Oi-events from Miller et al. (1991, 1998) and Pekar and Miller (1996), Oi2d is a possible additional $\delta^{18}\text{O}_{\text{BF}}$ event according to Pälike et al. (2006a), Oix is a possible additional $\delta^{18}\text{O}_{\text{BF}}$ event according to Miller et al. (1998). (B) Orbital solution for obliquity (blue) (Laskar et al., 2004). (C) Orbital solution for eccentricity (black) (Laskar et al., 2004). Geologic epochs of the Oligocene and onset of the Miocene (=M.) are marked on top of the graph (Vandenberghe et al., 2012).

Whereas ice-proximal geological records show significant, high-frequent obliquity-paced AIS oscillations on 40-kyr timescales (Naish et al., 2001; Salabarnada et al., 2018), ice-distal $\delta^{18}\text{O}_{\text{BF}}$ records display dynamics of the AIS responding to the ~ 1.2 -Myr-amplitude modulation of obliquity (Pekar and Miller, 1996; Wade and Pälike, 2004; Pälike et al., 2006b; Pekar et al., 2006), as well as to ~ 400 -kyr and ~ 100 -kyr eccentricity cycles (Wade and Pälike, 2004; Pälike et al., 2006b; Liebrand et al., 2017) (Figure 2.1-3). In addition to the ambiguity in relation to the pacing of the Late Oligocene AIS, there is a noticeable inconsistency in relation to the size of the AIS. The ODP Site 1264 $\delta^{18}\text{O}_{\text{BF}}$ record presented by Liebrand et al. (2017) was interpreted to represent recurrent episodes of high-amplitude variability in $\delta^{18}\text{O}_{\text{BF}}$ requiring waning and waxing of at least ~ 85 to 110 % of the present-day volume of the East Antarctic Ice Sheet (EAIS) on ~ 100 -kyr timescales with a distinct ice-volume decrease from 27 Ma onwards. In contrast, Hauptvogel et al. (2017) inferred a heavily glaciated Antarctic continent from 27.8–24.5 Ma with a near or larger than modern-sized ice sheet without indication of significant ice-sheet shrinking on the basis of the $\delta^{18}\text{O}_{\text{BF}}$ signal from ODP Site 690 (Maud Rise, Antarctica).

The underlying principle in deriving ice-volume estimates and pacing of the AIS from $\delta^{18}\text{O}_{\text{BF}}$ records is problematic, as the $\delta^{18}\text{O}_{\text{BF}}$ signal is a function of temperature and ice volume (see Section 2.4.1). However, a better understanding of temperature and ice sheet variability (on astronomical time scales) can be obtained when $\delta^{18}\text{O}_{\text{BF}}$ records are considered together with independently derived Mg/Ca-based deep-water temperatures since the combined signal of the two allows to assess the ice-volume component of $\delta^{18}\text{O}_{\text{BF}}$ (see Section 2.5.1). At present, there is no such high-resolution study available to test the true nature of Late Oligocene glacial dynamics and ice-volume extents of the AIS.

2.2 Foraminifera as proxies for paleoclimate and paleoceanography

Foraminifera are small-scale, ocean-dwelling, single-celled eukaryotic organisms (Vincent and Berger, 1981; Holbourn et al., 2013). Generally, there are two types of foraminifera: planktic and benthic foraminifera. Planktic foraminifera are free-floating in the surface ocean (Schiebel and Hemleben, 2017), whereas benthic foraminifera live on or in the uppermost centimeters of the sediment (Jorissen et al., 2007). Foraminifera secrete a test with one or more chambers added episodically throughout their life cycle that is most commonly composed of calcium carbonate (CaCO_3), and occasionally bears mineral grains and/or other particles glued together, depending on the species [(Holbourn et al., 2013) and references therein]. Generally, the chambers increase in size through the life cycle (ontogeny) (Schiebel, 2002).

Foraminifera are amongst the most commonly applied proxies for paleoclimatic, -oceanographic, and -ecological studies since (i) the chemical signature of the surrounding seawater is being incorporated into the test during its formation (Urey, 1947), (ii) foraminifera are mainly marine, yet are also found in estuarine environments and inhabit water depths ranging from the ocean's surface to the seafloor (Pearson, 2012), (iii) they are very diverse and widespread organisms covering a latitudinal distribution from the equator to the poles and have a geological range from the Paleozoic (earliest Cambrian) to the present [Binczewska et al. (2014) and references therein], and (iv) they are among the most abundant shelled organisms in marine environments and are an important component of marine sediments (Schiebel, 2002).

Over the last decades, characteristics of foraminifera, such as their fossil assemblages, morphological properties, and geochemical signature of their test have served as a useful geological archive for numerous studies of paleoclimatic, -oceanographic, and -ecological reconstructions. In the following, characteristics of foraminifera in the modern ocean, as well as their application in paleoclimate and paleoceanography, are discussed in more detail.

2.3 Benthic and planktic foraminifera in the modern ocean

2.3.1 *Benthic foraminifera*

Benthic foraminifera inhabit all marine environments in water depths ranging from the intertidal zone to the deep ocean (Corliss, 1985; Jorissen et al., 1998). Their microhabitat can be divided into epifaunal and infaunal: Epifaunal species are characterized by living on top or at maximum 0.5 cm within the sediment (Murray, 2003), whereas shallow infaunal benthic foraminiferal species are living in the uppermost centimeters of the sediment, while deep infaunal taxa penetrate deeper into the sediment column (Jorissen et al., 1995). In the deep sea, benthic foraminifera are the most important contributors to the meiofaunal (0.045–1 mm) biomass (Holbourn et al., 2013).

The distribution of benthic foraminifera is mainly controlled by parameters that can be classified into two groups: (1) Physico-chemical parameters acting as limiting factors (carbonate saturation, hydrodynamics, oxygen concentration, salinity and temperature of the bottom water) and (2) directly effective resource parameters (quality and quantity of the organic matter flux) regulating the amount of food available to a microhabitat (Jorissen et al., 2007). Of these, the two most crucial factors for the regulation of benthic foraminiferal microhabitats are food and oxygen. Whereas food is intrinsically correlated to the abundance or biomass in response to changes in the supply of organic matter (Van der Zwaan et al., 1999), oxygen acts as a limiting and stress factors (Lee, 1974; Gooday, 1988; Altenbach, 1992). Jorissen et al. (1995) developed a model for the interrelation of oxygen and food as controlling factors on the microhabitat of benthic foraminifera. The TROX-model (TROphic conditions and OXYgen concentrations) serves as a simplification to illustrate the influence of oxygen concentration and food availability on the penetration depth of a benthic foraminiferal microhabitat. Low nutrient and high oxygen levels characterize oligotrophic environments, whereas in eutrophic milieus low oxygen, but high nutrient supply is dominating. Mesotrophic ecosystems provide the biggest, habitable penetration depth (Figure 2.3-1).

Based on the above-mentioned dominant environmental parameters influencing the microhabitat of benthic foraminifera, i.e., bottom water oxygenation and organic flux to the ocean floor, benthic foraminiferal assemblages are a commonly used tool to reconstruct past oceanographic conditions: Reconstruction of changes in the oxygenation of bottom-waters have been illustrated based on changes in benthic foraminiferal faunal assemblages and diversity. Based on a study on Mediterranean sapropels, low oxygen environments were inhabited by specific faunas with generally lower diversity and adaptability for hostile, anoxic conditions (Schmiedl et al., 2003). The flux of organic matter to the ocean seafloor can be reconstructed through the abundance of specific benthic foraminiferal marker species characteristic for oligo-, meso- and/or eutrophic conditions [e.g., de Rijk et al. (2000); Schönfeld and Altenbach (2005)]. In addition, the benthic foraminiferal accumulation rate (BFAR), which describes the number of benthic foraminifera per unit of area per unit of time, has been widely applied as a semi-quantitative proxy for paleoproductivity. BFAR assumes that for every mg of organic carbon

reaching the ocean floor, a specific number of fossil foraminiferal tests is deposited [e.g., Herguera and Berger (1991); de Almeida et al. (2015)].

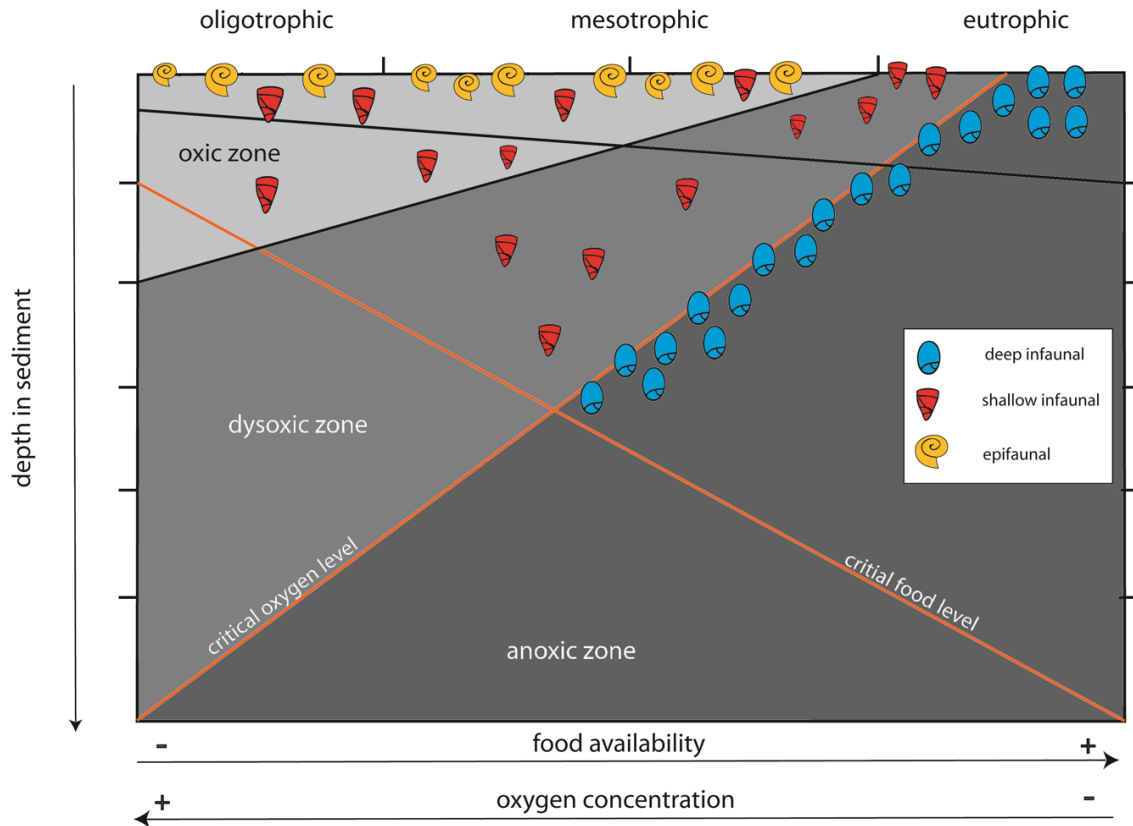


Figure 2.3-1: Conceptual TROX-Model. The microhabitat depth of epifaunal and infaunal benthic foraminifera is determined by a critical food level in oligotrophic milieus. In eutrophic environments, it is defined by a critical oxygen level [modified after Jorissen et al. (2007)].

2.3.2 Planktic foraminifera

Planktic foraminifera comprise a group of protists with a globularly chambered test (that provides buoyancy) composed of secreted calcite or aragonite. They are free-floating in the surface near-surface waters of the world's oceans (Vincent and Berger, 1981) and are part of the marine zooplankton (BouDagher-Fadel, 2015). At the end of the life cycle of a planktic foraminifera, the test rains down to the ocean floor, where it contributes 32–80% to the global deep-marine carbonate budget (Schiebel, 2002). Furthermore, planktic foraminifera are characterized by a global occurrence and occupation of a broad latitudinal and temperature zone. Yet, the vertical distribution in the water column (surface/ mixed layer/ thermocline/sub-thermocline), abundance, assemblage composition, and shell size of planktic foraminifera are influenced by surface-water properties, physiological requirements, food preferences, but dominantly controlled by the sea-surface temperature (SST) that varies locally (Rutherford et al., 1999; Schmidt et al., 2004; Morey et al., 2005). This has resulted in the grouping of modern planktic foraminifera into five main assemblages: Tropical, subtropical, temperate, subpolar, and polar provinces (Bradshaw, 1959; Bé and Tolderlund, 1971). Generally, the diversity and shell size increase with increasing SST, however it is inverted in equatorial and coastal upwelling zone (Kucera 2007), where

high population densities of smaller species are dominantly found (Rutherford et al., 1999; Schmidt et al., 2004a). The population density of planktic foraminifera is typically in the range of fewer than 100 individuals/m³ in oligotrophic gyres (due to missing prey) to >1000 individuals/m³ in polar ocean blooms (Bé, 1960; Schiebel and Hemleben, 2005). However, planktic foraminifera have adapted to warm, oligotrophic settings by hosting intracellular photosynthesizing algal symbionts (dinoflagellates or chrysophytes) providing a source of energy, which is especially advantageous in waters that are scarce in nutrients but abundant in light (Kucera, 2007). In polar regions, planktic foraminifera are most abundant during summer when light and temperature conditions allow for high primary productivity rates. Yet, in low-latitude settings, where seasonality is low due to high year-round temperature and light intensity, planktic foraminiferal abundance depends more on regional conditions such as upwelling intensity that controls primary productivity rates (Kucera, 2007 and references therein).

The abundance and distribution of recent planktic foraminiferal species can be empirically calibrated to environmental variables such as temperature, which is why fossil planktic foraminiferal assemblages can be statistically analyzed and used, for example, for paleotemperature reconstructions (Kucera et al., 2005; Kucera, 2007). When species-specific preferences for water temperature, oxygen concentration, and food availability or light intensity are known, these provide the possibility for the reconstruction of biochemical and hydrological changes in the water column. However, for such reconstructions, heterogeneities in the chemical composition of planktic foraminiferal tests have to be considered, that result from vertical migration as a function of ontogeny (see Section 2.4.1): Whereas surface-dwelling species migrate to greater depths (than the depth they usually inhabit) for reproduction, deep-dwelling planktic foraminifera reproduce in lower depths than their usual depth habitat. Hence, the geochemical signal of planktic foraminifera reflects an integrated signal of different water depths inhabited during their entire life cycle (Hemleben and Bijma, 1994). For the Oligocene for instance, this concept has allowed for the detection of thermocline deepening in the eastern equatorial Pacific Ocean (Matsui et al., 2016): Planktic foraminiferal accumulation rates were used to extract information on depth habitat changes of mixed-layer (shallow), thermocline (intermediate), and subthermocline (deep) dwelling planktic foraminiferal species as a consequence of changing upwelling intensities (Matsui et al., 2016).

2.4 The use of stable isotopes of foraminifera

2.4.1 *Stable oxygen isotopes ($\delta^{18}O$)*

The oxygen isotope composition of foraminiferal tests is mainly a function of the isotopic composition of the surrounding seawater ($\delta^{18}O_{sw}$) in which the test precipitates, and temperature during calcite precipitation (Urey, 1947; Emiliani, 1955; Duplessy et al., 1970). The resulting mathematical expression of this relationship, the so-called oxygen-isotope paleotemperature equation, was first published by (McCrea, 1950). Since then, many empirically derived equations have been established that generally take the following quadratic form:

$$T (^{\circ}\text{C}) = a - b(\delta^{18}\text{O}_{\text{cc}} - \delta^{18}\text{O}_{\text{sw}}) + c(\delta^{18}\text{O}_{\text{cc}} - \delta^{18}\text{O}_{\text{sw}})^2,$$

where $\delta^{18}\text{O}_{\text{cc}}$ is the oxygen isotope composition of the calcitic test and $\delta^{18}\text{O}_{\text{sw}}$ is the oxygen isotope composition of the seawater [standardized to Vienna Pee Dee Belemnite (VPDB)]. Coefficients a , b , and c are derived from experiments. “ a ” is representative of the temperature when $\delta^{18}\text{O}_{\text{cc}} = \delta^{18}\text{O}_{\text{sw}}$, “ b ” describes the inverse relationship between temperature and $\delta^{18}\text{O}_{\text{cc}}$ (slope) that is always negative, and “ c ” is a second-order term for the curvature of the slope, resulting from a decrease in isotopic fractionation that is causing an increase in temperature, and vice versa. The thermodynamic fractionation during calcite precipitation, i.e., the temperature component of $\delta^{18}\text{O}$, is considered as follows: Assuming calcite precipitation occurs in equilibrium with the surrounding seawater, the isotopic separation factor between calcite and seawater is inversely related to calcification temperature: If the temperature increases by 1°C , the $\delta^{18}\text{O}_{\text{cc}}$ decreases by $\sim 0.21\text{--}0.23\text{‰}$ for a given $\delta^{18}\text{O}_{\text{sw}}$ (Ravelo and Hillaire-Marcel, 2007). Therefore, the foraminiferal $\delta^{18}\text{O}$ signature can be used as a paleothermometer if $\delta^{18}\text{O}_{\text{sw}}$ is known [e.g., Bemis et al. (1998)].

The $\delta^{18}\text{O}_{\text{sw}}$ signal is temporally and locally variable due to influences on a local (river runoff, evaporation/precipitation balance) to global (amount of freshwater that is stored in ice sheets) scale (Rohling and Bigg, 1998; Ravelo and Hillaire-Marcel, 2007). Atmospheric water vapor is being transported from low to high latitudes through repeated cycles of evaporation and precipitation. During evaporation, the lighter ^{16}O isotopes of water vapor preferentially turn into the gas phase, while the heavier ^{18}O isotopes remain in seawater. During each cycle in this fractionation process, the $\delta^{18}\text{O}$ value of the water vapor decreases by $\sim 10\text{‰}$ in relation to that of the ocean water left behind [Figure 2.4-1, (Ruddiman, 2008)]. Because the water vapor that precipitates over ice-sheets at high latitudes is highly enriched in ^{16}O , the $\delta^{18}\text{O}$ composition of ice is highly negative (‘Rayleigh distillation process’) [-56.5‰ for the modern East Antarctic Ice Sheet (Lhomme, 2004); -41‰ for the modern West Antarctic Ice Sheet (Lhomme et al., 2005); -34‰ for the modern Greenland Ice Sheet (Lhomme et al., 2005)].

The balance of evaporation relative to precipitation simultaneously affects the sea-surface salinity: Salinity increases during evaporation - a change of 0.5‰ in mean global surface-water $\delta^{18}\text{O}$ causes the sea-surface salinity to change by 1.0 psu (practical salinity unit) (Ravelo and Hillaire-Marcel, 2007) (Figure 2.4-2). This relationship demonstrates the potential of oxygen isotopes for the reconstruction of paleosalinity (Craig et al., 1965), yet, tends to largely differ locally [an effect which a correction factor has been developed by (Zachos et al., 1994) to account for latitudinal variations in $\delta^{18}\text{O}_{\text{sw}}$].

Since the early application of foraminiferal $\delta^{18}\text{O}$ as a proxy in paleoceanography, there is evidence that several benthic and planktic foraminifera do not calcify in equilibrium with the surrounding seawater due to so-called ‘vital effects’ (Figure 2.4-2; Figure 2.4-1). Amongst those are (i) ontogenetic effects, (ii) symbiont photosynthesis effect, (iii) gametogenic calcite effect, and (iv) the carbonate-ion effect. These will be briefly discussed in the following:

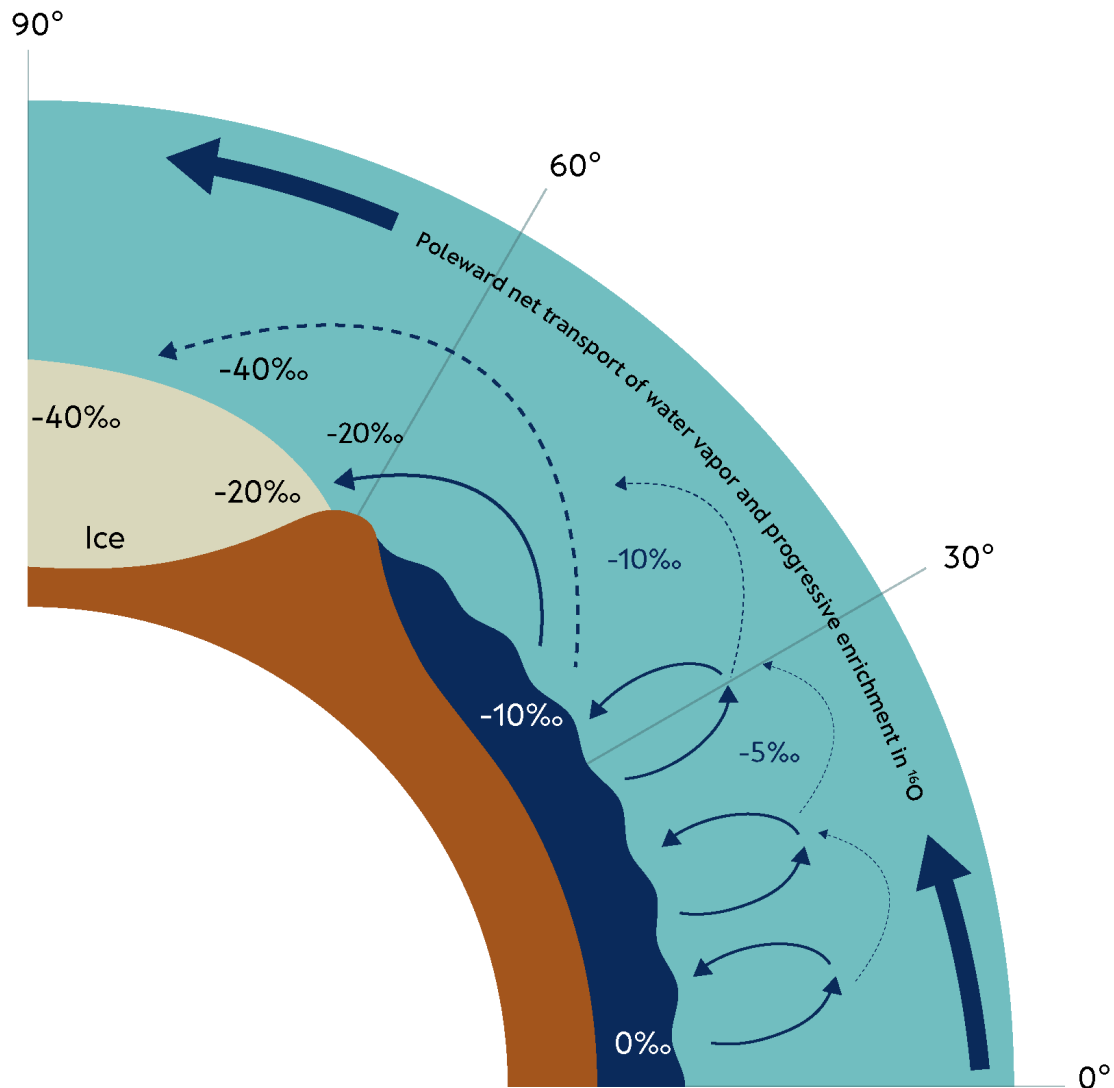


Figure 2.4-1: Meridional net transport of water vapor. Diagram displays the progressive enrichment in the lighter ^{16}O as it moves from low to high latitudes. Values are chosen to represent the progressive fractionation and are not based on published or measured values [modified after Ruddiman (2008)].

Ontogenetic effect: Studies have shown a species-specific test-size- $\delta^{18}\text{O}$ -relationship. For planktic foraminifera, both decreasing [e.g., Friedrich et al. (2012)] and increasing $\delta^{18}\text{O}$ [e.g., Elderfield et al. (2002)] have been observed with increasing test size. This is why only a narrow size-fraction should be used for the analysis of $\delta^{18}\text{O}_{\text{PF}}$. $\delta^{18}\text{O}_{\text{BF}}$ is less sensitive to the ontogenetic effect, especially amongst the epifaunal and shallow-infaunal species *Cibicidoides mundulus* (Franco-Fraguas et al., 2011) and *Oridorsalis umbonatus* (Rathmann and Kuhnert, 2008), species that are used for $\delta^{18}\text{O}$ analyses herein.

Symbiont photosynthesis effect: Amongst planktic foraminifera, whose microhabitat is confined to the photic zone (light-dependent) of the surface ocean often host intracellular photosynthesizing algal symbionts (dinoflagellates or chrysophytes), which is especially advantageous in warm oligotrophic waters that are scarce in nutrients but abundant in light (Kucera, 2007). During the symbiont-photosynthetic activity, increased CO_2 consumption favors rapid skeletogenesis and depletion in foraminiferal $\delta^{18}\text{O}$ of 0.35–0.5‰ of large (adult) tests relative to equilibrium values [see Ravelo and

The benthic foraminiferal $\delta^{18}\text{O}_{\text{sw}}$ signal is a commonly used proxy to infer changes in global ice-volume [e.g., Lear et al. (2000)]. By coupling $\delta^{18}\text{O}_{\text{BF}}$ data with independently derived deep-sea temperatures via Mg/Ca analysis (see Section 2.5.1), the $\delta^{18}\text{O}_{\text{sw}}$ component of $\delta^{18}\text{O}$ can be calculated (see Section 4.5). The $\delta^{18}\text{O}_{\text{sw}}$ -ice-volume-relationship is as follows: The higher the amount of fresh-water stored in continental ice, the higher the isotopic signature of the deep ocean's $\delta^{18}\text{O}_{\text{sw}}$ (Shackleton, 1967) (Figure 2.4-1). Since changes in global ice-volume are directly linked to global sea-level, $\delta^{18}\text{O}_{\text{sw}}$ is also used to approximate past sea-level changes: An increase in continental ice-volume, reflected by an increase in $\delta^{18}\text{O}_{\text{sw}}$, causes the sea-level to decrease (Fairbanks and Matthews, 1978; Lea et al., 2002; Gasson et al., 2016a). This relationship has served as a valuable proxy [e.g., Lear et al. (2000)] in addition to previous, low-resolution paleo-shoreline-derived sea-level reconstructions [e.g., Haq et al. (1987)]. There are several sea-level/ $\delta^{18}\text{O}_{\text{sw}}$ conversion factors available: For ice-volume changes occurring in the Northern Hemisphere during the Pleistocene, conversion factors range between 0.008 and 0.011 ‰ m^{-1} (Fairbanks and Matthews, 1978; Schrag et al., 1996; Lea et al., 2002). For Antarctic-based ice-volume changes of the Pliocene, the sea-level/ $\delta^{18}\text{O}_{\text{sw}}$ conversion factor is 0.014 ‰ m^{-1} (Gasson et al., 2016b). However, the relationship is non-linear when considering marine-based ice-loss, causing a more substantial change in $\delta^{18}\text{O}_{\text{sw}}$ than expected for the equivalent change in sea-level [see Gasson et al. (2016) for detailed discussion].

Planktic foraminiferal $\delta^{18}\text{O}$: Similar to $\delta^{18}\text{O}_{\text{BF}}$, $\delta^{18}\text{O}_{\text{PF}}$ is often used for isotope stratigraphy, providing valuable basis for age control (Ravelo and Hillaire-Marcel, 2007). Other applications of $\delta^{18}\text{O}_{\text{PF}}$, such as the reconstruction of SSTs, sea-surface salinity (SSS), the water column structure, and paleoceanographic evolution require the understanding of planktic foraminiferal paleoecology is essential [e.g., Wade et al. (2007)]. Significant information about the paleobiology of planktic foraminifera can be gained by a comparison of stable isotope signatures ($\delta^{13}\text{C}$, $\delta^{18}\text{O}$) of multiple species of planktic foraminifera. Marked offsets between species indicate different depth habitat preferences as well as 'vital-effects' of the respective species. Wade et al. (2007) have undertaken such multispecies-stable isotope analysis of Oligocene planktic foraminifera from the equatorial Atlantic (ODP Site 1218) and identified three depth habitats ranging from mixed-layer to sub-thermocline dwellers.

Another application of $\delta^{18}\text{O}_{\text{PF}}$ was presented by Arz et al. (1999), who reconstructed meridional $\delta^{18}\text{O}$ gradients inferred from single-species analysis from sediment cores located in the western tropical and subtropical South Atlantic. A decrease of the meridional $\delta^{18}\text{O}_{\text{PF}}$ gradient in the western South Atlantic was linked to perturbations of the AMOC due to intensification of southward and decline of northward flowing currents.

The planktic foraminiferal $\delta^{18}\text{O}_{\text{sw}}$ signal is a commonly used proxy to infer changes in SSS. By coupling planktic $\delta^{18}\text{O}$ data with independently derived SSTs via Mg/Ca analysis, the $\delta^{18}\text{O}_{\text{sw}}$ component of $\delta^{18}\text{O}_{\text{PF}}$ can be calculated [e.g., Bemis et al. (1998)] (see Section 4.5). Holbourn et al. (2018) used changes in planktic foraminiferal $\delta^{18}\text{O}_{\text{sw}}$ as a qualitative indicator for changes in the regional hydrology to elucidate changes in the Asian monsoon system during the Miocene: A shift towards lower planktic foraminiferal

$\delta^{18}\text{O}_{\text{sw}}$, decoupled from the $\delta^{18}\text{O}_{\text{sw}}$ signal of benthic foraminifera, was interpreted as a change in the regional hydrology (changes in the amount and/or $\delta^{18}\text{O}$ composition of precipitation and/or river runoff, linked to changes in the provenance and/or seasonality of precipitation) affecting the upper ocean. For constraining more quantitative salinity changes, planktic foraminiferal $\delta^{18}\text{O}_{\text{sw}}$ has to be corrected for global ice-volume [see (Waelbroeck et al., 2002) for more details]. This approach can likely be applied for reconstructing vertical SSS gradients in the water column by analyzing surface- to deep-dwelling planktic species. A study by Bahr et al. (2011) from the subtropical Atlantic, for example, indicated increasing salinities at intermediate depths, coinciding with relatively stable surface salinity conditions, which resulted in the identification of episodes of increased influence of southern sourced water in the tropical North Atlantic causing spatial expansions of the subtropical gyre.

2.4.2 Stable carbon isotopes ($\delta^{13}\text{C}$)

The $\delta^{13}\text{C}$ signature of foraminiferal tests is a function of dissolved inorganic carbon of the ocean water (seawater $\delta^{13}\text{C}_{\text{DIC}}$) (external factors), in which the calcitic foraminiferal test is precipitated (Epstein et al., 1953), as well as ‘vital effects’ (internal factors). In the following, influences on the seawater $\delta^{13}\text{C}_{\text{DIC}}$, which influences the $\delta^{13}\text{C}$ signature of foraminifera, are being discussed:

2.4.2.1 External factors

The ocean DIC pool comprises CO_2 , bicarbonate (HCO_3^-), and $[\text{CO}_3^{2-}]$, i.e., ocean pH, which controls the relative proportion of the different components of DIC (Figure 2.4-3). Yet, ocean DIC mainly consists of bicarbonate (>90%). Thus, seawater $\delta^{13}\text{C}_{\text{DIC}}$ mostly mirrors the $\delta^{13}\text{C}$ of bicarbonate (Zeebe and Wolf-Gladrow, 2001). Seawater $\delta^{13}\text{C}_{\text{DIC}}$ of the global ocean is a function of carbon partitioned between the ocean, atmosphere, and terrestrial biosphere (Figure 2.4-3). Release of carbon from the lithosphere (gas hydrates, volcanic outgassing, organic matter accumulation and sedimentation etc.) and the size of the terrestrial biosphere, which is generally a reservoir of ^{13}C -depleted carbon, govern the global control on ocean $\delta^{13}\text{C}_{\text{DIC}}$ [Ravelo and Hillaire-Marcel (2007) and references therein]. On a more regional level, changes in advection and upwelling of waters with different $\delta^{13}\text{C}_{\text{DIC}}$ (Kroopnick, 1974) (Figure 2.4-3).

The thermodynamic (equilibrium) fractionation of oceanic carbon during the exchange between atmospheric CO_2 and the surface water DIC is shown to increase by 0.1‰ per 1°C decrease (Zhang et al., 1995). For atmospheric $p\text{CO}_2$ signals and to be recorded in the marine reservoir, the signal needs to have a sufficient magnitude and duration since (i) the time for the surface ocean to reach equilibrium with the atmospheric $p\text{CO}_2$ [~ 10 years; Broecker and Peng (1982)] is longer than the residence time of water masses at the surface, and (ii) the ocean’s inorganic carbon reservoir is 50 times larger than the atmosphere’s so that a noticeable effect on the ocean’s surface and/or global ocean $\delta^{13}\text{C}_{\text{DIC}}$ should involve changes in the size of the terrestrial biosphere and/or changes of carbon release from the lithosphere (Rohling and Cooke, 2003). For the Miocene, a sufficiently long-term and robust increase

in the dominance of C₄ plants (grasses) that reduced the mean relative atmospheric ¹³C enrichment was used to explain the shift towards lower marine δ¹³C values (Galy et al., 1996).

During photosynthetic kinetic fractionation in the euphotic layer of the ocean, the preferential incorporation of ¹²C of marine phytoplankton leaves the ocean's surface waters enriched in δ¹³C_{DIC}. This, in turn, has an effect on surface water HCO₃⁻, and, hence, the carbonates formed thereof, i.e., the δ¹³C signature of planktic foraminiferal tests formed in the euphotic ocean layer (Figure 2.4-3). The deep water's δ¹³C signature is regulated by the sinking and recirculation of ¹³C-depleted particulate organic matter from the ocean's surface/mixed layer that is being degraded by microbial processes (remineralization). During degradation, ¹²C and nutrients are being released, which in turn lower the deep ocean's δ¹³C. Since this process sets in when surface water is disclosed from the atmosphere and sinks to greater depths of the ocean due to downwelling, the δ¹³C signature of ocean water decreases with age and can hence be used as a tracer of deep-water masses (Shackleton et al., 1983; McCorkle et al., 1994) (Figure 2.4-3).

2.4.2.2 *Internal factors*

In addition to external processes, 'vital effects' can cause disequilibrium of foraminiferal δ¹³C from seawater δ¹³C_{DIC} that include (i) ontogenetic effects, (ii) symbiont photosynthesis effect, (iii) incorporation of metabolic CO₂ during test precipitation, and (iii) (iv) the carbonate-ion effect (Erez, 1978; McConnaughey et al., 1997) (Figure 2.4-3). These will be briefly discussed in the following:

Ontogenetic effect: With increasing test size of symbiont-bearing planktic foraminifera, the symbiont density also increases [e.g., Spero and Parker (1985)]. Accordingly, the photosynthetic activity raises, which induces continuous ¹³C depletion with each new chamber formed. However, in non-symbiont-bearing planktic foraminiferal species, a change in test size induces decreasing δ¹³C caused by contamination of the δ¹³C signature of planktic foraminiferal tests with metabolic or respiratory CO₂ (Rohling and Cooke, 2003). The younger the cell age, and the smaller the size of the non-symbiont-bearing planktic foraminiferal test, the higher metabolic rates, the stronger the δ¹³C depletion [e.g., Wefer and Berger (1991)]. Hence, only a narrow size-fraction should be used for the analysis of planktic foraminiferal δ¹³C. The ontogenetic effect shows no significant change in skeletal δ¹³C with size in benthic foraminifera [e.g., Dunbar and Wefer (1984); Wefer and Berger (1991)].

Symbiont photosynthesis effect: Symbiont-bearing planktic foraminifera of the photic zone (light-dependent) of the surface ocean show increased skeletal ¹³C enrichment with increasing light intensity (McConnaughey, 1989; McConnaughey et al., 1997). Symbionts display elevated utilization of ¹²CO₂ during photosynthetic activity, which increases the calcifying environment in HCO₃⁻ and thereby produces ¹³C-enriched chambers [e.g., Spero and Lea (1993)].

Incorporation of metabolic CO₂ during test precipitation: The magnitude of isotopically light metabolic CO₂ incorporation into the calcitic foraminiferal test is proportional to the amount of metabolic CO₂ within the organism's internal CO₂ pool (Erez, 1978; Hesse et al., 2014). Generally, foraminiferal δ¹³C

decreases with the incorporation of metabolic CO_2 , yet the degree of this effect is species-specific [e.g., Spero and Lea (1993)].

Carbonate-ion effect: Similar to $\delta^{18}\text{O}$, $[\text{CO}_3^{2-}]$ also affects the $\delta^{13}\text{C}$ signature of foraminifera. Laboratory experiments have shown that foraminiferal $\delta^{13}\text{C}$ decreases with increasing $[\text{CO}_3^{2-}]$, however, the magnitude varies between different species of foraminifera (Spero et al., 1997).

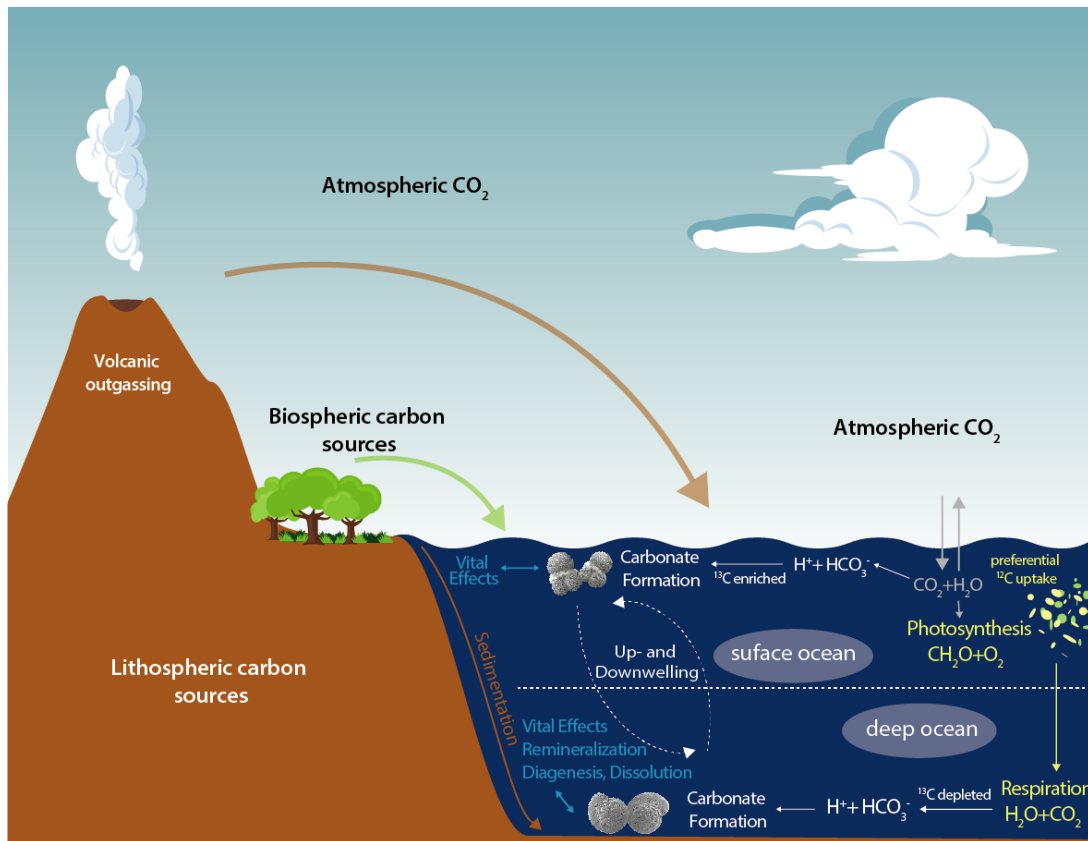


Figure 2.4-3: Influences of oceanic $\delta^{13}\text{C}_{\text{DIC}}$ on the carbon isotope composition of foraminifera (see text for references). Vital effects include ontogenetic effects, symbiont photosynthesis effect, incorporation of metabolic CO_2 during test precipitation, and the carbonate-ion effect (see text for details).

Benthic foraminiferal $\delta^{13}\text{C}$: Similar to $\delta^{18}\text{O}_{\text{BF}}$, the $\delta^{13}\text{C}_{\text{BF}}$ signature is a valuable component for isotope stratigraphy: Analogous to the $\delta^{18}\text{O}_{\text{BF}}$ ‘Zachos-stack’, there is a global $\delta^{13}\text{C}_{\text{BF}}$ -stack based on carbon isotope data of bottom-dwelling, deep-sea foraminifera from over 40 DSDP and ODP sites spanning the past 65 Myr (Zachos et al., 2001a).

Furthermore, the $\delta^{13}\text{C}$ signature of epifaunal benthic foraminifera of the deep ocean can be used to reconstruct the $\delta^{13}\text{C}_{\text{DIC}}$ signal of the bottom-water masses (Figure 2.4-3), if species-specific offsets from equilibrium fractionation with the ambient seawater are considered (Belanger et al., 1981; McCorkle and Emerson, 1988; Mackensen, 2012). In numerous studies, the species of the epifaunal benthic foraminiferal taxon *Cibicidoides* was chosen as a tracer for reconstructing circulation patterns and geometries of deep-sea water masses (Curry et al., 1988; Duplessy et al., 1988; Schmiedl et al., 2004) since it records bottom-water $\delta^{13}\text{C}_{\text{DIC}}$ in a one-to-one relationship (Duplessy et al., 1984; McCorkle et

al., 1994). Inter-ocean benthic $\delta^{13}\text{C}$ gradients allow for the recognition of bottom-water circulation changes: (Lear et al., 2003) calculated $\delta^{13}\text{C}$ gradients between the Atlantic and Pacific Ocean to display export strength of proto-NADW during the Miocene. Another application of $\delta^{13}\text{C}_{\text{BF}}$ is related to infaunal benthic foraminifera that are used as recorders of the sediment pore water in which they calcify. The gradient between epifaunal to infaunal benthic foraminifera can be used to track paleoproductivity and bottom-water oxygen contents [e.g., Schmiedl and Mackensen (2006); Hoogakker et al. (2015)]. Especially, the difference between epifaunal to shallow infaunal benthic foraminifera has shown great potential to reflect the organic carbon flux to the seafloor and related microbial rate of organic matter in the uppermost layers of the sediment (Hoogakker et al., 2015; Theodor et al., 2016).

Planktic foraminiferal $\delta^{13}\text{C}$: Similar to $\delta^{18}\text{O}_{\text{PF}}$, inter-species comparison of $\delta^{13}\text{C}_{\text{PF}}$ signatures delivers valuable information about the paleobiology of planktic foraminifera (e.g., preferred depth habitat), which are an essential basis for the paleoecology of planktonic foraminifera that allows for reliable reconstructions of SST, SSS, the water column structure and paleoceanographic evolution [e.g., Wade et al. (2007); Katz et al. (2010)].

$\delta^{13}\text{C}_{\text{PF}}$ can be used to track variations in $\delta^{13}\text{C}_{\text{DIC}}$ of surface waters due to changes in surface-water productivity. The higher the nutrient fluxes and productivity, the higher the depletion of $\delta^{13}\text{C}_{\text{DIC}}$ of the surface water, hence the $\delta^{13}\text{C}$ signature of planktic foraminifera (Maslin and Swann, 2006) (Figure 2.4-3).

A powerful tool to infer changes in water column stratification is the planktic-benthic $\delta^{13}\text{C}$ gradient ($\Delta\delta^{13}\text{C}_{\text{PF-BF}}$). The larger the vertical $\delta^{13}\text{C}$ differences, the higher the stratification of the water column. This signal served as a proxy for convection of water masses, as has been the case when reconstructing the onset of northern-sourced deep-water export across the EOT [e.g., Coxall et al. (2018)].

$\delta^{13}\text{C}_{\text{PF}}$ can be used to infer changes in atmospheric $p\text{CO}_2$. As an example, Campos et al. (2017) related a $>1\text{‰}$ decrease in planktic foraminiferal $\delta^{13}\text{C}$ to millennial-scale periods of weakening of the AMOC and the consequent increase in $p\text{CO}_2$ during Heinrich Stadials 3 and 2. They hypothesize two mechanisms that could account for the decreases observed in $\delta^{13}\text{C}_{\text{PF}}$, namely, strengthening Southern Ocean deep-water ventilation and weakening of the biological pump.

2.5 The use of foraminiferal Mg/Ca ratios as a paleothermometer

As outlined above, $\delta^{18}\text{O}$ -derived temperatures of foraminifera are dependent on assumptions made regarding past $\delta^{18}\text{O}_{\text{sw}}$, which itself reflects a change in continental ice-volume or salinity. Thus, the application of foraminiferal $\delta^{18}\text{O}$ for temperature reconstructions is limited (see Section 2.4). In the last few decades, the application of Mg/Ca ratios of foraminifera has shown great potential for paleotemperature reconstructions (Nürnberg et al., 1996; Rosenthal et al., 1997). Ca and Mg have relatively long residence times (~ 1 and ~ 10 Myr, respectively) in the ocean, implying nearly constant Mg/Ca ratios in seawater on timescales shorter than 1 Ma (Rosenthal, 2007). During calcite precipitation of foraminiferal tests, magnesium substitutes for calcium, which is a temperature-sensitive

(endothermic) process. A subject of ongoing debate is whether the relationship between thermodynamic controls on Mg incorporation/substitution into foraminiferal calcite is best described as linear (Toyofuku et al., 2000; Marchitto et al., 2007),

$$Mg/Ca = (A * T) + B ,$$

or as exponential [e.g., Rosenthal et al., (1997); Lear et al. (2002)]

$$Mg/Ca = B * exp(A * T),$$

where Mg/Ca is the calcite of the foraminiferal test, T is temperature, and A and B are species-specific constants. Nonetheless, the substitution of Mg²⁺ into marine calcite is thermodynamically favored at higher temperatures [see discussions by (Mucci and Morse, 1990; Rosenthal et al., 1997).

To generate a temperature record from Mg/Ca of foraminifera, several factors have to be considered. These include (i) the seasonal appearance or the depth habitat within the water and column, (ii) the carbonate-ion concentration in seawater, (iii) past variations in seawater Mg/Ca (Mg/Ca_{sw}), and (iv) changes in seawater salinity.

Sadekov et al. (2008) have shown that calcification temperatures of planktic foraminifera are correlated with the seasonal range in seawater temperature, as well as habitat depths, which have to be considered when interpreting the Mg/Ca ratio of planktic foraminifera. [CO₃²⁻ or pH (Lea et al., 1999; Russell et al., 2004; Rathmann and Kuhnert, 2008) might affect the foraminiferal Mg/Ca ration: A lower than modern pH (pH=8.2) causes the foraminiferal Mg/Ca to decrease by up to 16% per 0.1 unit increase in pH, whereas changes are insignificant if the pH is higher than modern (Russel et al., 2004). This pH sensitivity is species-specific.

When deriving Mg/Ca ratios of foraminifera over several million years, secular variations in Mg/Ca_{sw} present a significant influence on the Mg/Ca ratio of foraminifera (Evans and Müller, 2012). It has been shown that over the course of the Phanerozoic, Mg/Ca_{sw} has varied by up to a factor of 5, i.e., from ~1 to ~5 mol/mol at present [e.g., Gothmann et al. (2015); Dickson (2002)]. These variations are caused by changes in weathering rates, hydrothermal activity, dolomitization, or carbonate production [e.g., Coggon et al. (2010)]. Therefore, when converting foraminiferal Mg/Ca ratios into temperature estimates, a correction for secular variations of past Mg/Ca_{sw} than compared to modern have to be implemented (see Section 4.4).

A factor of ongoing debate is whether changes in seawater salinity influence the planktic foraminiferal Mg/Ca ratio: While a 3–5% increase in Mg/Ca per psu has resulted from laboratory culture studies (Kısakürek et al., 2008; Hönisch et al., 2013), core-top data suggests a much larger sensitivity (27 ± 4% per psu) derived from sub-tropical Atlantic core-top sediments (Mathien-Blard and Bassinot, 2009; Arbuszewski et al., 2010). Yet, Hönisch et al. (2013) suggest that these much larger sensitivities are not a direct effect of salinity, but rather arise from inappropriately applied corrections for dissolution to Mg/Ca dataset of the core-top study that ultimately causes a significant overestimation of temperatures [see Hönisch et al. (2013) for detailed discussion].

2.5.1 Benthic foraminiferal Mg/Ca

The Mg/Ca ratio of bathyal benthic foraminifera is an often-used proxy to infer changes in the bottom-water temperature (BWT) of the deep-sea (Rosenthal et al., 1997; Lear et al., 2002). Existing benthic foraminiferal Mg/Ca temperature calibrations span a temperature range of -1 to 26°C [see Barrientos et al. (2018) and references therein]. These have been generated based on species-specific core top-calibrations from various latitudes, and water depths of the world's ocean [see Barrientos et al. (2018) and references therein]. The calculated benthic foraminiferal Mg/Ca-BWT sensitivity derived from existing calibrations is around ~6–10±1% Mg/Ca increase per 1 °C increase in ambient seawater temperature during foraminiferal calcite precipitation (Rosenthal et al., 1997; Lear et al., 2002; Rosenthal, 2007).

For existing calibrations, there is a higher Mg/Ca-BWT sensitivity with lower Mg/Ca values for colder water temperatures when compared to global calibrations [e.g., Lear et al. (2015)]. This has been linked to the carbonate-ion-effect: Below a certain threshold of $[\text{CO}_3^{2-}]$ Mg/Ca in foraminiferal calcite decreases more as a consequence of a steep drop in bottom-water $[\text{CO}_3^{2-}]$ rather than temperature (Martin et al., 2002; Elderfield et al., 2006; Marchitto et al., 2007; Yu et al., 2008). To this effect, however, the use of infaunal benthic species has been shown to be a more reliable tracer of paleotemperature than epifaunal foraminifera because pore waters are buffered to some extent against changes in carbonate saturation (Elderfield et al., 2010). Due to the oxidation of organic matter, pore water carbonate saturation state is decreased. Hence, once waters become undersaturated, dissolution of carbonate grains buffers against a further decrease in saturation state [e.g., Zeebe (2007)]. This effect has been shown to be nonexistent for the shallow infaunal species *O. umbonatus* (Rathmann and Kuhnert, 2008). This species, for which species-specific core top calibrations exist (Lear et al., 2002; Rathmann et al., 2004; Healey et al., 2008; Brown et al., 2011; Tisserand et al., 2013), is used for Mg/Ca-based BWT reconstructions in this thesis.

The long-term evolution of BWTs through the past 50 Ma was inferred by (Lear et al., 2000) showing an overall 12 °C cooling in the deep oceans with four main cooling periods and striking similarity to the corresponding long-term $\delta^{18}\text{O}$ evolution. Furthermore, paired $\delta^{18}\text{O}$ -Mg/Ca data allowed these authors to assess $\delta^{18}\text{O}_{\text{sw}}$ to determine both the timing of initiation of continental ice accumulation on Antarctica and its record through the Cenozoic (Lear et al., 2000). This long-term trend was refined by more recent studies providing higher resolution studies on the Cenozoic glaciation history [e.g., Billups and Schrag (2002); Lear et al. (2004); Sossian and Rosenthal (2009); Bohaty et al. (2012)].

2.5.2 Planktic foraminiferal Mg/Ca

The Mg/Ca ratios of planktic foraminifera are used as a proxy of paleo sea-surface to subsurface temperatures (depending on the species-specific depth habitat) [e.g., Nürnberg et al. (1996); Russell et al. (2004)]. The Mg/Ca ratio of planktic foraminifera has been calibrated to temperature based on (i) core top, (ii) sediment trap and (iii) laboratory culture studies, and most of these studies have

demonstrated a ~9–10% exponential increase in Mg/Ca per degree Celsius in most species, similar to benthic foraminifera (Bryan and Marchitto, 2008).

On the one hand, planktic foraminiferal Mg/Ca calibrations determined through core-top material are valuable since they are based on material that will eventually form the sedimentary record and provide foraminifera that have completed a life cycle including. On the other hand, core-top calibrations bear the risks if the sample material has undergone post-depositional alteration (Barker et al., 2005). Planktic foraminiferal tests collected via sediment trap material have the advantage that they most closely represent the tests entering the sedimentary record without actually reaching the sediment surface, and are therefore free of risk of dissolution effects [e.g., Anand et al. (2003)]. Culture-based calibrations have the distinct advantage that temperature is constrained during the experiment and therefore is an independent variable [e.g., Nürnberg et al. (1996)]. A potential disadvantage of this method is that laboratory conditions may not realistically reproduce the natural environment sufficiently to ensure natural chamber growth. Additionally, culture-based calibrations cannot be carried out on juvenile planktic foraminifera since foraminiferal reproduction is not possible in the laboratory (Barker et al., 2005).

Available Mg/Ca calibrations are based on single- and multi-species, and data of planktic foraminifera cover a temperature range of 0–31 °C [see Rosenthal (2007) and references therein]. Of those, the core-top and sediment-trap-based calibrations were derived from material that covers areas under various hydrographic regimes of the world's oceans from well-stratified to areas with a deep mixed layer across a broad latitudinal range [see Rosenthal (2007) and references therein; Cléroux et al. (2008, 2013); Regenberg et al. (2009)]. Single-species calibrations are important since inter-species differences may cause significant offsets in Mg/Ca for a given temperature [e.g., Fairbanks et al. (1982)]. It has been shown that inter-species variability in planktic foraminiferal Mg/Ca is correlated to calcification depth: Whereas surface to mixed-layer dwellers have a high Mg/Ca ratio, deep dwellers are characterized by lower Mg/Ca ratios (Bender et al., 1975; Rosenthal and Boyle, 1993). However, for species showing a narrow temperature range prohibiting statistically significant calibrations, or for species that are now extinct, single-species calibrations present difficulties [e.g., Anand et al. (2003)]. Where it is not possible to use species-specific calibrations, multi-species calibrations have been demonstrated to be a useful tool [e.g., Anand et al. (2003)].

An example of planktic foraminiferal Mg/Ca-based temperature reconstruction is a study by Friedrich et al. (2013) who investigated summer SSTs in the central North Atlantic in order to reconstruct the position of the NAC during the late Pliocene to early Pleistocene. Results allowed them to elucidate the NAC position's role as a trigger for Northern Hemisphere cooling and subsequent ice-sheet growth. Greenop et al. (2019) analyzed SSTs across the Oligocene-Miocene transition, i.e., Mi-1 glaciation, inferring no clear temperature decrease albeit major glaciation occurring on Antarctica.

2.6 The influence of diagenesis on foraminifera-based geochemical proxies

Post depositional diagenetic alteration, i.e., the influence of undersaturated bottom-waters or pore-waters, can affect the accuracy of foraminiferal geochemical signatures.

Benthic foraminifera are generally less affected by diagenesis than planktic foraminifera for the following reasons: First, benthic foraminiferal tests are more heavily calcified than those of planktic foraminifera and therefore are more resistant to both dissolution and recrystallization (Sexton and Wilson, 2009). Second, the recrystallization of benthic foraminiferal tests occurs within the same water mass with the same temperature and chemical composition in which they originally calcified their test [e.g., Marchitto et al. (2007); Edgar et al. (2013)]. With regards on the Mg/Ca ratio of benthic foraminifera, calcite precipitated in cold water shows a lower tendency for dissolution (Marchitto et al., 2007): Since $[\text{CO}_3^{2-}]$ saturation is lower at colder sites, test growth of benthic foraminifera in cold waters can result in a steeper Mg/Ca response to temperature than compared to species from warmer waters [see Marchitto et al. (2007) and references therein].

In case of planktic foraminifera, it has been shown that selective dissolution preferentially occurs on Mg/Ca-rich chamber calcite formed in warmer waters. This causes a shift of the planktic foraminifera's bulk test Mg/Ca towards lower values, which generates lower paleotemperature reconstructions (Brown and Elderfield, 1996; Lea et al., 2000; Regenberg et al., 2014). The magnitude of such a temperature lowering depends on two factors: (i) the range of temperatures over which the shell calcified, and (ii) the degree of dissolution [e.g., Rosenthal et al. (2000)]. Similarly, post-deposition recrystallization (addition of inorganic calcite from sediment pore fluids onto foraminiferal tests) of planktic foraminifera can cause a shift of $\delta^{18}\text{O}$ towards higher values and paleotemperatures to increase (Regenberg et al., 2007) since recrystallization occurs in bottom waters that are significantly cooler than the water in which the planktic foraminiferal test was initially precipitated (Pearson et al., 2001).

Resulting from these findings, detailed monitoring of the foraminiferal preservation e.g., via Scanning Electron Microscopy (SEM) imaging to check for fine features such as the original wall structure, pore channels, or a lack of secondary calcite, is essential in order to generate high-fidelity geochemical records.

2.7 Investigated Foraminiferal Species

In this thesis, geochemical records were generated on benthic foraminiferal tests of the species *C. mundulus* and *O. umbonatus*, and tests of the planktic foraminiferal species *Catapsydrax dissimilis* from Site U1406.

2.7.1 *Cibicidoides mundulus*

Cibicidoides mundulus (Figure 2.7-1g-i) is an extant epifaunal benthic foraminifera living in the bathyal zone of the deep ocean (Yu and Elderfield, 2008). It is characterized by a global distribution (Holbourn

et al., 2013). The calcitic shell of *C. mundulus* is slightly trochospiral with a subcircular outline. Its umbilical side is slightly convex. Chamber walls are calcareous and finely perforate on the umbilical side, whereas they are coarsely perforate on the spiral side. The final whorl consists of 10 to 12 chambers (Holbourn et al., 2013).

Cibicoides mundulus is one of the most commonly used benthic foraminiferal species used to generate Cenozoic deep-sea stable oxygen and carbon isotope data [e.g., Lear et al. (2000, 2004); Pälike et al. (2006b)]: Due to its epifaunal habitat, *C. mundulus* is assumed to faithfully reflect the water chemistry of bottom waters at the seafloor (Yu and Elderfield, 2008). Additionally, isotopic offsets from equilibrium are well constrained for *C. mundulus*, which makes their isotopic signature comparable to that of other benthic species (Table 2.7-1) (Shackleton et al., 1984). For these reasons, tests of *C. mundulus* are used for stable oxygen and carbon analyses herein.

2.7.2 *Oridorsalis umbonatus*

Another benthic foraminiferal species often used in paleoceanographic studies is *O. umbonatus* [e.g., Lear et al. (2004)] (Figure 2.7-1a–f). *Oridorsalis umbonatus* is an endobenthic species (Rathmann et al., 2004) that inhabits lower-neritic to abyssal settings under oligotrophic and well-oxygenated conditions (Holbourn et al., 2013). Morphologically, the calcareous shell of *O. umbonatus* is lenticular, compressed, and low trochospiral with a slightly lobulate outline. The spiral side is evolute convex, while the umbilical side is involute and less convex. The final whorl consists of five to six chambers that gradually increase in size (Holbourn et al., 2013).

Because of its geographic (worldwide) and stratigraphic [late Cretaceous to present (Brown et al., 2011)] appearance, *O. umbonatus* has been used in numerous paleoceanographic studies [e.g., Lear et al. (2004); Friedrich et al. (2013)]. The isotopic offsets from equilibrium are well constrained for *O. umbonatus*, making their isotopic signature comparable to that of other benthic species (Table 2.7-1) (Shackleton et al., 1984; Wendler et al., 2013). In this thesis, only tests of *O. umbonatus* were utilized for Mg/Ca-based bottom-water temperatures (BWTs), because *O. umbonatus* is a more reliable Mg/Ca recorder than compared to other benthic foraminiferal species since (i) it is buffered from the influence of changing bottom-water carbonate ion saturation state (Rathmann and Kuhnert, 2008; Lear et al., 2015), (ii) it has a low sensitivity to temporal variations of Mg/Ca_{sw} (Lear et al., 2015), and (iii) due to its large chambers it is easier to clean for Mg/Ca analyses procedures compared to e.g., *C. mundulus*. Individuals of *O. umbonatus* were also utilized for stable isotope analyzes, so that coupled Mg/Ca-oxygen isotope measurements (see Section 2.5.1) could be carried out on the same species.

2.7.3 *Catapsydrax dissimilis*

Catapsydrax dissimilis is an extinct, global planktic foraminiferal species that occupies a deep-dwelling, sub-thermocline habitat (Biolzi, 1983; Wade et al., 2007) (Figure 2.7-1j, k). The stratigraphic range of *C. dissimilis* extends from the upper middle Eocene to the lower Miocene. The highest occurrence of *C.*

dissimilis is calibrated to 17.62 Ma [Coxall and Spezzaferri (2018) and references therein]. A coarsely cancellate, spinose wall characterizes tests of *C. dissimilis*. The test morphology is low-moderate trochospiral of 2.5 to 3 whorls, involute, lobate with four chambers in the final whorls. The primary aperture is a low umbilical arch covered by a single slightly inflated or flattened bulla that is less coarsely cancellate than the rest of the test with two or more rimmed openings (Coxall and Spezzaferri, 2018). In comparison to other planktic foraminifera, the stable isotope signature of *C. dissimilis* shows highest $\delta^{18}\text{O}$ and lowest $\delta^{13}\text{C}$ values, which is why its habitat is classified as sub-thermocline [e.g., Wade et al. (2007); Stewart et al. (2012); Matsui et al. (2016)]. Due to its sub-thermocline habitat, *C. dissimilis* can be used to track paleoceanographic changes at the bottom of the thermocline [e.g., Matsui et al. (2016)] and paleoecologic (paleoproductivity) changes of intermediate waters (Stewart et al., 2012), as is the case in this thesis.

Table 2.7-1: Deviations from oxygen and carbon isotopic equilibrium between foraminiferal tests and ambient seawater for selected species.

Species	Study	Correction Factor $\delta^{18}\text{O}$	Correction Factor $\delta^{13}\text{C}$
<i>C. mundulus</i>	Shackleton et al. (1984)	+0.5‰	Close to equilibrium
<i>O. umbonatus</i>	Shackleton et al. (1984)	Close to equilibrium	Close to equilibrium
	Wendler et al. (2013)	Close to equilibrium	Close to equilibrium
<i>C. dissimilis</i>	n.d.	n.d.	n.d.

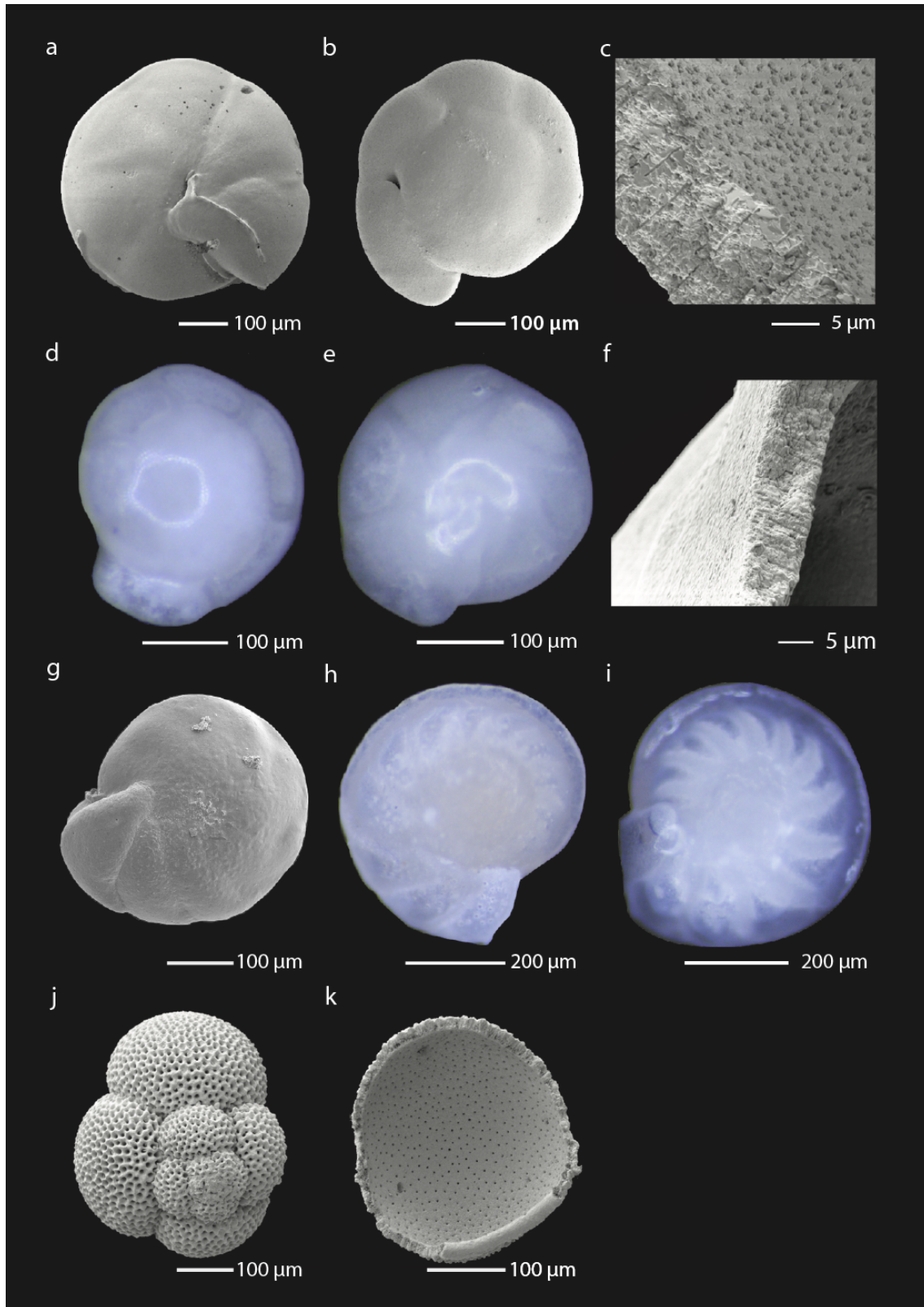


Figure 2.7-1: SEM and reflected light microscope micrographs of *O. umbonatus*, *C. mundulus* and *C. dissimilis* tests of Site U1406. (a–f) *O. umbonatus*, (g–i) *C. mundulus*, and (j, k) *C. dissimilis* tests of Site U1406. SEM pictures reveal smooth test surfaces with no signs of extensive recrystallization. Note the preservation of delicate pore channels (c, f, orange arrows). Reflected light microscope pictures of *O. umbonatus*, (d, e) and *C. mundulus* (h, i) show excellent glassy preservation.

3 STUDY AREA

3.1 The Northwestern Atlantic

3.1.1 Geography

IODP Site U1406 is located in the northwestern Atlantic Ocean (Figure 3.2-1). At modern, the North Atlantic Ocean is bounded by North America in the west, Europe and Africa in the east, and the Equatorial Counter Current in the south at about 8°N. In the north, it is adjoint to the Nordic Seas and Arctic Ocean and further to the Pacific Ocean. The most characteristic geographical feature of the North Atlantic Ocean is the Mid-Atlantic Ridge (MAR) as a divergent tectonic plate boundary between the Eurasian Plate and the North American Plate that bisects the Atlantic Ocean longitudinally (Tomczak and Godfrey, 2013).

The opening of the central North Atlantic Ocean started during the middle Jurassic, creating a transform boundary along the southwest margin of the Grand Banks offshore Newfoundland [e.g., Pe-Piper et al. (2007)]. Seafloor spreading north of this Jurassic transform boundary began in the Early Cretaceous with the separation of Newfoundland from Iberia [e.g., Tucholke et al. (2007)]. During the late Cretaceous (~80 Ma ago), Biscay ceased to spread as Iberia stopped rotating with respect to Europe. At the same time, spreading initiated along a NW running axis stretching from Biscay to the Labrador Sea [e.g., Pe-Piper et al. (2007)]. During the Paleocene (~60 Ma ago), a split between Greenland and the Rockall Plateau to the east of the Cretaceous trough axis grew into the Reykjanes Ridge and further NE into the Aegir and other ridges north of the Faeroes (Laughton, 1975). Spreading in the Labrador Sea ceased around the middle Eocene, while Greenland joined the North American Plate (Laughton, 1975). Around ~15 Ma ago, Iceland occurred as an area of significant magma output related to the development of the mantle plume. However, the existence of transverse ridges along either side of Iceland is speculated to have been active throughout the Tertiary. Spreading along the MAR as well as the Reykjanes Ridge continues to be active until present (Laughton, 1975).

3.1.2 Modern oceanography of the North Atlantic

The most prominent oceanographic feature of the North Atlantic Ocean is the AMOC (Rahmstorf, 2002; Talley et al., 2011), a large-scale circulation system that transports warm, near-surface water from low latitudes towards high northern latitudes via the Gulf Stream. During this poleward transport, surface waters cool and lose heat to the atmosphere that causes a density increase. In some regions, the increase in density is further enhanced by sea-ice formation (e.g., in the Arctic), producing very saline water through brine rejection (Rahmstorf, 2002). In the high northern latitudes, namely the Labrador and Nordic Seas, the densification and temperature decrease cause surface convection to deeper ocean waters (Rahmstorf, 2002). Newly formed deep-water masses return southward as a cold, dense deep-water current (Broecker, 1991).

In the modern North Atlantic Ocean, southward-flowing deep-water formed in the Nordic Seas overflows the Iceland-Scotland Ridge (Iceland-Scotland Overflow Water) and the Denmark Strait (Denmark-Strait Overflow Water) and forms the lower component NADW (INADW) (Rhein et al., 2015). Deep-water sourced from the Labrador Sea (Labrador Sea Water; LSW) is less dense and forms the upper component of NADW (uNADW). The combination of INADW and uNADW are transported south via the Deep Western Boundary Current (DWBC), which is a contour current that intersects the Newfoundland ridges along the western margin of the North Atlantic Ocean basin [e.g., Richardson et al. (1981); Schmitz et al. (1993)]. NADW accounts for 40% of Earth's deep-water formation and is, thus, a significant contributor to the thermohaline circulation and global heat transfer (Broecker et al., 1998; Talley, 2013). Southward flowing NADW is counterbalanced by Antarctic Intermediate Water (AAIW) that is upwelled in the Drake Passage. Below ~4500 m, AABW, sourced from the circum-Antarctic current follows the path of the DWBC southward along the continent (Ferreira and Kerr, 2017) (Figure 3.1-1).

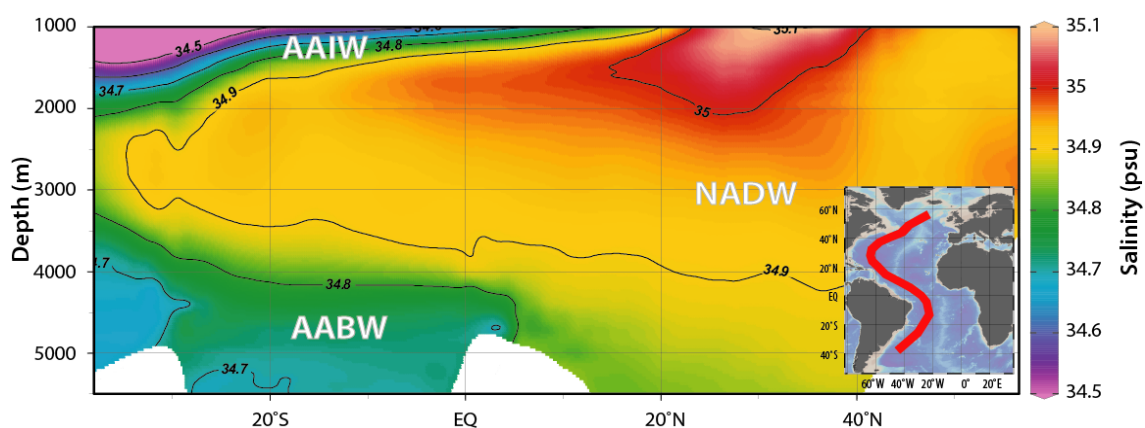


Figure 3.1-1: Modern north-south salinity profile of the deep western Atlantic (40°S to 60°N) after World Ocean Atlas (Boyer et al., 2013). Salinity distribution in depths greater than 1000 m: NADW is more saline (34.8–35 psu) than southern sourced AAIW (33.8–34.8 psu) and AABW (34.6–34.7 psu) (Emery, 2003). Map has been compiled using Ocean Data View (Schlitzer, 2019).

The surface circulation of the North Atlantic Ocean is characterized by an anticyclonic subtropical gyre (STG), and a cyclonic subpolar gyre (SPG) (Talley et al., 2011) (Figure 3.1-2). The STG encompasses the Gulf Stream (south of $\sim 40^\circ\text{N}$), an extensive western boundary current that plays a vital role in the poleward transfer of heat and salt and serves to warm the European subcontinent. In addition, the NAC (east of Newfoundland and north of 40°N) is part of the STG. The NAC begins as a northward western boundary current fed by the Gulf Stream, and turns eastward at $\sim 51^\circ\text{N}$, where it then splits into a northward (joins the subpolar circulation) and southward (joins the STG) flowing branch (Talley et al., 2011). The eastern and southern part of the STG of the North Atlantic consists of the Canary and Portugal Current System and the North Equatorial Current, respectively. The cyclonic SPG is composed of a narrow western boundary current along Greenland (East Greenland Current) and Labrador (Labrador Current) connected by the West Greenland Current on the eastern boundary of the subpolar gyre. As the NAC separates the subpolar and subtropical gyre, the sharp front across the NAC is called the Arctic Front ($\sim 40^\circ\text{N}$; Talley et al., 2011).

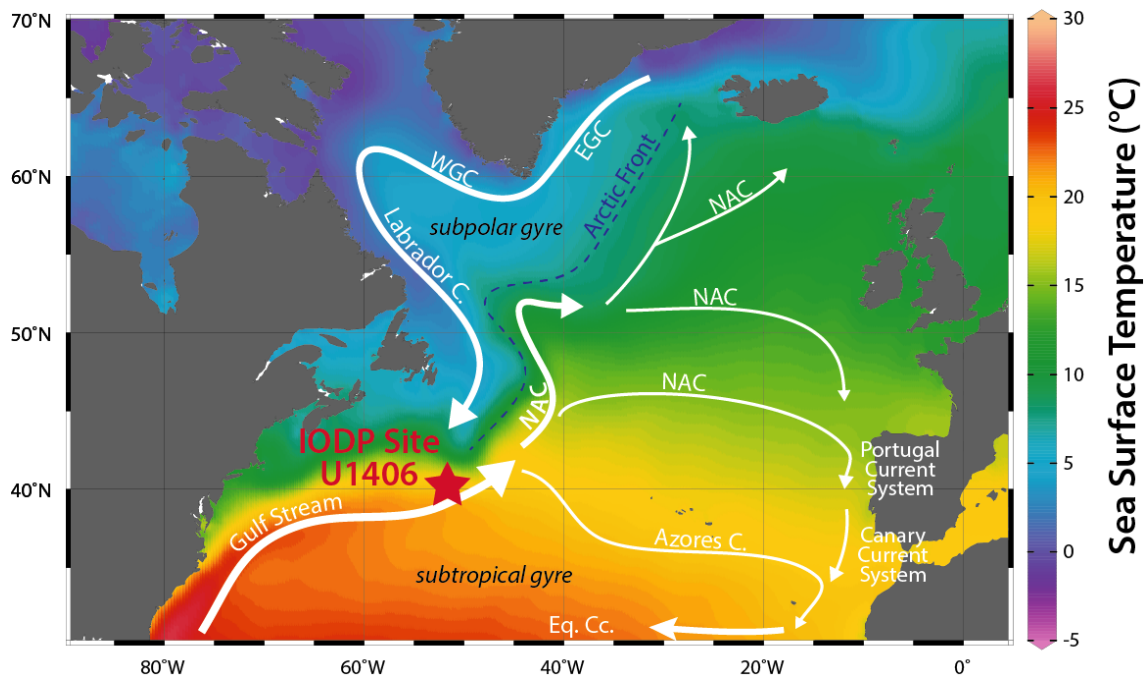


Figure 3.1-2: Modern sea-surface temperature distribution and surface circulation of the North Atlantic after World Ocean Atlas (Boyer et al., 2013). Location of IODP Site U1406 in the northwestern Atlantic indicated by red star. White arrows indicate the modern general circulation of major surface currents of the subpolar gyre (NAC = North Atlantic Current, EGC = Eastern Greenland Current, WGC = Western Greenland Current), separated by the Arctic Front from the subtropical gyre (Gulf Stream, NAC, Portugal Current System, Canary Current System, Azores Current, Eq. Cc. = Equatorial Counter Current) (Talley, 2013). Map has been compiled using Ocean Data View (Schlitzer, 2019).

3.1.3 Oligocene oceanography of the North Atlantic

The onset of the paleo pre-cursory NADW production, referred to as Northern Component Water (NCW), is a subject of discussion: Estimates for the onset of NCW export from the high northern latitudes range from as early as the middle to late Eocene (Hohbein et al., 2012; Borrelli et al., 2014;

Langton et al., 2016; Boyle et al., 2017), to the EOT around ~34 Ma, when ice-sheets initiated on Antarctica [e.g., Abelson and Erez (2017)], whereas others argue for a late Miocene initiation of significant NCW production [e.g., Wright and Miller (1996)]. According to a more recent study of Coxall et al. (2018), the initial stage of significant deep-water production in the North Atlantic is assumed to have initiated around 35 Ma ago: The northwestern Atlantic Ocean transitioned into a conduit for southward-flowing NCW triggered by tectonic adjustments in subarctic seas (Mosar et al., 2002). This allowed for an increased water exchange across the Greenland-Scotland Ridge (Coxall et al., 2018), therefore allowing southward flow of NCW, contributing to a modern-like deep-water circulation in the North Atlantic. The general circulation structure of the North Atlantic surface waters was similar to modern with evidence for ongoing southward transport of LSW from as early as the EOT (Coxall et al., 2018) and northward transport of warm equatorial-sourced waters via the Gulf Stream and further north via the NAC from as early as the late mid-Eocene (Wade et al., 2001).

A very small and shallow Tethys Seaway allowed small-scale circum-equatorial westward water transport from the Indian Ocean crossing the Atlantic Ocean (Hallam, 1969; Dercourt et al., 2000; von der Heydt and Dijkstra, 2006), and entering the Pacific Ocean through the Central American Seaway from the Cretaceous through the Miocene [e.g., Mikolajewicz et al., (1993); Schneider and Schmittner (2006); Campbell et al. (2010); Zhang et al. (2012)].

3.2 IODP Site U1406

Data presented in this thesis have been generated based on clay-rich sediments drilled within the framework of IODP from Site U1406 (40°21' N, 51°39' W, 3.8 km water depth) during Expedition 342 from June to July 2012 (Norris et al., 2014a). IODP Site U1406 is located on the J-Anomaly Ridge (JAR), which is part of the Newfoundland ridges, southeast of the southern Grand Banks offshore Newfoundland (Canada) in the northwestern Atlantic Ocean (Norris et al., 2014b) (Figure 3.2-1). At present, the location of Site U1406 is under the influence of the surface-water currents of the Gulf Stream and LSW, and deep-waters transported by the DWBC (see Section 3.1.2).

Three holes (A–C) were cored at Site U1406 using a combination of advanced piston corer (APC) and extended core barrel techniques (XCB) (Norris et al., 2014a). Post-cruise high-resolution X-Ray Fluorescence (XRF) core scanning was used for constructing a decimeter-composite-depth scale and a near-continuous [discontinuity does not affect the succession analyzed herein, see van Peer et al. (2017a) for details] splice record: Combining segments from Holes A–C, (van Peer et al., 2017a) constructed a composite section for Site U1406 with an approximate length of 340.55 m core composite depth below seafloor (CCSF-M), which is equivalent to meters composite depth below seafloor (mcd). In this thesis, a succession of Late Oligocene material is analyzed (see Section 4.1), characterized by light greenish grey colored nannofossil ooze (Norris et al., 2014b). Sedimentation rates are high, with an average ~2.3 cm/kyr, inferred from high-resolution magnetostratigraphy (van Peer et al., 2017b). Generally, sedimentation at IODP Site U1406 on the JAR has been active since the Early Cretaceous. Since ~47

Ma, persistent southward-flowing North Atlantic deep-water currents have facilitated the deposition of contourite drift sediments (Boyle et al., 2017). The highly dynamic nature of sediment drifts that are often deposited at elevated rates, therefore provides great potential for high-resolution studies of oceanic processes (Knutz, 2008; Rebesco et al., 2014).

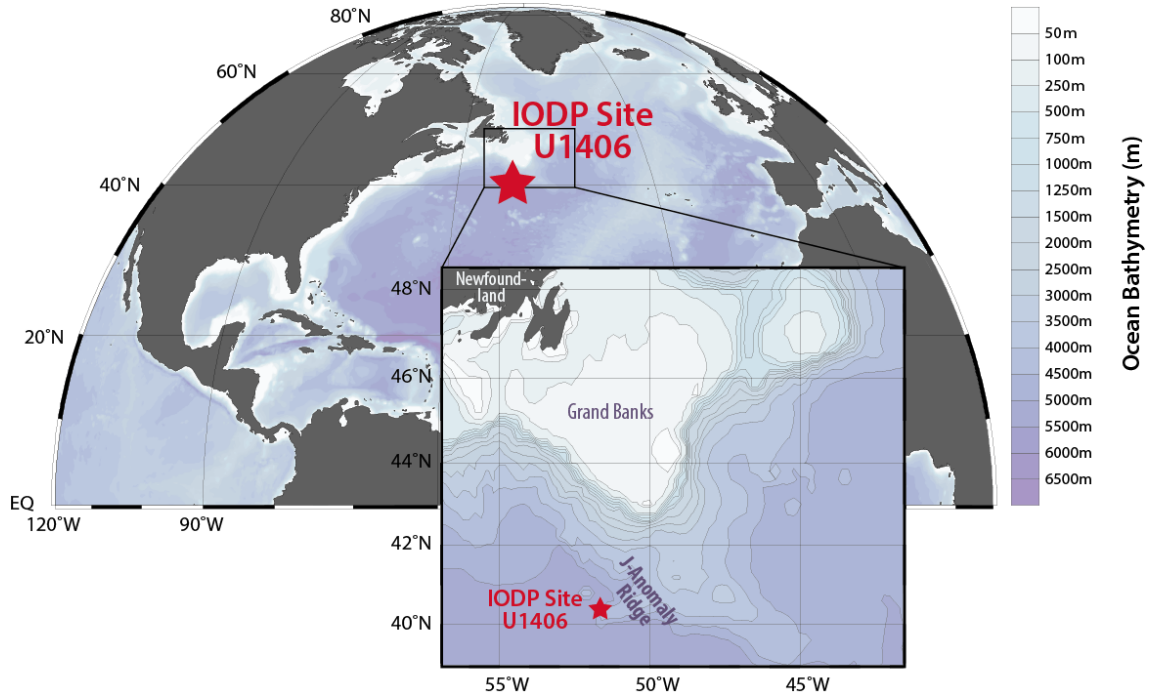


Figure 3.2-1: Location IODP Site U1406. Site U1406 (red star) is located in the northwestern Atlantic. A detailed map of the JAR on the Newfoundland ridges is presented. Map has been compiled using Ocean Data View (Schlitzer, 2019).

In addition to high-sedimentation rates, the clay-rich, Late Oligocene sediments from Site U1406 show exceptional preservation and abundant occurrence of well-preserved benthic and planktic foraminifera (Norris et al., 2014a). These prerequisites allow for high-resolution and high-fidelity geochemical analyses. SEM imaging of benthic (*C. mundulus* and *O. umbonatus*) and planktic (*C. dissimilis*) foraminifera conducted for this thesis further rule out signs of dissolution or recrystallization (see Section 2.6; Figure 2.7-1).

4 METHODS

4.1 Sample material and sediment processing

Samples from IODP Site U1406 with a volume of $\sim 20 \text{ cm}^3$ were taken with an average spacing of 2 cm between 116.02 and 145.90 m revised CCSF-A (core composite depth below seafloor, Method A) using the revised splice of (van Peer et al., 2017a) (cores U1406B-12H-4-22 cm through U1406B-12H-6-76 cm; U1406A-12H-3-8 cm through U1406A-12H-5-64 cm; U1406B-13H-2-14 cm through U1406B-13H-6-60 cm; U1406A-13H-3-30 cm through U1406A-13H-5-88 cm, U1406B-14H-2-54 cm through U1406B-14H-6-88 cm; U1406C-15H-1-104 cm through U1406C-15H-5-126 cm and U1406B-15H-3-0–34 cm). The specific sample intervals and spacings for individual analyses of the following chapters are listed below:

Chapter 5: Samples were collected from 141.29–145.90 m revised CCSF-A (van Peer et al., 2017a) at a spacing of 2–4 cm to generate a (sub)orbital, high resolution (~ 0.6 –1.5 kyr) benthic foraminiferal $\delta^{18}\text{O}$ and Mg/Ca data set for the Late Oligocene between 25.78 to 25.95 Ma.

Chapter 6: Samples were collected from 116.02–145.90 m revised CCSF-A (van Peer et al., 2017a) at a spacing of 2–4 cm to generate a high-resolution (~ 0.6 –2 kyr) benthic foraminiferal $\delta^{18}\text{O}$ and Mg/Ca data set for the Late Oligocene between 24.53 to 25.95 Ma.

Chapter 7: Samples were collected from 116.02–145.90 m revised CCSF-A (van Peer et al., 2017a) at a spacing of ~ 6 cm to generate a high resolution (~ 0.6 –2 kyr) benthic and planktic foraminiferal $\delta^{13}\text{C}$, $\delta^{18}\text{O}$ and planktic Mg/Ca data set for the Late Oligocene between 24.53 to 25.95 Ma.

In a first step, samples were oven-dried at 40°C and weighed. Subsequently, they were washed through a $>63 \mu\text{m}$ sieve to separate the fine ($<63 \mu\text{m}$) and coarse ($>63 \mu\text{m}$) fractions. Between 2 to 15 individuals of benthic foraminifera, and 15 to 25 individuals of the planktic foraminiferal species *C. dissimilis* were picked from the >125 –250 μm fraction to avoid ontogenetic effects (e.g., Friedrich et al., 2012). This range was, however, widened to 300 μm for a few cases of insufficient numbers. Subsequently, individuals of planktic foraminifera were weighed and isolated for geochemical analyses. Subsequently,

tests of picked individuals were cracked and split into sample aliquots that were isolated for geochemical analyses.

4.2 Stable isotope measurements

For stable carbon and oxygen isotope analyses on tests of the benthic foraminiferal species *C. mundulus* and *O. umbonatus*, and the planktic foraminiferal species *C. dissimilis*, ~20–80 µg of the sample aliquots have been analyzed using a ThermoFinnigan MAT253Plus gas source mass spectrometer equipped with a Thermo Fisher Scientific Kiel IV carbonate device at Heidelberg University. The results are reported relative to the Vienna Pee Dee Belemnite (VPDB) through the analysis of an in-house standard (Solnhofen limestone) calibrated to IAEA-603. The analytical precision is ±0.03‰ for δ¹³C and ±0.06‰ for δ¹⁸O.

Chapter 5: Of a total of 210 δ¹⁸O_{BF} measurements, 165 were primarily derived from the benthic foraminiferal taxa *O. umbonatus* and, where not abundant, substituted by analyses on *C. mundulus* (total of 45 measurements, of which 22 were previously analyzed by project collaborators). Measured δ¹⁸O_{BF} values of *C. mundulus* were adjusted to *O. umbonatus* values by adding 0.37‰ after calculating the average interspecies offset between *C. mundulus* and *O. umbonatus* (Figure 5.1-1). This isotopic correction factor applied to *C. mundulus* values is in close agreement with recent studies (0.4‰, Billups et al., 2004; 0.34‰, Coxall and Wilson, 2011) that infer rather similar offsets.

Chapter 6: Of a total of 1055 δ¹⁸O_{BF} measurements, 716 were primarily derived from the benthic foraminiferal taxa *O. umbonatus*, and, where not abundant, substituted by analyses on *C. mundulus* (total of 339 measurements, of which 219 were previously analyzed by project collaborators). Measured δ¹⁸O_{BF} values of *C. mundulus* were adjusted to *O. umbonatus* values by adding 0.36‰ after calculating the average interspecies offset between *C. mundulus* and *O. umbonatus* (see Figure 6.2-1). This isotopic correction factor applied to *C. mundulus* values is in close agreement with recent studies (0.4‰, Billups et al., 2004; 0.34‰, Coxall and Wilson, 2011) that infer rather similar offsets.

Chapter 7: Of a total of 973 δ¹³C_{BF} measurements on *C. mundulus*, 615 were previously analyzed by project collaborators. Following Shackleton et al. (1984), δ¹⁸O values of *C. mundulus* reported herein were adjusted for species-specific offset from equilibrium by the addition of +0.5‰ (see Table 2.7-1) (Shackleton et al., 1984). *Cibicidoides mundulus* precipitates its shell close to δ¹³C equilibrium. Therefore, no adjustment factor is required (e.g., Shackleton et al., 1984).

4.3 Mg/Ca measurements

For Mg/Ca analysis, ~150–200 µg of crushed test fragments of the benthic foraminifer *O. umbonatus* and the planktic foraminifer *C. dissimilis* were cleaned following the protocol of Barker et al. (2003). Subsamples were washed with Milli-Q ultrapure water (18.2 Ω) and methanol (CH₄O, ROTISOLV ≥99.98 %) to remove clays. Remaining organic material was removed by oxidative cleaning using 250 µl of an oxidizing agent (120 µl of 30 % H₂O₂ added to 12 ml of 0.1M NaOH). Reductive cleaning that

involves bathing the sample in a hot buffered solution of hydrazine was omitted because it lowers the Mg/Ca ratio by partial dissolution of foraminiferal calcite [see Barker et al. (2003, 2005) and Bian and Martin (2010) for detailed discussion]. Thereafter, samples were visually inspected under a binocular microscope to remove large non-carbonate particles with a fine brush. Subsequently, a weak acid leach was applied to remove any re-adsorbed contaminants from the surface of the foraminiferal tests by adding 250 μ l of 0.001M HNO₃, after which samples were dissolved in trace metal pure 0.075M HNO₃ to a final volume of 500 μ l. Samples were analyzed using an Agilent Inductively Coupled Plasma-Optical Emission Spectrometer 720 at Heidelberg University. Reported Mg/Ca values were normalized relative to the ECRM 752-1 standard with a reference value of 3.762 mmol/mol (Greaves et al., 2008). To ensure instrumental precision, an internal consistency standard was monitored every 12 samples. The precision was better than ± 0.03 mmol/mol.

Al/Ca, Fe/Ca and Mn/Ca ratios of foraminiferal tests exceeding 0.1 mmol/mol may be indicative for test contamination with clay, Fe-oxide or Mn-oxide coatings not removed during the Mg/Ca cleaning process, which may also affect the test Mg/Ca signature (Barker et al., 2003). To assess these potential contaminations, Al, Fe and Mn contents were monitored during Mg/Ca analysis (see 5.1.2).

4.4 Paleotemperature reconstruction and Mg/Ca_{sw} corrections

Numerous archives suggest that the major ion and isotopic composition of seawater have changed in parallel with significant variations in geologic processes and Earth's climate. As mentioned in Section 2.5, Mg/Ca_{sw} has varied by up to a factor of 5 throughout the Phanerozoic (Dickson, 2002; Gothmann et al., 2015). Hence, potential changes in Mg/Ca_{sw} since the Late Oligocene (see below) compared to the modern ocean have to be accounted for when applying Mg/Ca-paleothermometry. For the Late Oligocene, different Mg/Ca_{sw} ratios reconstructed from the composition of calcium carbonate veins (CCVs) formed in oceanic crust (Coggon et al., 2010; Rausch et al., 2013) and from fossil coral archives (Gothmann et al., 2015) are currently available that range from 1.8 to 3.6 mol/mol.

Because the relationship between seawater and shell Mg/Ca is not well constrained for corals (Evans et al., 2018), doubt has been raised about the use of corals as an archive for Mg/Ca_{sw}. In addition, the total range of Oligocene coral-based Mg/Ca_{sw} data spanning the time period of 33.6–23.7 Ma of Gothmann et al. (2015) is associated with a range of 2.5 mol/mol (1.8–4.3 mol/mol). A Mg/Ca_{sw} shift of 2.5 mol/mol over the course of the Oligocene is, however, unlikely due to the long residence time of Mg (~10 Ma) in seawater [see discussion in Zeebe and Tyrrell (2018)], as well as in light of the overall range (~5 mol/mol) that Mg/Ca_{sw} has varied over the Phanerozoic (Dickson, 2002; Gothmann et al., 2015).

In contrast to Gothmann et al. (2015), the studies by Coggon et al. (2010) and Rausch et al. (2013) reconstructed Mg/Ca_{sw} from CCVs formed in oceanic crust. Following a comparison of available archives used for Mg/Ca_{sw} reconstructions, CCV's were shown to result in relatively small uncertainties compared to other available Mg/Ca_{sw} reconstructions (Evans et al., 2018) and therefore, should provide a more reliable estimate of Late Oligocene Mg/Ca_{sw}. Yet, several factors that weaken the applicability

of the Mg/Ca_{sw} reconstructions from Coggon et al. (2010) to yield reliable Mg/Ca_{sw} values for the studied interval have been invoked (Broecker and Yu, 2011; Rausch et al., 2013): (i) Considerable uncertainties in the calculation of Mg/Ca_{sw} introduced from temperature extrapolation required for young ocean basement sites, (ii) post-precipitation alteration of CCVs due to sampling CCVs from older crustal ages, and (iii) the scarcity of Mg/Ca_{sw} data within the critical interval of the last 30 Ma years [see Broecker and Yu (2011) for detailed discussion]. In the study of Rausch et al. (2013), these shortcomings have been largely addressed (see publication for further details). Additional support to the approach of Rausch et al. (2013) is given by a good agreement of their Mg/Ca_{sw} reconstructions with modelled Mg/Ca_{sw} values of Demicco et al. (2005) and Farkaš et al. (2007). Based on the above arguments, the late Oligocene Mg/Ca_{sw} reconstruction of 3.6 mol/mol (Rausch et al., 2013) is being utilized for Mg/Ca-based paleothermometry in this thesis.

BWTs based on Mg/Ca ratios of *O. umbonatus* were calculated using the species-specific, exponential calibration for *O. umbonatus* of Lear et al. (2002) because the range of Mg/Ca ratios observed at Site U1406 (1.05–1.99 mmol/mol) is only captured within the calibration range of this specific calibration (1.09–3.43 mmol/mol):

$$Mg/Ca_c^{t=t} = \frac{Mg/Ca_{sw}^{t=t}}{Mg/Ca_{sw}^{t=0}} \times (1.008 \pm 0.08) \exp^{(0.114 \pm 0.02) \times T}.$$

Because this calibration is based on oxidative and reductive cleaning of foraminiferal tests, whereas only oxidative cleaning has been applied on foraminiferal tests in this thesis, measured Mg/Ca values were adjusted by reducing each value by 10 % (Barker et al., 2003).

Mg/Ca ratios measured on specimens of *C. dissimilis* were turned into temperature estimates using the multispecies equation of Anand et al. (2003):

$$Mg/Ca_c = \frac{Mg/Ca_{sw}^{t=t}}{Mg/Ca_{sw}^{t=0}} \times (0.38 \pm 0.02) \exp^{(0.09 \pm 0.003) \times T},$$

where Mg/Ca_c is the Mg/Ca of the foraminiferal calcite, Mg/Ca_{sw}^{t=t} is seawater Mg/Ca estimated for the Late Oligocene [3.6 mol/mol, Rausch et al. (2013)], Mg/Ca_{sw}^{t=0} is seawater Mg/Ca of the modern ocean [5.2 mol/mol, (Dickson, 2002)], and T is the temperature in degrees Celsius.

4.5 δ¹⁸O_{sw} calculations

To assess the ice-volume component, coupled Mg/Ca-oxygen isotope measurements on benthic foraminifera enable the δ¹⁸O paleotemperature equation to be solved for past δ¹⁸O_{sw} [relative to the Standard Mean Ocean Water (SMOW)]. In this chapter, δ¹⁸O_{sw} was calculated using *O. umbonatus*-based δ¹⁸O_{BF} and BWT estimates using the paleotemperature equation of Shackleton (1974), which, compared to other available paleotemperature equations, covers low water temperatures down to 0 °C, which is:

$$BWT (°C) = 16.9 - 4.0 \times (\delta^{18}O_{BF} - \delta^{18}O_{sw}),$$

where BWT is the bottom-water temperature estimate, $\delta^{18}\text{O}_{\text{BF}}$ is the measured benthic foraminiferal oxygen isotope value, and $\delta^{18}\text{O}_{\text{sw}}$ is past seawater $\delta^{18}\text{O}$. Values were converted to SMOW by adding 0.27‰ (Hut, 1987). This paleotemperature equation was chosen over other available calibrations since it covers a low temperature spectrum down to 0 °C (total range of 0–30°C), which covers Mg/Ca-based BWTs reconstructed for Site U1406 during the Late Oligocene (see Section 5.1.3 and 6.2.3).

For $\delta^{18}\text{O}_{\text{sw}}$ reconstructions of the sub-thermocline dwelling planktic foraminifera *C. dissimilis* (see Section 2.7.3), the temperature component of Mg/Ca-based sub-thermocline temperature (°C) from the planktic foraminiferal $\delta^{18}\text{O}$ (‰ VPDB) record by using the paleotemperature equation of Bemis et al. (1998)

$$T \text{ (}^\circ\text{C)} = 16.5(\pm 0.2) - 4.8(\pm 0.16) \times (\delta^{18}\text{O}_{\text{PF}} - \delta^{18}\text{O}_{\text{sw}}),$$

and converted to SMOW by adding +0.27‰ (Hut, 1987). The Bemis et al. (1998) paleotemperature equation was chosen over other available calibrations since it covers a temperature spectrum of 15° to 25 °C, which covers Mg/Ca-based sub-thermocline temperatures reconstructed for Site U1406 during the Late Oligocene (see Section 7.2.2).

4.5.1 $\delta^{18}\text{O}_{\text{ivf-sw}}$ reconstructions for Site U1406

The resulting planktic foraminiferal $\delta^{18}\text{O}_{\text{sw}}$ record reflects continental ice volume and local salinity variability (see Section 2.4.1). To deconvolve the salinity signal from the planktic $\delta^{18}\text{O}_{\text{sw}}$ signal, the ice-volume effect from planktic foraminiferal $\delta^{18}\text{O}_{\text{sw}}$ (hereafter referred to as $\delta^{18}\text{O}_{\text{ivf-sw}}$) was removed by subtracting Site U1406 benthic foraminiferal $\delta^{18}\text{O}_{\text{sw}}$ (see Section 5.1.4 and 6.2.4). Therefore, the benthic Site U1406 $\delta^{18}\text{O}_{\text{sw}}$ record was interpolated on the resolution given by the Site U1406 planktic $\delta^{18}\text{O}_{\text{sw}}$ record.

4.5.2 Uncertainties associated with seawater $\delta^{18}\text{O}_{\text{sw}}$ reconstruction

The uncertainty in the $\delta^{18}\text{O}_{\text{sw}}$ reconstruction was evaluated through Monte Carlo Simulations. Input data for the benthic foraminifera-based $\delta^{18}\text{O}_{\text{sw}}$ reconstruction were the $\delta^{18}\text{O}_{\text{BF}}$, Mg/Ca values with their analytical precision (0.06‰ and 0.03 mmol/mol, respectively), and the BWT, and $\delta^{18}\text{O}_{\text{sw}}$ equations with their calibration errors (Shackleton, 1974; Lear et al., 2015) (see Section 4.4 and 4.5). The propagated uncertainty for $\delta^{18}\text{O}_{\text{sw}}$ is ± 0.23 ‰.

Input data for the planktic foraminifera-based $\delta^{18}\text{O}_{\text{sw}}$ reconstruction were the $\delta^{18}\text{O}_{\text{PF}}$, Mg/Ca values with their analytical precision (0.06‰ and 0.03 mmol/mol, respectively), and the temperature and $\delta^{18}\text{O}_{\text{sw}}$ equations with their calibration errors (Bemis et al., 1998; Anand et al., 2003). The propagated uncertainty for $\delta^{18}\text{O}_{\text{sw}}$ is ± 0.2 ‰.

4.5.3 Spectral analyses

To investigate the presence and determine the dominance of orbital frequencies in the time-series of IODP Site U1406 proxy data presented in this thesis, spectral analyses were performed.

Chapter 5: REDFIT spectral analysis (Schulz and Mudelsee, 2002) was applied using the Paleontological Statistics Software Package (PAST) (Hammer et al., 2001). Before analysis, the $\delta^{18}\text{O}_{\text{BF}}$, Mg/Ca, and $\delta^{18}\text{O}_{\text{sw}}$ records were linearly detrended. The time series were interpolated at a sample resolution of 1 kyr. In the next step, Blackman-Tukey cross-spectral phase estimates between the $\delta^{18}\text{O}_{\text{BF}}$, Mg/Ca, and $\delta^{18}\text{O}_{\text{sw}}$ time series and the orbital solution for obliquity (Laskar et al., 2004) using the AnalySeries software package version 2.0.8 (Paillard et al., 1996) were carried out. Results were converted to lag times in kyr.

Chapter 6: Prior to all time series analyses, the data records were resampled using a simple interpolation (Paillard et al., 1996). Resampling was done at the average sampling resolution of each record, namely at 1.34, 2.01, and 2.06 kyr for $\delta^{18}\text{O}_{\text{BF}}$, BWT, and $\delta^{18}\text{O}_{\text{sw}}$, respectively. Subsequently, periodicities greater than 250 kyr were removed using a Gaussian notch filter.

For the wavelet analysis, a Morlet-window was used to transform the time series into the time-periodicity domain. The black contours in the wavelets indicate the 95% significance level. The shaded (grey) area in the wavelet plots (Figure 6.2-4) represents the cone-of-influence. Underneath this shaded area, edge-effects can distort the outcome of the wavelet analysis.

Amplitude responses of $\delta^{18}\text{O}_{\text{sw}}$ to eccentricity and obliquity were computed after band-pass filtering of the data. Frequency bandwidths of 0 to 17.8 and 17.8 to 35.6 Myr^{-1} (periodicities between ∞ and 56 kyr, and between 56 and 28 kyr) were used for eccentricity and obliquity paced cycles, respectively. After filtering, the Hilbert transform was computed to obtain the amplitude modulations. The eccentricity amplitude modulation of $\delta^{18}\text{O}_{\text{sw}}$ is directly compared to the orbital eccentricity solution, and the obliquity amplitude modulation of $\delta^{18}\text{O}_{\text{sw}}$ to the amplitude modulation of the obliquity solution (Laskar et al., 2004).

To obtain phase estimates with respect to the eccentricity and obliquity solutions, the $\delta^{18}\text{O}_{\text{sw}}$ data were first multiplied with -1 , because $\delta^{18}\text{O}_{\text{sw}}$ maxima generally coincide with eccentricity and obliquity minima. Blackman-Tukey cross-spectral analyses were subsequently computed using a Barlett window (Paillard et al., 1996). To obtain significant results, the confidence level was set on the error estimates at 80 % for the phase computations between $\delta^{18}\text{O}_{\text{sw}}$ and eccentricity, and at 95 % for those between $\delta^{18}\text{O}_{\text{sw}}$ and obliquity.

4.6 Age model

Post-cruise high-resolution X-Ray Fluorescence (XRF) core scanning was used to construct a composite-depth scale and a near-continuous splice record for the sedimentary record of IODP Site U1406 (van Peer et al., 2017a). The resulting splice has a length of 340.55 m core composite depth below seafloor (CCSF-A) [equivalent to meters composite depth below seafloor (mcd)] (van Peer et al.,

2017a). A sequence spanning ~36 to 160 m revised CCSF-A (van Peer et al., 2017a, b) of this U1406 splice was used as a basis to establish an initial magnetostratigraphic age model (van Peer et al., 2017b). Shore-based paleomagnetic analysis (natural remanent magnetisation measurements with complete shore-based demagnetization treatment) on 159 continuous U1406 u-channel samples in combination with a noise-masking protocol were used to accurately define magnetic reversals (van Peer et al., 2017b). The resulting magnetostratigraphic framework spans an expanded sequence of high-resolution early Miocene to Late Oligocene sediments encompassing six geomagnetic field reversals [C6Ar/C6AAn through C9n/C9r, ~21–27 Ma; (van Peer et al., 2017b)]. Sedimentation rates based on the correlation of the Site U1406 magnetostratigraphy to the Geological Time Scale 2012 [GTS2012, (Hilgen et al., 2012; Vandenberghe et al., 2012)] are on average ~2.3 cm/kyr (van Peer et al., 2017b).

Subsequently, this magnetostratigraphy was used in combination with high-resolution X-ray fluorescence (XRF) $\ln(\text{Ca}/\text{K})$ data from Site U1406 for cyclostratigraphic analysis (van Peer et al., in prep.). The $\ln(\text{Ca}/\text{K})$ data was calibrated to measurements of carbonate content using a logarithmic fit between $\ln(\text{Ca}/\text{K})$ and CaCO_3 (van Peer et al., in prep.). By matching cyclic variability imprinted in U1406 CaCO_3 data of the above-mentioned Oligo-Miocene section [C6Ar/C6AAn through C9n/C9r, ~21–27 Ma; (van Peer et al., 2017b)] to the orbital solution for obliquity (~41 kyr) (Laskar et al., 2004), van Peer et al. (in prep.) have established a further improved cyclostratigraphic age model.

The high-resolution proxy records of IODP Site U1406 presented in this thesis are based on the astrochronology of van Peer et al. (in prep.). Sedimentation rates vary between 1.7 cm/kyr and 3 cm/kyr with an average of ~2.3 cm/kyr (van Peer et al., 2017b).

5 OBLIQUITY-PACED ANTARCTIC ICE-VOLUME FLUCTUATIONS DURING THE LATE OLIGOCENE

While the long-term evolution of the Oligocene AIS has been well established over the last decade, the short-term dynamics of AIS variability are not well understood. A recent study (Liebrand et al., 2017) spanning the interval 30.1–17.1 Ma shows recurrent episodes of high-amplitude variability in $\delta^{18}\text{O}_{\text{BF}}$ requiring waning and waxing of at least ~85 to 110 % of the present-day volume of the EAIS following cyclicity of the short-term eccentricity (~100-kyr). From 27 Ma onwards, this record shows a decrease in AIS size, a finding that is in contrast to recent $\delta^{18}\text{O}_{\text{BF}}$ -based ice-volume reconstructions from Maud Rise (Antarctica) (Hauptvogel et al., 2017). Hauptvogel et al. (2017) infer a heavily glaciated Antarctic continent during the late Oligocene (27.8–24.5 Ma) yielding an ice sheet near or even larger than modern size and, notably, without significant collapse during interglacials. In addition to these uncertainties about Oligocene AIS volume, the pacing of AIS dynamics is unclear. Antarctic ice-volume fluctuations inferred from $\delta^{18}\text{O}_{\text{BF}}$ records suggest that Oligocene glacials were primarily paced by changes in the long (~400 kyr)- and short (~100 kyr)-period eccentricity, whereas the sensitivity to short-term obliquity forcing was low (Pälike et al., 2006b; Liebrand et al., 2016b). More recently, Levy et al. (2019) confirmed the dominance of eccentricity forcing in parallel with a very low sensitivity to obliquity forcing on the Oligocene AIS. In contrast to these ice-distal $\delta^{18}\text{O}_{\text{BF}}$ records, ice-proximal geological records not only show pacing related to periodicities of Earth's eccentricity but appear to document obliquity-paced AIS oscillations (~40 kyr) (Naish et al., 2001; Galeotti et al., 2016; Salabarnada et al., 2018). The apparent controversy of Oligocene AIS volumes and pacing inferred from ice-distal $\delta^{18}\text{O}_{\text{BF}}$ records and ice-proximal geological records might be partially caused by the methodology applied to infer ice-volume estimates and dynamics from $\delta^{18}\text{O}_{\text{BF}}$ records. Current Late Oligocene ice-volume estimates (Hauptvogel et al., 2017; Liebrand et al., 2017) and dynamics are derived from $\delta^{18}\text{O}_{\text{BF}}$ records paired with constant, modern BWT. However, as illustrated in the approach pioneered by Lear et al.

(2000), independent temperature records derived through Mg/Ca-paleothermometry (see Section 4.4) are needed to reliably deconvolve the ice volume component from a $\delta^{18}\text{O}_{\text{BF}}$ signal.

In this chapter, the existing controversy regarding AIS volumes during the Late Oligocene is being tested through the generation of high-resolution $\delta^{18}\text{O}_{\text{BF}}$ and Mg/Ca records from the northwestern Atlantic IODP Site U1406 (Figure 3.2-1) covering the time interval ~ 25.95 to 25.78 Ma. The temperature component of $\delta^{18}\text{O}_{\text{BF}}$ is independently assessed through Mg/Ca-paleothermometry, which is subsequently combined with $\delta^{18}\text{O}_{\text{BF}}$ data to deconvolve $\delta^{18}\text{O}_{\text{sw}}$, i.e., the ice-volume component. Furthermore, ice-volume estimates are calculated based on U1406 $\delta^{18}\text{O}_{\text{sw}}$ data that are subsequently compared to previous ice-volume estimates for the Late Oligocene. To investigate the apparent mismatch in relation to previously inferred pacing of the Oligocene AIS, the proxy records were generated (i) across an interval that falls into an episode of low eccentricity, yet high amplitude obliquity forcing to test for the actual influence of eccentricity forcing on the AIS or potentially higher frequency oscillations and (ii) generated at a high resolution (≤ 1 kyr) allowing for possible influences of higher orbital frequencies than eccentricity to be inspected.

5.1 Results and discussion

5.1.1 *Stable oxygen isotope record*

The Site U1406 $\delta^{18}\text{O}_{\text{BF}}$ record shows four well-pronounced sinusoidally shaped oscillations (hereafter, glacial-interglacial cycles) between ~ 25.95 – 25.78 (Figure 5.1-1). $\delta^{18}\text{O}_{\text{BF}}$ values vary between 1.8 and $\sim 2.7\text{‰}$, resulting in a total range of 0.9‰ across the studied interval of ~ 25.95 – 25.78 Ma (Figure 5.1-1). Higher values are associated with glacials, whereas lower values occur during interglacials. Notably, interglacial $\delta^{18}\text{O}_{\text{BF}}$ values remain invariant across the study interval (around $\sim 1.8\text{‰}$), whereas glacial $\delta^{18}\text{O}_{\text{BF}}$ values shift to higher values from $\sim 2.7\text{‰}$ to 2.4‰ around ~ 25.90 Ma. Spectral analysis of the $\delta^{18}\text{O}_{\text{BF}}$ record (Figure 5.1-4A) reveals a strong ~ 40 -kyr signal related to obliquity. Comparison to the orbital solution for obliquity (Laskar et al., 2004) shows correspondence of high (low) $\delta^{18}\text{O}_{\text{BF}}$ values with low (high) obliquity (Figure 5.1-3), yet lags obliquity by ~ 13 kyr (Figure 5.1-4D). This phase lag is longer than compared to reported phase lags of ~ 6.5 – 8 kyr of $\delta^{18}\text{O}_{\text{BF}}$ to obliquity periodicity from the Pleistocene and late Pliocene (Raymo and Nisancioglu, 2003; Lourens et al., 2010). The relatively longer phase lag of ~ 13 kyr of $\delta^{18}\text{O}_{\text{BF}}$ to obliquity could be an artifact arising from inaccuracies of astronomical tuning (personal communication with Tim van Peer).

5.1.2 *Assessment of contamination and diagenetic effects on the Mg/Ca ratios*

Elemental ratios of Al/Ca, Fe/Ca and Mn/Ca were monitored to identify contamination by clay particles or diagenetic coatings, which might affect the foraminiferal Mg/Ca ratios (Barker et al., 2003). Measured Al concentrations of the data are generally below the detection limit, arguing against the presence of detrital clay.

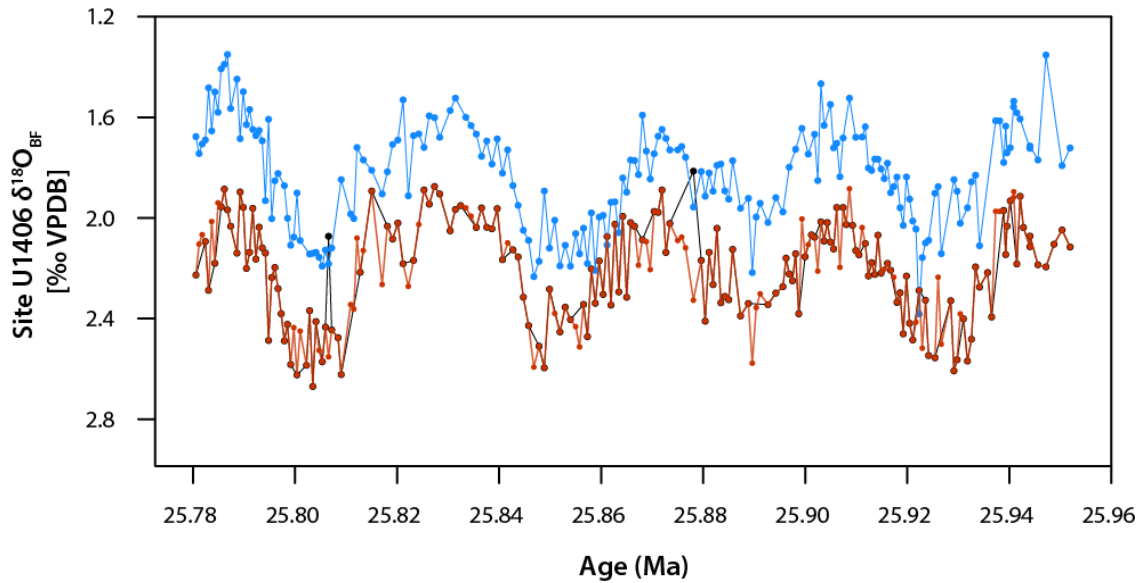


Figure 5.1-1: Paired isotope analyses of *C. mundulus* and *O. umbonatus*. Benthic foraminiferal $\delta^{18}\text{O}_{\text{BF}}$ analyses (in ‰ VPDB) of *C. mundulus* (blue), *O. umbonatus* (red), and the composite record (dashed black; *C. mundulus* converted to *O. umbonatus* by adding 0.37 ‰).

However, Fe/Ca and especially Mn/Ca ratios of *O. umbonatus* generally exceed the 0.1 mmol/mol threshold value defined by Barker et al. (2003) (Figure 5.1-2). Yet, a statistically significant correlation between Mg/Ca vs. Fe/Ca ($r^2=0.17$, $p<0.0001$) and Mg/Ca vs. Mn/Ca ($r^2=0.05$, $p<0.005$) is not observed (Figure 5.1-2), suggesting that Mn- and Fe-oxide coatings or Mn-carbonates (if present at all) did not considerably affect the measured Mg/Ca contents. In addition, SEM images rule out the presence of microcrystalline overgrowth on the measured *O. umbonatus* tests (Figure 2.7-1). It can therefore be concluded with reasonable certainty that early diagenetic overprinting has not affected Mg/Ca-based reconstructions for the interval 25.95–25.78 Ma at Site U1406.

5.1.3 BWT variability

The Mg/Ca-based BWT record from Site U1406 is characterized by obliquity-paced deep-sea temperatures of ~5 to 8 °C with an amplitude of ~2 to 3°C through the studied interval (Figure 5.1-3B; Figure 5.1-4B). Intervals of high $\delta^{18}\text{O}_{\text{BF}}$ values are paralleled by cooler BWT (5–6 °C) while intervals of low $\delta^{18}\text{O}_{\text{BF}}$ show warmer BWTs (7–8 °C). BWT values are in good agreement with low-resolution BWTs reconstructed from the equatorial Pacific (ODP Site 1218; Lear et al., 2004) (Figure 5.1-3B). Resulting from spectral analysis, the BWT record lags obliquity by ~2 kyr (Figure 5.1-4D).

5.1.4 Trends of Site U1406 $\delta^{18}\text{O}_{\text{sw}}$

Combining Mg/Ca-based BWTs with the $\delta^{18}\text{O}_{\text{BF}}$ data allows to deconvolve the influence of $\delta^{18}\text{O}_{\text{sw}}$ and temperature on $\delta^{18}\text{O}_{\text{BF}}$.

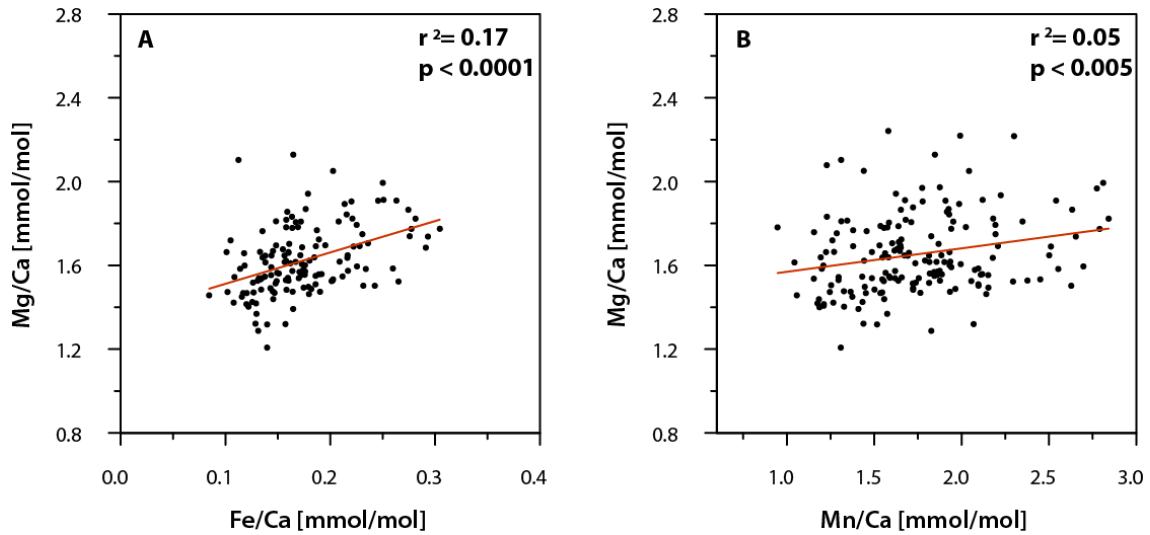


Figure 5.1-2: Evaluation of *Oridorsalis umbonatus* test contamination. Cross correlation plots of Mg/Ca versus Fe/Ca (A) and Mn/Ca (B), respectively, show no statistically significant correlation between Mg/Ca vs. Fe/Ca ($r^2 = 0.17$, $p < 0.0001$) and Mn/Ca ($r^2 = 0.05$, $p < 0.005$), indicating that measured Mg/Ca values are not systematically altered by clay particles or diagenetic coatings.

The Site U1406 $\delta^{18}\text{O}_{\text{sw}}$ record mimics the glacial-interglacial cyclicity of the $\delta^{18}\text{O}_{\text{BF}}$ record (Figure 5.1-3A, C) and shows values that range between -0.6 and 0.3‰ . $\delta^{18}\text{O}_{\text{sw}}$ values are higher during glacials (0 – 0.2‰), while interglacials are characterized by lower $\delta^{18}\text{O}_{\text{sw}}$ (-0.2 to -0.5‰) (Figure 5.1-3C). The average glacial-interglacial amplitude variability of Site U1406 $\delta^{18}\text{O}_{\text{sw}}$ of 0.5‰ is in good agreement with $\delta^{18}\text{O}_{\text{sw}}$ changes calculated for the equatorial Pacific ($\sim 0.5\text{‰}$; Lear et al., 2004) and the South Atlantic ($\sim 0.4\text{‰}$; Liebrand et al., 2017) for the studied interval. Resulting from spectral analysis, the signal is strong at the obliquity frequency, with a phase lag of ~ 10 kyr with respect to obliquity (Figure 5.1-4C, D). The Monte Carlo simulations indicate an uncertainty associated with the $\delta^{18}\text{O}_{\text{sw}}$ signal of $\pm 0.23\text{‰}$ (see Section 4.5.2).

5.1.5 Glacial-interglacial $\delta^{18}\text{O}_{\text{sw}}$ variability across study interval (25.95–25.78 Ma)

To constrain the magnitude of ice-volume change related to the observed $\delta^{18}\text{O}_{\text{sw}}$ amplitude, an assumption regarding the isotopic composition of the Late Oligocene ice-sheet ($\delta^{18}\text{O}_{\text{ice}}$) is required. Since major permanent Antarctic glaciation only initiated in the earliest Oligocene around ~ 33.6 Ma, the first ice to accumulate in the earliest Oligocene would have had a lighter isotopic composition (DeConto et al., 2008) than that of the modern EAIS (-56.6‰) and WAIS (-41‰) (Lhomme et al., 2004, 2005). State-of-the-art ice-sheet models yield varying $\delta^{18}\text{O}_{\text{ice}}$ of -48‰ to -35‰ spanning the earliest Oligocene to the early to mid-Miocene (DeConto et al., 2008; Gasson et al., 2016b) (Figure 5.1-5).

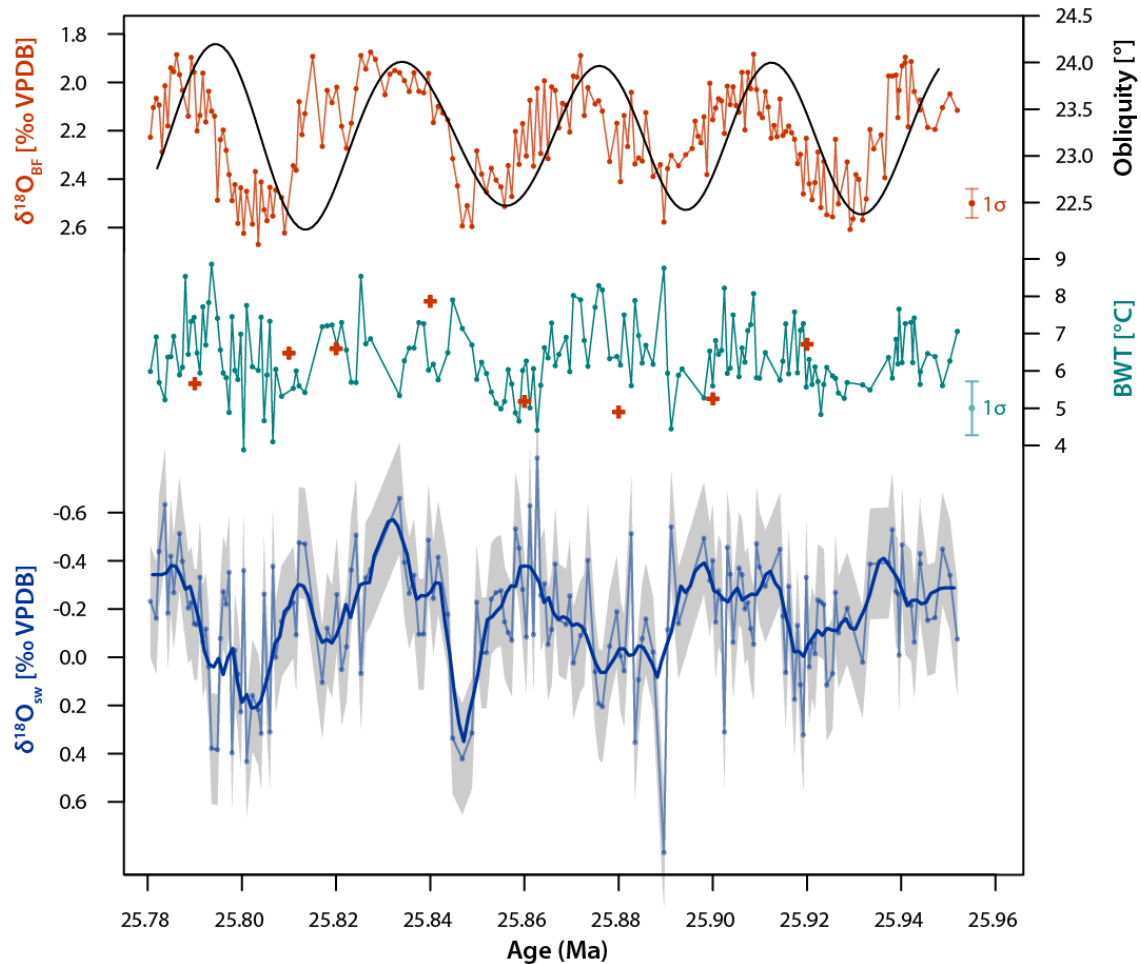


Figure 5.1-3: Geochemical proxy data from IODP Site U1406. (A) $\delta^{18}\text{O}_{\text{BF}}$ record (in ‰ VPDB; *C. mundulus* has been normalized to *O. umbonatus*, see Section 4.2) (red) from IODP Site U1406 together with the orbital solution for obliquity (black; Laskar et al., 2004). (B) Mg/Ca-based BWT estimate (in °C, green) with BWT estimates from ODP Site 1218 (Lear et al., 2004) [red crosses; recalculated following the same methodology as used herein (see Section 4.4)]. (C) Benthic foraminiferal $\delta^{18}\text{O}_{\text{sw}}$ (in ‰ SMOW) (blue) with 5-pt smoother (dark blue line) and ± 0.23 ‰ uncertainty resulting from Monte Carlo Simulations (grey envelop; see Section 4.5.2). Vertical bars indicate the 1σ standard deviation associated with the individual Site U1406 proxy records.

Modelled $\delta^{18}\text{O}_{\text{ice}}$ for the fully developed earliest Oligocene ice sheet had a maximum isotopic composition of -35 ‰, yet never became more negative than -42 ‰ as the AIS grew larger (DeConto et al., 2008). Following a more recent modelling study, average $\delta^{18}\text{O}_{\text{ice}}$ for the early to mid-Miocene AIS (based on an approximated mid-Miocene Antarctic bedrock topography) varied between -42 ‰ and -48 ‰ (Gasson et al., 2016b).

To test the sensitivity of the $\delta^{18}\text{O}_{\text{sw}}$ -based ice-volume estimates to $\delta^{18}\text{O}_{\text{ice}}$, the full range of modelled $\delta^{18}\text{O}_{\text{ice}}$ values is considered: Assuming $\delta^{18}\text{O}_{\text{ice}}$ between -48 ‰ and -35 ‰, ice-volume estimates can be made by inferring a pre-glacial $\delta^{18}\text{O}_{\text{sw}}$ of -1.05 ‰ (hereafter referred to as ‘ice-free baseline’) (Bohaty et al., 2012) and a growth of 3.8 million km^3 ($\times 10^6 \text{ km}^3$) of ice per 0.1 ‰ change in $\delta^{18}\text{O}_{\text{sw}}$ (Bohaty et al., 2012; Liebrand et al., 2017).

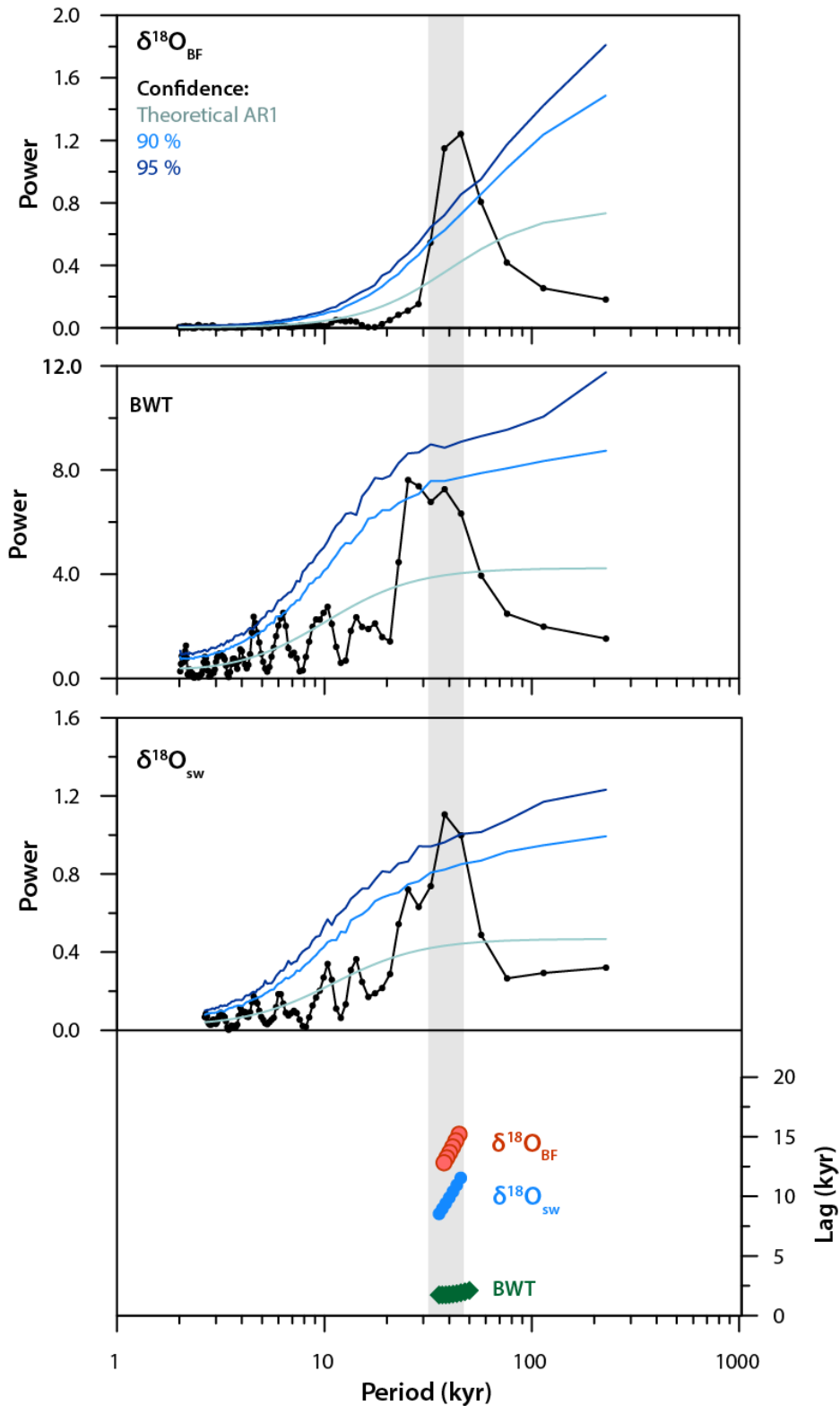


Figure 5.1-4: Spectral Analysis of $\delta^{18}\text{O}_{\text{BF}}$, Mg/Ca and $\delta^{18}\text{O}_{\text{sw}}$ time series. REDFIT spectral analysis (Schulz and Mudelsee, 2002) of $\delta^{18}\text{O}_{\text{BF}}$, BWT, and $\delta^{18}\text{O}_{\text{sw}}$ time series. Theoretical AR1 limit (light blue-green), Monte Carlo confidence intervals of 90 % (light blue) and 95 % (dark blue) are shown. The signal at the obliquity frequency is highlighted in all time series with a grey bar. (lower panel) Blackman-Tukey cross-spectral phase estimates between $\delta^{18}\text{O}_{\text{BF}}$ (red), BWT (green), and $\delta^{18}\text{O}_{\text{sw}}$ (blue) time series and the orbital solution for obliquity (Laskar et al., 2004), converted to lag times in kyr.

Sensitivity tests using the average U1406 $\delta^{18}\text{O}_{\text{sw}}$ glacial-interglacial amplitude of 0.5‰ (see Section 5.1.4) show that the more positive $\delta^{18}\text{O}_{\text{ice}}$, the bigger the resulting AIS volume and the bigger the amplitude of relative ice-volume change across the study interval (Figure 5.1-5). The glacial-interglacial $\delta^{18}\text{O}_{\text{sw}}$ amplitude of 0.5‰ results in $23 \times 10^6 \text{ km}^3$ assuming $\delta^{18}\text{O}_{\text{ice}}$ is -35‰. In contrast, using the most negative $\delta^{18}\text{O}_{\text{ice}}$ of -48‰ results in an amplitude change of $16.6 \times 10^6 \text{ km}^3$ ice (Figure 5.1-5; Table 5.1-1). Since the focus of this thesis is on the Late Oligocene, a $\delta^{18}\text{O}_{\text{ice}}$ value of -42‰, reconstructed both as the minimum $\delta^{18}\text{O}_{\text{ice}}$ for the early to mid-Miocene (Gasson et al., 2016b) and the maximum $\delta^{18}\text{O}_{\text{ice}}$ for the early Oligocene (DeConto et al., 2008), is regarded most appropriate to estimate Late Oligocene Antarctic ice-volume fluctuations and used for ice-volume estimates discussed in the following.

Average interglacial ice-volumes across the study interval have a volume of $\sim 26 \times 10^6 \text{ km}^3$ of ice (based on average interglacial $\delta^{18}\text{O}_{\text{sw}}$ range of -0.2 to -0.5‰), while average glacial ice-volumes reach a size of $\sim 43 \times 10^6 \text{ km}^3$ (based on maximum Site U1406 $\delta^{18}\text{O}_{\text{sw}}$ value of 0 to 0.2‰) during glacial episodes. Translating the average Site U1406 $\delta^{18}\text{O}_{\text{sw}}$ glacial-interglacial amplitude of 0.5‰ to ice-volume estimates equates to $19 \times 10^6 \text{ km}^3$ of ice (Table 5.1-1), which requires the waning and waxing of $\sim 63\%$ of the modern global ice-volume [$30.13 \times 10^6 \text{ km}^3$; Grinsted (2013); Fretwell et al. (2013); Bamber et al. (2013)] within 20 kyr (half an obliquity cycle). These results, therefore, imply a very dynamic AIS across the study interval (25.95–25.78 Ma), which is in stark contrast to previous ice-volumes estimates: $\delta^{18}\text{O}_{\text{BF}}$ -based ice-volume reconstructions from ODP Site 690 [Maud Rise, Antarctica; Hauptvogel et al. (2017)] infer a heavily glaciated Antarctic continent during the Late Oligocene (27.8–24.5 Ma) yielding an AIS near or even larger than modern size and, notably, without significant AIS disintegration during interglacials. On the contrary, a previous $\delta^{18}\text{O}_{\text{BF}}$ -based study from ODP Site 1264 [South Atlantic; Liebrand et al. (2017)] estimated ice-volumes in the range of $\sim 1\text{--}20 \times 10^6 \text{ km}^3$ of ice across the study interval (25.95–25.78 Ma), which translates to an AIS in the range of ~ 3 to 75% of its modern size (Grinsted, 2013; Fretwell et al., 2013; Bamber et al., 2013). While the relative ODP Site 1264 magnitude of ice-volume change ($19 \times 10^6 \text{ km}^3$) is comparable to that inferred herein, absolute minimum and maximum ice-volume estimates are $\sim 50\%$ smaller than compared to those estimates from the Site U1406 $\delta^{18}\text{O}_{\text{sw}}$ record (Figure 5.1-6B).

The apparent offset between ice-volume estimates between those presented in this chapter and previous studies arises due to the records used for constraining ice-volume estimates: Herein, ice-volume estimates are calculated based on the high-resolution Site U1406 $\delta^{18}\text{O}_{\text{sw}}$ record. The deep ocean $\delta^{18}\text{O}_{\text{sw}}$ signal is a recorder of global continental ice-volume, which is deconvolved from the $\delta^{18}\text{O}_{\text{BF}}$ signal through coupled $\delta^{18}\text{O}_{\text{BF}}$ -Mg/Ca measurements allowing both the temperature and $\delta^{18}\text{O}_{\text{sw}}$ of the $\delta^{18}\text{O}_{\text{BF}}$ signal to be evaluated (see Section 4.5). Yet, ice-volume estimates both from ODP Site 1264 and 690 are based on $\delta^{18}\text{O}_{\text{BF}}$ threshold values that are interpreted to reflect $\delta^{18}\text{O}_{\text{sw}}$ changes implying Antarctic ice-volume growth [see Liebrand et al. (2017) and Hauptvogel et al. (2017) for details]. These $\delta^{18}\text{O}_{\text{BF}}$ values have been paired with constant, modern BWTs [$2.5\text{ }^\circ\text{C}$ for Site 1264, Liebrand et al. (2017); $2\text{ }^\circ\text{C}$ for Site 690, Hauptvogel et al. (2017)]. However, these modern and cold BWTs assumed for ODP

Site 690 and 1264 seem unrealistic in comparison to BWTs from ODP Site 1218 (Lear et al., 2004) and Site U1406 BWTs across the study interval that show higher temperatures (5–8 °C) with distinct glacial-interglacial variability (Figure 5.1-3). Hence, the missing assessment of the temperature component of ODP Site 1264 and 690 $\delta^{18}\text{O}_{\text{BF}}$ records that would allow for the separation and elucidation of $\delta^{18}\text{O}_{\text{sw}}$, causes the ice-volume estimates of Liebrand et al. (2017) and Hauptvogel et al. (2017) to lack fidelity. Comparing the newly generated ice-volume estimates from IODP Site U1406 with those from ODP Site 690 and 1264 provides powerful means to the coupled $\delta^{18}\text{O}_{\text{BF}}$ -Mg/Ca measurements to more accurately interpret the $\delta^{18}\text{O}_{\text{BF}}$ signal in terms of changing dynamics of the Antarctic cryosphere.

Table 5.1-1: Comparison of ice-volume estimates resulting from Site U1406 $\delta^{18}\text{O}_{\text{sw}}$ -based sensitivity tests. Calculated ice-volume changes based on the average glacial-interglacial $\delta^{18}\text{O}_{\text{sw}}$ amplitude change of 0.5‰ assuming a growth of $3.8 \times 10^6 \text{ km}^3$ of ice per 0.1‰ change in $\delta^{18}\text{O}_{\text{sw}}$ with an ice-free baseline of -1.05‰ (Bohaty et al., 2012; Liebrand et al., 2017) in relation to the modern global ice-volume ($30.13 \times 10^6 \text{ km}^3$) (Grinsted, 2013; Fretwell et al., 2013; Bamber et al., 2013).

Average $\delta^{18}\text{O}_{\text{ice}}$ [‰, SMOW]	Growth of ice per 0.1 change in $\delta^{18}\text{O}_{\text{sw}}$ [$\times 10^6 \text{ km}^3$]	Size of ice-volume assuming 0.5‰ $\delta^{18}\text{O}_{\text{sw}}$ amplitude change (this chapter) [$\times 10^6$ km^3]	% Δ relative to modern global ice volume
-35*	4.56	22.8	75.7
-42*★	3.80	19.0	63.1
-48 ^a	3.33	16.6	55.2

* DeConto et al. (2008); ★ Gasson et al. (2016)

5.1.6 Possibility of a precursory bipolar glaciation

Interesting features of the Site U1406 $\delta^{18}\text{O}_{\text{sw}}$ record are glacial periods displaying higher than modern $\delta^{18}\text{O}_{\text{sw}}$ values ($\geq 0\text{‰}$) by up to $\sim 0.3\text{‰}$ (Figure 5.1-6C). Since the Late Oligocene is characterized by unipolar glaciation with ice restricted to Antarctica (DeConto et al., 2008), these high ice-volumes imply the possibility of ice-sheet built-up in the Northern Hemisphere. The sporadic presence of potential ice-rafted debris in the Greenland Sea and the Arctic Ocean (Eldrett et al., 2007; Tripathi et al., 2008; St John, 2008) has been used to infer the presence of Northern Hemisphere ice sheets as early as the Eocene. However, climate model simulations have shown that for significant ice-sheet growth to occur in the Northern Hemisphere, $p\text{CO}_2$ values would have had to cross a threshold value of ~ 280 p.p.m.v. (DeConto et al., 2008) (Figure 2.1-1). Yet proxy $p\text{CO}_2$ estimates clearly remain above the northern-hemispheric glaciation threshold across the study interval (25.95–25.78 Ma) [Beerling and Royer (2011); Zhang et al. (2013) and references therein]. In addition, there is proxy-based evidence arguing against a precursory bipolar glaciation: Firstly, marine sediment-based ice-budget calculations used to test the upper limit of possible ice-growth for a late Eocene interval (~ 43 – 40.5 Ma) do not require ice storage in the Northern Hemisphere (Edgar et al., 2007). Secondly, EOT to mid-Oligocene-aged detrital sands from IODP Site U1406 and U1411 initially interpreted to represent Northern Hemisphere ice-rafting, indicate a source from the mid-latitudes of North America transported to the Newfoundland

margin by fluvial and downslope processes (Spray et al., 2019). In addition, it is general consensus that only short-lived, isolated glaciers thrived in the Northern Hemisphere throughout most of the Cenozoic (Moran et al., 2006; Wilson et al., 2012). An alternative explanation for the observed higher than modern $\delta^{18}\text{O}_{\text{sw}}$ values (Figure 5.1-6) would be more ice that was stored on the Antarctic continent. Topographic reconstructions for the EOT infer a $\sim 20\%$ larger surface area of Antarctica than compared to the present-day topography (Wilson et al., 2012). Approximating a mid-Miocene Antarctic bedrock topography coupled to a general circulation model reveals a mid-Miocene Antarctic ice volume of $35.5 \times 10^6 \text{ km}^3$ [$\sim 131\%$ of its modern size; Gasson et al., (2016)]. Assuming that the Late Oligocene palaeotopography of Antarctica was rather similar to the EOT and mid-Miocene, the reconstructed higher than modern glacial $\delta^{18}\text{O}_{\text{sw}}$ values ($\geq 0\text{‰}$) from Site U1406 could reflect a larger AIS rather than a precursory Northern Hemisphere glaciation. The presence of Oligocene-aged glacial and proglacial diamictites (Fielding, 2018) and detrital apatite grains (Olivetti et al., 2015) in the Victoria Land Basin infer that the AIS advanced beyond its terrestrial margins into the marine environment during the Late Oligocene, which corroborates a larger than modern AIS.

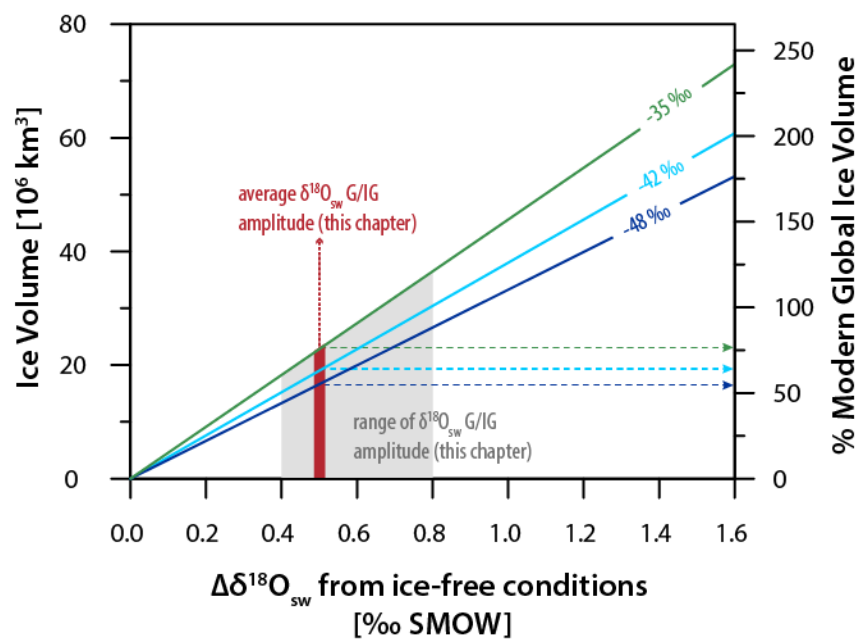


Figure 5.1-5: Sensitivity tests for Site U1406 $\delta^{18}\text{O}_{\text{sw}}$ -based ice-volume estimates. Ice-volume estimates assuming a linear relationship between changing $\delta^{18}\text{O}_{\text{sw}}$ and $\delta^{18}\text{O}_{\text{ice}}$ using a range of $\delta^{18}\text{O}_{\text{ice}}$ from -35‰ to -48‰ (DeConto et al., 2008; Gasson et al., 2016b) and an initial ice-free state (-1.05‰ ; Bohaty et al., 2012). Grey area marks the Site U1406 $\delta^{18}\text{O}_{\text{sw}}$ range of glacial-interglacial (=G/IG) amplitudes ($0.4\text{--}0.8\text{‰}$) observed; dark red line indicates the average $\delta^{18}\text{O}_{\text{sw}}$ amplitude of 0.5‰ .

5.1.7 Influence of orbital pacing on the Late Oligocene AIS

As inferred from the Site U1406 average glacial-interglacial fluctuations of the AIS in the order of $\sim 19 \times 10^6 \text{ km}^3$, the data provide clear evidence for a highly dynamic cryosphere across the studied time period during the Late Oligocene in tune with frequency variations of the Earth's obliquity. Generally, the selected study interval (25.95–25.78 Ma) falls into an episode of broadly low eccentricity forcing

and high amplitude changes in obliquity forcing (Laskar et al., 2004) (Figure 5.1-6a). The low eccentricity baseline effects low (summer) insolation forcing.

High amplitude changes in obliquity cause an alternation between high (obliquity minimum) and low (obliquity maximum) meridional insolation gradients between high and low latitudes (Mantsis et al., 2014), which itself regulates the poleward moisture and heat transport through atmospheric and oceanic circulation (Vimeux et al., 1999). Effectively, a minimum latitudinal insolation gradient at high obliquity weakens the atmospheric and oceanic meridional circulation and reduces the contribution of moisture sourced from low latitudes to Antarctic precipitation (Vimeux et al., 1999; Raymo and Nisancioglu, 2003; Langebroek et al., 2009). A change in the Earth's axial tilt also affects the seasonal distribution of insolation: At high latitudes, low (high) obliquity causes a weakening (strengthening) of the seasonal cycle resulting in milder (colder) winters and cooler (warmer) summers (Mantsis et al., 2014). Given these considerations, a high intrahemispheric (equator-to-pole) insolation gradient during obliquity minima would provide a potent moisture source for glacial ice-sheet built-up that is then promoted to grow and to be preserved due to the minimum high-latitude summer insolation (Figure 5.1-3A, C; Figure 5.1-6C). Accordingly, phases of high obliquity with longer summer periods and an increase in total summer energy received at high latitudes (Berger, 1988; Huybers and Wunsch, 2005), in parallel with a reduced moisture delivery, inhibit ice-sheet growth and induce significant ice-sheet melting (Figure 5.1-3A, C; Figure 5.1-6C).

The obliquity-paced high-frequency oscillations imprinted in the Site U1406 $\delta^{18}\text{O}_{\text{sw}}$ record across the study interval provides new context for AIS variability of the Late Oligocene. Yet, this finding contradicts the lack of high-frequency obliquity forcing in AIS dynamics based on $\delta^{18}\text{O}_{\text{BF}}$ records from the equatorial Pacific [ODP Site 1218, Pälike et al. (2006b)], the equatorial Atlantic [ODP Site 926, Pälike et al. (2006a)] and the South Atlantic [ODP Site 1264; Liebrand et al. (2017)] (Figure 2.1-2; Figure 2.1-3). These studies conclude that recurring Oligocene glaciations are dominantly paced by long (~400 kyr)- and short-term (~100 kyr) eccentricity periodicities and the ~1.2-Myr amplitude modulation of the obliquity cycle. The dominant eccentricity forcing has been confirmed by a recent study of Levy et al. (2019), showing that most of the Oligocene AIS behavior is dominated by eccentricity while a significant influence of obliquity forcing is missing. Yet, the U1406 $\delta^{18}\text{O}_{\text{sw}}$ data clearly present a ~170-kyr long interval of AIS dynamics that is dominated by high-frequency obliquity forcing in unprecedented detail.

5.1.8 $p\text{CO}_2$ forcing

While the beat of obliquity is interpreted to be the primary pacer of ice-volume fluctuations across the studied interval (25.95–25.78 Ma), it still leaves the mechanism/modulator causing the dynamic ice-sheet behavior enigmatic. For the Mid-Oligocene Glacial Interval (MOGI; 28 to 26.3 Ma ago), high-amplitude changes in glacial/interglacial $p\text{CO}_2$ are proposed (Liebrand et al., 2017) to have triggered similar rates of AIS growth and decay than inferred by Site U1406 records.

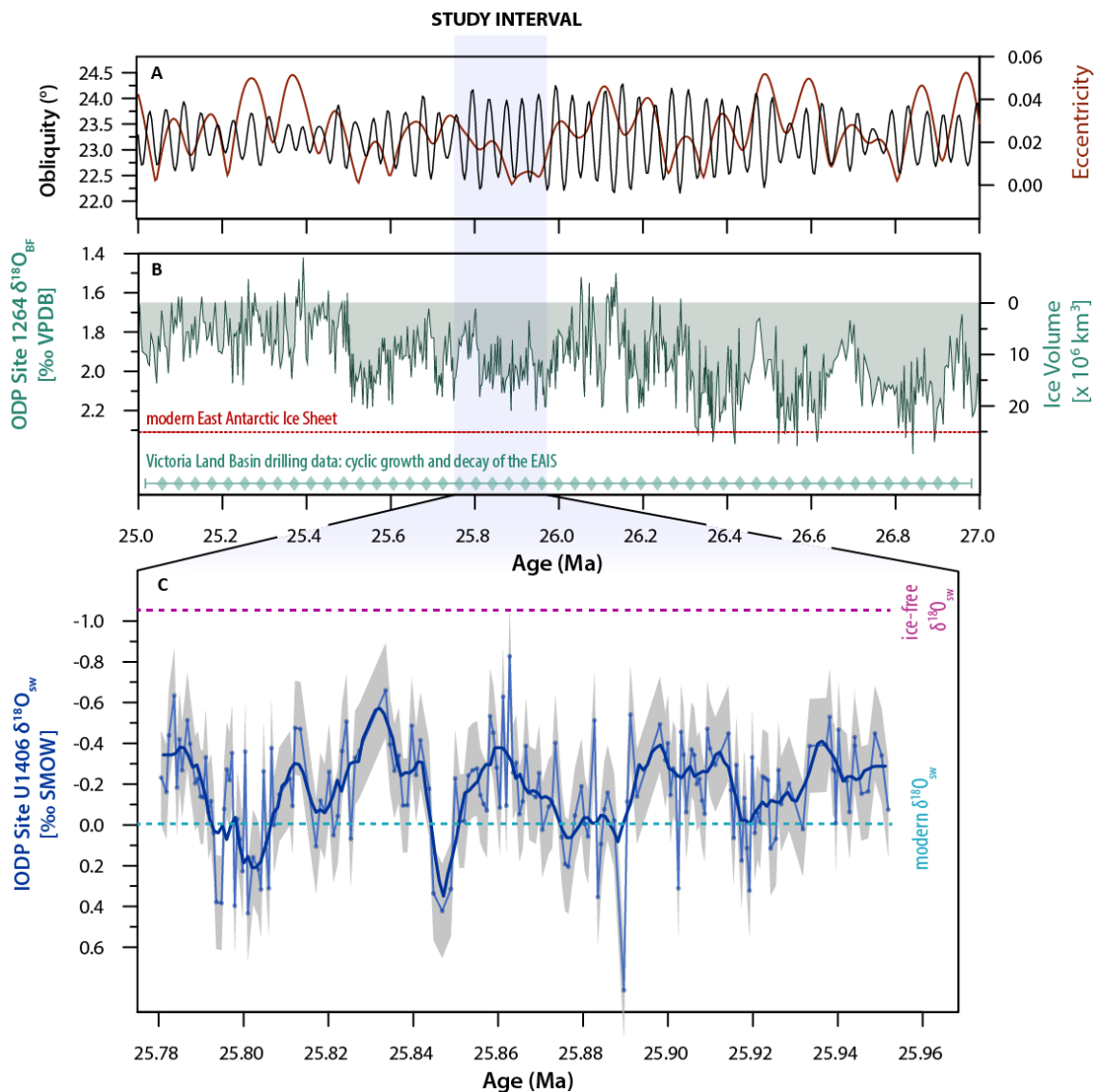


Figure 5.1-6: Comparison of ice-sheet dynamics across the study interval during the Late Oligocene. (A) Long-term evolution of orbital solution for eccentricity (brown) and obliquity (black) (Laskar et al., 2004). (B) Late Oligocene (27–25 Ma) $\delta^{18}\text{O}_{\text{BF}}$ record (in ‰ VPDB, left axis) of ODP Site 1264 with proposed ice-volume estimates (light green, right axis; Liebrand et al., 2017). Dashed red line represents present-day-sized EAIS (Fretwell et al., 2013). Green diamonds display sedimentological evidence of a dynamic EAIS (Fielding, 2018). (C) Site U1406 $\delta^{18}\text{O}_{\text{sw}}$ (in ‰ SMOW, blue) with 5-pt smoother (dark blue line) and ± 0.23 ‰ uncertainty resulting from Monte Carlo Simulations (grey envelop; see Section 4.5.2). Dashed lines indicate ice-free (purple; Bohaty et al., 2012) and modern (turquoise; Adkins et al., 2002) $\delta^{18}\text{O}_{\text{sw}}$ conditions. Violet shading indicates the study interval (25.95–25.78 Ma).

While $p\text{CO}_2$ is an obvious driver to modulate the extent of ice-sheet advance and retreat, the apparent data gap in $p\text{CO}_2$ reconstructions between 26–25.3 Ma (Henderiks and Pagani, 2008; Zhang et al., 2013) currently prevents a one-to-one correlation and testing of this mechanism. Nonetheless, assuming high-amplitude changes in $p\text{CO}_2$ affecting radiative forcing and thereby causing feedback mechanisms is a plausible scenario for the observed fluctuations (Figure 5.1-3). Further evidence for this scenario comes from model studies that show a tight temporal coupling between deep-sea temperature and changes in $p\text{CO}_2$ (Stouffer and Manabe, 2003; Stap et al., 2014), while ice-sheets show a slow response to $p\text{CO}_2$

forcing with a lag of ~5000–8000 years (Ruddiman, 2006). The herein observed lag between bottom-water cooling and ice-sheet growth of ~10 kyr suggests that this process also acted during the Late Oligocene.

6 ANTARCTIC ICE-SHEET RESPONSE TO COMBINED ECCENTRICITY AND OBLIQUITY FORCING OF THE LATE OLIGOCENE

6.1 Introduction

Controversy exists regarding the pacing of AIS dynamics across the Late Oligocene. Ice-proximal geological records show significant, high-frequent obliquity-paced AIS oscillations (~40 kyr) (Naish et al., 2001; Salabarnada et al., 2018). Contrarily, ice-distal $\delta^{18}\text{O}_{\text{BF}}$ records infer dynamics of the AIS responding to the ~1.2-Myr-amplitude modulation of obliquity (Pekar and Miller, 1996; Wade and Pälike, 2004; Pälike et al., 2006b; Pekar et al., 2006), as well as to ~400-kyr and ~100-kyr eccentricity cycles, derived from higher resolution (≤ 10 kyr) $\delta^{18}\text{O}_{\text{BF}}$ records that revealed a larger number of heavy $\delta^{18}\text{O}_{\text{BF}}$ time intervals that have been linked to Antarctic glaciation (Wade and Pälike, 2004; Pälike et al., 2006b; Liebrand et al., 2017) (Figure 2.1-3). In addition to elucidating orbitally-paced variability of the AIS, recent $\delta^{18}\text{O}_{\text{BF}}$ records have been used to illustrate the variability of the Antarctic ice volume across the Oligocene. While Liebrand et al. (2017) showed recurrent episodes of high-amplitude variability in $\delta^{18}\text{O}_{\text{BF}}$ requiring waning and waxing of at least ~85 to 110 % of the present-day volume of the EAIS on ~100-kyr timescales with a distinct ice-volume decrease from 27 Ma onwards, $\delta^{18}\text{O}_{\text{BF}}$ -based ice-volume reconstructions from Maud Rise (Antarctica) of Hauptvogel et al. (2017) display a heavily glaciated Antarctic continent from 27.8–24.5 Ma with a near or larger than modern-sized ice sheet free of indications for ice-sheet disintegration. The apparent controversy of Oligocene AIS pacing and volumes inferred from ice-distal $\delta^{18}\text{O}_{\text{BF}}$ records and ice-proximal geological records might be partially caused by the methodology applied to infer ice-volume estimates and dynamics from $\delta^{18}\text{O}_{\text{BF}}$ records. Since the

$\delta^{18}\text{O}_{\text{BF}}$ signal is a function of temperature and global ice volume, the approach of relating astronomical forcing imprinted in $\delta^{18}\text{O}_{\text{BF}}$ to AIS dynamics, as well as the estimation of ice-volumes from the $\delta^{18}\text{O}_{\text{BF}}$ signal is likely deficient, as these studies have not assessed the individual contribution of the temperature component of $\delta^{18}\text{O}_{\text{BF}}$. Therefore, these $\delta^{18}\text{O}_{\text{BF}}$ -based studies bear the possibility that the reconstructed AIS pacing and volume have partially arisen from changes in the individual contribution of temperature and ice-volume to the $\delta^{18}\text{O}_{\text{BF}}$ signal.

As the results of chapter 5 have delivered new context to Late Oligocene glaciation dynamics, high-resolution $\delta^{18}\text{O}_{\text{BF}}$ and Mg/Ca records from the northwestern Atlantic IODP Site U1406 (Figure 2.1-3) have been extended from the interval presented in chapter 5 covering the interval from 25.95 to 24.53 Ma. These proxy records will be used in this chapter to further explore the existing controversy regarding AIS volumes and pacing during the Late Oligocene. Using Mg/Ca-paleothermometry, the temperature component of $\delta^{18}\text{O}_{\text{BF}}$ is independently assessed and subsequently combined with $\delta^{18}\text{O}_{\text{BF}}$ data to deconvolve $\delta^{18}\text{O}_{\text{sw}}$, i.e., the ice-volume component.

In a first step, previous concepts of Oligocene glaciation dynamics will be reassessed by comparing previously identified $\delta^{18}\text{O}_{\text{BF}}$ maxima to signals imprinted in the Site U1406 $\delta^{18}\text{O}_{\text{BF}}$ record that can be tested for being a true recorder of glaciation through one-to-one correlation to the corresponding signal in the BWT and $\delta^{18}\text{O}_{\text{sw}}$ record, respectively. Secondly, ice volumes will be estimated based on the Site U1406 $\delta^{18}\text{O}_{\text{sw}}$ record and set into comparison to previously inferred ice-volumes across the study interval. In a last step, the orbital pacing of the high-resolution Site U1406 $\delta^{18}\text{O}_{\text{sw}}$ record will be analyzed in detail to gain more accurate insights into AIS dynamics than compared to previously derived AIS dynamics based on $\delta^{18}\text{O}_{\text{BF}}$ records only. Following up on the obliquity-dominance on Site U1406 records shown in chapter 5, the ~ 1.4 -Myr long high-resolution Site U1406 proxy records presented herein will further permit to elucidate possible high-frequency obliquity forcing across the study interval.

6.2 Results and discussion

6.2.1 Stable oxygen isotope record

Site U1406 $\delta^{18}\text{O}_{\text{BF}}$ values vary between ~ 1.4 and $\sim 2.7\text{‰}$, resulting in a total range of 1.3‰ over the studied interval of 25.95 to 24.53 Ma (Figure 6.2-1; Figure 6.2-3A). From the early to the late part of the record, there is a general increase toward lighter $\delta^{18}\text{O}_{\text{BF}}$ values. Additionally, the $\delta^{18}\text{O}_{\text{BF}}$ record displays high-amplitude longer-term variability with alternating phases of generally heavier values (~ 1.8 – 2.7‰) and lighter values (~ 1.4 – 2.0‰), which is superimposed by shorter-term variability approximately in the range of 0.2 – 0.5‰ . These phase shifts allow for a division of the $\delta^{18}\text{O}_{\text{BF}}$ record into six phases (Figure 6.2-3A): The first 250 kyr of Phase I are characterized by five cyclic, sinusoidal oscillations of relatively heavy $\delta^{18}\text{O}_{\text{BF}}$ values between 1.9 and 2.6‰ , followed by an amplitude decrease and increasing values over the following 200 kyr. During Phase II, (from ~ 25.55 Ma onwards) $\delta^{18}\text{O}_{\text{BF}}$ values shift towards lighter values of ~ 1.5 to 2.1‰ over a 250 kyr long interval with rhythmic fluctuations of $\sim 0.5\text{‰}$. At the transition of Phase II to III, $\delta^{18}\text{O}_{\text{BF}}$ values increase by $\sim 0.7\text{‰}$. Until 25

Ma across Phase III, the $\delta^{18}\text{O}_{\text{BF}}$ record displays fluctuations of sharp decreases immediately followed by increases. The onset of Phase IV at 25 Ma is characterized by $\delta^{18}\text{O}_{\text{BF}}$ shifting to light values of 1.4 to 1.8‰ lasting until ~24.85 Ma when values reach a maximum of 2.2‰ at the transition into Phase V. Minimal fluctuations of ~0.2 to 0.3‰ are displayed in Phase V, whereas in Phase VI, $\delta^{18}\text{O}_{\text{BF}}$ increase to ~1.5‰ (Figure 6.2-3A).

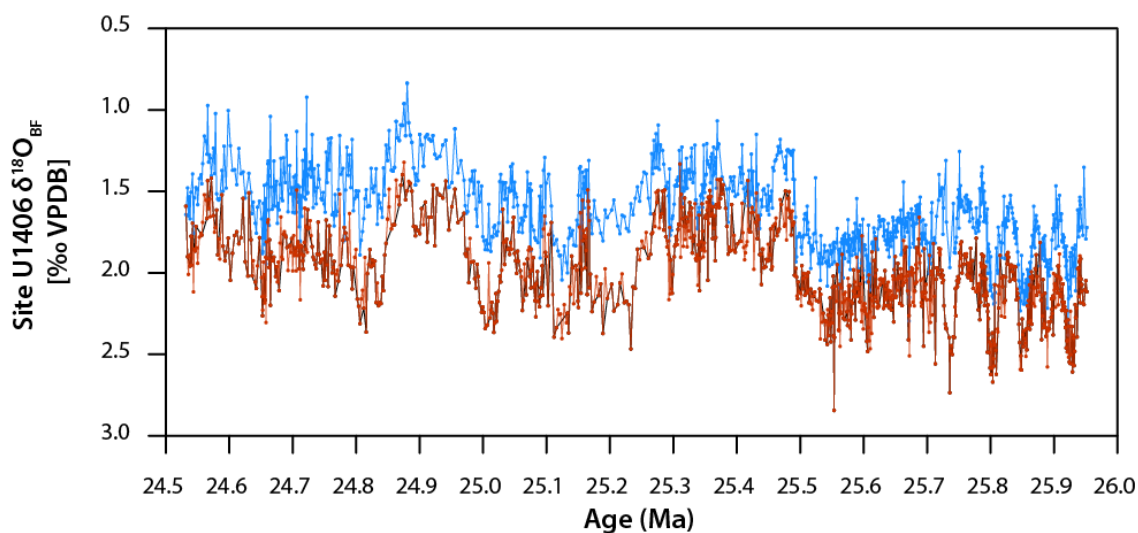


Figure 6.2-1: Paired isotope analyses of *C. mundulus* and *O. umbonatus*. Benthic foraminiferal $\delta^{18}\text{O}_{\text{BF}}$ analyses (in ‰ VPDB) of *C. mundulus* (blue), *O. umbonatus* (red), and the composite record (dashed black; *C. mundulus* converted to *O. umbonatus*).

6.2.2 Assessment of contamination and diagenetic effects on the Mg/Ca ratios

Elemental ratios of Al/Ca, Fe/Ca and Mn/Ca were monitored to identify contamination by clay particles or diagenetic coatings, which might affect the foraminiferal Mg/Ca ratios (Barker et al., 2003). Measured Al concentrations of the data are generally below the detection limit, arguing against the presence of detrital clay. However, Fe/Ca and especially Mn/Ca ratios of *O. umbonatus* generally exceed the 0.1 mmol/mol threshold value defined by Barker et al. (2003) (Figure 6.2-2). A statistically significant correlation between Fe/Ca vs. Mg/Ca ($r^2=0.11$, $p<0.0001$) and Mn/Ca vs. Mg/Ca ($r^2=0.06$, $p<0.0001$), however, is not observed (Figure 6.2-2), suggesting that Mn- and Fe-oxide coatings or Mn-carbonates (if present at all) did not considerably affect the measured Mg/Ca. In addition, SEM images rule out the presence of microcrystalline overgrowth on the measured *O. umbonatus* tests (Figure 2.7-1). It can, therefore, be concluded with reasonable certainty that early diagenetic overprinting has not affected Mg/Ca-based data for the interval 24.53–25.95 Ma at Site U1406.

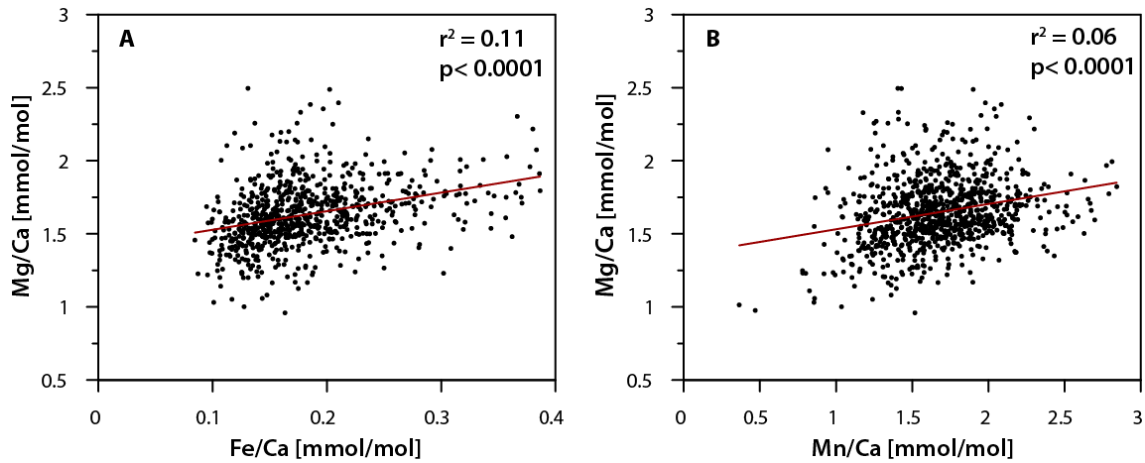


Figure 6.2-2: Evaluation of *O. umbonatus* test contamination. Cross correlation plots of Mg/Ca versus Fe/Ca (A) and Mn/Ca (B), respectively, show no statistically significant correlation between Fe/Ca vs. Mg/Ca ($r^2 = 0.11$, $p < 0.0001$) and Mn/Ca ($r^2 = 0.06$, $p < 0.0001$), indicating that measured Mg/Ca values are not systematically altered by clay particles or diagenetic coatings.

6.2.3 Late Oligocene BWT variability

The Site U1406 BWT record documents a deep-sea temperature range of ~ 5 to 9 °C through the studied interval, which is in good agreement with low-resolution BWTs reconstructed from the equatorial Pacific (ODP Site 1218; Lear et al., 2004) (Figure 6.2-3B). The long-term trend of Site U1406 BWTs is characterized by moderate and gradual warming across the record. The majority of this shift occurs younger than ~ 25.11 Ma following a marked, ~ 50 -kyr long deep-sea cooling event (Figure 6.2-3B).

Albeit generally reminiscent of the cyclicity observed in the $\delta^{18}\text{O}_{\text{BF}}$, the BWT signal is not always synchronous (Figure 6.2-3A, B). Notably, BWTs does not show a lowering of values over the interval ~ 25.72 to 25.55 Ma during Phase I, while $\delta^{18}\text{O}_{\text{BF}}$ values are increasing. After BWTs warm by ~ 2.5 °C at the onset of Phase II at ~ 25.55 Ma, values display cooling of ~ 2.5 °C some ~ 100 kyr later at 25.45 Ma, whereas the $\delta^{18}\text{O}_{\text{BF}}$ signal displays rhythmic fluctuations until 25.25 Ma. Similarly, following a marked warming in BWT at the transition from Phase III to IV, BWTs drop by ~ 3 °C some ~ 100 kyr later at 24.95 Ma, contrary to $\delta^{18}\text{O}_{\text{BF}}$ values that remain light until the end of Phase IV (~ 24.85 Ma). Thereafter, BWTs gradually warm to the earliest part of the record (24.53 Ma), superimposed by fluctuations of 1 – 1.5 °C (Figure 6.2-3B).

6.2.4 Trends of Site U1406 $\delta^{18}\text{O}_{\text{sw}}$

The pairing of $\delta^{18}\text{O}_{\text{BF}}$ with Mg/Ca-based BWTs allows to deconvolve the ice-volume signal, i.e., $\delta^{18}\text{O}_{\text{sw}}$, from the $\delta^{18}\text{O}_{\text{BF}}$ signal (see Section 4.5). The $\delta^{18}\text{O}_{\text{sw}}$ record displays a total range of values between -0.80 and 0.35 ‰ with typical average amplitude variability of 0.4 – 0.7 ‰ (Figure 6.2-3C). These trends are in good agreement with $\delta^{18}\text{O}_{\text{sw}}$ changes calculated for the equatorial Pacific (0.5 ‰; Lear et al., 2004) and the South Atlantic (~ 0.4 ‰; Liebrand et al., 2017) across the studied interval. The Monte Carlo simulations indicate an uncertainty associated with the $\delta^{18}\text{O}_{\text{sw}}$ signal of ± 0.23 ‰.

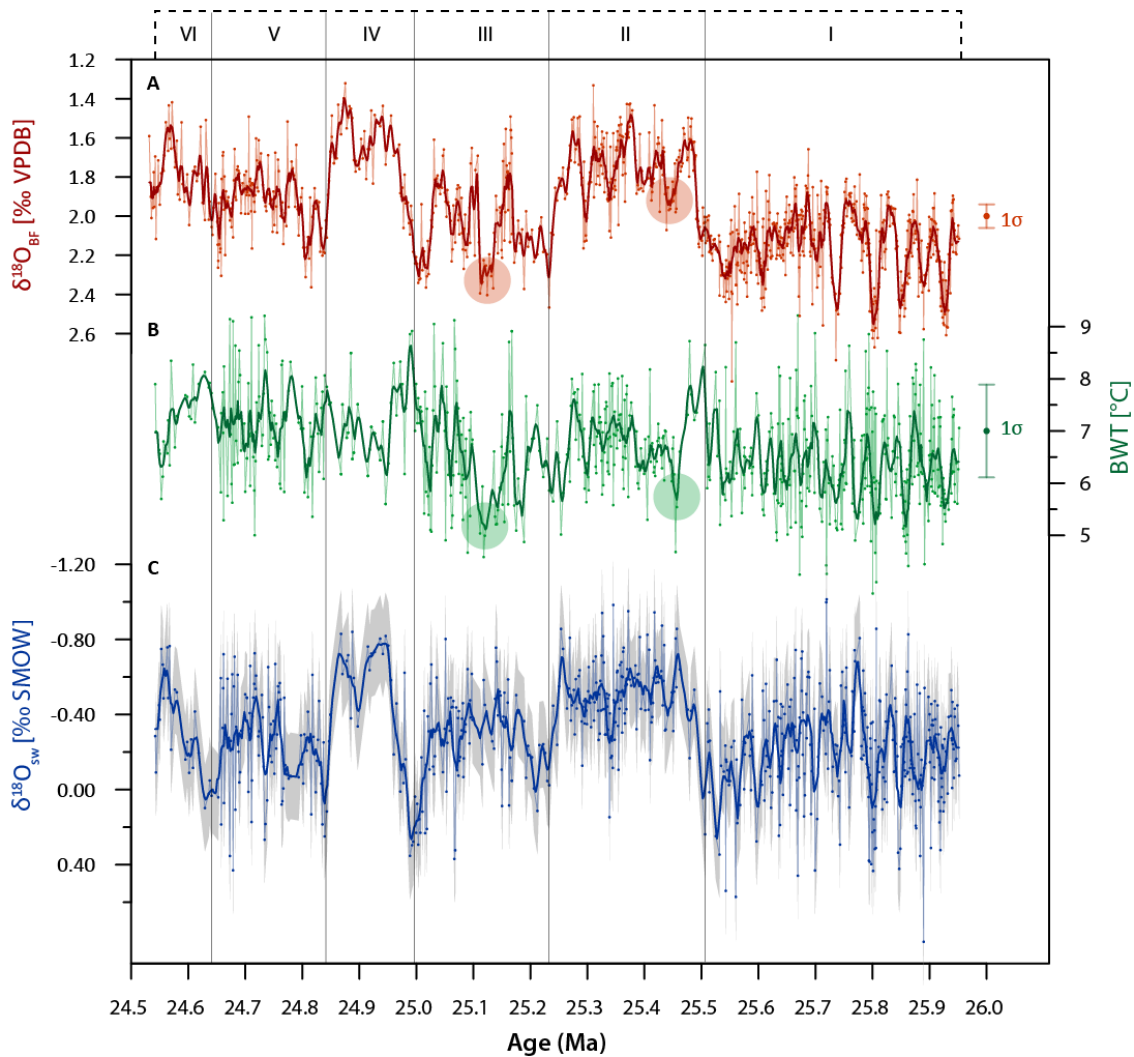


Figure 6.2-3: Geochemical proxy data from IODP Site U1406 for the interval 25.95 to 24.53 Ma. (A) Benthic foraminiferal composite $\delta^{18}\text{O}_{\text{BF}}$ record with 5-pt smoother (thick red line). (B) Mg/Ca-based BWT estimates (in $^{\circ}\text{C}$, green) with 5-pt smoother (thick green line) with BWT estimates from ODP Site 1218 (Lear et al., 2004) (blue, recalculated following the same methodology as used in this study (see Section 4.4)). (C) Site U1406 $\delta^{18}\text{O}_{\text{sw}}$ data with 5-pt smoother (thick blue line) and $\pm 0.23\text{‰}$ uncertainty resulting from Monte Carlo Simulations (grey envelope; see Section 4.5.2). Vertical bars indicate the 1σ standard deviation associated with the individual Site U1406 proxy records. Boxes on top of the graph indicate Phases I to VI, as mentioned in the text. Colored dots indicate enrichments in $\delta^{18}\text{O}_{\text{BF}}$ that are only mirrored in BWT as noticeable cooling.

Similar to the $\delta^{18}\text{O}_{\text{BF}}$ record, the Site U1406 $\delta^{18}\text{O}_{\text{sw}}$ displays pronounced cyclic variations with alternating phases of generally heavier (-0.5 to 0.35‰) and lighter (-0.8 to -0.3‰) values (Figure 6.2-3A, C). In parallel with $\delta^{18}\text{O}_{\text{BF}}$, the first 250 kyr of Phase I (~ 25.95 – 25.5 Ma) are characterized by five pronounced sinusoidally shaped oscillations of relatively heavy $\delta^{18}\text{O}_{\text{sw}}$ (average range of -0.6 to 0.2‰). The subsequent ~ 200 kyr are marked by gradually increasing $\delta^{18}\text{O}_{\text{sw}}$ values, superimposed by fluctuations of $\sim 0.3\text{‰}$, and terminating in a positive $\delta^{18}\text{O}_{\text{sw}}$ maximum of $\sim 0.2\text{‰}$ at ~ 25.5 Ma. Analogous to the $\delta^{18}\text{O}_{\text{BF}}$ and BWT signal, the transition into Phase II is marked by an abrupt shift of $\delta^{18}\text{O}_{\text{sw}}$ to lighter values. Across Phase II, $\delta^{18}\text{O}_{\text{sw}}$ values are relatively light (-0.7 to -0.3‰) and show very little amplitude variability. Following the positive excursion of $\delta^{18}\text{O}_{\text{sw}}$ to $\sim 0.1\text{‰}$ at ~ 25.25 Ma, Phase III displays

relatively light $\delta^{18}\text{O}_{\text{sw}}$ values with little variability for the subsequent ~ 300 kyr, which is in contrast to the $\delta^{18}\text{O}_{\text{BF}}$ and BWT signals that show significant variability. In the following, $\delta^{18}\text{O}_{\text{sw}}$ displays a notable positive $\delta^{18}\text{O}_{\text{sw}}$ maximum of 0.35% at ~ 25 Ma. In parallel with $\delta^{18}\text{O}_{\text{BF}}$, the transition into Phase IV is marked by a decrease in $\delta^{18}\text{O}_{\text{sw}}$ of $\sim 1.0\%$, whereupon $\delta^{18}\text{O}_{\text{sw}}$ values remain relatively light over a ~ 130 kyr long interval, terminated by a rapid increase in $\delta^{18}\text{O}_{\text{sw}}$ at ~ 24.85 Ma. Phase V is characterized by heavy $\delta^{18}\text{O}_{\text{sw}}$ values and amplitude variability of 0.5% that ceases in a positive $\delta^{18}\text{O}_{\text{sw}}$ maximum at ~ 24.62 Ma, followed by decreasing $\delta^{18}\text{O}_{\text{sw}}$ until 24.53 Ma (Figure 6.2-3).

6.2.5 Spectral and time series analysis

Spectral analyses for $\delta^{18}\text{O}_{\text{BF}}$, BWT, and $\delta^{18}\text{O}_{\text{sw}}$ display peaks at astronomical frequencies above the significance level (Figure 6.2-4A–C). The most dominant signal in all three data sets is strong power at the longer eccentricity periodicity (~ 400 kyr), and significant power at the shorter eccentricity (~ 100 kyr). In comparison to $\delta^{18}\text{O}_{\text{BF}}$ and BWT, the ~ 100 -kyr short eccentricity imprint is smaller in the $\delta^{18}\text{O}_{\text{sw}}$ series. There is strong power corresponding to periodicities of the ~ 180 to 200 -kyr modulation of obliquity, a sixth-order sequence to the fundamental obliquity (~ 40 kyr) (Boulila et al., 2011), in records of $\delta^{18}\text{O}_{\text{BF}}$ and $\delta^{18}\text{O}_{\text{sw}}$ (Figure 6.2-4A, C). The peak at shorter obliquity periods (~ 29 , ~ 40 , ~ 54 kyr) in $\delta^{18}\text{O}_{\text{BF}}$, BWT and $\delta^{18}\text{O}_{\text{sw}}$ is relatively small.

Prior to wavelet analysis, periodicities greater than 250 kyr were removed from the $\delta^{18}\text{O}_{\text{BF}}$, BWT, and $\delta^{18}\text{O}_{\text{sw}}$ time series due to the strong power at the ~ 400 -kyr eccentricity frequency resulting from spectral analysis, (see Section 4.5.3). The wavelet for $\delta^{18}\text{O}_{\text{BF}}$ reveals a consistent imprint of the ~ 100 -kyr eccentricity, whereas it only intermittently appears in the BWT and $\delta^{18}\text{O}_{\text{sw}}$ record (Figure 6.2-4D–E). However, there is a consistent imprint of the ~ 200 -kyr modulation of obliquity in wavelets of $\delta^{18}\text{O}_{\text{BF}}$, BWT, and $\delta^{18}\text{O}_{\text{sw}}$ from the earliest part of the record (24.53 Ma) to ~ 25.7 Ma. The ~ 40 -kyr frequency of obliquity notably appears in the interval of 25.95 – 25.5 Ma and in recurring episodes from ~ 25.1 Ma onwards (Figure 6.2-4D–E).

6.2.6 Re-evaluation of previously defined Oligocene glacial events

The Oligocene glaciation history was first constrained based on low-resolution $\delta^{18}\text{O}_{\text{BF}}$ records (Miller et al., 1991b, 1991a) from which Myr-long oxygen-isotope zones were defined and interpreted to represent glaciation. These were correlated to glacioeustatic lowerings imprinted in sequence boundaries identified by Haq et al. (1987). With the generation of more and higher resolved $\delta^{18}\text{O}_{\text{BF}}$ records, the Oi-zonation scheme was updated by referring to prominent, recurring $\delta^{18}\text{O}_{\text{BF}}$ excursions of $>0.5\%$ with high maximum $\delta^{18}\text{O}_{\text{BF}}$ of $>2.0\%$ as Oi-events, i.e., glaciation events [see Pekar and Miller (1996) and references therein] (see Section 2.1.1). More recent generation of high-resolution (≤ 10 kyr) $\delta^{18}\text{O}_{\text{BF}}$ records revealed a larger number of heavy $\delta^{18}\text{O}_{\text{BF}}$ time intervals that were renamed based on the 400 -kyr cycle of Earth's eccentricity (Wade and Pälike, 2004). The largest variability in glaciation events based on these ≤ 10 kyr-resolution $\delta^{18}\text{O}_{\text{BF}}$ records is associated with a ~ 400 kyr to ~ 100 kyr pacing (Wade

and Pälike, 2004; Pälike et al., 2006b; Liebrand et al., 2017) (Figure 2.1-3). However, despite an improvement in the identification of high-frequency $\delta^{18}\text{O}_{\text{BF}}$ variability on orbital timescales in previous studies, the underlying strategy of correlating these $\delta^{18}\text{O}_{\text{BF}}$ variabilities with ice-volume dynamics is likely deficient: As outlined in Section 2.4.1, the benthic foraminiferal $\delta^{18}\text{O}_{\text{BF}}$ signal is a function of temperature and global ice volume. If the temperature component of $\delta^{18}\text{O}_{\text{BF}}$ is not assessed, the individual contribution of ice-volume to the $\delta^{18}\text{O}_{\text{BF}}$ signal cannot be adequately be evaluated. On the basis of the Site U1406 proxy records, the temperature (BWT) and ice volume ($\delta^{18}\text{O}_{\text{sw}}$ signal) constituents of Site U1406 $\delta^{18}\text{O}_{\text{BF}}$ can be separated from the $\delta^{18}\text{O}_{\text{BF}}$ signal via coupled $\delta^{18}\text{O}_{\text{BF}}$ -Mg/Ca measurements (see Section 2.5.1). Moreover, a one-to-one correlation of positive maxima in $\delta^{18}\text{O}_{\text{BF}}$ to the corresponding signal in the BWT and $\delta^{18}\text{O}_{\text{sw}}$ record, respectively, allows for an unambiguous allocation of the signal to either deep-sea cooling and/or glaciation. This approach gives new context to glaciation history and BWT dynamics across the study interval and permits to re-evaluate previous conceptions of glaciation across the Oligocene (see Section 2.1.1).

Of the previously defined Oi-events, the so-called Oi-2c glaciation event at ~ 25.1 Ma (Pekar et al., 2006) (Figure 2.1-3) falls into the studied interval herein. The Oi-2c event is characterized by global 0.4–0.5‰ increase in $\delta^{18}\text{O}_{\text{BF}}$, for which a sea-level equivalent of ~ 50 m was inferred (Pekar et al., 2002, 2006) (Figure 2.1-3). This equates to the melting of an ice-sheet almost the size of the EAIS [given the sea-level equivalent of the full-size EAIS is 53.3 m; Fretwell et al. (2013)]. Comparison to the high-resolution Site U1406 $\delta^{18}\text{O}_{\text{BF}}$ record at 25.1 Ma reveals a similar, yet slightly larger enrichment of $\sim 0.7\%$.

Interestingly, however, there is no corresponding increase shown in the Site U1406 $\delta^{18}\text{O}_{\text{sw}}$ signal, but a notable cooling of ~ 2.5 °C imprinted in the Site U1406 BWT record (Figure 6.2-3). This constellation imprinted in Site U1406 $\delta^{18}\text{O}_{\text{BF}}$, BWT, and $\delta^{18}\text{O}_{\text{sw}}$ at 25.1 Ma indicates that the Oi-2c event might rather be a signal of significant global deep-sea cooling rather than major glaciation. Expanding the correlation of significant enrichments in Site U1406 $\delta^{18}\text{O}_{\text{BF}}$ to the BWT and $\delta^{18}\text{O}_{\text{sw}}$ records across the entire study interval reveals another instance at ~ 25.45 Ma where a $\geq 0.5\%$ increase in $\delta^{18}\text{O}_{\text{BF}}$ is mainly caused by a ~ 2.5 °C cooling in BWTs. In contrast, the contribution of changes in $\delta^{18}\text{O}_{\text{sw}}$ to $\delta^{18}\text{O}_{\text{BF}}$ is relatively small (Figure 6.2-3A, B). Nonetheless, in several other instances, marked enrichments in Site U1406 $\delta^{18}\text{O}_{\text{BF}}$ are mirrored in significant maxima in $\delta^{18}\text{O}_{\text{sw}}$, which reflects increases in ice-volume (Figure 6.2-3C). On the basis of the signal correspondence of Site U1406 $\delta^{18}\text{O}_{\text{BF}}$, BWT and $\delta^{18}\text{O}_{\text{sw}}$ records, new insights into Oligocene deep-sea temperature, and Antarctic cryosphere dynamics across the studied interval from ~ 25.95 to 24.53 Ma, can be gained. As has been demonstrated with the example of the Oi-2c event and the $\geq 0.5\%$ increase in Site U1406 $\delta^{18}\text{O}_{\text{BF}}$ record at ~ 25.45 Ma, the simple allocation of increases in $\delta^{18}\text{O}_{\text{BF}}$ to significant ice-sheet built-up is inadequate if the temperature component of $\delta^{18}\text{O}_{\text{BF}}$ is not considered. Therefore, previous interpretations of positive maxima in $\delta^{18}\text{O}_{\text{BF}}$ across the entire Oligocene require reconsideration to be more accurately interpreted regarding Antarctic glaciation events (Zachos et al., 1997; Pekar et al., 2002, 2006; Wade and Pälike, 2004; Pälike et al., 2006b).

To that effect, coupled $\delta^{18}\text{O}_{\text{BF}}$ -Mg/Ca measurements provide powerful means to accurately interpret the $\delta^{18}\text{O}_{\text{BF}}$ signal in terms of changing dynamics of the Antarctic cryosphere.

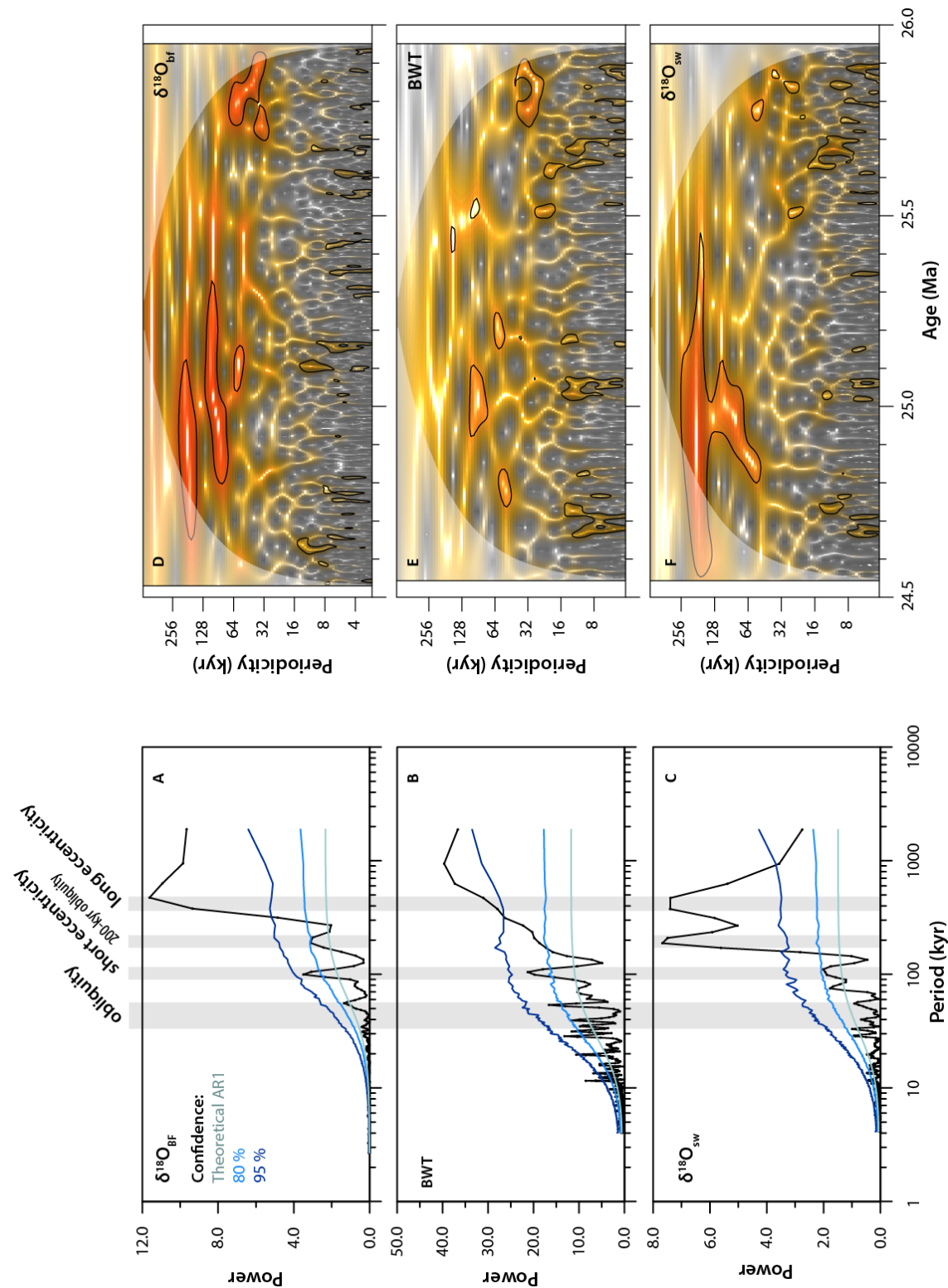


Figure 6.2-4: Time series analysis of $\delta^{18}\text{O}_{\text{BF}}$, Mg/Ca and $\delta^{18}\text{O}_{\text{sw}}$. (A–C) REDFIT spectral analysis (Schulz and Mudelsee, 2002) of $\delta^{18}\text{O}_{\text{BF}}$, BWT, and $\delta^{18}\text{O}_{\text{sw}}$ time series. Theoretical AR1 limit (light blue-green), Monte Carlo confidence intervals of 80 % (light blue) and 95 % (dark blue) are shown. The signal at the obliquity and the short and long eccentricity frequencies are highlighted in all times series with grey bars. (D–F) Wavelet analysis of $\delta^{18}\text{O}_{\text{BF}}$, BWT, and $\delta^{18}\text{O}_{\text{sw}}$. Before analysis, records were linearly detrended, and a Gaussian notch filter removed frequencies longer than ~ 250 kyr (see Methods).

6.2.7 AIS variability across the study interval inferred from the Site U1406

$\delta^{18}\text{O}_{\text{sw}}$ record

To constrain the magnitude of ice-volume change related to the observed amplitude changes in Site U1406 $\delta^{18}\text{O}_{\text{sw}}$, the same methodology for estimating ice-volumes as applied in chapter 5 (see Section 5.1.5) is used herein: Assuming $\delta^{18}\text{O}_{\text{ice}}$ of -42‰, ice-volume estimates can be assessed by inferring a pre-glacial $\delta^{18}\text{O}_{\text{sw}}$ of -1.05‰ (Bohaty et al., 2012) and a growth of $3.8 \times 10^6 \text{ km}^3$ of ice per 0.1‰ change in $\delta^{18}\text{O}_{\text{sw}}$ (Bohaty et al., 2012; Liebrand et al., 2017). Using the phase division introduced in Section 6.2.1, Phases I, III, and V with $\delta^{18}\text{O}_{\text{sw}}$ values ranging from -0.5 to 0.35‰ require average ice-volumes of $37 \times 10^6 \text{ km}^3$. $\delta^{18}\text{O}_{\text{sw}}$ values of -0.8 to -0.3‰ during Phases II, IV and VI average ice-volumes of $19 \times 10^6 \text{ km}^3$ of ice. Based on these ice-volume estimates, the Site U1406 $\delta^{18}\text{O}_{\text{sw}}$ record implies shifts between two states of glaciation, i.e., near modern to slightly larger than modern global ice-volumes during Phases I, III, and V, and less than half the modern to slightly smaller than modern global ice-volumes during Phases II, IV, and VI (Adkins et al., 2002; Bohaty et al., 2012) (Figure 6.2-5). Notably, the $\delta^{18}\text{O}_{\text{sw}}$ record never crosses the ice-free baseline, i.e., the Late Oligocene cryosphere never experienced full deglaciation across the study interval.

These Site U1406 $\delta^{18}\text{O}_{\text{sw}}$ -based ice-volumes and AIS dynamics across the study interval (25.95–24.53 Ma) are in stark contrast to previous ice-volumes estimates. $\delta^{18}\text{O}_{\text{BF}}$ -based ice-volume reconstructions from ODP Site 690 [Maud Rise, Antarctica; Hauptvogel et al. (2017)] infer a slightly smaller than modern-sized to larger than modern AIS across the study interval, and, notably, without significant ice-loss. On the contrary, previous $\delta^{18}\text{O}_{\text{BF}}$ -based ice-volume estimates from ODP Site 1264 [South Atlantic; Liebrand et al. (2017)] indicate climate states showing an ice sheet slightly smaller ($\sim 20 \times 10^6 \text{ km}^3$) than the present EAIS [$\sim 25 \times 10^6 \text{ km}^3$; Liebrand et al. (2017)] in alternation with full deglaciation during the interval of 25.95 to 24.53 Ma (Figure 6.2-5). Accordingly, absolute ice-volume estimates of Liebrand et al. (2017) from ODP Site 1264 are only comparable to ice volumes of Phases II, IV, and VI but only half the size compared to average ice-volumes of Phases I, III, and V (Figure 6.2-5).

The apparent offset between ice-volume estimates of those presented in this chapter from Site U1406 and previous studies of Hauptvogel et al. (2017) and Liebrand et al. (2017) likely arises due to the methods used to constrain ice-volume estimates. The $\delta^{18}\text{O}_{\text{BF}}$ signal is a function of temperature and ice-volume (see Section 2.4.1). Via coupled $\delta^{18}\text{O}_{\text{BF}}$ -Mg/Ca measurements, both the temperature and $\delta^{18}\text{O}_{\text{sw}}$ of the $\delta^{18}\text{O}_{\text{BF}}$ signal can be independently evaluated. However, as elaborated in Section 5.1.5, the ice-volume estimation approach of Hauptvogel et al. (2017) and Liebrand et al. (2017) rely on the $\delta^{18}\text{O}_{\text{BF}}$ signal paired with modern, constant BWTs [2.5 °C for Site 1264, Liebrand et al. (2017); 2 °C for Site 690, Hauptvogel et al. (2017)]. However, these modern and cold BWTs assumed for ODP Site 690 and 1264 seem unrealistic in comparison to BWTs from ODP Site 1218 (Lear et al., 2004) and Site U1406 BWTs across the study interval (Figure 6.2-3B) that show higher temperatures (5–9 °C) with distinct variability. Therefore, the missing evaluation of the temperature component of ODP Site 1264 and 690 $\delta^{18}\text{O}_{\text{BF}}$ records carry the risk that reconstructed ice-volume changes have arisen partially from changes

in the individual contributions of temperature and/or ice volume to the $\delta^{18}\text{O}_{\text{BF}}$ signal. To that end, ice-volume estimates from ODP Site 1264 and 690 are not reliable.

6.2.8 Possibility of a precursory bipolar glaciation

Notably, during Phase I and individual $\delta^{18}\text{O}_{\text{sw}}$ maxima (~25.5 Ma, 25 Ma, 24.85 Ma, 24.7 Ma, 24.65 Ma), $\delta^{18}\text{O}_{\text{sw}}$ displays values exceeding the reference line of the modern $\delta^{18}\text{O}_{\text{sw}}$ (i.e., 0‰; Adkins et al. (2002) by up to +0.3‰ (Figure 6.2-5). These positive values indicate ice volumes greater than the modern global ice-volume and therefore imply ice-sheet built-up in the Northern Hemisphere during the studied interval. As elaborated in Section 5.1.6, the occurrence of IRD and dropstones in the North Atlantic as early as the middle Eocene has been used to infer the presence of Northern Hemisphere ice sheets (Eldrett et al., 2007; Tripathi et al., 2008; St John, 2008), while modelling (DeConto et al., 2008) and proxy-based (Edgar et al., 2013; Spray et al., 2019) studies contradict a precursory Late Oligocene bipolar glaciation scenario. Additionally, it is general consensus that only short-lived, isolated glaciers (Stickley et al., 2009, 2012) thrived in the Northern Hemisphere throughout most of the early Cenozoic (Moran et al., 2006; Wilson et al., 2012). Similar to Section 5.1.6, higher than modern Site U1406 $\delta^{18}\text{O}_{\text{sw}}$ values ($\geq 0\text{‰}$) across the study interval from 25.95 to 24.53 Ma are interpreted to reflect a larger than modern AIS since the Late Oligocene surface area of Antarctica was able to store more ice than at modern (Wilson et al., 2012; Gasson et al., 2016b). This interpretation is further supported by ice-proximal geologic records that imply the extent of a wet-based AIS towards the paleo-coastlines of Antarctica and into the marine realm, which supports a larger than modern AIS (Olivetti et al., 2015; Fielding, 2018) (see Section 5.1.6).

6.2.9 Orbital Forcing of the Late Oligocene AIS

High-resolution stable isotope stratigraphy established an orbital influence on recurring $\delta^{18}\text{O}_{\text{BF}}$ maxima on astronomical timescales (see Section 2.1.1 and 2.1.2): Whereas previous studies established the ~1.2-Myr amplitude modulation of obliquity as the beat of major Antarctic glaciation pulses displayed in maximum $\delta^{18}\text{O}_{\text{BF}}$ (Pekar and Miller, 1996; Wade and Pälike, 2004; Pälike et al., 2006b; Pekar et al., 2006), a more recent study of Liebrand et al. (2017) emphasized that the ~2.4-Myr cycle of eccentricity is pacing recurring episodes of ~100 kyr variability in $\delta^{18}\text{O}_{\text{BF}}$, representative of a highly dynamic AIS. However, as outlined in the previous two paragraphs, the interpretation of Oligocene $\delta^{18}\text{O}_{\text{BF}}$ records for dynamics of the AIS without independently assessing its temperature component is likely to lack fidelity. Hence, the inferred orbital imprint in previously published $\delta^{18}\text{O}_{\text{BF}}$ records might not be entirely representative for orbitally-forced variations of the AIS but partly derived from deep-sea temperature variability. Therefore, the high-resolution Site U1406 $\delta^{18}\text{O}_{\text{sw}}$ signal and imprinted orbital forcing will be analyzed in the following to more thoroughly elucidate the link between astronomical forcing and the dynamics of the AIS across the study interval.

Comparison of the orbital solution for eccentricity and obliquity (Laskar et al., 2004) and the Site U1406 $\delta^{18}\text{O}_{\text{sw}}$ -based dynamics of the AIS across the study interval show a close link, also displayed in spectral and wavelet analysis. The amplitude variability of Site U1406 $\delta^{18}\text{O}_{\text{sw}}$ across the study interval occurs on timescales in the order of 10^4 to 10^5 kyr (Figure 6.2-6). This conflicts with previous assumptions that glaciations are spaced ~ 1.2 -Myr apart and triggered by minima in the amplitude modulation of obliquity (Pekar and Miller, 1996; Wade and Pälike, 2004; Pälike et al., 2006b; Pekar et al., 2006).

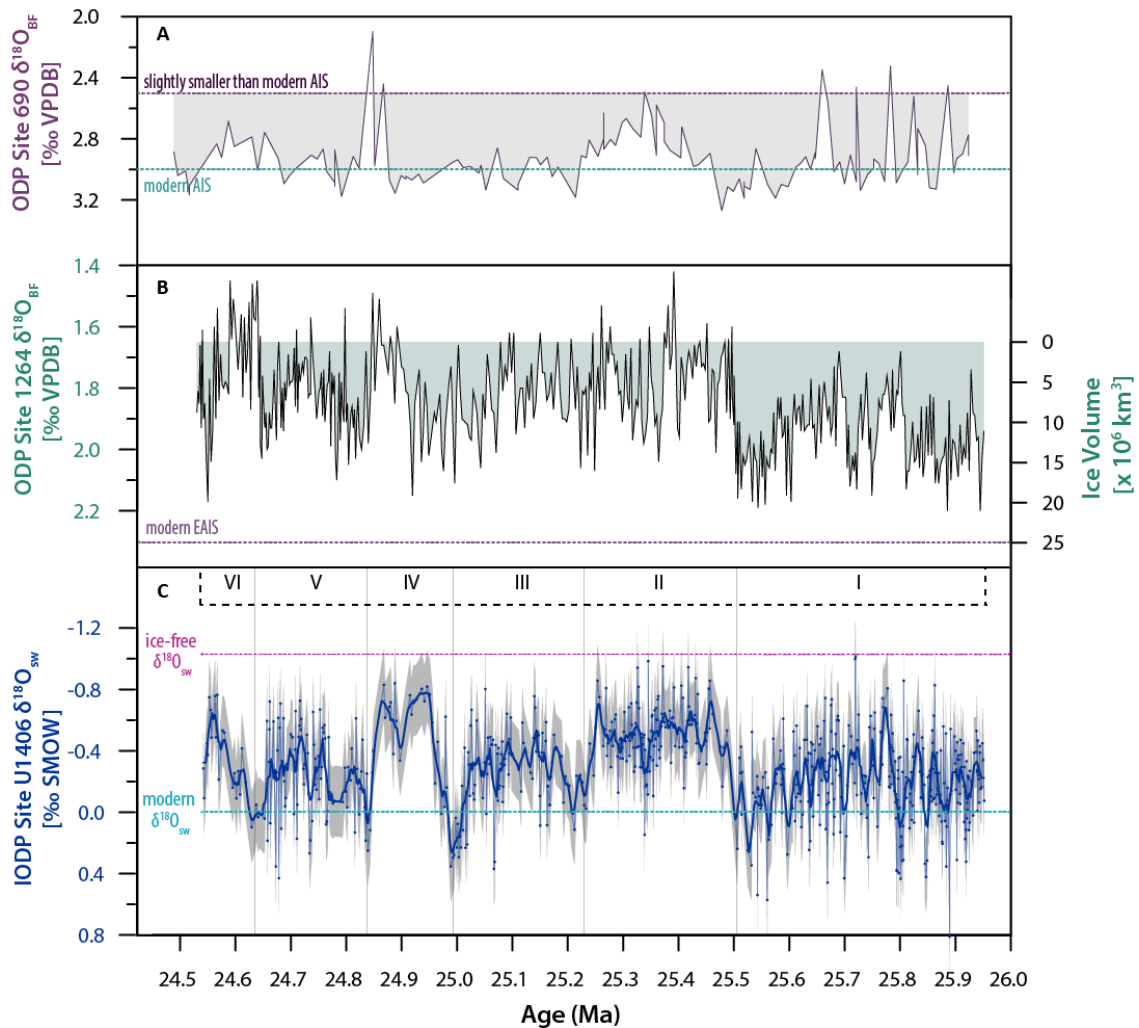


Figure 6.2-5: Ice-volume estimates of ODP Site 690 and 1264 in comparison to Site U1406. (A) Late Oligocene (25.95–24.53 Ma) $\delta^{18}\text{O}_{\text{BF}}$ record (in ‰ VPDB) of ODP Site 690 with proposed ice-volume estimates (light purple area) (Hauptvogel et al., 2017). Dashed purple line represents slightly smaller than modern AIS ($\delta^{18}\text{O}_{\text{BF}}$ of 2.5‰; Hauptvogel et al., 2017) and the dashed blue line represents modern AIS ($\delta^{18}\text{O}_{\text{BF}}$ of 3‰; Hauptvogel et al., 2017). (B) Late Oligocene (25.95–24.53 Ma) $\delta^{18}\text{O}_{\text{BF}}$ record (in ‰ VPDB, left axis) of ODP Site 1264 with proposed ice-volume estimates (light green area, right axis). Dashed purple line represents present-day-sized EAIS (Fretwell et al., 2013). (C) Site U1406 $\delta^{18}\text{O}_{\text{sw}}$ data with 5-pt smoother (thick blue line) and $\pm 0.23\%$ uncertainty resulting from Monte Carlo Simulations (grey envelope; see Section 4.5.3). Dashed lines indicate pre-glacial, i.e., ice-free $\delta^{18}\text{O}_{\text{sw}}$ (rose; Bohaty et al., 2012) and modern $\delta^{18}\text{O}_{\text{sw}}$ value (red; Adkins et al., 2002). Boxes indicate division into Phases I–VI (see text).

Agreement to previous studies (Wade and Pälike, 2004; Pälike et al., 2006b; Liebrand et al., 2017) is found in longer-term oscillations of Site U1406 $\delta^{18}\text{O}_{\text{sw}}$ on 10^5 -kyr timescales that follow the ~ 100 -kyr

variability, and recurring glacial maxima, i.e., positive $\delta^{18}\text{O}_{\text{sw}}$ maxima, are shown to coincide with minima of ~ 400 kyr eccentricity. Previous studies have inferred a strong coupling of glacial dynamics, the global carbon cycle, and insolation changes related to the ~ 400 kyr eccentricity band (Zachos et al., 1997, 2001b; Wade and Pälike, 2004; Pälike et al., 2006b). Using box model experiments, Pälike et al. (2006) have suggested that the seasonal insolation cycle could drive changes in productivity and carbon burial on eccentricity timescales due to the long residence time of carbon in the ocean.

Periods of increased carbon burial would cause a drawdown of atmospheric $p\text{CO}_2$ and thereby facilitate global cooling and ice-sheet expansion (DeConto et al., 2008). Given the coincidence of glacial maxima shown in the Site U1406 $\delta^{18}\text{O}_{\text{sw}}$ with eccentricity minima might be an indication of insolation-forced atmospheric $p\text{CO}_2$ decrease modulating maximum glacial extents. However, on occasion, a shorter than ~ 400 -kyr spacing of maxima in $\delta^{18}\text{O}_{\text{sw}}$ results in ~ 200 kyr cycles, which could be related to the sixth-order sequences to the ~ 40 kyr cycles (Boulila et al., 2011). Reminiscent ~ 180 -kyr peaks related to sixth order sequences of obliquity have been recorded in the Oligocene amplitude modulation of sliced magnetic susceptibility records from the equatorial Atlantic (ODP Leg 154; (Shackleton et al., 1999), in power spectra of a 13 Myr-long Oligo-Miocene record from the South Atlantic [ODP Site 1264; Liebrand et al. (2016)]. Therefore, the ~ 180 -kyr peaks are suggestive of a broader global signal, and hence, a teleconnection between Oligocene climate dynamics and 10^5 -kyr cycles of obliquity. However, explanations for the influence of sixth order sequences of obliquity onto glaciation cyclicity and other proxy records of the Oligocene are not well constrained and need further analysis. Additional indication for obliquity forcing across the study interval is given by the strong beat of obliquity that is imprinted in $\delta^{18}\text{O}_{\text{sw}}$ in the first 250 kyr of Phase I (~ 25.95 – 25.78 Ma, see Section 5.1.7), characterized by pronounced sinusoidally shaped oscillations of the AIS. The connection between AIS variability and obliquity during the Oligocene is also supported by ice-proximal geologic records around Antarctica. Obliquity-controlled oscillations of glacial-marine sequences representing highly dynamic ice margin advance and retreat of the EAIS have been identified in Early and latest Oligocene strata (between 34 Ma to 31 Ma, and 24 Ma to 23.5 Ma, respectively) in the CRP-2/2A drill core, Ross Sea (Naish et al., 2001; Galeotti et al., 2016; Fielding, 2018). In addition, obliquity-paced glacial-interglacial facies changes observed in sediments from off-shore the Wilkes Land margin (East Antarctica, IODP Site 1356), are interpreted to reflect environmental shifts influencing the size of the EAIS (Salabarnada et al., 2018).

6.2.10 Amplitude response of Site U1406 $\delta^{18}\text{O}_{\text{sw}}$ to eccentricity and obliquity forcing

The Site U1406 $\delta^{18}\text{O}_{\text{sw}}$ record allows for the evaluation of long-term relationships between radiative forcing and the Antarctic cryosphere response as it is imprinted in the $\delta^{18}\text{O}_{\text{sw}}$ signal. As elaborated in the previous paragraph, the pacing of $\delta^{18}\text{O}_{\text{sw}}$ oscillations displays distinct cyclicity on astronomical timescales. To evaluate the sensitivity response of the $\delta^{18}\text{O}_{\text{sw}}$ signal to (changing) orbital frequencies

across the study interval from 25.95 to 24.53 Ma, amplitude modulations for $\delta^{18}\text{O}_{\text{sw}}$ to both the short eccentricity (~ 100 -kyr) and obliquity (~ 40 kyr) are calculated (Figure 6.2-7).

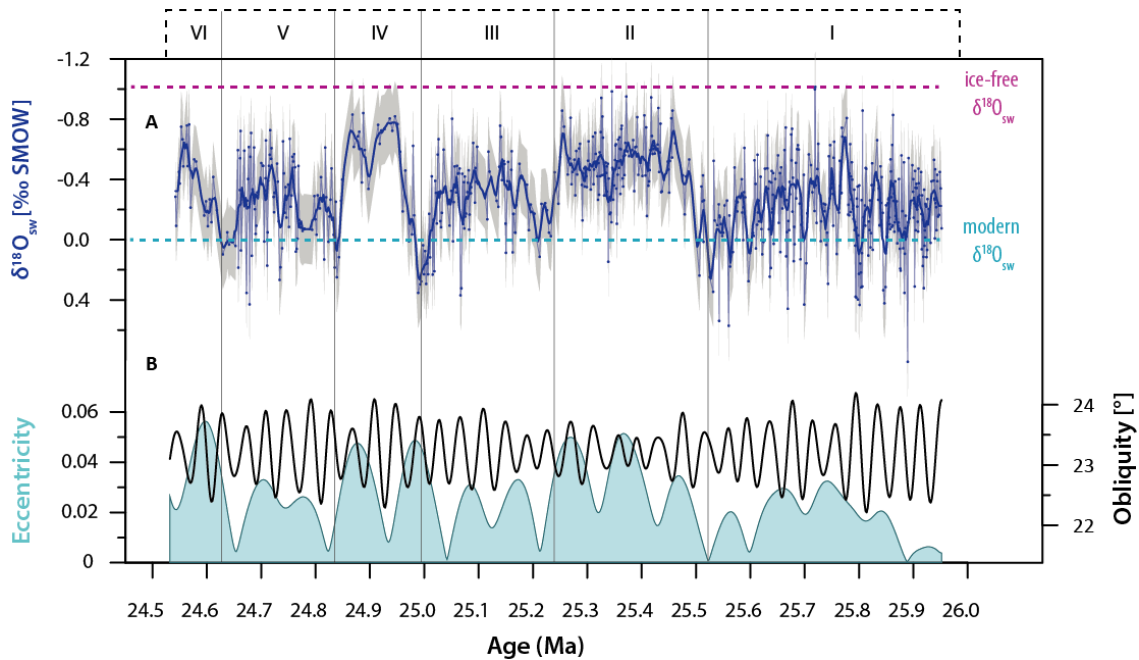


Figure 6.2-6: Orbital forcing of Site U1406 $\delta^{18}\text{O}_{\text{sw}}$. (A) Site U1406 $\delta^{18}\text{O}_{\text{sw}}$ data with 5-pt smoother (thick blue line) and $\pm 0.23\%$ uncertainty resulting from Monte Carlo Simulations (grey envelope; see Section 4.5.2). Dashed lines indicate pre-glacial, i.e., ice-free $\delta^{18}\text{O}_{\text{sw}}$ (blue; Bohaty et al., 2012) and modern $\delta^{18}\text{O}_{\text{sw}}$ value (red; Adkins et al., 2002). Boxes indicate division into Phases I–VI (see text). (B) Orbital solutions of eccentricity (light turquoise) and obliquity (grey) (Laskar et al., 2004).

During Phases I, III, and V, amplitude modulated $\delta^{18}\text{O}_{\text{sw}}$ filters show a high response of $\delta^{18}\text{O}_{\text{sw}}$ to obliquity forcing. The amplitude response of $\delta^{18}\text{O}_{\text{sw}}$ to eccentricity forcing is very low, in parallel with a generally low eccentricity baseline (≤ 0.03) (Figure 6.2-7). This response of $\delta^{18}\text{O}_{\text{sw}}$ to eccentricity and obliquity forcing points to the following: Phases I, III, and V fall into episodes of low eccentricity forcing during which summer insolation extremes in the high latitudes are suppressed (Pälike et al., 2006b). Concurrently, high-amplitude changes in obliquity observed during Phases I, III, and V (Figure 6.2-7) cause alternations of high and low solar radiation contrasts between the high and low latitudes (Mantsis et al., 2014), which itself regulate the poleward moisture and heat transport through atmospheric and oceanic circulation (Vimeux et al., 1999; Raymo and Nisancioglu, 2003; Langebroek et al., 2009). This mechanism has been observed in an Antarctic deuterium-excess record spanning glacial-interglacial cycles of the last 150 kyr: A minimum latitudinal insolation gradient at high obliquity weakened the atmospheric and oceanic meridional circulation and thereby reduced the contribution of moisture sourced from low latitudes to Antarctic precipitation, inhibiting ice-sheet built-up (Vimeux et al., 1999) (see Section 5.1.7). A change in the Earth's axial tilt also affects the seasonal distribution of insolation: At high latitudes, low (high) obliquity causes a weakening (strengthening) of the seasonal cycle resulting in milder (colder) winters and cooler (warmer) summers (Mantsis et al., 2014). Given these effects of obliquity on high-latitude climate, ice-sheet built-up was fueled during the low obliquity

phase, based on a potent moisture source originating from low-latitudes and low seasonal cycle (mild winter, cool summer). During phases of high obliquity, moisture delivered from low-latitude declined and/or ceased, and a strengthened seasonal cycle likely caused partial ice-sheet melting. Severe ice-sheet disintegration during Phases I, III, and V was prohibited due to the low eccentricity configuration suppressing extreme insolation forcing. This orbital configuration provided ideal background conditions for the observed heavier glaciated AIS during Phases I, III, and V inferred from the Site U1406 $\delta^{18}\text{O}_{\text{sw}}$ signal.

The notably high amplitude modulation of $\delta^{18}\text{O}_{\text{sw}}$ to obliquity, yet low amplitude modulation of $\delta^{18}\text{O}_{\text{sw}}$ to eccentricity during Phases I, III, and V (Figure 6.2-7) are in stark contrast to the dominance of eccentricity paced dynamics of the AIS inferred from ODP Site 1264 (Liebrand et al., 2017) and ODP Site 1218 (Pälike et al., 2006b) across the study interval (25.95–24.53 Ma). It is also partly in contrast to findings of Levy et al. (2019). They (i) generally characterized the Oligocene as an epoch with low sensitivity to obliquity forcing [obliquity sensitivity calculated by dividing obliquity variance in $\delta^{18}\text{O}_{\text{BFW}}$ by the variance of the theoretical obliquity solution; see Levy et al. (2019) for details] and (ii) only attributed high sensitivity of the AIS to obliquity forcing when the AIS extended from its terrestrial boundaries into the marine environment. The latter argument implies that the AIS must have reached a threshold extent/volume before it became sensitive to changes in the Earth's axial tilt. However, the lower end of ice-volume estimates of $\sim 20 \times 10^6 \text{ km}^3$ of ice (based on $\delta^{18}\text{O}_{\text{sw}}$ of -0.5‰) during Phases I, III, and V indicate a terrestrial-based AIS given that they are 20% smaller than the modern-sized EAIS (Fretwell et al., 2013). Therefore, these results imply that (i) the AIS was generally sensitive to obliquity forcing during an interval previously perceived as eccentricity dominated and (ii) the sensitivity of the AIS to obliquity forcing is not restricted to an AIS extending into the marine realm. In addition, resulting from amplitude modulations of Site U1406 $\delta^{18}\text{O}_{\text{sw}}$ to orbital forcing of obliquity and eccentricity, the interpretation of the obliquity sensitivity parameter of Levy et al. (2019) might be insufficient since the temperature effect of $\delta^{18}\text{O}$ has not been addressed. It therefore could cause the apparent mismatch to the findings inferred from the Site U1406 $\delta^{18}\text{O}_{\text{sw}}$ record herein.

During Phases II, IV, and VI the amplitude modulation of $\delta^{18}\text{O}_{\text{sw}}$ to obliquity forcing is small in comparison to Phases I, III and V. In contrast, the amplitude response of $\delta^{18}\text{O}_{\text{sw}}$ to eccentricity forcing is high, in parallel with a generally high eccentricity baseline (≥ 0.03) (Figure 6.2-7). Eccentricity has been correlated to direct insolation forcing pacing atmospheric temperature changes (Levy et al., 2019). Given the high eccentricity baseline during Phases II, IV, and VI in parallel with the high response of $\delta^{18}\text{O}_{\text{sw}}$ to eccentricity forcing (Figure 6.2-7), this orbital constellation might cause episodes of insolation extremes affecting the high latitudes (Pälike et al., 2006b) leading to elevated atmospheric temperatures (Levy et al., 2019) that ultimately cause transient ice-sheet disintegration, as yet suggested for the late Miocene under a similar orbital configuration (Holbourn et al., 2018).

Inferred from previous studies demonstrating an overall dominance of eccentricity across the study interval from 25.95–24.53 Ma (Pälike et al., 2006b; Liebrand et al., 2016; Levy et al., 2019), the restriction of a high sensitivity to eccentricity forcing of Site U1406 $\delta^{18}\text{O}_{\text{sw}}$ to Phases II, IV, and VI

when AIS volumes were smaller (than compared to Phases I, III, and V) provides new context to the sensitivity of the AIS to eccentricity forcing. Site U1406 $\delta^{18}\text{O}_{\text{sw}}$ is, therefore, the first record showing dominant eccentricity forcing of the AIS is limited to intervals of reduced AIS volume across the interval from 25.95 to 24.53 Ma (Figure 6.2-7).

Notably, the $\delta^{18}\text{O}_{\text{sw}}$ record displays three rapid transitions (~ 25.53 Ma; ~ 25 Ma; ~ 24.63 Ma) from glacial maxima, i.e., positive maxima in $\delta^{18}\text{O}_{\text{sw}}$, to distinctly smaller AIS volumes. These transitions are paralleled by notable increases in the eccentricity baseline and by high amplitude modulation of $\delta^{18}\text{O}_{\text{sw}}$ to eccentricity forcing (Figure 6.2-7). Modelled ice-sheet variations for the past 400 kyr of Abe-Ouchi et al. (2013) showed that after an ice-sheet has grown large enough during a glacial/cold period in times of reduced eccentricity, the subsequent eccentricity increase provides enough energy and time through summer insolation forcing to trigger a negative mass balance of the ice sheet causing rapid deglaciation. Given the marked increases in eccentricity following minimum eccentricity during glacial maxima at ~ 25.53 Ma, ~ 25 Ma, and ~ 24.63 Ma suggests that the same mechanism as proposed by Abe-Ouchi et al. (2013) worked during these transitions of rapid ice-sheet disintegration displayed in the Site U1406 $\delta^{18}\text{O}_{\text{sw}}$ record (Figure 6.2-7). However, detailed comparison of the individual rapid ice-sheet disintegration events evident in the $\delta^{18}\text{O}_{\text{sw}}$ record at ~ 25.53 Ma, ~ 25 Ma, and ~ 24.63 Ma reveals that the degree of deglaciation varies depending on the amplitude of obliquity: the bigger the amplitude of obliquity in congruence with a general increase in eccentricity during the transition from high to low AIS volumes, the bigger the decrease in size of the AIS (Figure 6.2-7). These results indicate that it is the tilt of the Earth's spin axis that modulates the degree of ice loss during these transitional ice-sheet disintegration events. Similar observations have been drawn from the Plio-Pleistocene glacials [e.g., Naish et al. (2009)] and glacial terminations (Huybers and Wunsch, 2005; Drysdale et al., 2009): While the role of seasonal insolation intensity on polar ice volume in times of high eccentricity is undisputed to influence polar ice-volumes (Berger, 1988), however, a stronger emphasis was put on mean annual insolation with additional influence of summer energy, both paced by obliquity, to force large-scale glacial dynamics (Huybers and Wunsch, 2005). Very large angles of the Earth's tilt anomalously increase the total summer energy received at high latitudes of up to $10\text{--}40\text{ W/m}^2$ (Berger, 1988; Huybers and Wunsch, 2005) lasting up to 10 kyr due to the long period of obliquity (Huybers, 2011). This effect, therefore, has a significant control over the surface melting of ice-sheets (Huybers and Wunsch, 2005) and presents a plausible mechanism for strong obliquity forcing in glacial terminations.

6.2.11 $p\text{CO}_2$ forcing

Although the Site U1406 $\delta^{18}\text{O}_{\text{sw}}$ signal shows a close connection to orbital forcing, which is interpreted as the main driver of the observed variability of the AIS across the study interval, an alternative and/or additional driving mechanism to the observed pacing of AIS variability is atmospheric $p\text{CO}_2$. Atmospheric $p\text{CO}_2$ has a direct effect on radiative forcing and air temperature. Those factors in turn regulate the line between ablation and accumulation of snow on ice sheets (Ruddiman, 2006). Therefore,

a change in $p\text{CO}_2$ could also present a possible mechanism causing the high-amplitude variability of AIS dynamics observed in the Site U1406 $\delta^{18}\text{O}_{\text{sw}}$ record. However, no high-resolution Late Oligocene $p\text{CO}_2$ reconstructions have been published to date (Henderiks and Pagani, 2008; Beerling and Royer, 2011; Zhang et al., 2013), which prevents a one-to-one correlation and testing of this mechanism.

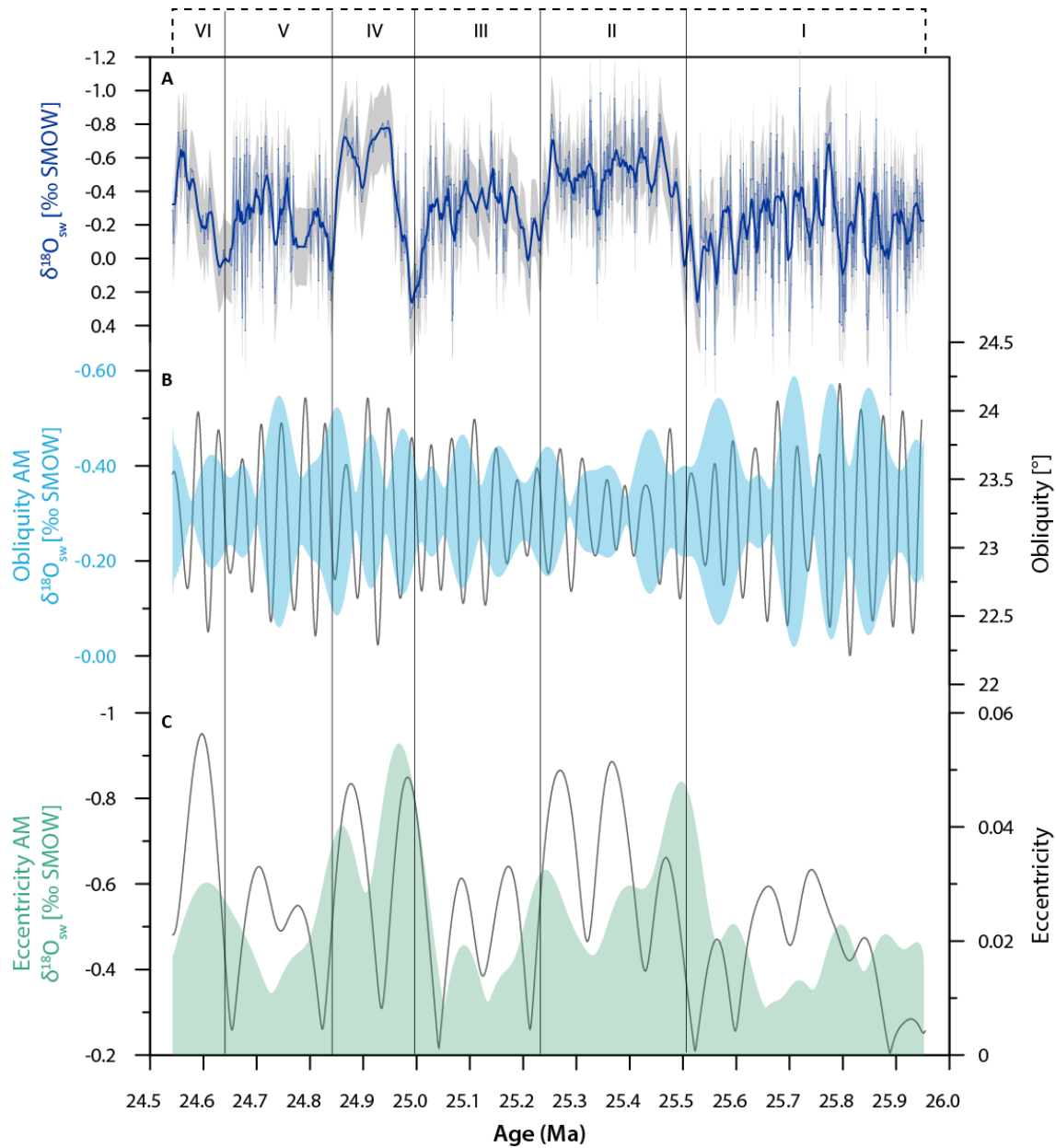


Figure 6.2-7: Amplitude response of Site U1406 $\delta^{18}\text{O}_{\text{sw}}$ to eccentricity and obliquity forcing. (A) Site U1406 $\delta^{18}\text{O}_{\text{sw}}$ data with 5-pt smoother (thick blue line) and $\pm 0.23\text{‰}$ uncertainty resulting from Monte Carlo Simulations (grey envelope; see Section 4.5.2). (B) Amplitude modulation of the Site U1406 $\delta^{18}\text{O}_{\text{sw}}$ record centered around the $\sim 41\text{-kyr}$ obliquity periodicity (blue area) and orbital solution for obliquity (black line; Laskar et al., 2004). (C) Amplitude modulation of the Site U1406 $\delta^{18}\text{O}_{\text{sw}}$ record centered around the $\sim 110\text{-kyr}$ eccentricity periodicity (green area) and orbital solution for eccentricity (black line; Laskar et al., 2004). Numbering at the top of the figure indicate division into Phases I–VI.

7 RESPONSE OF THE HIGH NORTH ATLANTIC OCEAN TO AIS DYNAMICS DURING THE LATE OLIGOCENE

7.1 Introduction

The Earth transitioned from greenhouse conditions of the Paleogene characterized by warm, largely unglaciated conditions with weak latitudinal temperature gradients into the Neogene icehouse world that was cold enough at high latitudes to host ice-sheets on Antarctica (Zachos et al., 2001, 2008; Scher, 2017). Across the EOT, permanent continental ice-sheets initiated on Antarctica between ~34 and 33 Ma ago caused by a drawdown of atmospheric $p\text{CO}_2$ concentrations (DeConto et al., 2008). The growth of the AIS caused a substantial climatic and oceanic reorganization resulting in strengthening of the meridional temperature gradient and cooling of the deep ocean and enhanced meridional overturning (Goldner et al., 2014) with evidence of a thermal decoupling of the North Atlantic Ocean from the southern high latitudes (Liu et al., 2018). As evidenced in chapters 5 and 6, the AIS is shown to be variable in size across the study interval from 25.95 to 24.53 Ma. These Late Oligocene AIS fluctuations beg the questions as to whether such dynamics affected the AMOC and thermal dynamics of the North Atlantic during the Late Oligocene. However, to date, nothing is known about how the North Atlantic responded to the dynamics of the AIS across the Late Oligocene as data on for this interval are non-existent. The paleoceanographic setting of Site U1406 is located along the flow path of the NAC, that is part of the return flow of the AMOC and therefore is intrinsically linked to the strength of the AMOC [e.g., Schmitz Jr. and McCartney (1993); Häkkinen et al. (2011)]. Therefore, Site U1406 bears great potential for reconstructing past variabilities of the strength of northward heat and salt transport thorough the NAC, and thus, strength of the AMOC.

As the North Atlantic subsurface has shown ubiquitous evidence for being sensitive to changes in the strength of the AMOC [e.g., Chang et al. (2008)], high-resolution records of sub-thermocline proxy data from Site U1406 will be analyzed to trace the strength of the NAC and the efficiency of the AMOC across the interval of 25.95 to 24.53 Ma. Furthermore, the NAC's strength and position are also coupled to the position of the Arctic Front, which has a substantial influence on the nutrient distribution in the North Atlantic [e.g., Naafs et al. (2010)]. For this purpose, the gradient between planktic and benthic foraminiferal carbon isotopic signatures along with coarse fraction data of U1406 across the study interval will be additionally be investigated to further draw evidence for the strength of the NAC.

7.2 Results and discussion

7.2.1 Assessment of contamination and diagenetic effects on the Mg/Ca ratios

Elemental ratios of Al/Ca, Fe/Ca and Mn/Ca were monitored carefully to identify contamination by clay particles or diagenetic coatings which may affect the foraminiferal Mg/Ca ratios (Barker et al., 2003). Measured Al concentrations of the data are generally below the detection limit, arguing against the presence of detrital clay. However, Fe/Ca and especially Mn/Ca ratios of *C. dissimilis* generally exceed the 0.1 mmol/mol threshold value defined by Barker et al. (2003) (Figure 7.2-1A, B). Yet, a statistically significant correlation between Mg/Ca vs. Fe/Ca ($r^2=0.2$, $p<0.0001$) is not observed (Figure 7.2-1A), suggesting that Fe-oxide coatings (if present at all) did not considerably affect the measured Mg/Ca contents. There is, however, a weak correlation between Mg/Ca and Mn/Ca ratios for *C. dissimilis* samples ($r^2 = 0.35$, $p<0.0001$) (Figure 7.2-1B) that indeed might indicate a bias of measured Mg/Ca ratios due to a Mn-rich overgrowth. Diagenetic overgrowth usually has a Mg/Mn ratio of ~ 0.1 mol/mol (Barker et al., 2003 and references therein); if an unrealistically high Mg/Mn ratio of 1 in the diagenetic overgrowth is assumed, this might bias the temperature estimate by on average ~ 0.5 °C. It should be noted that this would not affect the overall shape of the Mg/Ca-based temperature record (Figure 7.2-1D). Additionally, the ~ 0.5 °C temperature bias is smaller than the error associated with the Mg/Ca-paleotemperature estimation (~ 0.8 °C) (Figure 7.2-1D). Although the possibility of diagenetic changes in tests of *C. dissimilis* cannot be completely ruled out due to the enriched Mn/Ca ratios, SEM images unambiguously rule out the presence of microcrystalline overgrowth on the measured *C. dissimilis* tests (Figure 2.7-1). It can, therefore, be concluded with reasonable certainty that early diagenetic overprinting has not affected Mg/Ca-based reconstructions for the interval 25.95–24.53 Ma at Site U1406.

7.2.2 Sub-thermocline temperatures

The total range of subthermocline temperature (subT) changes is ~ 6 °C, with values varying between 15 to 21 °C (Figure 7.2-2D).

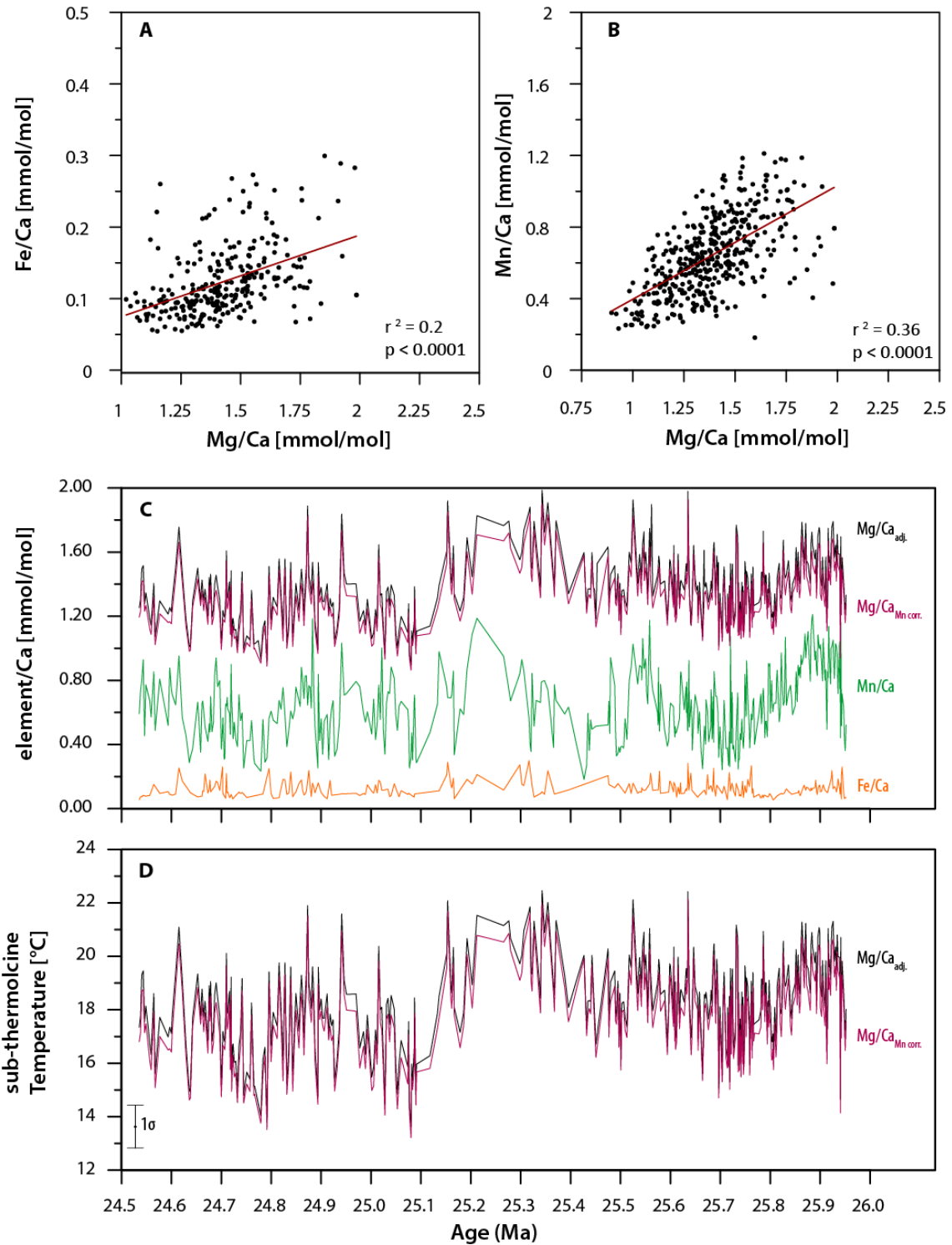


Figure 7.2-1: Evaluation of *C. dissimilis* test contamination. Cross correlation plots of (A) Mg/Ca versus Fe/Ca that show no statistically significant correlation between Fe/Ca vs. Mg/Ca ($r^2 = 0.2$, $p < 0.0001$). (B) Mn/Ca versus Mg/Ca shows a significant statistical correlation ($r^2 = 0.35$, $p < 0.0001$), indicating that measured Mg/Ca values might be altered by clay particles or diagenetic coatings. (C) Downcore Mg/Ca ratios [black; normalized relative to the ECRM752-1 standard applying the Mg/Ca reference value of 3.762 mmol/mol (Greaves et al., 2008)], Mg/Ca ratios corrected for Mn-bearing overgrowths using the assumption of a Mn:Mg ratio of 1:1; red), Mn/Ca (green) and Fe/Ca (orange) ratios. (D) Mg/Ca-based temperatures calculation (black; see Methods for details), and Mg/Ca-based temperatures with Mg/Ca ratios corrected for Mn-bearing overgrowths using the assumption of a Mn:Mg ratio of 1:1 (red) causing an average temperature bias of 0.5 °C.

From the late to the early part of the record, subTs are characterized by a long-term trend towards cooler temperatures with a marked shift towards lower temperatures from 25.22 Ma onwards. From 25.95 to 25.52 Ma, a U-shaped trend of subTs displays variability of 3 °C between 17 and 20 °C. Subsequently, subTs drop sharply by ~2 °C towards 25.5 Ma. A two-step-like warming feature of ~4 °C occurs until ~25.3 Ma, and within that phase, subTs reach maximum values of 21°C at ~25.35 Ma. SubTs remain warm with small variability of ~2 °C until 25.22 Ma, when temperatures drop by 6 °C in a two-step manner to 16 °C at ~25 Ma. A two-step increase in subTs is shown between 25.1 to 24.95 Ma, intersected by cooler temperatures around 25 Ma. SubTs increase towards 19°C at 24.95 Ma. Subsequently, values successively decrease to lowest subTs displayed over the studied interval with temperatures of ~15 °C at 24.77 Ma. A ~4 to 5 °C warming follows, before subTs sharply drop again to 15 °C at ~24.64 Ma. Short-lived pulses of warming (± 4 –5 °C) and cooling set in from 24.63 to 24.59 Ma; a feature that is well-mirrored in $\delta^{18}\text{O}_{\text{BF}}$, $\delta^{18}\text{O}_{\text{PF}}$, $\delta^{13}\text{C}_{\text{BF}}$, $\delta^{13}\text{C}_{\text{PF}}$ and $\delta^{18}\text{O}_{\text{ivf-sw}}$ (Figure 7.2-2D). Towards the earliest part of the record, subTs display a slight warming to 18 °C.

Compared to the modern temperature at thermocline depths (~600 m, annual subT of 9 °C) at Site U1406 (Figure 7.2-4B), reconstructed Mg/Ca-based subTs are relatively warmer by 6 to 15 °C. Support for the relatively warmer subTs at Site U1406 is given by warmer than compared to modern SST reconstructions of Liu et al. (2018) from IODP Site U1404, a neighboring site to the study Site U1406 at the Newfoundland margin. Liu et al. (2018) reconstructed SSTs in the range of 24 to 26 °C, which are 4 to 6 °C warmer than the modern annual SSTs (20 °C). Despite the lower resolution, Site U1404 SST reconstructions generally follow the trend displayed in Site U1406 subTs (Figure 7.2-2D).

7.2.3 Stable Site U1406 $\delta^{18}\text{O}$ and $\delta^{13}\text{C}$ records

7.2.3.1 Stable oxygen isotopes

The $\delta^{18}\text{O}_{\text{PF}}$ record is characterized by values between 0.7 to 1.9‰ resulting in a total range of 1.2‰ across the study interval (Figure 7.2-2A). There is a general decrease towards lighter $\delta^{18}\text{O}_{\text{PF}}$ value from the late to the early part of the record. From 25.95–25.85 Ma, $\delta^{18}\text{O}_{\text{PF}}$ values show an increase from 1.4 to 1.8‰, followed by a steady long-term decrease until 25.5 Ma towards $\delta^{18}\text{O}_{\text{PF}}$ of 0.8‰. The subsequent ~300 kyr are characterized by an increase in $\delta^{18}\text{O}_{\text{PF}}$ to 1.9‰ at 25.2 Ma, superimposed by variabilities of 0.2–0.4‰. From 25.2 Ma onwards to 25 Ma, values gradually decrease to 1.6‰ with a significant excursion to 0.9‰ between 25.16 to 25.14 Ma. A plateau of lighter values develops between 25 and 24.8 Ma, which is followed by an interval of values constantly varying between 0.9 and 1.6‰ until the end of the record at 24.53 Ma.

The evolution of the benthic $\delta^{18}\text{O}$ ($\delta^{18}\text{O}_{\text{BF}}$) record is relatively similar to the planktic $\delta^{18}\text{O}$ ($\delta^{18}\text{O}_{\text{PF}}$) record with the exception of the interval from 25.75 to 25.5 Ma when $\delta^{18}\text{O}_{\text{BF}}$ displays a notable long-term increase while $\delta^{18}\text{O}_{\text{PF}}$ gradually decreases (Figure 7.2-2A). Following Shackleton et al. (1984), $\delta^{18}\text{O}$ values of *C. mundulus* reported herein were adjusted for species-specific offset from equilibrium by the

addition of +0.5‰ (Table 2.7-1) (Shackleton et al., 1984). Trends of $\delta^{18}\text{O}_{\text{BF}}$ (Figure 7.2-2A) are described in detail in Section 6.2.1.

7.2.3.2 Stable carbon isotopes

Cibicidoides mundulus precipitates its shell close to $\delta^{13}\text{C}$ equilibrium. Therefore, no adjustment factor is required (e.g., Shackleton et al., 1984). The planktic ($\delta^{13}\text{C}_{\text{PF}}$) and benthic ($\delta^{13}\text{C}_{\text{BF}}$) carbon isotope records show an exceedingly parallel trend at similar values throughout most of the record, with the $\delta^{13}\text{C}_{\text{PF}}$ and $\delta^{13}\text{C}_{\text{BF}}$ signals slightly diverging by a maximum of 0.3‰ from 25.2 Ma onwards (Figure 7.2-2B). $\delta^{13}\text{C}_{\text{PF}}$ and $\delta^{13}\text{C}_{\text{BF}}$ values display a total range of 0 to 0.9‰. Alternating phases of increase and decreases in $\delta^{13}\text{C}_{\text{PF}}$ and $\delta^{13}\text{C}_{\text{BF}}$ characterize the older part of the record between 25.95 to 25.5 Ma with values varying between 0.2 to 0.8‰. From 25.5 Ma onwards, there is a long-term decrease of 0.8‰ to minimum values of 0‰, which is intersected by a short-term decrease to 0.4‰ at ~25.42 Ma, in line with similar changes in $\delta^{18}\text{O}_{\text{PF}}$ and $\delta^{18}\text{O}_{\text{BF}}$. An increase in $\delta^{13}\text{C}$ to maximum values of 0.6‰ sets in at 25.3 Ma and lasts until 25.2 Ma. Thereafter, both the $\delta^{13}\text{C}_{\text{PF}}$ and $\delta^{13}\text{C}_{\text{BF}}$ record display distinct variability of ~0.2–0.4‰, (mostly in-phase), with values ranging between 0.1‰ and 0.8‰ until the earliest part of the record, following the cyclicity shown in both planktic and benthic $\delta^{18}\text{O}$ records (Figure 7.2-2B).

7.2.4 Site U1406 $\delta^{18}\text{O}_{\text{ivf-sw}}$

The Site U1406 $\delta^{18}\text{O}_{\text{ivf-sw}}$ (‰ SMOW) record, that mirrors salinity at sub-thermocline depths (subS) (see Section 2.5.2), record shows variability of 0.8 to 3‰ across the studied interval resulting in a total range of 2.2‰ (Figure 7.2-2E). In parallel to Site 1406 subTs, the long-term-trend of $\delta^{18}\text{O}_{\text{ivf-sw}}$ values throughout the entire record is decreasing.

While $\delta^{18}\text{O}_{\text{ivf-sw}}$ increases from the base of the record to 25.84 Ma, there is a long-term decrease in $\delta^{18}\text{O}_{\text{ivf-sw}}$ of ~1‰ from 25.84 Ma to 25.45 Ma. A significant increase of 1.5‰ characterizes the interval between 25.45 and 25.1 Ma. A three-step-like decrease in $\delta^{18}\text{O}_{\text{ivf-sw}}$ of >1.5‰ follows until 25 Ma. Subsequently, a short increase in $\delta^{18}\text{O}_{\text{ivf-sw}}$ to 2.4‰ at 24.95 Ma is followed by a successive decrease to lowest $\delta^{18}\text{O}_{\text{ivf-sw}}$ displayed over the studied interval of ~1.1‰ at 24.77 Ma. Values rise to 2.4‰ at 24.66 Ma, superimposed by smaller-scale variability.

Subsequently, $\delta^{18}\text{O}_{\text{ivf-sw}}$ values drop sharply towards 1.2‰, followed by a short-lived pulse of increasing salinity (+1.4‰); a feature that is well mirrored in $\delta^{18}\text{O}_{\text{BF}}$, $\delta^{18}\text{O}_{\text{PF}}$, $\delta^{13}\text{C}_{\text{BF}}$, $\delta^{13}\text{C}_{\text{PF}}$, and subTs. To the earliest part of the record, $\delta^{18}\text{O}_{\text{ivf-sw}}$ generally displays constant values of about 2‰ (Figure 7.2-2E).

7.2.5 Variations in Site U1406 coarse fraction as a tracer for paleoproductivity

The weight % of the coarse fraction (%CF) record of Site U1406 shows values between 0.1 to ~3.1 wt% (Figure 7.2-3F). Values gradually increase and decrease throughout the study interval, with some more pronounced variability with higher %CF values, e.g., at 25.8, 25.3, around 24.9, 24.7 and 24.6 Ma.

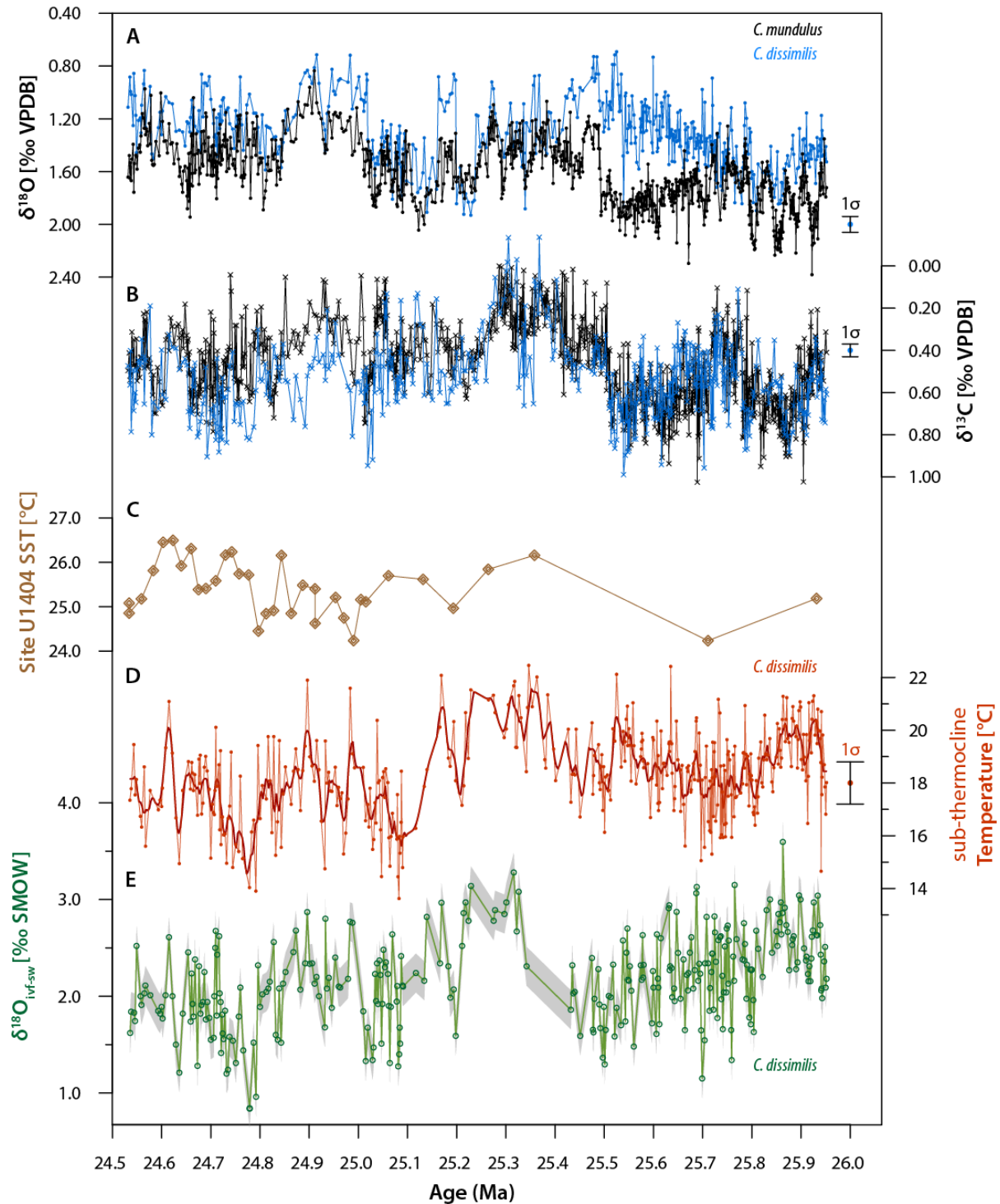


Figure 7.2-2: Benthic and planktic proxy records of Site U1406. (A) Site U1406 $\delta^{18}\text{O}_{\text{PF}}$ (*C. dissimilis*, blue) and $\delta^{18}\text{O}_{\text{BF}}$ (*C. mundulus*, black) (‰ VPDB). (B) Site U1406 $\delta^{13}\text{C}_{\text{PF}}$ (*C. dissimilis*, blue) and $\delta^{13}\text{C}_{\text{BF}}$ (*C. mundulus*, black) (‰ VPDB). (C) SST reconstruction of Liu et al. (2018) from IODP Site U1404 (brown). (D) Site U1406 Mg/Ca-based subT data (°C; red) with 5-pt smooth (dark red). (E) Site U1406 $\delta^{18}\text{O}_{\text{ivf-sw}}$ (‰ SMOW) (green) and $\pm 0.2\%$ uncertainty resulting from Monte Carlo Simulations (grey envelope; see Section 4.5.2).

When interpreting the %CF record, there are three main aspects to consider: (i) carbonate dissolution (Berger et al., 1982; Bickert et al., 2004), (ii) changes in the strength of bottom-water currents causing winnowing (Berstad et al., 2003), and (iii) changes in export productivity (Diester-Haass et al., 2006).

Carbonate dissolution: %CF has been employed as a proxy for carbonate dissolution with %CF decreasing as dissolution increases (Berger et al., 1982; Bickert et al., 2004). Given the excellent preservation of planktic and benthic foraminifera at Site U1406 across the study interval (Figure 2.7-1), dissolution is not a plausible explanation responsible for low %CF data.

Winnowing: Winnowing is excluded as a factor influencing %CF data due to the constant regular clay deposition at Site U1406 across the study interval (Norris et al., 2014b; Boyle et al., 2017; van Peer et al., 2017a).

Changes in export productivity: A remaining explanation for the small-scale variability in the %CF record are changes in marine productivity, with the relation that an increase in productivity would cause the %CF to increase (Diester-Haass et al., 2006).

As mentioned in Section 2.4.2, a powerful tool to infer changes in nutrient distribution in the water column is $\Delta\delta^{13}\text{C}_{\text{PF-BF}}$. Since an increase in primary production results in the fixation of carbon, which induces preferential removal of ^{12}C from the photic zone, it leaves the surface ocean enriched in ^{13}C (traceable in surface-dwelling planktic $\delta^{13}\text{C}$ signals) [e.g., Bostock et al. (2004)]. As the organic particulate matter sinks through the water column to the seafloor, it is being remineralized via respiration and metabolism. Hence, $\delta^{13}\text{C}$ progressively decreases with depth, (recorded in deeper-dwelling planktic foraminifera and epibenthic foraminifera) (Mackensen and Schmiedl, 2019). Interpreting Site U1406 $\Delta\delta^{13}\text{C}_{\text{PF-BF}}$ for surface-water productivity changes might be potentially biased due to the deeper habitat than compared to surface-dwelling planktic foraminifera [e.g., Coxall and Spezzaferri (2018)]. However, despite the potential attenuation of the primary productivity signal from the surface to the habitat depth of *C. dissimilis*, increases in surface water primary productivity would nonetheless cause the $\delta^{13}\text{C}_{\text{PF}}$ signal to decrease relative to $\delta^{13}\text{C}_{\text{BF}}$ and therefore cause a higher gradient between surface and deep waters, i.e., a positive $\Delta\delta^{13}\text{C}_{\text{PF-BF}}$ signal. In addition to surface-water-induced productivity changes, introduction of nutrients through the inflow of nutrient-rich water masses at intermediate depths can also cause a steepening of $\Delta\delta^{13}\text{C}_{\text{PF-BF}}$ (Coxall et al., 2018).

7.2.6 Changing influences of water masses in the North Atlantic as a driver of productivity changes at Site U1406

A process to consider for causing a steepening of Site U1406 $\Delta\delta^{13}\text{C}_{\text{PF-BF}}$ is the intrusion of nutrient-rich Antarctic Intermediate Water (AAIW) (Talley et al., 2011), which would cause the Site U1406 $\delta^{13}\text{C}_{\text{PF}}$ signature to decrease [e.g., Bostock et al. (2004); Coxall et al. (2018)]. There is evidence that across the abrupt cooling events of Heinrich 1 (~18–14.6 ka) and the Younger Dryas (~12.8–11.5 ka), AAIW extended into the high latitudes (61°N) of the North Atlantic Ocean. AAIW was traced in rapid and distinct increases of Cd/Ca (up to ~0.08 $\mu\text{mol/mol}$) and $\delta^{13}\text{C}$ (up to ~1‰) values of benthic and intermediate depth-dwelling planktic foraminifera (Rickaby and Elderfield, 2005). The presence of AAIW in the high northern Atlantic is argued to be a coherent response to weakened NADW formation due to freshwater forcing in the high northern latitudes across Heinrich Stadial 1 and Younger Dryas

(Bard, 2000; Barker et al., 2009; Shakun et al., 2012; Bradtmiller et al., 2014). The resulting decrease in NADW salinity is counterbalanced by a salinity excess in AAIW relative to NADW. To that effect, it is argued that a southern-sourced circulation cell at intermediate depths was established in the northern Atlantic Ocean (Keeling and Stephens, 2001; Weaver, 2003; Saenko et al., 2003). However, it is unlikely that AAIW was present at Site U1406 across the study interval due to the following reasoning. Firstly, there is no imprint of a steep, distinct Heinrich Stadial 1-like increase in $\delta^{13}\text{C}$ of $\sim 1\text{‰}$ that would cause a steepening in the Site U1406 $\Delta\delta^{13}\text{C}_{\text{PF-BF}}$ (Figure 7.2-3) as has been argued by Rickaby and Elderfield (2005). Secondly, the argued freshwater forcing derived by large-scale deglaciation in the Northern Hemisphere through which a northward penetration of AAIW is facilitated, is an unlikely scenario for the Late Oligocene since there is no evidence of large-scale Northern Hemisphere glaciation in the high northern latitudes (Eldrett et al., 2007; DeConto et al., 2008; Tripathi et al., 2008; St John, 2008) (see Section 5.1.6 and 6.2.8). Further evidence against freshwater forcing across the study interval is given through SSTs at Site U1404 (Liu et al., 2018) that are warmer than modern SSTs (see Section 7.2.2; Figure 7.2-3) and do not indicate abrupt cooling.

Several studies have shown that surface water productivity of the mid-latitude North Atlantic depends on the position and the strength of the NAC, which in turn determines the position of the Arctic Front (Versteegh et al., 1996; Villanueva et al., 2001; Naafs et al., 2010). To that effect, in studies from the late Pliocene to late Pleistocene, the movement of the high productivity zone associated with the position of the Arctic Front was traced based on alkenone accumulation rates and coccolith carbonate abundance as an index for surface water productivity (Versteegh et al., 1996; Villanueva et al., 2001; Naafs et al., 2010). Productivity maxima during glacials were accordingly associated to a southward shift of the AF into the mid-latitudes of the North Atlantic, thereby introducing cold, nutrient-rich (high productivity) polar waters to lower latitudes replacing less productive, warmer surface waters of the STG. Additionally, cold, high-productivity polar waters of the SPG are associated with lower salinities and temperatures than southern-sourced warm waters with a higher salinity and temperatures of the NAC (Talley et al., 2011) (Figure 7.2-4). At present, Site U1406 is located at almost the exact position at which the NAC turns eastward (40°N , 50°W) (Talley et al., 2011; Norris et al., 2014b) (Figure 3.2-1). Along with evidence of a (proto)Gulf Stream, from which the NAC branches off, from as early as the late mid-Eocene (Wade et al., 2001), it is likely that Site U1406 has sensitively recorded the position of the NAC in the Late Oligocene. Therefore, dynamics in signals of $\Delta\delta^{13}\text{C}_{\text{PF-BF}}$, subT, and subS ($\delta^{18}\text{O}_{\text{ivf-sw}}$) and can be discussed in relation to the position of the NAC across the study interval.

As mentioned above, previous studies (Versteegh et al., 1996; Calvo et al., 2001; Villanueva et al., 2001; Naafs et al., 2010) observed a shift in the strength of the NAC and the position of the Arctic Front on glacial-interglacial timescales. In comparison, however, Site U1406 $\Delta\delta^{13}\text{C}_{\text{PF-BF}}$, subT, and subS data and Site U1404 SSTs show different dynamics (Figure 7.2-3A–C). The record of Site U1406 is generally characterized by a more erratic pattern and exhibits time intervals of different prevailing dynamics. Hence, as there is no consistent glacial-interglacial imprint that has been inferred for the Plio-Pleistocene (Versteegh et al., 1996; Calvo et al., 2001; Villanueva et al., 2001; Naafs et al., 2010), the variability

imprinted in Site U1406 data implies that the Arctic Front most likely responded to different dynamics than those of the Plio-Pleistocene.

Instances of subT cooling and decreasing subS with no coincident increases in $\Delta\delta^{13}\text{C}_{\text{PF-BF}}$ (low productivity) are displayed at ~ 25.71 , ~ 25.12 and ~ 24.83 Ma (Figure 7.2-3A–C). These instances challenge a southward shift of the Arctic Front and call for a different mechanism. A similar lack in correlation between surface-water productivity inferred from the ecologic preference of dinocyst assemblages, and surface-water temperature was observed in a study of Egger et al. (2018) from Site U1406 across the latest Oligocene to earliest Miocene. This led Egger et al. (2018) to conclude that cool surface waters were not induced by a southward shift of high-productivity waters associated with the AF but rather by a possible long-term intensification of the (proto-)Labrador Current. Given the same study site and the temporal proximity to the study interval herein, these findings lend support to events of subT cooling and decreasing subS with no parallel increase in productivity, i.e., low $\Delta\delta^{13}\text{C}_{\text{PF-BF}}$ at ~ 25.71 , ~ 25.12 , and ~ 24.83 Ma (Figure 7.2-3A–C) that could be explained by pulses of higher influences of the (proto-)Labrador Current.

7.2.7 *The response of the high North Atlantic to AIS dynamics during the Late Oligocene*

The dynamics in Site U1406 $\Delta\delta^{13}\text{C}_{\text{PF-BF}}$ and especially the pronounced variability in subT and subS point towards dynamics of the NAC associated with the positions of the SPG and STG. Yet, an important question remains what processes drove these dynamics in the Northern Atlantic across the study interval. As mentioned above, Plio-Pleistocene studies have correlated the position and strength of the NAC (Versteegh et al., 1996; Villanueva et al., 2001; Naafs et al., 2010) with the efficiency of northward transport of warm tropical waters, which depends on the strength of the AMOC [e.g., Schmitz Jr. and McCartney (1993); Häkkinen et al. (2011)].

For the unipolar glaciated world of the Late Oligocene (DeConto et al., 2008), the strength of the AMOC is intrinsically coupled to the glaciation state of the AIS, as evidenced in a modelling study of Goldner et al. (2014): AIS growth causes the high southern latitudes to cool. The interplay of cool SST's and strengthened surface winds around Antarctica lead to enhanced downwelling of cool, salty waters into the abyss, thereby contributing to enhanced deep-water formation. Strengthening of the AMOC implies an intensified oceanic heat advection from the southern into the northern hemisphere [e.g., Fratantoni et al. (2000)]. In times of enhanced AMOC, the production of NADW is compensated by increased advection of warm, low-latitude derived water masses within the northward flowing upper limb of the AMOC return-flow [e.g., Fratantoni et al. (2000)]. This way, the strength of the AMOC is coupled to the latitudinal extension of the STG. The STG itself plays an important role for the upper ocean circulation in the North Atlantic as it is a large reservoir of heat and salt (Schmitz Jr. and McCartney, 1993; Häkkinen et al., 2011) that is intrinsically recorded at the subsurface depths (Chang et al., 2008). Given a strong AMOC during periods of AIS growth (Goldner et al., 2014), northward transport of

warm and high-saline North Atlantic STG waters from subtropical Atlantic via the Gulf Stream and NAC to the higher northern latitudes would be facilitated [e.g., Barker et al. (2009)].

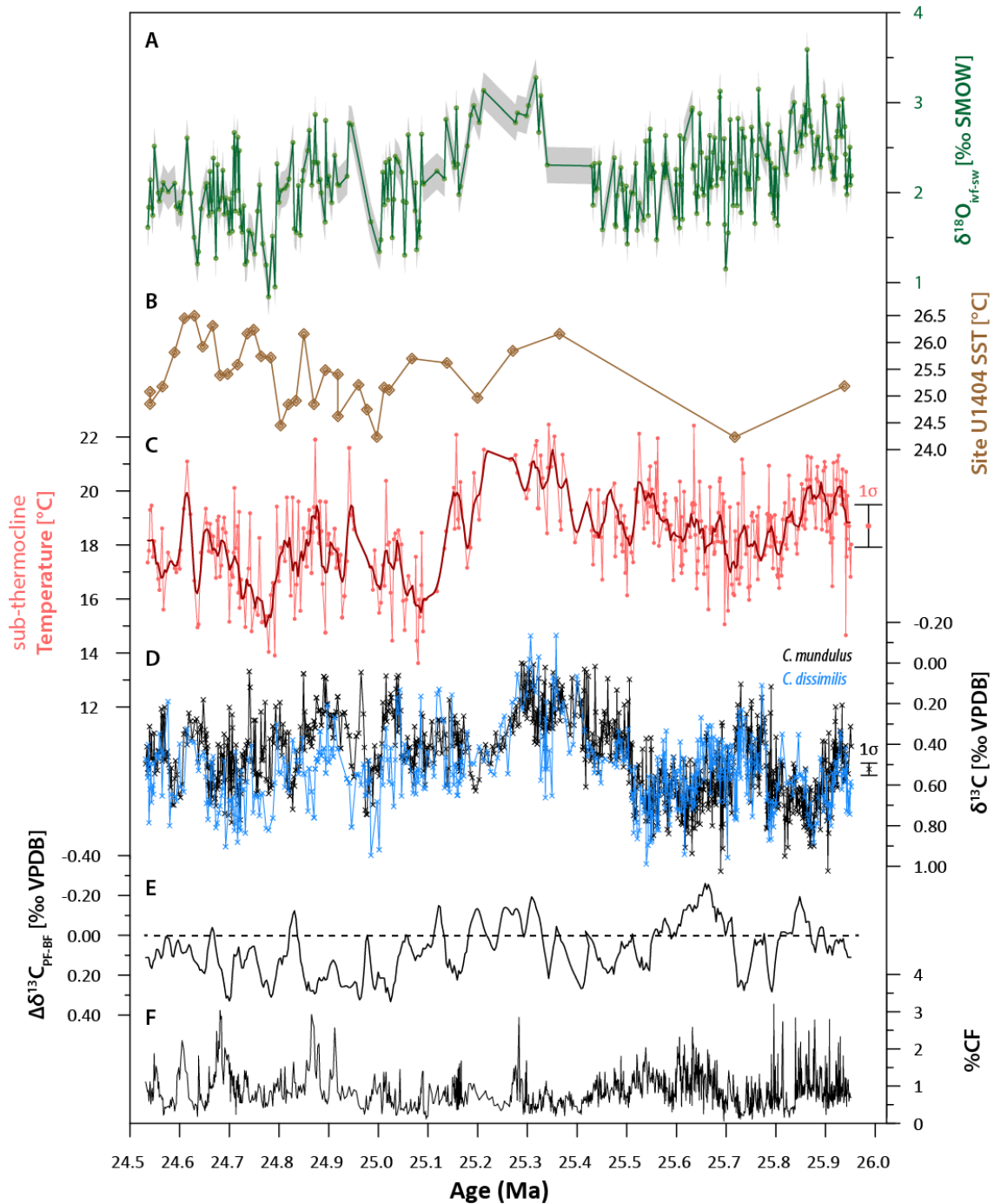


Figure 7.2-3: Evaluation of surface-water productivity at Site U1406. (A) Site U1406 $\delta^{18}\text{O}_{\text{ivf-sw}}$ (‰ SMOW) and $\pm 0.2\text{‰}$ uncertainty resulting from Monte Carlo Simulations (grey envelope; see Section 4.5.2). (B) SST reconstruction of Liu et al. (2018) from IODP Site U1404 (brown). (C) Site U1406 Mg/Ca-based subT data ($^{\circ}\text{C}$; red) with 5-pt smoother (dark red). (D) Site U1406 $\delta^{13}\text{C}_{\text{PF}}$ (*C. dissimilis*, blue) and $\delta^{13}\text{C}_{\text{BF}}$ (*C. mundulus*, black) (‰ VPDB). (E) Site U1406 gradient between $\delta^{13}\text{C}_{\text{PF}}$ and $\delta^{13}\text{C}_{\text{BF}}$ ($\Delta\delta^{13}\text{C}_{\text{PF-BF}}$) (‰ VPDB). (F) Site U1406 weight % of the coarse fraction (%CF).

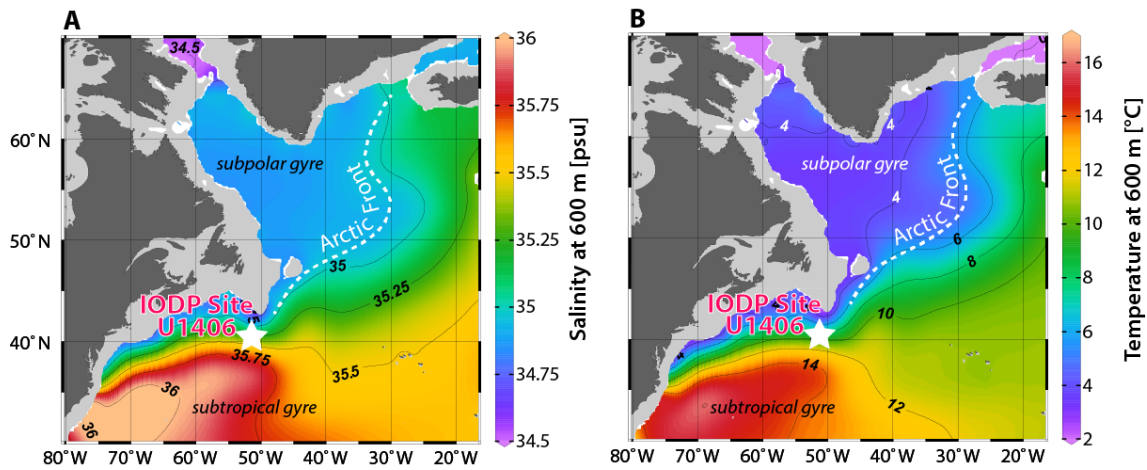


Figure 7.2-4: Modern subsurface (600 m water depth) salinity (A) and temperature distribution (B) of the North Atlantic after World Ocean Atlas (Boyer et al., 2013). Location of IODP Site U1406 in the northwestern Atlantic indicated by a white star. White dashed lines indicate the Arctic Front position that separates the subtropical and subpolar gyre (Talley, 2013). Map has been compiled using Ocean Data View (Schlitzer, 2019).

Whether the strength of the AMOC was responsible for the dynamics observed in the Site U1406 $\Delta\delta^{13}\text{C}_{\text{PF-BF}}$ and subT and subS data, can be constrained from the benthic Site U1406 $\delta^{18}\text{O}_{\text{sw}}$ record, which displays the dynamics of the AIS across the study interval (see Sections 5.1.5 and 6.2.7; Figure 7.2-5). Accordingly, a strong AMOC would be expected during times of glaciation, mirrored in high benthic Site U1406 $\delta^{18}\text{O}_{\text{sw}}$ values, in line with warm subTs and heavy subS values (higher salinities) at Site U1406 as an indicator for the northward transport of warm and high-saline North Atlantic STG waters [e.g., Chang et al. (2008)]. Evidently, a strong AMOC induced by southern high latitude cooling as a consequence to ice-sheet build-up on Antarctica (as evidenced in positive maxima in benthic Site U1406 $\delta^{18}\text{O}_{\text{sw}}$) stabilizes or even shifts the position of the STG northward in the North Atlantic. This allows warm, high saline waters of the North Atlantic STG to migrate further north to Site U1406 in the mid-latitude northwestern Atlantic. The AIS-induced strengthening of the AMOC (Figure 7.2-5D) is recorded in the distinct and parallel subsurface warming and increase in salinity (Figure 7.2-5B, C), as well as in the general agreement of SST data at Site U1404, reflecting this warming effect (albeit the low resolution and possible temporal offsets due to age model differences) (Figure 7.2-5A).

Conversely, a weakened AMOC caused by ice-sheet disintegration of the AIS (shown in light benthic $\delta^{18}\text{O}_{\text{sw}}$ values) (Figure 7.2-5D), goes along with subT cooling and freshening, displayed in decreasing values of Site U1406 subTs and subS, respectively. Melting of the AIS introduces an enhanced flux of freshwater into the surrounding ocean waters of the Antarctic continent, which may substantially weaken deep-water formation and hence cause an attenuation of the AMOC [e.g., Vellinga and Wood (2002)]. In accordance to a weakened AMOC, several proxy studies from the Holocene and Pleistocene at the northern boundary of the North Atlantic STG have pointed to a southward displacement of the STG during periods of cooling in the Northern Atlantic (Calvo et al., 2001; Repschläger et al., 2015; Schiebel et al., 2002; Schwab et al., 2012). Effectively, there is less northward transport of warm and high-saline North Atlantic STG waters via the NAC, which, adapting this mechanism to the study

interval, causes the cooling and freshening signals imprinted in the Site U1406 subTs and subS records (Figure 7.2-5B, C). Additional support for subT cooling is given by modelling outcome of Chang et al. (2008), who inferred cooling of subsurface water masses north of 20°N as a response of AMOC slowdown. Thus, AMOC attenuation along with a southward displacement of the North Atlantic STG in response to melting of the AIS appears to be a viable mechanism for cooling and freshening of the subsurface in the mid-latitude North Atlantic recorded in cooler subTs and lighter subS signals at Site U1406 (Figure 7.2-5).

Interestingly, the above-described dynamics between benthic Site U1406 $\delta^{18}\text{O}_{\text{sw}}$ and U1406 subT and subS records reveals a clear asymmetry. Increases in AIS volume in the Southern Hemisphere, displayed as positive maxima in benthic Site U1406 $\delta^{18}\text{O}_{\text{sw}}$, coincide with low U1406 subT and subS data as well as low SSTs from Site U1404 (Liu et al., 2018) in the North Atlantic (Figure 7.2-5A). This suggests a thermal decoupling of the Southern Hemisphere from the Northern Hemisphere. Such a distinct interhemispheric asymmetry in the surface and subsurface ocean of the Northern Hemisphere to glacial dynamics in the Southern Hemisphere points to considerable changes in the oceanic and atmospheric circulation affecting the interhemispheric heat balance.

An interhemispheric thermal asymmetric pattern is especially well documented from the late Pleistocene $\delta^{18}\text{O}$ record of Greenland and Antarctic ice cores (e.g., Barbante et al., 2006). In simplest terms, the data reflect warming in one hemisphere as the other cools down. This mechanism is referred to as the interhemispheric bi-polar see-saw (Broecker, 1998; Stocker, 1998; Stocker and Johnsen, 2003). Numerous studies of oceanic temperature reconstructions from the late Pleistocene reflect this asymmetric temperature pattern and most commonly describe the asymmetric thermal pattern in times of rapid climate perturbations in the North Atlantic, which profoundly affects the strength of the AMOC (i.e., Heinrich Events and Dansgaard/Oeschger cycles) (Bard, 2000; Barker et al., 2009; Shakun et al., 2012; Bradtmiller et al., 2014). These records show, that the North Atlantic reacted highly sensitive to perturbations of the AMOC intensity, displayed in distinct cooling events and ice growth in the high-latitude North Atlantic. Simultaneously, the Southern Hemisphere, especially the (sub)tropical South Atlantic, acted as a large heat reservoir and kept oceanic heat within the Southern Hemisphere reflected by increasing atmospheric and surface-ocean temperatures. The asymmetric thermal pattern imprinted in the U1406 proxy records (Figure 7.2-5) points to a similar bi-polar see-saw mechanism. However, and most intriguingly, the U1406 records suggests that during the Late Oligocene the Northern and Southern Hemispheric parts of the Atlantic Ocean changed their roles. From the Site U1406 proxy records, it is clearly visible that in times of substantial AIS built-up, the North Atlantic acted most likely as heat and salt reservoir. A similar hemispheric temperature asymmetry has been observed across the EOT by Liu et al. (2018), who observed warming in the Northern Hemisphere concomitant with the initiation of the AIS. Additional support for an Oligocene thermal asymmetry between the Northern and Southern Hemisphere is given by a study of de Vleeschouwer et al. (2017), who demonstrated that while the Oligocene AIS was in full glacial mode, the Northern Hemisphere responded with warming, possibly effected through strong deep-water circulation, hence an active AMOC.

These findings have important implications: (i) In light of ongoing discussions about Northern Hemisphere glaciations during the Late Oligocene, the evidenced heat and salt accumulation at Site U1406 in the North Atlantic during intervals of AIS built-up devalue significant Northern Hemisphere glaciation (Eldrett et al., 2007; Tripathi et al., 2008; St John, 2008). (ii) These see-saw like dynamics of the Late Oligocene clearly depict a strong Southern Hemisphere glaciation-driven dynamics of the AMOC – contrary to the Plio-Pleistocene when AMOC strength was regulated by dynamics of Northern Hemisphere ice-sheets (Bard, 2000; Barker et al., 2009; Shakun et al., 2012; Bradtmiller et al., 2014). (iii) AMOC perturbations were strong, albeit the unopilar glaciation of the Late Oligocene (DeConto et al., 2008).

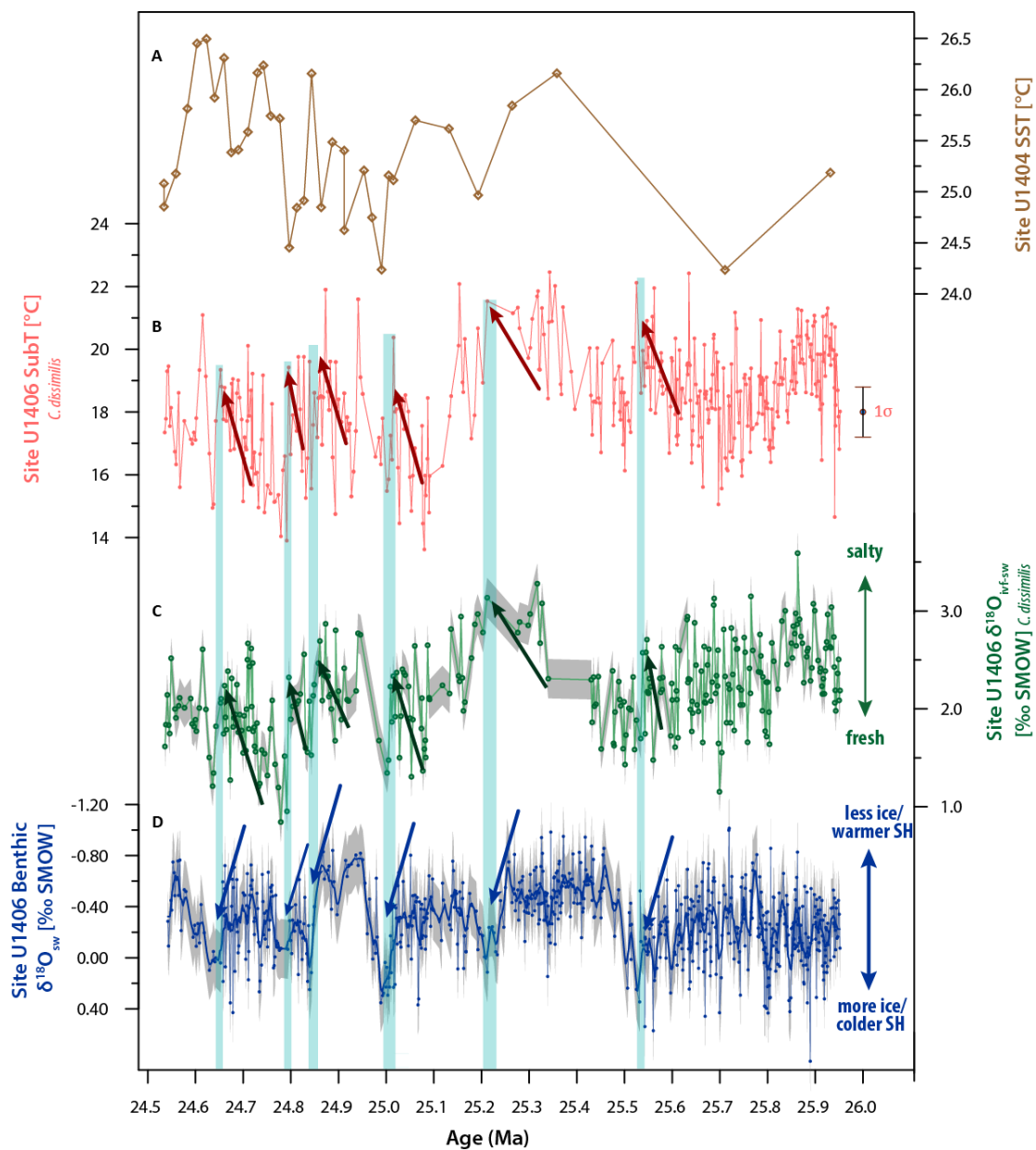


Figure 7.2-5: Response of the North Atlantic to Southern Hemisphere glaciation dynamics. (A) IODP Site U1404 SST ($^{\circ}\text{C}$) reconstructions (Liu et al., 2018). (B) Site U1406 Mg/Ca-based subT data ($^{\circ}\text{C}$; red). (C) Site U1406 $\delta^{18}\text{O}_{\text{ivf-sw}}$ (‰ SMOW, green) and $\pm 0.2\text{‰}$ uncertainty resulting from Monte Carlo Simulations (grey envelope; see Section 4.5.2). (D) Site U1406 benthic $\delta^{18}\text{O}_{\text{sw}}$ (‰ SMOW) and $\pm 0.23\text{‰}$ uncertainty resulting from Monte Carlo Simulations (grey envelope; see Section 4.5.2).

8 CONCLUSIONS AND OUTLOOK

In this thesis, deep-sea sediment cores from Site U1406, drilled within the framework of IODP Expedition 342, were investigated. New high-resolution proxy records of planktic and benthic foraminiferal stable isotope ($\delta^{13}\text{C}$, $\delta^{18}\text{O}$) and Mg/Ca ratios were generated over the time interval 25.95 to 24.53 Ma (Late Oligocene). This final chapter will summarize and evaluate the research results and discussions of **Chapters 5 to 7** to identify the main conclusions of the research presented in this thesis. Implications of this research are discussed in a societal context. An outlook on future work that can be undertaken to further the understanding of the Late Oligocene is also presented.

8.1 Conclusions

8.1.1 Late Oligocene AIS dynamics

The first objective was to investigate the dynamics of the AIS during the Late Oligocene based on the newly established high-resolution Site U1406 benthic foraminiferal $\delta^{18}\text{O}_{\text{BF}}$ and Mg/Ca records within the meaningful climatic framework of warmer-than modern climatic boundary conditions, which potentially displays a future climatic scenario.

The first study of this thesis (**Chapter 5**) focused on a short interval from 25.95 to 25.78 Ma. The benthic Site U1406 $\delta^{18}\text{O}_{\text{sw}}$ record revealed pronounced glacial-interglacial cyclicity on obliquity timescales. These dynamics challenge the dominant eccentricity forcing displayed in previously published $\delta^{18}\text{O}_{\text{BF}}$ records (Pälike et al., 2006a, 2006b; Liebrand et al., 2017; Levy et al., 2019), however, support the reliability of ice-proximal geologic records showing obliquity pacing in early and latest Oligocene strata (Naish et al., 2001; Galeotti et al., 2016; Fielding, 2018). Findings of this study further revealed that the synergetic effect of two obliquity-modulated mechanisms most likely controlled the waning and waxing of the AIS on obliquity timescales across the study interval (25.95 to 25.78 Ma): (i) The strength of the poleward moisture transport – that provides a potent moisture source for glacial ice-sheet built-up – and (ii) the seasonal distribution of insolation with direct control on the duration of summers and, hence, the rate of surface-melting of ice-sheets. The average glacial-interglacial amplitude variability of the benthic

Site U1406 $\delta^{18}\text{O}_{\text{sw}}$ record of 0.5‰ was turned into an ice-volume estimate that requires the waning and waxing of $19 \times 10^6 \text{ km}^3$ of ice within half an obliquity cycle.

In **Chapter 6**, high-resolution benthic foraminiferal $\delta^{18}\text{O}_{\text{BF}}$ and Mg/Ca measurements were combined and investigated to further explore the existing controversy in regard to variability in AIS volumes and pacing theories during the Late Oligocene. The concept of $\delta^{18}\text{O}_{\text{BF}}$ -based glaciation events (Oi-events) was re-evaluated with the conclusion that a simple allocation of marked increases in $\delta^{18}\text{O}_{\text{BF}}$ ($\geq 0.5\text{‰}$) to ice-sheet built-up is inadequate and not reliable if the temperature component of the $\delta^{18}\text{O}_{\text{BF}}$ signal is not considered. To that effect, the application of the established concept of coupled $\delta^{18}\text{O}_{\text{BF}}$ -Mg/Ca measurements was reinforced and shown to provide powerful means to interpret the $\delta^{18}\text{O}_{\text{BF}}$ signal in terms of changing dynamics of the Antarctic cryosphere. It was found that the Late Oligocene AIS varied between two major states of glaciation across the study interval: (i) near modern to slightly larger than modern global ice-volumes and (ii) less than half the modern to slightly smaller than modern global ice-volumes. These unprecedented Site U1406 $\delta^{18}\text{O}_{\text{sw}}$ -based AIS dynamics clearly contradict (i) the long-established view of the Late Oligocene as a general period of pronounced warming (Zachos et al., 2001a; Pekar et al., 2006; Lee and Jo, 2019), (ii) previously inferred stable AIS conditions by Hauptvogel et al. (2017), and (iii) previously identified (nearly) ice-free episodes across the study interval of Liebrand et al. (2017). Amplitude modulations for $\delta^{18}\text{O}_{\text{sw}}$ to both the eccentricity ($\sim 100\text{-kyr}$) and obliquity ($\sim 40\text{ kyr}$) periodicities unveiled unprecedented sensitivities of the Late Oligocene AIS to orbital forcing: It was shown that (i) the AIS was generally sensitive to obliquity forcing during an interval previously perceived as eccentricity dominated; (ii) the sensitivity of the AIS to obliquity forcing is invariant of its size and does not require a connection to the ocean for sea-ice feedbacks, contrary to recent findings of Levy et al. (2019); and (iii) dominant eccentricity forcing onto the AIS is limited to intervals of reduced AIS volume across the interval from 25.95–24.53 Ma. Moreover, amplitude modulations for $\delta^{18}\text{O}_{\text{sw}}$ infer that the tilt of the Earth's spin axis modulated the degree of ice loss during Late Oligocene-like termination events – strikingly reminiscent to Plio-Pleistocene glacial terminations that were similarly forced by very large angles of the Earth's tilt (Berger, 1988; Huybers and Wunsch, 2005). The magnitude in AIS volume change shown in **Chapters 5** and **6** provides new insights into the dynamics of ice-volume change under warmer-than modern climatic boundary conditions during the Late Oligocene. It delivers new context in which to view the dynamics of the AIS in light of future climate change.

8.1.2 The response of the North Atlantic to AIS dynamics during the Late Oligocene

The second objective of this thesis was to examine the response of the Northern Atlantic Ocean in light of glacial dynamics of the AIS during the Late Oligocene (inferred from the benthic Site U1406 $\delta^{18}\text{O}_{\text{sw}}$ signal shown in **Chapters 5** and **6**). Changes in subsurface-water characteristics at Site U1406 in the North Atlantic Ocean were investigated to infer dynamics in the strength and position of the NAC. These

NAC dynamics were discussed regarding consequences for the Late Oligocene climatological and oceanographical configuration of the North Atlantic.

High-resolution planktic foraminiferal $\delta^{13}\text{C}$, $\delta^{18}\text{O}$, and Mg/Ca records from IODP Site U1406 presented in **Chapter 7** are the very first data of their kind for the higher northern latitudes for the studied interval of 25.95 to 24.53 Ma. The new data revealed that productivity levels at Site U1406 primarily changed in line with subT and subS as a function of the relative influence of high (low) productive waters of the SPG (STG). A stronger influence of the (proto-)Labrador Current at Site U1406 was concluded for periods of subT cooling and subS freshening with no concomitant productivity increase. Ultimately, the Site U1406 proxy records unambiguously showed that the dominant mechanism controlling the dynamics in the high-latitude North Atlantic is the strength of the AMOC as a function of the glaciation state of the AIS (Goldner et al., 2014). Also, the data infer a strong AMOC in parallel with marked subsurface warming and an increase in salinity at Site U1406 in the high-latitude North Atlantic. The warming and salinity increases at Site U1406 are interpreted to be related to an increased northward surface water advection of equatorial-Atlantic-derived STG waters, facilitated by an amplified AMOC. These dynamics in the high Northern Atlantic, especially the marked warming intervals, strongly support the unlikelihood of a precursory bipolar glaciation across the Late Oligocene, that is a matter of ongoing debate (Eldrett et al., 2007; DeConto et al., 2008; Tripathi et al., 2008; St John, 2008; Edgar et al., 2013; Spray et al., 2019).

Simultaneously, these dynamics inferred an interhemispheric thermal asymmetry – a phenomenon that has been well studied across the Pleistocene and is referred to as the bipolar see-saw (Broecker, 1998; Stocker, 1998; Stocker and Johnsen, 2003). However, as evidenced in **Chapter 7**, the Late Oligocene bipolar see-saw is driven by ice dynamics of the Southern Hemisphere. These results have important implications: (i) Phases of heat and salt accumulation in times of a strong AMOC invalidates the concept of a precursory bipolar glaciation across the study interval; (ii) compared to the bipolar glaciated world of the Plio-Pleistocene [e.g., Barker et al. (2009)], AMOC perturbations during the unipolar glaciated world of the Late Oligocene were of similar severe character; (iii) in light of future climate change with projected ice-volume melting pulses of the AIS, the dynamics shown in **Chapter 7** point towards the possibility of severe disruptions of the AMOC with general consequences for the northward heat transport and, thus, for the climate of the circum-North Atlantic region.

8.2 Societal significance of Late Oligocene AIS dynamics

The greater availability of deep-sea sediment cores recovered within the framework of DSDP, ODP and IODP drilling campaigns have increased the number of climate archives that contributed a wealth of information to better understand Cenozoic climate and climate change. Specifically, high-resolution paleoclimatic and paleoceanographic proxy records have inarguably presented a promising avenue towards obtaining deeper insight into mechanisms and processes driving large-scale climate variability of the geologic past. The research presented in this thesis is an additional testimony to the potential of

deep-sea drilling and its importance in deepening the understanding of past climate variability that provide a valuable basis to generate more reliable predictions for future climate change.

As the world warms due to rising greenhouse gas concentrations, the Earth system moves toward climate states without Northern Hemisphere ice-sheets (Pachauri et al., 2014). The unipolar glaciated world of the Late Oligocene presents a merit option in search of past Earth system states that serve as a suitable analog to the warming world of the coming decade to century. The herein presented Late Oligocene AIS dynamics under warmer-than-modern boundary conditions imply substantial waning and waxing on orbital timescales and infer that considerable sea-level rise and land-ice loss on Antarctica is to be expected in the future. Climate simulations also predict the AMOC to slow by the end of this century (Pachauri et al., 2014). Significant ocean circulation changes in the Late Oligocene North Atlantic in response to AIS-modulated changes in the AMOC are presented. This research outcome illustrates a picture in which substantial circulation changes in the North Atlantic are to be expected if the future faces substantial melting of the AIS. Given the herein presented results, the Late Oligocene shows great potential to answer pressing questions like (i) What is the role of SH ice-sheet dynamics in global climate dynamics in light of the ongoing anthropogenic forcing? (ii) What boundary conditions modulate severe AIS dynamics? (iii) What are maximum rates of sea-level change? And how do these dynamics precisely relate to present-day rates of climate change? These are only some of many more aspects that merit attention for further studying Late Oligocene climate dynamics.

8.3 Future perspectives

To further improve the understanding of Late Oligocene AIS dynamics, the following aspects present fruitful opportunities to explore in the future:

- The generation of similar high-fidelity, high-resolution coupled $\delta^{18}\text{O}$ -Mg/Ca measurements on existing deep-sea sediment records of Late Oligocene age akin to those from Site U1406 could potentially validate and reproduce the herein observed AIS dynamics. Such an approach, however, requires (i) a steady and continuous sedimentation rate, (ii) abundant occurrence of well-preserved benthic foraminifera, and (iii) a reliable magnetostratigraphy, or preferably an orbitally-tuned age model (that would allow for a global synthesis of the records).
- Proxy-based [e.g., Beerling and Royer (2011); Zhang et al. (2013); Anagnostou et al. (2016)] and modelling-based studies [e.g., DeConto et al. (2008)] have evidenced the influence and power of $p\text{CO}_2$ forcing onto ice-volume dynamics across the EOT. This raises the question whether and to what degree the observed AIS dynamics across the study interval shown in this thesis are driven by changes in $p\text{CO}_2$ concentrations. To further explore and fully understand the role of $p\text{CO}_2$ forcing on Late Oligocene AIS dynamics, more and higher resolution $p\text{CO}_2$ reconstructions are needed.
- The herein observed ice-volume fluctuations across the study interval infer substantial fluctuations of the Antarctic ice-cover that would have caused a change in the locus of glacial

erosion and, thus, the source area of weathering products that are eroded from the Antarctic continent and introduced into the surrounding ocean. Such fluctuations could be constrained from sediments in the source area of the AIS through the application of Nd isotopes as a weathering proxy for source-area changes for Antarctic detrital discharge.

Site U1406 proxy records illustrating circulation dynamics in the high Northern Atlantic presented herein are the first of their kind for the interval 25.95 to 24.53 Ma. This data presents a first attempt in constraining North Atlantic Ocean dynamics during the Late Oligocene. The following aspects present fruitful opportunities to explore this subject in the future:

- To further constrain the variability of primary productivity driven by the meridional position of the Arctic Front across the study interval, more detailed work on productivity proxies is needed. In that regard, the existing U1406 data set could be complemented by analyses of surface-dwelling planktic foraminifera to get a more direct signal of the surface ocean. Likely, the coccolith carbonate and alkenone abundances rates have proven to be a good indicator to constrain changes in surface water productivity of the North Atlantic associated with shifts in the position of the Arctic Front in studies of the Plio-Pleistocene (Versteegh et al., 1996; Villanueva et al., 2001; Naafs et al., 2010) and could be analyzed to that effect in sediment records of Site U1406.
- Since the position of the Arctic Front is intrinsically coupled to the strength of the NAC and Gulf Stream, complementary analysis of surface-water properties from locations north, east or south of Site U1406 in the North Atlantic located within the flow path of the NAC and Gulf Stream during the Late Oligocene could be helpful to address this issue. However, given the sparseness of high-resolution Late Oligocene deep-sea sediment records in the North Atlantic, more drilling efforts might be needed to complement proxy records from IODP Site U1406.
- In light of the inferred interhemispheric thermal asymmetry there is a need for high-resolution SST data from the Southern Hemisphere to validate the herein observed dynamics. To that effect, sediment records of ODP Site 1264, located in the South Atlantic (Figure 2.1-2), as well as newly recovered high-resolution sediment records of IODP Site U1553 [South Pacific Ocean; Thomas et al. (2020)] could provide potential to deepen the understanding of the Southern Hemisphere response to dynamics of the AIS during the Late Oligocene.

9 REFERENCES

- Abe-Ouchi, A., Saito, F., Kawamura, K., Raymo, M.E., Okuno, J., Takahashi, K., and Blatter, H., 2013, Insolation-driven 100,000-year glacial cycles and hysteresis of ice-sheet volume: *Nature*, v. 500, p. 190–193, doi:10.1038/nature12374.
- Abelson, M., and Erez, J., 2017, The onset of modern-like Atlantic meridional overturning circulation at the Eocene-Oligocene transition: Evidence, causes, and possible implications for global cooling: *Geochemistry, Geophysics, Geosystems*, v. 18, p. 2177–2199, doi:10.1002/2017GC006826.
- Adkins, J.F., McIntyre, K., and Schrag, D.P., 2002, The salinity, temperature, and $\delta^{18}\text{O}$ of the glacial deep ocean: *Science*, v. 298, p. 1769–1773, doi:10.1126/science.1076252.
- de Almeida, F.K., de Mello, R.M., Costa, K.B., and Toledo, F.A.L., 2015, The response of deep-water benthic foraminiferal assemblages to changes in paleoproductivity during the Pleistocene (last 769.2 kyr), western South Atlantic Ocean: *Palaeogeography, Palaeoclimatology, Palaeoecology*, v. 440, p. 201–212, doi: 10.1016/j.palaeo.2015.09.005.
- Altenbach, A. V., 1992, Short term processes and patterns in the foraminiferal response to organic flux rates: *Marine Micropaleontology*, v. 19, p. 119–129, doi:10.1016/0377-8398(92)90024-E.
- Anagnostou, E., John, E.H., Edgar, K.M., Foster, G.L., Ridgwell, A., Inglis, G.N., Pancost, R.D., Lunt, D.J., and Pearson, P.N., 2016, Changing atmospheric CO_2 concentration was the primary driver of early Cenozoic climate: *Nature*, v. 533, p. 380–384, doi:10.1038/nature17423.
- Anand, P., Elderfield, H., and Conte, M.H., 2003, Calibration of Mg/Ca thermometry in planktonic foraminifera from a sediment trap time series: *Paleoceanography*, v. 18, 1050, doi:10.1029/2002PA000846.
- Arbuszewski, J.A., DeMenocal, P.B., Kaplan, A., and Farmer, E.C., 2010, On the fidelity of shell-derived $\delta^{18}\text{O}$ seawater estimates: *Earth and Planetary Science Letters*, v. 300, p. 185–196, doi:10.1016/j.epsl.2010.10.035.
- Arz, H.W., Pätzold, J., and Wefer, G., 1999, The deglacial history of the western tropical Atlantic as inferred from high resolution stable isotope records off northeastern Brazil: *Earth and Planetary Science Letters*, v. 167, p. 105–117, doi:10.1016/S0012-821X(99)00025-4.
- Bahr, A., Nürnberg, D., Schönfeld, J., and Schönberg, D.G., 2011, Hydrological variability in Florida Straits during Marine Isotope Stage 5 cold events: *Paleoceanography*, v. 26, p. 1–14, doi:10.1029/2010PA002015.
- Bamber, J.L. et al., 2013, A new bed elevation dataset for Greenland: *The Cryosphere*, v. 7, p. 499–510, doi:10.5194/tc-7-499-2013.
- Barbante, C. et al., 2006, One-to-one coupling of glacial climate variability in Greenland and Antarctica: *Nature*, v. 444, p. 195–198, doi:10.1038/nature05301.
- Bard, E., 2000, Hydrological Impact of Heinrich Events in the Subtropical Northeast Atlantic: *Science*, v. 289, p. 1321–1324, doi:10.1126/science.289.5483.1321.

- Barker, S., Cacho, I., Benway, H., and Tachikawa, K., 2005, Planktonic foraminiferal Mg/Ca as a proxy for past oceanic temperatures: A methodological overview and data compilation for the Last Glacial Maximum: *Quaternary Science Reviews*, v. 24, p. 821–834, doi:10.1016/j.quascirev.2004.07.016.
- Barker, S., Diz, P., Vautravers, M.J., Pike, J., Knorr, G., Hall, I.R., and Broecker, W.S., 2009, Interhemispheric Atlantic seesaw response during the last deglaciation: *Nature*, v. 457, p. 1097–1102, doi:10.1038/nature07770.
- Barker, S., Greaves, M., and Elderfield, H., 2003, A study of cleaning procedures used for foraminiferal Mg/Ca paleothermometry: *Geochemistry, Geophysics, Geosystems*, v. 4, p. 8407, doi:10.1029/2003GC000559.
- Barrett, P.J., 1986, Antarctic Cenozoic history from the MSSTS-1 drillhole, McMurdo Sound (P. J. Barrett, Ed.): DSIR Science Information Publishing Centre, v. 237, 173 p.
- Barrett, P.J., 1989, Antarctic Cenozoic history from the MSSTS-1 drillhole McMurdo Sound: DSIR Bulletin, 254 p.
- Barrientos, N., Lear, C.H., Jakobsson, M., Stranne, C., O'Regan, M., Cronin, T.M., Gukov, A.Y., and Coxall, H.K., 2018, Arctic Ocean benthic foraminifera Mg/Ca ratios and global Mg/Ca-temperature calibrations: New constraints at low temperatures: *Geochimica et Cosmochimica Acta*, v. 236, p. 240–259, doi:10.1016/j.gca.2018.02.036.
- Barron, J., and Larsen, B., 1989, Proceedings of the Ocean Drilling Program, 119 Initial Reports (J. Barron & B. Larsen, Eds.): Ocean Drilling Program, Proceedings of the Ocean Drilling Program, v. 119, 942 p., doi:10.2973/odp.proc.ir.119.1989.
- Bé, A.W.H., 1960, Ecology of Recent Planktonic Foraminifera: Part 2: Bathymetric and Seasonal Distributions in the Sargasso Sea off Bermuda: *Micropaleontology*, v. 6, p. 373–392, doi:10.2307/1484218.
- Bé, A.W.H., and Tolderlund, D.S., 1971, Distribution and ecology of living planktonic foraminifera in surface waters of the Atlantic and Indian Oceans, in Funnell, B.M. and Riedel, W. eds., *Micropaleontology of the Oceans*, Cambridge University Press, London, p. 105–150.
- Beerling, D.J., and Royer, D.L., 2011, Convergent Cenozoic CO₂ history: *Nature Geoscience*, v. 4, p. 418–420, doi:10.1038/ngeo1186.
- Belanger, P.E., Curry, W.B., and Matthews, R.K., 1981, Core-top evaluation of benthic foraminiferal isotopic ratios for paleo-oceanographic interpretations: *Palaeogeography, Palaeoclimatology, Palaeoecology*, v. 33, p. 205–220, doi:10.1016/0031-0182(81)90039-0.
- Bemis, B.E., Spero, H.J., Bijma, J., and Lea, D.W., 1998, Reevaluation of the oxygen isotopic composition of planktonic foraminifera: Experimental results and revised paleotemperature equations: *Paleoceanography*, v. 13, p. 150–160, doi:10.1029/98PA00070.
- Bender, M.L., Lorenz, R.B., and Williams, D.F., 1975, Sodium, Magnesium and Strontium in the Tests of Planktonic Foraminifera: *Micropaleontology*, v. 21, p. 448–459, doi:10.2307/1485293.
- Berger, A., 1988, Milankovitch Theory and Climate: *Reviews of Geophysics*, v. 26, p. 624–657, doi:10.1029/RG026i004p00624.
- Berger, W.H., Bonneau, M.C., and Parker, F.L., 1982, Foraminifera on the deep-sea floor - Lysocline and dissolution rate: *Oceanologica Acta*, v. 5, p. 249–258, doi:10.1016/0198-0254(82)90178-9.
- Berstad, I.M., Sejrup, H.P., Klitgaard-Kristensen, D., and Haflidason, H., 2003, Variability in temperature and geometry of the Norwegian Current over the past 600 yr; stable isotope and grain size evidence from the Norwegian margin: *Journal of Quaternary Science*, v. 18, p. 591–602, doi:10.1002/jqs.790.
- Bian, N., and Martin, P.A., 2010, Investigating the fidelity of Mg/Ca and other elemental data from reductively cleaned planktonic foraminifera: *Paleoceanography*, v. 25, PA2215, doi:10.1029/2009PA001796.
- Bickert, T., Haug, G.H., and Tiedemann, R., 2004, Late Neogene benthic stable isotope record of Ocean Drilling Program Site 999: Implications for Caribbean paleoceanography, organic carbon burial, and the Messinian Salinity Crisis: *Paleoceanography*, v. 19, PA1023, doi:10.1029/2002PA000799.

- Billups, K., Pälike, H., Channell, J.E.T., Zachos, J.C., and Shackleton, N.J., 2004, Astronomic calibration of the late Oligocene through early Miocene geomagnetic polarity time scale: *Earth and Planetary Science Letters*, v. 224, p. 33–44, doi:10.1016/j.epsl.2004.05.004.
- Billups, K., and Schrag, D.P., 2002, Paleotemperatures and ice volume of the past 27 Myr revisited with paired Mg/Ca and $^{18}\text{O}/^{16}\text{O}$ measurements on benthic foraminifera: *Paleoceanography*, v. 17, p. 3–11, doi:10.1029/2000PA000567.
- Binczewska, A., Polovodova Asteman, I., and Farmer, E.J., 2014, Foraminifers (Benthic), in Harff, J., Meschede, M., Petersen, S., and Thiede, J. eds., *Encyclopedia of Marine Geosciences*, Dordrecht, Springer Netherlands, p. 1–8, doi:10.1007/978-94-007-6644-0_60-1.
- Biolzi, M., 1983, Stable isotopic study of Oligocene-Miocene sediments from DSDP Site 354, Equatorial Atlantic: *Marine Micropaleontology*, v. 8, p. 121–139, doi:10.1016/0377-8398(83)90008-7.
- Bohaty, S.M.M., Zachos, J.C., and Delaney, M.L.L., 2012, Foraminiferal Mg/Ca evidence for Southern Ocean cooling across the Eocene–Oligocene transition: *Earth and Planetary Science Letters*, v. 317–318, p. 251–261, doi:10.1016/j.epsl.2011.11.037.
- Bohaty, S.M., Zachos, J.C., Florindo, F., and Delaney, M.L., 2009, Coupled greenhouse warming and deep-sea acidification in the middle Eocene: *Paleoceanography*, v. 24, p. 1–16, doi:10.1029/2008PA001676.
- Borrelli, C., Cramer, B.S., and Katz, M.E., 2014, Bipolar Atlantic deepwater circulation in the middle-late Eocene: Effects of Southern Ocean gateway openings: *Paleoceanography*, v. 29, p. 308–327, doi:10.1002/2012PA002444.
- Bostock, H.C., Opdyke, B.N., Gagan, M.K., and Fifield, L.K., 2004, Carbon isotope evidence for changes in Antarctic Intermediate Water circulation and ocean ventilation in the southwest Pacific during the last deglaciation: *Paleoceanography*, v. 19, p. 1–15, doi:10.1029/2004PA001047.
- BouDagher-Fadel, M.K., 2015, *Biostratigraphic and Geological Significance of Planktonic Foraminifera*: UCL Press, <http://www.jstor.org/stable/j.ctt1g69xwk>.
- Boulila, S., Galbrun, B., Miller, K.G., Pekar, S.F., Browning, J. V., Laskar, J., and Wright, J.D., 2011, On the origin of Cenozoic and Mesozoic “third-order” eustatic sequences: *Earth-Science Reviews*, v. 109, p. 94–112, doi:10.1016/j.earscirev.2011.09.003.
- Boyer, T.P., Antonov, J.I., Baranova, O.K., Garcia, H.E., Johnson, D.R., Mishonov, A. V, O’Brien, T.D., Seidov, D., Smolyar, I., and Zweng, M.M., 2013, World ocean database 2013, in S. Levitus, Ed., U.S.G. ed., NOAA Atlas NESDIS, p. 209.
- Boyle, P.R., Romans, B.W., Tucholke, B.E., Norris, R.D., Swift, S.A., and Sexton, P.F., 2017, Cenozoic North Atlantic deep circulation history recorded in contourite drifts, offshore Newfoundland, Canada: *Marine Geology*, v. 385, p. 185–203, doi:10.1016/j.margeo.2016.12.014.
- Bradshaw, J.S., 1959, Ecology of living planktonic foraminifera in the north and equatorial Pacific Ocean: *Contribution from the Cushman Foundation for Foraminiferal Research*, v. 10.
- Bradt Miller, L.I., McManus, J.F., and Robinson, L.F., 2014, $^{231}\text{Pa}/^{230}\text{Th}$ evidence for a weakened but persistent Atlantic meridional overturning circulation during Heinrich Stadial 1: *Nature Communications*, v. 5, p. 5817, doi:10.1038/ncomms6817.
- Broecker, W.S. et al., 1998, How much deep water is formed in the Southern Ocean? *Journal of Geophysical Research: Oceans*, v. 103, p. 15833–15843, doi:10.1029/98JC00248.
- Broecker, W.S., 1998, Paleocan circulation during the Last Deglaciation: A bipolar seesaw? *Paleoceanography*, v. 13, p. 119–121, doi:10.1029/97PA03707.
- Broecker, W.S., 1991, The Great Ocean Conveyor: *Oceanography*, v. 4, p. 79–89, <http://www.jstor.org/stable/43924572>.
- Broecker, W.S., and Peng, T.-H., 1982, Tracers in the sea: *Lamont-Doherty Geological Observatory, Palisades, NY*, 690 p., doi:10.1017/S0033822200005221.
- Broecker, W., and Yu, J., 2011, What do we know about the evolution of Mg to Ca ratios in seawater? *Paleoceanography*, v. 26, PA3203, doi:10.1029/2011PA002120.
- Brown, R.E., Anderson, L.D., Thomas, E., and Zachos, J.C., 2011, A core-top calibration of B/Ca in the benthic foraminifers *Nuttallides umbonifera* and *Oridorsalis umbonatus*: A proxy for Cenozoic bottom water carbonate saturation: *Earth and Planetary Science Letters*, v. 310, p. 360–368, doi:10.1016/j.epsl.2011.08.023.

- Brown, S.J., and Elderfield, H., 1996, Variations in Mg/Ca and Sr/Ca ratios of planktonic foraminifera caused by postdepositional dissolution: Evidence of shallow Mg-dependent dissolution: *Paleoceanography*, v. 11, p. 543–551, doi:10.1029/96PA01491.
- Bryan, S.P., and Marchitto, T.M., 2008, Mg/Ca–temperature proxy in benthic foraminifera: New calibrations from the Florida Straits and a hypothesis regarding Mg/Li: *Paleoceanography*, v. 23, PA2220, doi:10.1029/2007PA001553.
- Calvo, E., Villanueva, J., Grimalt, J.O., Boelaert, A., and Labeyrie, L., 2001, New insights into the glacial latitudinal temperature gradients in the North Atlantic. Results from U^{K}_{37} sea surface temperatures and terrigenous inputs: *Earth and Planetary Science Letters*, v. 188, p. 509–519, doi:10.1016/S0012-821X(01)00316-8.
- Campbell, K.E., Prothero, D.R., Romero-Pittman, L., Hertel, F., and Rivera, N., 2010, Amazonian magnetostratigraphy: Dating the first pulse of the Great American Faunal Interchange: *Journal of South American Earth Sciences*, v. 29, p. 619–626, doi: 10.1016/j.jsames.2009.11.007.
- Campos, M.C., Chiessi, C.M., Voigt, I., Piola, A.R., Kuhnert, H., and Mulitza, S., 2017, $\delta^{13}C$ decreases in the upper western South Atlantic during Heinrich Stadials 3 and 2: *Climate of the Past*, v. 13, doi:10.5194/cp-13-345-2017.
- Chang, P., Zhang, R., Hazeleger, W., Wen, C., Wan, X., Ji, L., Haarsma, R.J., Breugem, W.-P., and Seidel, H., 2008, Oceanic link between abrupt changes in the North Atlantic Ocean and the African monsoon: *Nature Geoscience*, v. 1, p. 444–448, doi:10.1038/ngeo218.
- Cléroux, C., Cortijo, E., Anand, P., Labeyrie, L., Bassinot, F., Caillon, N., and Duplessy, J.C., 2008, Mg/Ca and Sr/Ca ratios in planktonic foraminifera: Proxies for upper water column temperature reconstruction: *Paleoceanography*, v. 23, PA3214, doi:10.1029/2007PA001505.
- Cléroux, C., Demenocal, P., Arbuszewski, J.A., and Linsley, B., 2013, Reconstructing the upper water column thermal structure in the Atlantic Ocean: *Paleoceanography*, v. 28, p. 503–516, doi:10.1002/palo.20050.
- Coggon, R.M., Teagle, D.A.H., Smith-Duque, C.E., Alt, J.C., and Cooper, M.J., 2010, Reconstructing Past Seawater Mg/Ca and Sr/Ca from Mid-Ocean Ridge Flank Calcium Carbonate Veins: *Science*, v. 327, p. 1114–1117, doi:10.1126/science.1182252.
- Corliss, B.H., 1985, Microhabitats of benthic foraminifera within deep-sea sediments: *Nature*, v. 314, p. 435–438.
- Coxall, H.K. et al., 2018, Export of nutrient rich Northern Component Water preceded early Oligocene Antarctic glaciation: *Nature Geoscience*, v. 11, p. 190–196, doi:10.1038/s41561-018-0069-9.
- Coxall, H.K., and Spezzaferri, S., 2018, Taxonomy, biostratigraphy, and phylogeny of Oligocene *Catapsydrax*, *Globorotaloides* and *Protentelloides*, in: Wade, B. et al. (Eds.), *Atlas of Oligocene Planktonic Foraminifera*. Cushman Foundation Special Publication, No. 46, p. 79–124.
- Coxall, H.K., and Wilson, P.A., 2011, Early Oligocene glaciation and productivity in the eastern equatorial Pacific: Insights into global carbon cycling: *Paleoceanography*, v. 26, p. PA2221, doi:10.1029/2010PA002021.
- Craig, H., Gordon, L.I., 1965, Deuterium and oxygen 18 variations in the ocean and the marine atmosphere, in: Pisa, Consiglio nazionale delle ricerche, Laboratorio de geologia nucleare.
- Curry, W.B., Duplessy, J.C., Labeyrie, L.D., and Shackleton, N.J., 1988, Changes in the distribution of $\delta^{13}C$ of deep water ΣCO_2 between the Last Glaciation and the Holocene: *Paleoceanography*, v. 3, p. 317–341, doi:10.1029/PA003i003p00317.
- DeConto, R.M., and Pollard, D., 2003, Rapid Cenozoic glaciation of Antarctica induced by declining atmospheric CO_2 : *Nature*, v. 421, p. 245–249, doi:10.1038/nature01290.
- DeConto, R.M., Pollard, D., Wilson, P.A., Pälike, H., Lear, C.H., and Pagani, M., 2008, Thresholds for Cenozoic bipolar glaciation: *Nature*, v. 455, p. 652–657, doi:10.1038/nature07337.
- Demico, R. V., Lowenstein, T.K., Hardie, L.A., and Spencer, R.J., 2005, Model of seawater composition for the Phanerozoic: *Geology*, v. 33, p. 877–880, doi:10.1130/G21945.1.
- Dercourt, J., Gaetani, M., Vrielynck, B., Barrier, E., Biju-Duval, B., Brunet, M.F., Cadet, J.P., Crasquin, S., and Sandulescu, M., 2000, Atlas peri-Tethys palaeogeographical maps. Late Cenomanian (94.7–93.5), p. 129–136, Paris.

- Dickson, J.A.D., 2002, Fossil Echinoderms As Monitor of the Mg/Ca Ratio of Phanerozoic Oceans: *Science*, v. 298, p. 1222–1224, doi:10.1126/science.1075882.
- Diester-Haass, L., Billups, K., and Emeis, K.C., 2006, Late Miocene carbon isotope records and marine biological productivity: Was there a (dusty) link? *Paleoceanography*, v. 21, PA4216, doi:10.1029/2006PA001267.
- Drysdale, R.N., Hellstrom, J.C., Zanchetta, G., Fallick, A.E., Sanchez Goni, M.F., Couchoud, I., McDonald, J., Maas, R., Lohmann, G., and Isola, I., 2009, Evidence for Obliquity Forcing of Glacial Termination II: *Science*, v. 325, p. 1527–1531, doi:10.1126/science.1170371.
- Dunbar, R.B., and Wefer, G., 1984, Stable isotope fractionation in benthic foraminifera from the Peruvian continental margin: *Marine Geology*, v. 59, p. 215–225, doi:10.1016/0025-3227(84)90094-X.
- Duplessy, J.C., Lalou, C., and Vinot, A.C., 1970, Differential Isotopic Fractionation in Benthic Foraminifera and Paleotemperatures Reassessed: *Science*, v. 168, p. 250–251, doi:10.1126/science.168.3928.250.
- Duplessy, J.C., Shackleton, N.J., Fairbanks, R.G., Labeyrie, L., Oppo, D., and Kallel, N., 1988, Deepwater source variations during the last climatic cycle and their impact on the global deepwater circulation: *Paleoceanography*, v. 3, p. 343–360, doi:10.1029/PA003i003p00343.
- Duplessy, J.-C., Shackleton, N.J., Matthews, R.K., Prell, W., Ruddiman, W.F., Caralp, M., and Hendy, C.H., 1984, ^{13}C Record of benthic foraminifera in the last interglacial ocean: Implications for the carbon cycle and the global deep water circulation: *Quaternary Research*, v. 21, p. 225–243, doi:10.1016/0033-5894(84)90099-1.
- Edgar, K.M., Pälike, H., and Wilson, P.A., 2013, Testing the impact of diagenesis on the $\delta^{18}\text{O}$ and $\delta^{13}\text{C}$ of benthic foraminiferal calcite from a sediment burial depth transect in the equatorial Pacific: *Paleoceanography*, v. 28, p. 468–480, doi:10.1002/palo.20045.
- Edgar, K.M., Wilson, P.A., Sexton, P.F., and Sukanuma, Y., 2007, No extreme bipolar glaciation during the main Eocene calcite compensation shift: *Nature*, v. 448, p. 908–911, doi:10.1038/nature06053.
- Egger, L.M., Bahr, A., Friedrich, O., Wilson, P.A., Norris, R.D., Peer, T.E. Van, Lippert, P.C., Liebrand, D., and Pross, J., 2018, Marine Micropaleontology Sea-level and surface-water change in the western North Atlantic across the Oligocene – Miocene Transition : A palynological perspective from IODP Site U1406 (Newfoundland margin): *Marine Micropaleontology*, v. 139, p. 57–71, doi:10.1016/j.marmicro.2017.11.003.
- Elderfield, H., Greaves, M., Barker, S., Hall, I.R., Tripathi, A., Ferretti, P., Crowhurst, S., Booth, L., and Daunt, C., 2010, A record of bottom water temperature and seawater $\delta^{18}\text{O}$ for the Southern Ocean over the past 440 kyr based on Mg/Ca of benthic foraminiferal *Uvigerina* spp.: *Quaternary Science Reviews*, v. 29, p. 160–169, doi:10.1016/j.quascirev.2009.07.013.
- Elderfield, H., Vautravers, M., and Cooper, M., 2002, The relationship between shell size and Mg/Ca, Sr/Ca, $\delta^{18}\text{O}$, and $\delta^{13}\text{C}$ of species of planktonic foraminifera: *Geochemistry, Geophysics, Geosystems*, v. 3, p. 1–13, doi:10.1029/2001GC000194.
- Elderfield, H., Yu, J., Anand, P., Kiefer, T., and Nyland, B., 2006, Calibrations for benthic foraminiferal Mg/Ca paleothermometry and the carbonate ion hypothesis: *Earth and Planetary Science Letters*, v. 250, p. 633–649, doi:10.1016/j.epsl.2006.07.041.
- Eldrett, J.S., Harding, I.C., Wilson, P.A., Butler, E., and Roberts, A.P., 2007, Continental ice in Greenland during the Eocene and Oligocene: *Nature*, v. 446, p. 14–17, doi:10.1038/nature05591.
- Emery, W.J., 2003, Water types and water masses, in Holton, J.R., Curry, J.A., Pyle, J.A. ed., *Encyclopedia of Atmospheric Sciences*, Elsevier, p. 1556–1567, doi:10.1006/rwos.2001.0108.
- Emiliani, C., 1955, Pleistocene Temperatures: *The Journal of Geology*, v. 63, p. 538–578, doi:10.1086/626295.
- Epstein, S., Buchsbaum, R., Lowenstam, H.A., and Urey, H.C., 1953, Revised Carbonate-Water Isotopic Temperature Scale: *GSA Bulletin*, v. 64, p. 1315–1326, doi:10.1130/0016-7606(1953)64[1315:RCITS]2.0.CO;2.
- Erez, J., 1978, Vital effect on stable-isotope composition seen in foraminifera and coral skeletons: *Nature*, v. 273, p. 199–202, doi:10.1038/273199a0.

- Evans, D., Badger, M.P.S., Foster, G.L., Henehan, M.J., Lear, C.H., and Zachos, J.C., 2018, No substantial long-term bias in the Cenozoic benthic foraminifera oxygen-isotope record: *Nature Communications*, v. 9, p. 17–19, doi:10.1038/s41467-018-05303-4.
- Evans, D., and Müller, W., 2012, Deep time foraminifera Mg/Ca paleothermometry: Nonlinear correction for secular change in seawater Mg/Ca: *Paleoceanography*, v. 27, PA4205, doi:10.1029/2012PA002315.
- Fairbanks, R.G., and Matthews, R.K., 1978, The Marine Oxygen Isotope Record in Pleistocene Coral, Barbados, West Indies: *Quaternary Research*, v. 10, p. 181–196, doi:10.1016/0033-5894(78)90100-X.
- Fairbanks, R.G., Sverdrlove, M., Free, R., Wiebe, P.H., and Bé, A.W.H., 1982, Vertical distribution and isotopic fractionation of living planktonic foraminifera from the Panama Basin: *Nature*, v. 298, p. 841–844, doi:10.1038/298841a0.
- Farkaš, J. et al., 2007, Calcium isotope record of Phanerozoic oceans: Implications for chemical evolution of seawater and its causative mechanisms: *Geochimica et Cosmochimica Acta*, v. 71, p. 5117–5134, doi:10.1016/j.gca.2007.09.004.
- Ferreira, M.L. de C., and Kerr, R., 2017, Source water distribution and quantification of North Atlantic Deep Water and Antarctic Bottom Water in the Atlantic Ocean: *Progress in Oceanography*, v. 153, p. 66–83, doi:10.1016/j.pocean.2017.04.003.
- Fielding, C.R., 2018, Stratigraphic architecture of the Cenozoic succession in the McMurdo Sound region, Antarctica: An archive of polar palaeoenvironmental change in a failed rift setting: *Sedimentology*, v. 65, p. 1–61, doi:10.1111/sed.12413.
- Franco-Fraguas, P., Costa, K.B., and Toledo, F.A. de L., 2011, Stable isotope/test size relationship in *Cibicides wuellerstorfi*: *Brazilian Journal of Oceanography*, v. 59, p. 287–291, doi:10.1590/S1679-87592011000300010.
- Fratantoni, D.M., Johns, W.E., Townsend, T.L., and Hurlburt, H.E., 2000, Low-Latitude Circulation and Mass Transport Pathways in a Model of the Tropical Atlantic Ocean: *Journal of Physical Oceanography*, v. 30, p. 1944–1966, doi:10.1175/1520-0485(2000)030<1944:LLCMT>2.0.CO;2.
- Fretwell, P. et al., 2013, Bedmap2: improved ice bed, surface and thickness datasets for Antarctica: *The Cryosphere*, v. 7, p. 375–393, doi:10.5194/tc-7-375-2013.
- Friedrich, O., Schiebel, R., Wilson, P.A., Weldeab, S., Beer, C.J., Cooper, M.J., and Fiebig, J., 2012, Influence of test size, water depth, and ecology on Mg/Ca, Sr/Ca, $\delta^{18}\text{O}$ and $\delta^{13}\text{C}$ in nine modern species of planktic foraminifera: *Earth and Planetary Science Letters*, v. 319–320, p. 133–145, doi:10.1016/j.epsl.2011.12.002.
- Friedrich, O., Wilson, P.A., Bolton, C.T., Beer, C.J., and Schiebel, R., 2013, Late Pliocene to early Pleistocene changes in the North Atlantic Current and suborbital-scale sea-surface temperature variability: *Paleoceanography*, v. 28, p. 274–282, doi:10.1002/palo.20029.
- Galeotti, S. et al., 2016, Antarctic Ice Sheet variability across the Eocene-Oligocene boundary climate transition: *Science*, v. 352, p. 76–80, doi:10.1126/science.aab0669.
- Galy, A., France-Lanord, C., and Derry, L.A., 1996, The Late Oligocene-Early Miocene Himalayan belt Constraints deduced from isotopic compositions of Early Miocene turbidites in the Bengal Fan: *Tectonophysics*, v. 260, p. 109–118, doi:10.1016/0040-1951(96)00079-0.
- Gasson, E.G.W., Deconto, R.M., and Pollard, D., 2016a, Modeling the oxygen isotope composition of the Antarctic ice sheet and its significance to Pliocene sea level: *Geology*, v. 44, p. 827–830, doi:10.1130/G38104.1.
- Gasson, E.G.W., Deconto, R.M., Pollard, D., and Levy, R.H., 2016b, Dynamic Antarctic ice sheet during the early to mid-Miocene: *Proceedings of the National Academy of Sciences*, v. 113, p. 3459–3464, doi:10.1073/pnas.1516130113.
- Goldner, A., Herold, N., Huber, M., 2014. Antarctic glaciation caused ocean circulation changes at the Eocene-Oligocene transition: *Nature*, v. 511, p. 574–577, doi:10.1038/nature13597.
- Gooday, A.J., 1988, A response by benthic foraminifera to the deposition of phytodetritus in the deep sea: *Nature*, v. 332, p. 70–73, doi:10.1038/332070a0.
- Gothmann, A.M., Stolarski, J., Adkins, J.F., Schoene, B., Dennis, K.J., Schrag, D.P., Mazur, M., and Bender, M.L., 2015, Fossil corals as an archive of secular variations in seawater chemistry since the Mesozoic: *Geochimica et Cosmochimica Acta*, v. 160, p. 188–208, doi:10.1016/j.gca.2015.03.018.

- Greaves, M. et al., 2008, Interlaboratory comparison study of calibration standards for foraminiferal Mg/Ca thermometry: *Geochemistry, Geophysics, Geosystems*, v. 9, p. Q08010, doi:10.1029/2008GC001974.
- Greenop, R., Sosdian, S.M., Henahan, M.J., Wilson, P.A., Lear, C.H., and Foster, G.L., 2019, Orbital Forcing, Ice Volume, and CO₂ Across the Oligocene-Miocene Transition: *Paleoceanography and Paleoclimatology*, v. 34, p. 316–328, doi:10.1029/2018PA003420.
- Grinsted, A., 2013, The Cryosphere An estimate of global glacier volume: *The Cryosphere*, v. 7, p. 141–151, doi:10.5194/tc-7-141-2013.
- Hallam, A., 1969, Faunal realms and facies in the Jurassic: *Palaeontology*, v. 12, p. 1–18.
- Hambrey, M.J., Barrett, P.J., and Powell, R.D., 2002, Late Oligocene and early Miocene glacial marine sedimentation in the SW Ross Sea, Antarctica: the record from offshore drilling: *Geological Society, London, Special Publications*, v. 203, p. 105–128, doi:10.1144/GSL.SP.2002.203.01.07.
- Hammer, R., Harper, D.A.T., and Ryan, P.D., 2001, PAST: Paleontological Statistics Software Package for Education and Data Analysis: *Palaeontologia electronica*, v. 1, p. 9, http://palaeo-electronica.org/2001_1/past/issue1_01.htm.
- Haq, B.U., Hardenbol, J.A.N., and Vail, P.R., 1987, Chronology of Fluctuating Sea Levels Since the Triassic: *Science*, v. 235, p. 1156–1167, doi:10.1126/science.235.4793.1156.
- Hauptvogel, D.W., Pekar, S.F., and Pincay, V., 2017, Evidence for a heavily glaciated Antarctica during the late Oligocene “warming” (27.8–24.5 Ma): Stable isotope records from ODP Site 690: *Paleoceanography*, v. 32, p. 384–396, doi:10.1002/2016PA002972.
- Healey, S.L., Thunell, R.C., and Corliss, B.H., 2008, The Mg/Ca-temperature relationship of benthic foraminiferal calcite: New core-top calibrations in the <4 °C temperature range: *Earth and Planetary Science Letters*, v. 272, p. 523–530, doi:10.1016/j.epsl.2008.05.023.
- Hemleben, C., and Bijma, J., 1994, Foraminiferal Population Dynamics And Stable Carbon Isotopes, in: Zahn, R., Pedersen, T.F., Kaminski, M.A., and Labeyrie, L. eds., *Carbon Cycling in the Glacial Ocean: Constraints on the Ocean’s Role in Global Change*, Springer Berlin Heidelberg, p. 145–166.
- Henderiks, J., and Pagani, M., 2008, Coccolithophore cell size and the Paleogene decline in atmospheric CO₂: *Earth and Planetary Science Letters*, v. 269, p. 576–584, doi:10.1016/j.epsl.2008.03.016.
- Herguera, J.C., and Berger, W.H., 1991, Paleoproductivity from benthic foraminifera abundance: Glacial to postglacial change in the west-equatorial Pacific: *Geology*, v. 19, p. 1173–1176, doi:10.1130/0091-7613(1991)019<1173:PFBFAG>2.3.CO;2.
- Hesse, T., Wolf-Gladrow, D., Lohmann, G., Bijma, J., Mackensen, A., and Zeebe, R.E., 2014, Modelling $\delta^{13}\text{C}$ in benthic foraminifera: Insights from model sensitivity experiments: *Marine Micropaleontology*, v. 112, p. 50–61, doi:10.1016/j.marmicro.2014.08.001.
- von der Heydt, A., and Dijkstra, H.A., 2006, Effect of ocean gateways on the global ocean circulation in the late Oligocene and early Miocene: *Paleoceanography*, v. 21, p. 1–18, doi:10.1029/2005PA001149.
- Hohbein, M.W., Sexton, P.F., and Cartwright, J.A., 2012, Onset of North Atlantic Deep Water production coincident with inception of the Cenozoic global cooling trend: *Geology*, v. 40, p. 255–258, doi:10.1130/G32461.1.
- Holbourn, A., Henderson, A.S., and MacLeod, N., 2013, *Atlas of Benthic Foraminifera*: John Wiley & Sons, 642 p., doi:10.1002/9781118452493.
- Holbourn, A.E., Kuhnt, W., Clemens, S.C., Kochhann, K.G.D., Jöhnck, J., Lübbers, J., and Andersen, N., 2018, Late Miocene climate cooling and intensification of southeast Asian winter monsoon: *Nature Communications*, v. 9, p. 1584, doi:10.1038/s41467-018-03950-1.
- Hönisch, B., Allen, K.A., Lea, D.W., Spero, H.J., Eggins, S.M., Arbuszewski, J.A., deMenocal, P., Rosenthal, Y., Russell, A.D., and Elderfield, H., 2013, The influence of salinity on Mg/Ca in planktic foraminifers – Evidence from cultures, core-top sediments and complementary $\delta^{18}\text{O}$: *Geochimica et Cosmochimica Acta*, v. 121, p. 196–213, doi:10.1016/j.gca.2013.07.028.
- Hoogakker, B.A.A., Elderfield, H., Schmiedl, G., McCave, I.N., and Rickaby, R.E.M., 2015, Glacial–interglacial changes in bottom-water oxygen content on the Portuguese margin: *Nature Geoscience*, v. 8, p. 40–43, doi:10.1038/ngeo2317.

- Hut, G., 1987, Consultant's group meeting on stable isotope reference samples for geochemical and hydrological investigations. Report to the Director General, International Atomic Energy Agency: 42p.
- Huybers, P., 2011, Combined obliquity and precession pacing of late Pleistocene deglaciations: *Nature*, v. 480, p. 229–232, doi:10.1038/nature10626.
- Huybers, P., and Wunsch, C., 2005, Obliquity pacing of the late Pleistocene glacial terminations: *Nature*, v. 434, p. 491–494, doi:10.1038/nature03401.
- Jorissen, F.J., Fontanier, C., and Thomas, E., 2007, Paleoceanographical Proxies Based on Deep-Sea Benthic Foraminiferal Assemblage Characteristics, in Claude Hillaire-Marcel, A.D.V. ed., *Developments in Marine Geology*, Elsevier B.V, v. 1, p. 263–325, doi:10.1016/S1572-5480(07)01012-3.
- Jorissen, F.J., de Stigter, H.C., and Widmark, J.G. V, 1995, A conceptual model explaining benthic foraminiferal microhabitats: *Marine micropaleontology*, v. 26, p. 3–15, doi:10.1016/0377-8398(95)00047-X.
- Jorissen, F.J., Wittling, I., Peypouquet, J.P., Rabouille, C., and Relexans, J.C., 1998, Live benthic foraminiferal faunas off Cape Blanc, NW-Africa: community structure and microhabitats: *Deep Sea Research Part I: Oceanographic Research Papers*, v. 45, p. 2157–2188, doi:10.1016/S0967-0637(98)00056-9.
- Katz, M.E., Cramer, B.S., Franzese, A., Hönisch, B., Miller, K.G., Rosenthal, Y., and Wright, J.D., 2010, Traditional and emerging geochemical proxies in foraminifera: *Journal of Foraminiferal Research*, v. 40, p. 165–192, doi:10.2113/gsjfr.40.2.165.
- Keeling, R.F., and Stephens, B.B., 2001, Antarctic sea ice and the control of Pleistocene climate instability: *Paleoceanography*, v. 16, p. 112–131, doi:10.1029/2000PA000529.
- Kısakürek, B., Eisenhauer, A., Böhm, F., Garbe-Schönberg, D., and Erez, J., 2008, Controls on shell Mg/Ca and Sr/Ca in cultured planktonic foraminifera, *Globigerinoides ruber* (white): *Earth and Planetary Science Letters*, v. 273, p. 260–269, doi:10.1016/j.epsl.2008.06.026.
- Knutz, P.C., 2008, Palaeoceanographic Significance of Contourite Drifts, in Rebesco, M. and Camerlenghi, A.B.T.-D. in S. eds., *Contourites*, Elsevier, v. 60, p. 511–535, doi:10.1016/S0070-4571(08)10024-3.
- Kroopnick, P., 1974, The dissolved O₂-CO₂-¹³C system in the eastern equatorial pacific: *Deep Sea Research and Oceanographic Abstracts*, v. 21, p. 211–227, doi:10.1016/0011-7471(74)90059-X.
- Kucera, M., 2007, Planktonic Foraminifera as Tracers of Past Oceanic Environments, in *Developments in Marine Geology*, Elsevier, Oxford, v. 1, p. 213–262, doi:10.1016/S1572-5480(07)01011-1.
- Kucera, M. et al., 2005, Reconstruction of sea-surface temperatures from assemblages of planktonic foraminifera: multi-technique approach based on geographically constrained calibration data sets and its application to glacial Atlantic and Pacific Oceans: *Quaternary Science Reviews*, v. 24, p. 951–998, doi:https://doi.org/10.1016/j.quascirev.2004.07.014.
- Langebroek, P.M., Paul, A., and Schulz, M., 2009, Antarctic ice-sheet response to atmospheric CO₂ and insolation in the Middle Miocene: *Climate of the Past*, v. 5, p. 633–646, doi:10.5194/cp-5-633-2009, 2009.
- Langton, S.J., Rabideaux, N.M., Borrelli, C., and Katz, M.E., 2016, Southeastern Atlantic deep-water evolution during the late-middle Eocene to earliest Oligocene (Ocean Drilling Program Site 1263 and Deep Sea Drilling Project Site 366): *Geosphere*, v. 12, p. 1032–1047, doi:10.1130/GES01268.1.
- Laskar, J., Robutel, P., Joutel, F., Gastineau, M., Correia, A.C.M., and Levrard, B., 2004, Astrophysics A long-term numerical solution for the insolation quantities of the Earth: *Astronomy & Astrophysics*, v. 428, p. 261–285, doi:10.1051/0004-6361:20041335.
- Laughton, A.S., 1975, Tectonic evolution of the northeast Atlantic Ocean; a review: *Norges Geol. Unders*, v. 316, p. 169–193.
- Lea, D.W., Martin, P.A., Pak, D.K., and Spero, H.J., 2002, Reconstructing a 350 ky history of sea level using planktonic Mg/Ca and oxygen isotope records from a Cocos Ridge core: *Quaternary Science Reviews*, v. 21, p. 283–293, doi:10.1016/S0277-3791(01)00081-6.

- Lea, D.W., Mashiotta, T.A., and Spero, H.J., 1999, Controls on magnesium and strontium uptake in planktonic foraminifera determined by live culturing: *Geochimica et Cosmochimica Acta*, v. 63, p. 2369–2379, doi:10.1016/S0016-7037(99)00197-0.
- Lea, D.W., Pak, D.K., and Spero, H.J., 2000, Climate Impact of Late Quaternary Equatorial Pacific Sea Surface Temperature Variations: *Science*, v. 289, p. 1719–1724, doi:10.1126/science.289.5485.1719.
- Lear, C.H., Coxall, H.K., Foster, G.L., Lunt, D.J., Mawbey, E.M., Rosenthal, Y., Sosdian, S.M., Thomas, E., and Wilson, P.A., 2015, Neogene ice volume and ocean temperatures: Insights from infaunal foraminiferal Mg/Ca paleothermometry: *Paleoceanography*, v. 30, p. 1437–1454, doi:10.1002/2015PA002833.
- Lear, C.H., Elderfield, H., and Wilson, P.A., 2000, Cenozoic Deep-Sea Temperatures and Global Ice Volumes from Mg/Ca in Benthic Foraminiferal Calcite: *Science*, v. 287, p. 269–273, doi:10.1126/science.287.5451.269.
- Lear, C.H., Rosenthal, Y., Coxall, H.K., and Wilson, P.A., 2004, Late Eocene to early Miocene ice sheet dynamics and the global carbon cycle: *Paleoceanography*, v. 19, PA4015, doi:10.1029/2004PA001039.
- Lear, C.H., Rosenthal, Y., and Slowey, N., 2002, Benthic foraminiferal Mg/Ca-paleothermometry: A revised core-top calibration: *Geochimica et Cosmochimica Acta*, v. 66, p. 3375–3387, doi:10.1016/S0016-7037(02)00941-9.
- Lear, C.H., Rosenthal, Y., and Wright, J.D., 2003, The closing of a seaway: ocean water masses and global climate change: *Earth and Planetary Science Letters*, v. 210, p. 425–436, doi:10.1016/S0012-821X(03)00164-X.
- Lee, J.J., 1974, Towards understanding the niche of foraminifera: *Foraminifera*, v. 1, p. 207–260.
- Lee, H., and Jo, K., 2019, Oligocene paleoceanographic changes based on an interbasinal comparison of *Cibicidoides* spp. $\delta^{18}\text{O}$ records and a new compilation of data: *Palaeogeography, Palaeoclimatology, Palaeoecology*, v. 514, p. 800–812, doi:10.1016/j.palaeo.2018.09.016.
- Levy, R.H. et al., 2019, Antarctic ice-sheet sensitivity to obliquity forcing enhanced through ocean connections: *Nature Geoscience*, v. 12, p. 132–137, doi:10.1038/s41561-018-0284-4.
- Lhomme, N., 2004, Modelling water isotopes in polar ice sheets: University of British Columbia and Université Joseph Fourier, 172 p.
- Lhomme, N., Clarke, G.K.C., and Ritz, C., 2005, Global budget of water isotopes inferred from polar ice sheets: *Geophysical Research Letters*, v. 32, doi:10.1029/2005GL023774.
- Liebrand, D. et al., 2016, Cyclostratigraphy and eccentricity tuning of the early Oligocene through early Miocene (30.1–17.1 Ma): *Cibicides mundulus* stable oxygen and carbon isotope records from Walvis Ridge Site 1264: *Earth and Planetary Science Letters*, v. 450, p. 392–405, doi:10.1016/j.epsl.2016.06.007.
- Liebrand, D. et al., 2017, Evolution of the early Antarctic ice ages: *Proceedings of the National Academy of Sciences*, v. 114, p. 3867–3872, doi:10.1073/pnas.1615440114.
- Lisiecki, L.E., and Raymo, M.E., 2005, A Pliocene-Pleistocene stack of 57 globally distributed benthic $\delta^{18}\text{O}$ records: *Paleoceanography*, v. 20, p. 1–17, doi:10.1029/2004PA001071.
- Liu, Z., He, Y., Jiang, Y., Wang, H., Liu, W., Bohaty, S.M., and Wilson, P.A., 2018, Transient temperature asymmetry between hemispheres in the Palaeogene Atlantic Ocean: *Nature Geoscience*, v. 11, p. 656–660, doi:10.1038/s41561-018-0182-9.
- Lourens, L.J., Becker, J., Bintanja, R., Hilgen, F.J., Tuenter, E., van de Wal, R.S.W., and Ziegler, M., 2010, Linear and non-linear response of late Neogene glacial cycles to obliquity forcing and implications for the Milankovitch theory: *Quaternary Science Reviews*, v. 29, p. 352–365, doi:10.1016/j.quascirev.2009.10.018.
- Mackensen, A., 2012, Strong thermodynamic imprint on Recent bottom-water and epibenthic $\delta^{13}\text{C}$ in the Weddell Sea revealed: Implications for glacial Southern Ocean ventilation: *Earth and Planetary Science Letters*, v. 317–318, p. 20–26, doi:10.1016/j.epsl.2011.11.030.
- Mackensen, A., and Schmiedl, G., 2019, Stable carbon isotopes in paleoceanography: atmosphere, oceans, and sediments: *Earth-Science Reviews*, v. 197, p. 102893, doi:10.1016/j.earscirev.2019.102893.
- Mantsis, D.F., Linter, B.R., Broccoli, A.J., and Erb, M.P., 2014, The Response of Large-Scale Circulation to Obliquity-Induced Changes in Meridional Heating Gradients: *Journal of Climate*, v. 27, p. 5504–5516, doi:10.1175/JCLI-D-13-00526.1.

- Marchitto, T.M., Bryan, S.P., Curry, W.B., and McCorkle, D.C., 2007, Mg/Ca temperature calibration for the benthic foraminifer *Cibicidoides pachyderma*: *Paleoceanography*, v. 22, p. 1–11, doi:10.1029/2006PA001287.
- Martin, P.A., Lea, D.W., Rosenthal, Y., Shackleton, N.J., Sarnthein, M., and Papenfuss, T., 2002, Quaternary deep sea temperature histories derived from benthic foraminiferal Mg/Ca: *Earth and Planetary Science Letters*, v. 198, p. 193–209, doi:10.1016/S0012-821X(02)00472-7.
- Maslin, M.A., and Swann, G.E.A., 2006, Isotopes in Marine Sediments, in Leng, M.J. ed., *Isotopes in Paleoenvironmental Research*, Dordrecht, Springer Netherlands, p. 227–290, doi:10.1007/1-4020-2504-1_06.
- Mathien-Blard, E., and Bassinot, F., 2009, Salinity bias on the foraminifera Mg/Ca thermometry: Correction procedure and implications for past ocean hydrographic reconstructions: *Geochemistry, Geophysics, Geosystems*, v. 10, doi:10.1029/2008GC002353.
- Matsui, H., Nishi, H., Takashima, R., Kuroyanagi, A., Ikehara, M., Takayanagi, H., and Iryu, Y., 2016, Changes in the depth habitat of the Oligocene planktic foraminifera (*Dentoglobigerina venezuelana*) induced by thermocline deepening in the eastern equatorial Pacific: *Paleoceanography*, v. 31, p. 715–731, doi:10.1002/2016PA002950. Received.
- McConnaughey, T., 1989, ^{13}C and ^{18}O isotopic disequilibrium in biological carbonates: I. Patterns: *Geochimica et Cosmochimica Acta*, v. 53, p. 151–162, doi:10.1016/0016-7037(89)90282-2.
- McConnaughey, T.A., Burdett, J., Whelan, J.F., and Paull, C.K., 1997, Carbon isotopes in biological carbonates: Respiration and photosynthesis: *Geochimica et Cosmochimica Acta*, v. 61, p. 611–622, doi:10.1016/S0016-7037(96)00361-4.
- McCorkle, D.C., and Emerson, S.R., 1988, The relationship between pore water carbon isotopic composition and bottom water oxygen concentration: *Geochimica et Cosmochimica Acta*, v. 52, p. 1169–1178, doi:10.1016/0016-7037(88)90270-0.
- McCorkle, D.C., Veeh, H.H., and Heggge, D.T., 1994, Glacial-Holocene Paleoproductivity off Western Australia: A Comparison of Proxy Records - Carbon Cycling in the Glacial Ocean: Constraints on the Ocean's Role in Global Change, in Zahn, R., Pedersen, T.F., Kaminski, M.A., and Labeyrie, L. eds., Berlin, Heidelberg, Springer Berlin Heidelberg, p. 443–479.
- McCrea, J.M., 1950, On the isotopic chemistry of carbonates and a paleotemperature scale: *The Journal of Chemical Physics*, v. 18, p. 849–857, doi: 10.1063/1.1747785.
- Mikolajewicz, U., Maier-Reimer, E., Crowley, T.J., and Kim, K.-Y., 1993, Effect of Drake and Panamanian Gateways on the circulation of an ocean model: *Paleoceanography*, v. 8, p. 409–426, doi:10.1029/93PA00893.
- Miller, K.G., and Fairbanks, R.G., 1985, Oligocene to Miocene Carbon Isotope Cycles and Abyssal Circulation Changes: The Carbon Cycle and Atmospheric CO_2 : Natural Variations Archean to Present, v. 32, p. 469–486, doi:doi:10.1029/GM032p0469.
- Miller, K.G., Fairbanks, R.G., and Mountain, G.S., 1987, Tertiary oxygen isotope synthesis, sea level history, and continental margin erosion: *Paleoceanography*, v. 2, p. 1–19, doi:10.1029/PA002i001p00001.
- Miller, K.G., Feigenson, M.D., Wright, J.D., and Clement, B.M., 1991a, Miocene isotope reference section, Deep Sea Drilling Project Site 608: An evaluation of isotope and biostratigraphic resolution: *Paleoceanography*, v. 6, p. 33–52, doi:10.1029/90PA01941.
- Miller, K.G., Mountain, G.S., Browning, J. V., Kominz, M.A., Sugarman, P.J., Katz, M.E., and Wright, J.D., 1998, Cenozoic global sea level, sequences, and the New Jersey transect: results from coastal plain and continental slope drilling: *Reviews of Geophysics*, v. 36, p. 569–601, doi:10.1029/98RG01624.
- Miller, K.G., Wright, J.D., and Fairbanks, R.G., 1991b, Unlocking the Ice House: Oligocene-Miocene Oxygen Isotopes, Eustasy, and Margin Erosion: *Journal of Geophysical Research*, v. 96, p. 6829–6848, doi:10.1029/90JB02015.
- Moran, K. et al., 2006, The Cenozoic palaeoenvironment of the Arctic Ocean: *Nature*, v. 441, p. 601–605, doi:10.1038/nature04800.
- Morey, A.E., Mix, A.C., and Pisias, N.G., 2005, Planktonic foraminiferal assemblages preserved in surface sediments correspond to multiple environment variables: *Quaternary Science Reviews*, v. 24, p. 925–950, doi:10.1016/j.quascirev.2003.09.011.

- Mosar, J., Eide, E.A., Osmundsen, P.T., Sommaruga, A., and Torsvik, T.H., 2002, Greenland–Norway separation: a geodynamic model for the North Atlantic, in *Norwegian Journal of Geology*, v. 82, p. 281–298.
- Mucci, A., and Morse, J.W., 1990, Chemistry of Low-Temperature Abiotic Calcites-Experimental Studies on Coprecipitation, Stability, and Fractionation: *Reviews in Aquatic Sciences*, v. 3, p. 217–254.
- Murray, J.W., 2003, An illustrated guide to the benthic foraminifera of the Hebridean shelf, west of Scotland, with notes on their mode of life: *Palaeontologia Electronica*, v. 5, p. 31, http://palaeo-electronica.org/paleo/2002_2/guide/issue2_02.htm.
- Naafs, B.D.A., Stein, R., Hefter, J., Khélifi, N., De Schepper, S., and Haug, G.H., 2010, Late Pliocene changes in the North Atlantic Current: *Earth and Planetary Science Letters*, v. 298, p. 434–442, doi:10.1016/j.epsl.2010.08.023.
- Naish, T.R. et al., 2009, Obliquity-paced Pliocene West Antarctic ice sheet oscillations: *Nature*, v. 458, p. 322, <https://doi.org/10.1038/nature07867>.
- Naish, T.R. et al., 2001, Orbitally induced oscillations in the East Antarctic ice sheet at the Oligocene/Miocene boundary: *Nature*, v. 413, p. 719–723, doi:10.1038/35099534.
- Norris, R.D. et al., 2014a, Expedition 342 summary, in *Proceedings of the Integrated Ocean Drilling Program*, v. 342, *Proceedings of the Integrated Ocean Drilling Program*, v. 342, p. 1–149, doi:10.2204/iodp.proc.342.101.2014.
- Norris, R.D. et al., 2014b, Site U1406, in R. D. Norris et al. ed., *Proceedings of the Integrated Ocean Drilling Program*, v. 342, *Integrated Ocean Drilling Program*, College Station, TX., doi:10.2204/iodp.proc.342.107.2014.
- Nürnberg, D., Bijma, J., and Hemleben, C., 1996, Assessing the reliability of magnesium in foraminiferal calcite as a proxy for water mass temperatures: *Geochimica et Cosmochimica Acta*, v. 60, p. 803–814, doi:10.1016/0016-7037(95)00446-7.
- Olivetti, V., Balestrieri, M.L., Rossetti, F., Thomson, S.N., Talarico, F.M., and Zattin, M., 2015, Evidence of a full West Antarctic Ice Sheet back to the early Oligocene: insight from double dating of detrital apatites in Ross Sea sediments.: *Terra Nova*, v. 27, p. 238–246, doi:10.1111/ter.12153.
- Pachauri, R.K., Allen, M.R., Barros, V.R., Broome, J., Cramer, W., Christ, R., Church, J.A., Clarke, L., Dahe, Q., and Dasgupta, P., 2014, IPCC, 2014: *Climate Change 2014: Synthesis Report. Contribution of Working Groups I, II and III to the Fifth Assessment Report of the Intergovernmental Panel on Climate Change: IPCC*, Geneva, Switzerland, 151 p.
- Paillard, D., Labeyrie, L., and Yiou, P., 1996, Macintosh program performs time-series analysis: *Eos, Transactions American Geophysical Union*, v. 77, p. 379, doi:10.1029/1096EO00259.
- Pälike, H., Frazier, J., and Zachos, J.C., 2006a, Extended orbitally forced palaeoclimatic records from the equatorial Atlantic Ceara Rise: *Quaternary Science Reviews*, v. 25, p. 3138–3149, doi:10.1016/j.quascirev.2006.02.011.
- Pälike, H., Norris, R.D., Herrle, J.O., Wilson, P.A., Coxall, H.K., Lear, C.H., Shackleton, N.J., Tripathi, A.K., and Wade, B.S., 2006b, The Heartbeat of the Oligocene Climate System: *Science*, v. 314, p. 1894–1899, doi:10.1126/science.1133822.
- Pe-Piper, G., Piper, D.J.W., Jansa, L.F., and de Jonge, A., 2007, Early Cretaceous opening of the North Atlantic Ocean: Implications of the petrology and tectonic setting of the Fogo Seamounts off the SW Grand Banks, Newfoundland: *GSA Bulletin*, v. 119, p. 712–724, doi:10.1130/B26008.1.
- Pearson, P.N., 2012, Oxygen Isotopes in Foraminifera: Overview and Historical Review: *The Paleontological Society Papers*, v. 18, p. 1–38, doi:10.1017/S1089332600002539.
- van Peer, T.E. et al., 2017a, Data report: revised composite depth scale and splice for IODP Site U1406, in *Proceedings of the Integrated Ocean Drilling Program*, v. 342, *Integrated Ocean Drilling Program*, College Station, TX., p. 1–23, doi:10.2204/iodp.proc.342.202.2017.
- van Peer, T.E., Xuan, C., Lippert, P.C., Liebrand, D., Agnini, C., and Wilson, P.A., 2017b, Extracting a Detailed Magnetostratigraphy From Weakly Magnetized, Oligocene to Early Miocene Sediment Drifts Recovered at IODP Site U1406 (Newfoundland Margin, Northwest Atlantic Ocean): *Geochemistry, Geophysics, Geosystems*, v. 18, p. 3910–3928, doi:10.1002/2017GC007185.

- Pekar, S.F., Christie-Blick, N., Kominz, M.A., and Miller, K.G., 2002, Calibration between eustatic estimates from backstripping and oxygen isotopic records for the Oligocene: *Geology*, v. 30, p. 903–906, doi:10.1130/0091-7613(2002)030<0903:CBEEFB>2.0.CO;2.
- Pekar, S.F., DeConto, R.M., and Harwood, D.M., 2006, Resolving a late Oligocene conundrum: Deep-sea warming and Antarctic glaciation: *Palaeogeography, Palaeoclimatology, Palaeoecology*, v. 231, p. 29–40, doi:10.1016/j.palaeo.2005.07.024.
- Pekar, S.F., and Miller, K.G., 1996, New Jersey Oligocene “Icehouse” sequences (ODP Leg 150X) correlated with global $\delta^{18}\text{O}$ and Exxon eustatic records: *Geology*, v. 4, p. 567–570, doi:10.1130/0091-7613(1996)024<0567:NJOISO>2.3.CO;2.
- Pollard, D., and DeConto, R.M., 2005, Hysteresis in Cenozoic Antarctic ice-sheet variations: *Global and Planetary Change*, v. 45, p. 9–21, doi:10.1016/j.gloplacha.2004.09.011.
- Rahmstorf, S., 2002, Ocean circulation and climate during the past 120,000 years: *Nature*, v. 419, p. 207–214, doi:10.1038/nature01090.
- Rathmann, S., Hess, S., Kuhnert, H., and Mulitza, S., 2004, Mg/Ca ratios of the benthic foraminifera *Oridorsalis umbonatus* obtained by laser ablation from core top sediments: Relationship to bottom water temperature: *Geochemistry, Geophysics, Geosystems*, v. 5, Q12013, doi:10.1029/2004GC000808.
- Rathmann, S., and Kuhnert, H., 2008, Carbonate ion effect on Mg/Ca, Sr/Ca and stable isotopes on the benthic foraminifera *Oridorsalis umbonatus* off Namibia: *Marine Micropaleontology*, v. 66, p. 120–133, doi:10.1016/j.marmicro.2007.08.001.
- Rausch, S., Böhm, F., Bach, W., Klügel, A., and Eisenhauer, A., 2013, Calcium carbonate veins in ocean crust record a threefold increase of seawater Mg/Ca in the past 30 million years: *Earth and Planetary Science Letters*, v. 362, p. 215–224, doi:10.1016/j.epsl.2012.12.005.
- Ravelo, A.C., and Fairbanks, R.G., 1992, Oxygen Isotopic Composition of Multiple Species of Planktonic Foraminifera: Recorders of the Modern Photic Zone Temperature Gradient: *Paleoceanography*, v. 7, p. 815–831, doi:10.1029/92PA02092.
- Ravelo, A.C., and Hillaire-Marcel, C., 2007, The Use of Oxygen and Carbon Isotopes of Foraminifera in Paleoceanography, in Hillaire-Marcel, C., De Vernal, A. ed., *Developments in Marine Geology*, Elsevier B.V, v. 1, p. 735–764, doi:10.1016/S1572-5480(07)01023-8.
- Raymo, M.E., and Nisancioglu, K., 2003, The 41 kyr world: Milankovitch’s other unsolved mystery: *Paleoceanography*, v. 18, PA1011, doi:10.1029/2002PA000791.
- Rebesco, M., Hernández-Molina, F.J., Van Rooij, D., and Wåhlin, A., 2014, Contourites and associated sediments controlled by deep-water circulation processes: State-of-the-art and future considerations: *Marine Geology*, v. 352, p. 111–154, doi:10.1016/j.margeo.2014.03.011.
- Regenberg, M., Nürnberg, D., Schönfeld, J., and Reichert, G.-J., 2007, Early diagenetic overprint in Caribbean sediment cores and its effect on the geochemical composition of planktonic foraminifera: *Biogeosciences Discussions*, v. 4, p. 2179–2213, doi:10.5194/bgd-4-2179-2007.
- Regenberg, M., Regenberg, A., Garbe-Schönberg, D., and Lea, D.W., 2014, Global dissolution effects on planktonic foraminiferal Mg/Ca ratios controlled by the calcite-saturation state of bottom waters: *Paleoceanography*, v. 29, p. 127–142, doi:10.1002/2013PA002492.
- Regenberg, M., Steph, S., Nürnberg, D., Tiedemann, R., and Garbe-Schönberg, D., 2009, Calibrating Mg/Ca ratios of multiple planktonic foraminiferal species with $\delta^{18}\text{O}$ -calcification temperatures: *Paleothermometry for the upper water column: Earth and Planetary Science Letters*, v. 278, p. 324–336, doi:10.1016/j.epsl.2008.12.019.
- Repschläger, J., Weinelt, M., Kinkel, H., Andersen, N., Garbe-Schönberg, D., and Schwab, C., 2015, Response of the subtropical North Atlantic surface hydrography on deglacial and Holocene AMOC changes: *Paleoceanography*, v. 30, p. 456–476, doi:10.1002/2014PA002637.
- Rhein, M., Kieke, D., and Steinfeldt, R., 2015, Advection of North Atlantic Deep Water from the Labrador Sea to the southern hemisphere: *Journal of Geophysical Research: Oceans*, v. 120, p. 2471–2487, doi:10.1002/2014JC010605.
- Richardson, M.J., Wimbush, M., and Mayer, L., 1981, Exceptionally Strong Near-Bottom Flows on the Continental Rise of Nova Scotia: *Science*, v. 213, p. 887–888, doi:10.1126/science.213.4510.887.

- Rickaby, R.E.M., and Elderfield, H., 2005, Evidence from the high-latitude North Atlantic for variations in Antarctic Intermediate water flow during the last deglaciation: *Geochemistry, Geophysics, Geosystems*, v. 6, Q05001, doi:10.1029/2004GC000858.
- de Rijk, S., Jorissen, F.J., Rohling, E.J., and Troelstra, S.R., 2000, Organic flux control on bathymetric zonation of Mediterranean benthic foraminifera: *Marine Micropaleontology*, v. 40, p. 151–166, doi:https://doi.org/10.1016/S0377-8398(00)00037-2.
- Rohling, E.J., and Bigg, G.R., 1998, Paleosalinity and $\delta^{18}\text{O}$: A critical assessment: *Journal of Geophysical Research: Oceans*, v. 103, p. 1307–1318, doi:10.1029/97JC01047.
- Rohling, E.J., and Cooke, S., 2003, Stable oxygen and carbon isotopes in foraminiferal carbonate shells, in *Modern Foraminifera*, Dordrecht, Springer Netherlands, p. 239–258, doi:10.1007/0-306-48104-9_14.
- Rosenthal, Y., 2007, Elemental Proxies for Reconstructing Cenozoic Seawater Paleotemperatures from Calcareous Fossils, in Claude Hillaire-Marcel, A.D.V. ed., *Developments in Marine Geology*, Elsevier B.V., v. 1, p. 765–797, doi:10.1016/S1572-5480(07)01024-X.
- Rosenthal, Y., and Boyle, E.A., 1993, Factors controlling the fluoride content of planktonic foraminifera: An evaluation of its paleoceanographic applicability: *Geochimica et Cosmochimica Acta*, v. 57, p. 335–346, doi:10.1016/0016-7037(93)90435-Y.
- Rosenthal, Y., Boyle, E.A., and Slowey, N., 1997, Temperature control on the incorporation of magnesium, strontium, fluorine, and cadmium into benthic foraminiferal shells from Little Bahama Bank: Prospects for thermocline paleoceanography: *Geochimica et Cosmochimica Acta*, v. 61, p. 3633–3643, doi:10.1016/S0016-7037(97)00181-6.
- Rosenthal, Y., Lohmann, G.P., Lohmann, K.C., and Sherrell, R.M., 2000, Incorporation and preservation of Mg in *Globigerinoides sacculifer*: implications for reconstructing the temperature and $^{18}\text{O}/^{16}\text{O}$ of seawater: *Paleoceanography*, v. 15, p. 135–145, doi:10.1029/1999PA000415.
- Ruddiman, W.F., 2008, *Earth's Climate: Past and Future*: Macmillan.
- Ruddiman, W.F., 2006, Ice-driven CO_2 feedback on ice volume: *Climate of the Past Discussions*, v. 2, p. 43–78, doi:10.5194/cpd-2-43-2006.
- Russell, A.D., Hönisch, B., Spero, H.J., and Lea, D.W., 2004, Effects of seawater carbonate ion concentration and temperature on shell U, Mg, and Sr in cultured planktonic foraminifera: *Geochimica et Cosmochimica Acta*, v. 68, p. 4347–4361, doi:10.1016/j.gca.2004.03.013.
- Rutherford, S., D'Hondt, S., and Prell, W., 1999, Environmental controls on the geographic distribution of zooplankton diversity: *Nature*, v. 400, p. 749–753, doi:10.1038/23449.
- Sadekov, A., Eggins, S.M., de Deckker, P., and Kroon, D., 2008, Uncertainties in seawater thermometry deriving from intratest and intertest Mg/Ca variability in *Globigerinoides ruber*: *Paleoceanography*, v. 23, PA1215, doi:10.1029/2007PA001452.
- Saenko, O.A., Weaver, A.J., and Schmittner, A., 2003, Atlantic deep circulation controlled by freshening in the Southern Ocean: *Geophysical Research Letters*, v. 30, 1754, doi:10.1029/2003GL017681.
- Salabarnada, A. et al., 2018, Paleoceanography and ice sheet variability offshore Wilkes Land, Antarctica – Part 1: Insights from late Oligocene astronomically paced contourite sedimentation: *Climate of the Past*, v. 14, p. 991–1014, doi:10.5194/cp-14-991-2018.
- Schiebel, R., 2002, Planktic foraminiferal sedimentation and the marine calcite budget: *Global Biogeochemical Cycles*, v. 16, 1065, doi:10.1029/2001GB001459, 2002.
- Schiebel, R., and Hemleben, C., 2005, Modern planktic foraminifera: *Paläontologische Zeitschrift*, v. 79, p. 135–148, doi: 10.1007/BF03021758.
- Schiebel, R., and Hemleben, C., 2017, *Planktic foraminifera in the modern ocean*: Springer Berlin Heidelberg, 358 p., doi:10.1007/978-3-662-50297-6.
- Schlitzer, R., 2019, Ocean data view: <https://odv.awi.de>.
- Schmidt, D.N., Renaud, S., Bollmann, J., Schiebel, R., and Thierstein, H.R., 2004, Size distribution of Holocene planktic foraminifer assemblages: biogeography, ecology and adaptation: *Marine Micropaleontology*, v. 50, p. 319–338, doi:10.1016/S0377-8398(03)00098-7.
- Schmiedl, G., and Mackensen, A., 2006, Multispecies stable isotopes of benthic foraminifera reveal past changes of organic matter decomposition and deepwater oxygenation in the Arabian Sea: *Paleoceanography*, v. 21, PA4213, doi:10.1029/2006PA001284.

- Schmiedl, G., Mitschele, A., Beck, S., Emeis, K.-C., Hemleben, C., Schulz, H., Sperling, M., and Weldeab, S., 2003, Benthic foraminiferal record of ecosystem variability in the eastern Mediterranean Sea during times of sapropel S5 and S6 deposition: *Palaeogeography, Palaeoclimatology, Palaeoecology*, v. 190, p. 139–164, doi:[https://doi.org/10.1016/S0031-0182\(02\)00603-X](https://doi.org/10.1016/S0031-0182(02)00603-X).
- Schmiedl, G., Pfeilsticker, M., Hemleben, C., and Mackensen, A., 2004, Environmental and biological effects on the stable isotope composition of recent deep-sea benthic foraminifera from the western Mediterranean Sea: *Marine Micropaleontology*, v. 51, p. 129–152, doi:<https://doi.org/10.1016/j.marmicro.2003.10.001>.
- Schmitz, W.J., McCartney, M.S., Schmitz Jr., W.J., McCartney, M.S., Schmitz, W.J., McCartney, M.S., Schmitz Jr., W.J., McCartney, M.S., Schmitz, W.J., and McCartney, M.S., 1993, On the North Atlantic Circulation: *Reviews of Geophysics*, v. 31, p. 29–49, doi:10.1029/92RG02583.
- Schneider, B., and Schmittner, A., 2006, Simulating the impact of the Panamanian seaway closure on ocean circulation, marine productivity and nutrient cycling: *Earth and Planetary Science Letters*, v. 246, p. 367–380, doi:10.1016/j.epsl.2006.04.028.
- Schönfeld, J., and Altenbach, A.V., 2005, Late Glacial to Recent distribution pattern of deep-water *Uvigerina* species in the north-eastern Atlantic: *Marine Micropaleontology*, v. 57, p. 1–24, doi:10.1016/j.marmicro.2005.05.004.
- Schrag, D.P., Hampt, G., and Murray, D.W., 1996, Pore Fluid Constraints on the Temperature and Oxygen Isotopic Composition of the Glacial Ocean: *Science*, v. 272, p. 1930–1932, doi:10.1126/science.272.5270.1930.
- Schulz, M., Mudelsee, M., 2002. REDFIT: estimating red-noise spectra directly from unevenly spaced paleoclimatic time series. *Comput. Geosci.* 28, p. 421–426, doi:10.1016/S0098-3004(01)00044-9.
- Schwab, C., Kinkel, H., Weinelt, M., and Repschläger, J., 2012, Coccolithophore paleoproductivity and ecology response to deglacial and Holocene changes in the Azores Current System: *Paleoceanography*, v. 27, PA3210, doi:10.1029/2012PA002281.
- Sexton, P.F., and Wilson, P.A., 2009, Preservation of benthic foraminifera and reliability of deep-sea temperature records: Importance of sedimentation rates, lithology, and the need to examine test wall structure: *Paleoceanography*, v. 24, PA2208, doi:10.1029/2008PA001650.
- Shackleton, N.J., 1974, Attainment of isotopic equilibrium between ocean water and the benthonic foraminifera genus *Uvigerina*: isotopic changes in the ocean during the last glacial: *University of Cambridge*, p. 203–210, doi:10.1021/la3005486.
- Shackleton, N., 1967, Oxygen isotope analyses and Pleistocene temperatures re-assessed: *Nature*, v. 215, p. 15–17, doi:10.1038/215015a0.
- Shackleton, N.J., Crowhurst, S.J., Weedon, G.P., and Laskar, J., 1999, Astronomical calibration of Oligocene–Miocene time: *Philosophical Transactions of the Royal Society of London. Series A: Mathematical, Physical and Engineering Sciences*, v. 357, p. 1907–1929, doi:10.1098/rsta.1999.0407.
- Shackleton, N.J., Hall, M.A., and Boersma, A., 1984, Oxygen and carbon isotope data from Leg-74 foraminifers: *Initial Reports of the Deep Sea Drilling Project, Volume 74*, p. 599–612, doi:10.2973/dsdp.proc.74.115.1984.
- Shackleton, N.J., Imbrie, J., and Hall, M.A., 1983, Oxygen and carbon isotope record of East Pacific core V19-30: implications for the formation of deep water in the late Pleistocene North Atlantic: *Earth and Planetary Science Letters*, v. 65, p. 233–244, doi: 10.1016/0012-821X(83)90162-0.
- Shakun, J.D., Clark, P.U., He, F., Marcott, S.A., Mix, A.C., Liu, Z., Otto-Bliesner, B., Schmittner, A., and Bard, E., 2012, Global warming preceded by increasing carbon dioxide concentrations during the last deglaciation: *Nature*, v. 484, p. 49–54, doi:10.1038/nature10915.
- Sosdian, S.M., and Rosenthal, Y., 2009, Deep-Sea Temperature and Ice Volume Changes Across the Pliocene-Pleistocene Climate Transitions: *Science*, v. 325, p. 306–310, doi:10.1126/science.1169938.
- Spero, H.J., Bijma, J., Lea, D.W., and Bemis, B.E., 1997, Effect of seawater carbonate concentration on foraminiferal carbon and oxygen isotopes: *Nature*, v. 390, p. 497–500, doi:10.1038/37333.

- Spero, H.J., and Lea, D.W., 1993, Intraspecific stable isotope variability in the planktic foraminifera *Globigerinoides sacculifer*: Results from laboratory experiments: *Marine Micropaleontology*, v. 22, p. 221–234, doi: 10.1016/0377-8398(93)90045-Y.
- Spero, H.J., and Parker, S.L., 1985, Photosynthesis in the symbiotic planktonic foraminifer *Orbulina universa*, and its potential contribution to oceanic primary productivity: *Journal of Foraminiferal Research*, v. 15, p. 273–281, doi:10.2113/gsjfr.15.4.273.
- Spray, J.F., Bohaty, S.M., Davies, A., Bailey, I., Romans, B.W., Cooper, M.J., Milton, J.A., and Wilson, P.A., 2019, North Atlantic Evidence for a Unipolar Icehouse Climate State at the Eocene-Oligocene Transition: *Paleoceanography and Paleoclimatology*, v. 34, p. 1124–1138, doi:10.1029/2019PA003563.
- St John, K., 2008, Cenozoic ice-rafting history of the central Arctic Ocean: Terrigenous sands on the Lomonosov Ridge: *Paleoceanography*, v. 23, PA1S05, doi:10.1029/2007PA001483.
- Stap, L.B., van de Wal, R.S.W., de Boer, B., Bintanja, R., and Lourens, L.J., 2014, Interaction of ice sheets and climate during the past 800,000 years: *Climate of the Past*, v. 10, p. 2135–2152, doi:10.5194/cp-10-2135-2014.
- Stewart, J.A., Wilson, P.A., Edgar, K.M., Anand, P., and James, R.H., 2012, Geochemical assessment of the palaeoecology, ontogeny, morphotypic variability and palaeoceanographic utility of “*Dentoglobigerina*” *venezuelana*: *Marine Micropaleontology*, v. 84, p. 74–86, doi: 10.1016/j.marmicro.2011.11.003.
- Stickley, C.E., Koç, N., Pearce, R.B., Kemp, A.E.S., Jordan, R.W., Sangiorgi, F., and St John, K., 2012, Variability in the length of the sea ice season in the middle eocene arctic: *Geology*, v. 40, p. 727–730, doi:10.1130/G32976.1.
- Stickley, C.E., St John, K., Koç, N., Jordan, R.W., Passchier, S., Pearce, R.B., and Kearns, L.E., 2009, Evidence for middle Eocene Arctic sea ice from diatoms and ice-rafted debris: *Nature*, v. 460, p. 376–379, doi:10.1038/nature08163.
- Stocker, T.F., 1998, Climate Change: The Seesaw Effect: *Science*, v. 282, p. 61–62, doi:10.1126/science.282.5386.61.
- Stocker, T.F., and Johnsen, S.J., 2003, A minimum thermodynamic model for the bipolar seesaw: *Paleoceanography*, v. 18, 1087, doi:10.1029/2003PA000920.
- Stouffer, R.J., and Manabe, S., 2003, Equilibrium response of thermohaline circulation to large changes in atmospheric CO₂ concentration: *Climate Dynamics*, v. 20, p. 759–773, doi:10.1007/s00382-002-0302-4.
- Talley, L.D., 2013, Closure of the Global Overturning Circulation Through the Indian, Pacific, and Southern Oceans: *Oceanography*, v. 26, p. 80–97, doi:10.5670/oceanog.2013.07.
- Talley, L.D., Pickard, G.L., Emery, W.J.H., and Swift, J., 2011, *Descriptive Physical Oceanography: An Introduction*: Academic Press.
- Theodor, M., Schmiedl, G., and Mackensen, A., 2016, Stable isotope composition of deep-sea benthic foraminifera under contrasting trophic conditions in the western Mediterranean Sea: *Marine Micropaleontology*, v. 124, p. 16–28, doi:10.1016/j.marmicro.2016.02.001.
- Thomas, D.J., Röhl, U., and Childress, L.B., 2020, Expedition 378 Preliminary Report: South Pacific Paleogene Climate: International Ocean Discovery Program, International Ocean Discovery Program Preliminary Report, v. 378, doi:10.14379/iodp.pr.378.2020.
- Tisserand, A.A., Dokken, T.M., Waelbroeck, C., Gherardi, J.-M., Scao, V., Fontanier, C., and Jorissen, F.J., 2013, Refining benthic foraminiferal Mg/Ca-temperature calibrations using core-tops from the western tropical Atlantic: Implication for paleotemperature estimation: *Geochemistry, Geophysics, Geosystems*, v. 14, p. 929–946, doi:10.1002/ggge.20043.
- Tomczak, M., and Godfrey, J.S., 2013, *Regional oceanography: an introduction*: Elsevier, 390 p.
- Toyofuku, T., Kitazato, H., Kawahata, H., Tsuchiya, M., and Nohara, M., 2000, Evaluation of Mg/Ca thermometry in foraminifera: Comparison of experimental results and measurements in nature: *Paleoceanography*, v. 15, p. 456–464, doi:10.1029/1999PA000460.
- Tripathi, A.K. et al., 2008, Evidence for glaciation in the Northern Hemisphere back to 44 Ma from ice-rafted debris in the Greenland Sea: *Earth and Planetary Science Letters*, v. 265, p. 112–122, doi:10.1016/j.epsl.2007.09.045.

- Tucholke, B.E., Sawyer, D.S., and Sibuet, J.-C., 2007, Breakup of the Newfoundland–Iberia rift: Geological Society, London, Special Publications, v. 282, p. 9–46, doi:10.1144/SP282.2.
- Urey, H.C., 1947, The thermodynamic properties of isotopic substances: *Journal of the Chemical Society (Resumed)*, p. 562–581.
- Vandenbergh, N., Hilgen, F.J., Speijer, R.P., Ogg, J.G., Gradstein, F.M., Hammer, O., Hollis, C.J., and Hooker, J.J., 2012, The Paleogene Period, in Gradstein, F.M., Ogg, J.G., Schmitz, M.D., and Ogg, G.M.B.T.-T.G.T.S. eds., *The Geologic Time Scale*, Boston, Elsevier, p. 855–921, doi:10.1016/B978-0-444-59425-9.00028-7.
- Vellinga, M., and Wood, R.A., 2002, Global Climatic Impacts of a Collapse of the Atlantic Thermohaline Circulation: *Climatic Change*, v. 54, p. 251–267, doi:10.1023/A:1016168827653.
- Versteegh, G.J.M., Brinkhuis, H., Visscher, H., and Zonneveld, K.A.F., 1996, The relation between productivity and temperature in the Pliocene North Atlantic at the onset of northern hemisphere glaciation: a palynological study: *Global and Planetary Change*, v. 11, p. 155–165, doi:10.1016/0921-8181(95)00054-2.
- Villanueva, J., Calvo, E., Pelejero, C., Grimalt, J.O., Boelaert, A., and Labeyrie, L., 2001, A latitudinal productivity band in the central North Atlantic over the last 270 kyr: An alkenone perspective: *Paleoceanography*, v. 16, p. 617–626, doi:10.1029/2000PA000543.
- Vimeux, F., Masson, V., Jouzel, J., Stievenard, M., and Petit, J.R., 1999, Glacial–interglacial changes in ocean surface conditions in the Southern Hemisphere: *Nature*, v. 398, p. 410–413, doi:10.1038/18860.
- Vincent, E., and Berger, W.H., 1981, Planktonic foraminifera and their use in paleoceanography, in *The oceanic lithosphere*, Wiley-Interscience New York, v. 7, p. 1025–1119.
- de Vleeschouwer, D., Vahlenkamp, M., Crucifix, M., and Pälike, H., 2017, Alternating Southern and Northern Hemisphere climate response to astronomical forcing during the past 35 m.y.: *Geology*, v. 45, p. 375–378, doi:10.1130/G38663.1.
- Wade, B.S., Berggren, W.A., and Olsson, R.K., 2007, The biostratigraphy and paleobiology of Oligocene planktonic foraminifera from the equatorial Pacific Ocean (ODP Site 1218): *Marine Micropaleontology*, v. 62, p. 168–179, doi:10.1016/j.marmicro.2006.08.005.
- Wade, B.S., Kroon, D., and Norris, R.D., 2001, Orbitally forced climate change in late mid-Eocene time at Blake Nose (Leg 171B): evidence from stable isotopes in foraminifera: Geological Society, London, Special Publications, v. 183, p. 273–291, doi:10.1144/GSL.SP.2001.183.01.13.
- Wade, B.S., and Pälike, H., 2004, Oligocene climate dynamics: *Paleoceanography*, v. 19, PA4019, doi:10.1029/2004PA001042.
- Waelbroeck, C., Labeyrie, L., Michel, E., Duplessy, J.C., McManus, J.F., Lambeck, K., Balbon, E., and Labracherie, M., 2002, Sea-level and deep water temperature changes derived from benthic foraminifera isotopic records: *Quaternary Science Reviews*, v. 21, p. 295–305, doi:10.1016/S0277-3791(01)00101-9.
- Weaver, A.J., 2003, Meltwater Pulse 1A from Antarctica as a Trigger of the Bolling-Allerod Warm Interval: *Science*, v. 299, p. 1709–1713, doi:10.1126/science.1081002.
- Wefer, G., and Berger, W.H., 1991, Isotope paleontology: growth and composition of extant calcareous species: *Marine Geology*, v. 100, p. 207–248, doi:10.1016/0025-3227(91)90234-U.
- Wendler, I., Huber, B.T., MacLeod, K.G., and Wendler, J.E., 2013, Stable oxygen and carbon isotope systematics of exquisitely preserved Turonian foraminifera from Tanzania - Understanding isotopic signatures in fossils: *Marine Micropaleontology*, v. 102, p. 1–33, doi:10.1016/j.marmicro.2013.04.003.
- Wilson, D.S., Jamieson, S.S.R., Barrett, P.J., Leitchenkov, G., Gohl, K., and Larter, R.D., 2012, Antarctic topography at the Eocene–Oligocene boundary: *Palaeogeography, Palaeoclimatology, Palaeoecology*, v. 335–336, p. 24–34, doi:10.1016/j.palaeo.2011.05.028.
- Wilson, D.S., and Luyendyk, B.P., 2009, West Antarctic paleotopography estimated at the Eocene–Oligocene climate transition: *Geophysical Research Letters*, v. 36, L16302, doi:10.1029/2009GL039297.
- Wright, J.D., and Miller, K.G., 1996, Control of North Atlantic Deep Water Circulation by the Greenland–Scotland Ridge: *Paleoceanography*, v. 11, p. 157–170, doi:10.1029/95PA03696.

- Yu, J., and Elderfield, H., 2008, Mg/Ca in the benthic foraminifera *Cibicidoides wuellerstorfi* and *Cibicidoides mundulus*: Temperature versus carbonate ion saturation: Earth and Planetary Science Letters, v. 276, p. 129–139, doi:10.1016/j.epsl.2008.09.015.
- Yu, J., Elderfield, H., and Piotrowski, A.M., 2008, Seawater carbonate ion- $\delta^{13}\text{C}$ systematics and application to glacial–interglacial North Atlantic ocean circulation: Earth and Planetary Science Letters, v. 271, p. 209–220, doi:10.1016/j.epsl.2008.04.010.
- Zachos, J.C., Berggren, W.A., Aubry, M.-P., and Mackensen, A., 1992, Isotope and Trace Element Geochemistry of Eocene and Oligocene Foraminifers from Site 748, Kerguelen Plateau, in Wise Jr, S.W. and Schlich, R. eds., Proceedings of the Ocean Drilling Program, Volume 120 Scientific Results, Ocean Drilling Program, doi:10.2973/odp.proc.sr.120.183.1992.
- Zachos, J.C., Dickens, G.R., and Zeebe, R.E., 2008, An early Cenozoic perspective on greenhouse warming and carbon-cycle dynamics: Nature, v. 451, p. 279–283, doi:10.1038/nature06588.
- Zachos, J.C., Flower, B.P., and Paul, H.A., 1997, Orbitally paced climate oscillations across the Oligocene/Miocene boundary: Nature, v. 388, p. 567–570, doi:10.1038/41528.
- Zachos, J.C., Pagani, M., Sloan, L., Thomas, E., and Billups, K., 2001a, Trends, Rhythms, and Aberrations in Global Climate 65 Ma to Present: Science, v. 292, p. 686–693, doi:10.1126/science.1059412.
- Zachos, J.C., Quinn, T.M., and Salamy, K.A., 1996, High-resolution (10^4 years) deep-sea foraminiferal stable isotope records of the Eocene-Oligocene climate transition: Paleoceanography, v. 11, p. 251–266, doi:10.1029/96PA00571.
- Zachos, J.C., Shackleton, N.J., Revenaugh, J.S., Pälike, H., and Flower, B.P., 2001b, Climate Response to Orbital Forcing Across the Oligocene-Miocene Boundary: Science, v. 292, p. 274–279, doi: 10.1126/science.1058288.
- Zachos, J.C., Stott, L.D., and Lohmann, K.C., 1994, Evolution of Early Cenozoic marine temperatures: Paleoceanography, v. 9, p. 353–387, doi:10.1029/93PA03266.
- Zeebe, R.E., 2007, Modeling CO_2 chemistry, $\delta^{13}\text{C}$, and oxidation of organic carbon and methane in sediment porewater: Implications for paleo-proxies in benthic foraminifera: Geochimica et Cosmochimica Acta, v. 71, p. 3238–3256, doi:10.1016/j.gca.2007.05.004.
- Zeebe, R.E., and Tyrrell, T., 2018, Comment on “The Effects of Secular Calcium and Magnesium Concentration Changes on the Thermodynamics of Seawater Acid/Base Chemistry: Implications for Eocene and Cretaceous Ocean Carbon Chemistry and Buffering” by Hain et al. (2015): Global Biogeochemical Cycles, v. 32, p. 895–897, doi:10.1002/2017GB005786.
- Zeebe, R.E., and Wolf-Gladrow, D., 2001, CO_2 in Seawater: Equilibrium, Kinetics, Isotopes: Elsevier Science, 346 p.
- Zhang, X. et al., 2012, Changes in equatorial Pacific thermocline depth in response to Panamanian seaway closure: Insights from a multi-model study: Earth and Planetary Science Letters, v. 317–318, p. 76–84, doi:https://doi.org/10.1016/j.epsl.2011.11.028.
- Zhang, Y.G., Pagani, M., Liu, Z., Bohaty, S.M., and DeConto, R.M., 2013, A 40-million-year history of atmospheric CO_2 : Philosophical Transactions of the Royal Society A, v. 371, p. 20130096, doi:10.1098/rsta.2013.0096.
- Zhang, J., Quay, P.D., and Wilbur, D.O., 1995, Carbon isotope fractionation during gas-water exchange and dissolution of CO_2 : Geochimica et Cosmochimica Acta, v. 59, p. 107–114, doi:10.1016/0016-7037(95)91550-D.
- van der Zwaan, G.J., Duijnste, I.A.P., Den Dulk, M., Ernst, S.R., Jannink, N.T., and Kouwenhoven, T.J., 1999, Benthic foraminifers: proxies or problems?: a review of paleoecological concepts: Earth-Science Reviews, v. 46, p. 213–236, doi: 10.1016/S0012-8252(99)00011-2

APPENDIX

All data produced and presented in this thesis have been uploaded to the World Data Center PANGAEA online repository at www.pangaea.de.

- Dynamics of the late Oligocene Antarctic Ice Sheet - Dataset 1 (data presented in Chapter 5)
- Dynamics of the late Oligocene Antarctic Ice Sheet - Dataset 2 (data presented in Chapter 6)
- Dynamics of the late Oligocene Antarctic Ice Sheet - Dataset 3 (data presented in Chapter 7)



**Eidesstattliche Versicherung gemäß § 8 der Promotionsordnung für die
Naturwissenschaftlich-Mathematische Gesamtfakultät der Universität Heidelberg /
Sworn Affidavit according to § 8 of the doctoral degree regulations of the Combined
Faculty of Natural Sciences and Mathematics**

1. Bei der eingereichten Dissertation zu dem Thema / **The thesis I have submitted entitled**

Dynamics of the Late Oligocene Antarctic Ice Sheet

.....
handelt es sich um meine eigenständig erbrachte Leistung / **is my own work.**

2. Ich habe nur die angegebenen Quellen und Hilfsmittel benutzt und mich keiner unzulässigen Hilfe Dritter bedient. Insbesondere habe ich wörtlich oder sinngemäß aus anderen Werken übernommene Inhalte als solche kenntlich gemacht. / **I have only used the sources indicated and have not made unauthorised use of services of a third party. Where the work of others has been quoted or reproduced, the source is always given.**

3. Die Arbeit oder Teile davon habe ich wie folgt/bislang nicht¹⁾ an einer Hochschule des In- oder Auslands als Bestandteil einer Prüfungs- oder Qualifikationsleistung vorgelegt. / **I have not yet/have already¹⁾ presented this thesis or parts thereof to a university as part of an examination or degree.**

Titel der Arbeit / **Title of the thesis:** Dynamics of the Late Oligocene Antarctic Ice Sheet

Hochschule und Jahr / **University and year:** Heidelberg University, 2020

Art der Prüfungs- oder Qualifikationsleistung / **Type of examination or degree:**

4. Die Richtigkeit der vorstehenden Erklärungen bestätige ich. / **I confirm that the declarations made above are correct.**

5. Die Bedeutung der eidesstattlichen Versicherung und die strafrechtlichen Folgen einer unrichtigen oder unvollständigen eidesstattlichen Versicherung sind mir bekannt. / **I am aware of the importance of a sworn affidavit and the criminal prosecution in case of a false or incomplete affidavit.**

Ich versichere an Eides statt, dass ich nach bestem Wissen die reine Wahrheit erklärt und nichts verschwiegen habe. / **I affirm that the above is the absolute truth to the best of my knowledge and that I have not concealed anything.**

.....
Ort und Datum / **Place and date**

.....
Unterschrift / **Signature**

¹⁾ Nicht Zutreffendes streichen. Bei Bejahung sind anzugeben: der Titel der andernorts vorgelegten Arbeit, die Hochschule, das Jahr der Vorlage und die Art der Prüfungs- oder Qualifikationsleistung. / **Please cross out what is not applicable. If applicable, please provide: the title of the thesis that was presented elsewhere, the name of the university, the year of presentation and the type of examination or degree.**